

CONTROLLING THERMAL LIGHT-MATTER INTERACTIONS

BY

SEAN MOLESKY

A THESIS SUBMITTED IN PARTIAL FULFILLMENT OF THE REQUIREMENTS FOR THE
DEGREE OF

DOCTOR OF PHILOSOPHY
IN
MICROSYSTEMS AND NANODEVICES

DEPARTMENT OF ELECTRICAL AND COMPUTER ENGINEERING
UNIVERSITY OF ALBERTA

©SEAN MOLESKY, 2017

Abstract

Since the development of the fluctuation dissipation theorem for electromagnetics in 1956 by Landau, Lipschitz and Rytov, field correlations have gradually come to be understood as a consistent framework for treating all optical aspects of linear response. In turn, the theory of electromagnetic correlations acts as a central unifying thread running through a diverse collection of optical phenomena: ranging from the definition of a medium's relative permittivity and rate of spontaneous emission to its electromagnetic entropy, extractable energy density and thermal radiation characteristics. With the maturation of the field of nanophotonics, an array of techniques have recently emerged for controlling these correlations via resonant wavelength scale structuring and polaritonic excitations. These results challenge long held views of the equivalence between high temperature and incoherence, and through the discovery of modified scaling laws open a new landscape of possibilities for heat energy harvesting devices.

This dissertation brings together our original results examining the role that permittivity properties play in shaping these correlations; addressing open problems in far-field radiative engineering, near-field energy harvesting, and the theory of hyperbolic media. Background on the field and motivation of our approach is provided in Chapter One. Chapters Two and Three are then dedicated to the control of radiative thermal emission for energy harvesting applications. Here, we begin by presenting a new perspective for understanding the far-field thermal radiation arising from any nanostructure through the use of effective medium parameters. This metamaterial approach to radiative emission control is then used to originate two

classes of selective emitter designs to meet the engineering challenges of capturing latent heat energy. As a functional example, we conceive and demonstrate a refractory metamaterial using simple multilayer nanostructuring to regulate thermal emission in the near infrared. Mastery of thermal radiation in this spectral range is crucial to thermophotovoltaic energy harvesting technologies, and we analyze the usefulness of metamaterial concepts for this application in detail. In Chapter Four, we reveal the influence of electronic characteristics on near-field electromagnetic energy transfer. Approaching relative permittivity as a black box response function, subject only to the requirements of causality and bandgap absorption, we derive the ideal response characteristics for maximizing the magnitude and efficiency of electromagnetic energy transfer in the near-field. This analysis reveals that the traditional bulk semiconductors, considered in previous near-field thermophotovoltaic work, are ill-suited for this type of energy capture. Moreover, it also shows that the presence of van Hove singularities, seen in any semiconductor with a quantum-confined dimension, offer a clear path for improving future near-field devices. Chapter Five then develops a definitive, and first numerically predictive, framework for regularizing electromagnetic field fluctuations inside natural hyperbolic media based on the presence of previously overlooked charge oscillations. These media have long been considered one of the most promising directions for nanophotonics, but long standing divergence issues have left their fundamental electromagnetic correlation characteristics undefined. Our theory overcomes this hurdle, and places definite upper bounds on the enhancement features and thermal energy density of these exotic media. To showcase the flexibility of our results, concrete, experimentally verifiable, predictions of the enhancement properties of the naturally hyperbolic materials bismuth selenide and hexagonal boron nitride are given. Finally, in Chapter Six, we summarize our results, and provide a brief outlook of the field.

Preface

Some of the research conducted for this thesis forms part of an international research collaboration, led by Professor M. Eich at the Hamburg University of Technology, and Professor Z. Jacob at the University of Alberta. The result of this collaboration, reproduced in their entirety in Chapter 2, have been previously published as

- P. N. Dyachenko^{1*}, S. Molesky^{2*}, A. Yu. Petrov^{1,3}, M. Störmer⁴, T. Krekeler⁵, S. Lang¹, M. Ritter⁵, Z. Jacob^{2,6} and M. Eich¹. (*equal contributions) “Controlling thermal emission with refractory epsilon-near-zero metamaterials via topological transitions.” Nature communications 7 (2016).

1. Institute of Optical and Electronic Materials, Hamburg University of Technology, Eissendorfer Strasse 38, 21073 Hamburg, Germany.

2. University of Alberta, Department of Electrical and Computer Engineering, 9107-116 Street, T6G 2V4, Edmonton, Canada.

3. ITMO University, 49 Kronverskii Ave., 197101, St. Petersburg, Russia.

4. Institute of Materials Research, Helmholtz-Zentrum Geesthacht Centre for Materials and Coastal Research, Max-Planck-Strae 1, 21502, Geesthacht, Germany.

5. Electron Microscopy Unit, Hamburg University of Technology, Eissendorfer

Strasse 42, 21073 Hamburg, Germany.

6. Birck Nanotechnology Center, School of Electrical and Computer Engineering, Purdue University, West Lafayette, IN 47906, USA

My original contribution to this project consisted of the design of the reported metamaterial, numerical modeling of results in collaboration with S. Lang, measurement of all reported room temperature optical properties and preparation of the manuscript for publication.

Similarly, Chapters 2, 4 and 5 are direct reproductions, published respectively as

- S. Molesky, C.J. Dewalt, and Z. Jacob. “High temperature epsilon-near-zero and epsilon-near-pole metamaterial emitters for thermophotovoltaics.” *Optics express* 21, no. 101 (2013): A96-A110

University of Alberta, Department of Electrical and Computer Engineering, 9107 - 116 Street, T6G 2V4, Edmonton, Canada.

- S. Molesky, and Z. Jacob “Ideal near-field thermophotovoltaic cells.” *Physical Review B* 91, no. 20 (2015): 205435

University of Alberta, Department of Electrical and Computer Engineering, 9107 - 116 Street, T6G 2V4, Edmonton, Canada.

- S. Molesky and Z.Jacob “Quantum Optical Sum Rules and Field Fluctuations inside Natural Hyperbolic Media: Hexagonal Boron Nitride and Bismuth Selenide” arXiv:1702.01862 (2017) Feb 7

1. University of Alberta, Department of Electrical and Computer Engineering, 9107-116 Street, T6G 2V4, Edmonton, Canada.

2. Birck Nanotechnology Center, School of Electrical and Computer Engineering, Purdue University, West Lafayette, IN 47906, USA

In these works, Z. Jacob served as the supervising author and was involved with concept formation and finalizing the manuscripts for publication. I am responsible for all other aspects.

To my parents

Acknowledgments

Above all, I would like to thank my advisor Zubin Jacob, whose passion and patience for understanding have been ever present guides throughout my studies. Zubin's uncanny ability to sense the most important aspects of a problem and ask the right questions has unquestionably been the single most important influence in shaping my scientific views and abilities over the past six year. Through all the meetings, emails, and drafts I can only hope some of this instinct has rubbed off. My shortcomings are my own, and my successes directly owed to you.

I am comparably indebted to my steadfast friends Cris Cortes, Prashant Shekhar, and Ward Newman, who I have worked alongside since my first day as a graduate student. The time we have spent together sharing ideas, perspectives and experiences has been some of the happiest of my life. I don't care to imagine what my studies would have been without your friendships.

I am also extremely grateful to the rest of the talented group of colleagues that I have had the pleasure of getting to know along the way. In particular, I would like to thank Yu Guo, for his unique philosophical outlook, and introducing me to some new topics in mathematics, Fahrid Kalhor, Saman Jahani, and Dirk Jalas, for their careful approaches to scientific reasoning, Ryan Starko-Bowes, Pavel Dyachenkov, and Slawa Lang for their practical physical insights and openness to collaboration, and Marvin Schulz for his comradery during my stay in Hamburg.

There are few proverbs I believe more than *It takes a village to raise a child*, and I am very appreciative of the staff and faculty in the departments of Electrical Engineering and Physics at the University of Alberta, and the Institute of Optical and Electronic Materials at the Technical University of Hamburg that have supported my academic development and kept the administrative side running smoothly in the background. Specifically, I would like to recognize Frank Hegmann, for giving me a start in research, always coming through to get me out of a jam, and serving as a member of my supervisory committee; Manfred Eich and Alexander Petrov for their extraordinary commitment and support for our collaborative research projects; Pinder Bains for her administrative dedication to the Jacob research group; and Professors Ashwin Iyer, Manisha Gupta, and Robert Fedosejevs for taking the time to serve on my supervisory committee.

Moreover, the work presented in this thesis would not have been possible without the funding I received from the National Science and Research Council of Canada (NSERC), the University of Alberta, Alberta Innovates Technology Futures (AITF), and the government of Alberta. And so, to every Canadian that has supported the funding of these programs I am throughly grateful.

My fascination with science has clearly been inherited from my father, Stephen, who gave me my first glimpse of the amazing explanatory power of physics, and has continually inspired me to push my abilities. Beyond academics, the unconditional love and support of my entire family, mother, Deborah, brother, Cameron, sister, Allison, and grandmother Leona have been the current pulling me along through the highs and lows of the day to day as long as I can remember. I am undeniably lucky to have you all.

Finally, I want to thank my assuredly better half, Mariana. Having you in my life makes all the difference in the world.

Contents

1	Background and Motivation	1
1.1	Thesis structure and motivation	5
1.2	Linear response and the fluctuation dissipation theorem	8
1.3	Electromagnetic field correlations	10
1.3.1	The classical fluctuation dissipation theorem	10
1.3.2	Stochastic Maxwell equations	13
1.3.3	Energy and heat transfer from field correlations	14
2	Designing Thermal Emission with Metamaterials	19
2.1	Introduction	20
2.2	Epsilon-near-zero (ENZ) and epsilon-near-pole (ENP) narrow band absorbers and emitters	22
2.2.1	Tailored emission and optical absorption	22
2.2.2	ENZ and ENP absorption	22
2.3	Practical ENZ and ENP with metamaterials	25
2.3.1	Natural ENZ and ENP resonances	25
2.3.2	One-dimensional multilayer structure	26
2.3.3	Two-dimensional nanowire structure	28
2.3.4	Metamaterial thermal antenna	28
2.4	High temperature plasmonic metamaterials	31
2.5	Energy conversion efficiency of TPV devices	32
2.5.1	Characteristics of ENZ and ENP emitters for TPVs	32
2.5.2	Shockley-Queisser efficiency analysis	33
2.5.3	Energy conversion results	36
2.6	Summary	38
3	Controlling Thermal Emission with Refractory Epsilon-near-zero Metamaterials via Topological Transitions	39
3.1	Introduction	41
3.2	Results	42
3.2.1	Metamaterial design	42
3.2.2	Experimental verification	47
3.3	Discussion	52
3.4	Experimental Methods	52
3.5	Summary	56

4	Ideal Near-field Thermophotovoltaic Cells	57
4.1	Introduction	58
4.2	Energy considerations for maximal photonic heat transfer	61
4.3	Model thermophotovoltaic system	65
4.4	Summary	69
5	Quantum Optical Sum Rules and Field Fluctuations inside Natural Hyperbolic Media	70
5.1	Introduction	72
5.2	Polariton excitations in anisotropic media	75
5.2.1	Characteristics of the microscopic decomposition	76
5.2.2	Isotropic media	76
5.2.3	Anisotropic media	77
5.3	Normal variable decomposition of the anisotropic green function . .	80
5.4	Model-independent regularization of the fluctuation density through spatial non-locality	82
5.5	The sum rule for modified spontaneous emission enhancement in hyperbolic media	86
5.6	Thermal fluctuations in hexagonal boron nitride and bismuth selenide	90
5.7	Summary	94
6	Summary	96
6.1	Outlook	98
	Bibliography	100
	Appendices	130
A	Historical Perspective	131
B	The Blackbody Distribution	137
B.1	Density of free space states	137
B.2	State expectation in the canonical ensemble	138
B.3	Planck's quantization	139
C	Power Transfer between Half Spaces	141
C.1	S-polarized components	141
C.2	P-polarized components	142
C.3	Final forms	144
D	General Green Function Results	146
D.1	Mathematical basis of Green functions	146
D.2	Electromagnetic Green function relations	146
D.3	Electromagnetic Green function in Cartesian coordinates	147
D.4	Lehmann representation and the density of states	149
D.5	Connection to energy dissipation	150
E	Optical Properties of Carbon Nanotubes	152

F	Additional Results for Natural Hyperbolic Media	155
F.1	Issues in the Purcell factor and photonic density of states	155
F.2	Dipole emission in anisotropic media	161
F.3	Calculation of the Purcell factor	163
F.4	Physical constraints on non-locality in polarization response	165
F.5	Validity of the local response approximation for hexagonal boron ni- tride and bismuth selenide in the infrared	166
F.6	Half-Space transverse thermal electric field fluctuations	167

List of Figures

1.1	General relations for thermal electromagnetic field correlations of nanophotonic structures.	4
1.2	Half space thermal electromagnetic power transfer.	16
2.1	Emission characteristics of ENZ and ENP type resonances.	24
2.2	Metamaterial implementations of ENZ and ENP behavior.	26
2.3	Radiative spectral control of a ENZ metamaterial.	27
2.4	Radiative spectral control of a ENP metamaterial.	29
2.5	Metamaterial thermal antenna.	30
2.6	Alternative plasmonic materials and ENP tuning.	32
2.7	Metamaterial emitter for thermophotovoltaics.	34
2.8	Efficiency of metamaterial thermophotovoltaic systems.	37
3.1	Thermal emission across an optical topological transition.	40
3.2	Overlap of the spectral irradiance of a blackbody half-space with natural optical resonances.	43
3.3	Concept and implementation of the tungsten/hafnium dioxide refractory metamaterial.	45
3.4	Absorptivity of the metamaterial versus incidence angle.	47
3.5	Measured absorptivity versus incidence angle.	48
3.6	Thermal stability of refractory metamaterial.	49
3.7	Elemental analysis of thermal stability.	50
3.8	Absorptivity and emissivity at high temperature.	51

3.9	Schematic of experimental setup for measuring metamaterial thermal emission.	55
4.1	Comparison of photonic heat transfer between the near-field and far-field.	59
4.2	Electronic density and energy harvesting	60
4.3	Dimensional scaling of near-field energy transfer.	65
4.4	Optical permittivity of a carbon nanotube metamaterial.	67
4.5	Carbon nanotubes for near-field thermophotovoltaic cells.	68
5.1	Wave conditions and fluctuation density.	73
5.2	Quantum optical sum rule for transverse spontaneous emission enhancement in hyperbolic media.	87
5.3	Polaritonic spontaneous emission enhancement surpassing the sum rule in hyperbolic media.	88
5.4	Scaling with material absorption of fluctuation densities in hyperbolic media.	89
5.5	Relative thermal energy and fluctuation densities in natural hyperbolic media.	91
5.6	Angular polaritonic fluctuation density in natural hyperbolic media.	92
5.7	Near-field electromagnetic energy density of natural hyperbolic media.	94
F.1	Overview of material properties and Purcell factor.	156
F.2	Relative scaling of the photonic density of states and Purcell factor.	158
F.3	Dipole emission patterns in a uniaxial media.	160
F.4	Dipole emission across a hyperbolic transition.	163

List of Tables

2.1	Optical quality and melting point of infrared plasmonic media. . . .	31
F.1	Permittivity proportionality of the photonic density of states and Purcell factor.	158

Chapter 1

Background and Motivation

In this first chapter, we motivate the general study of thermal electromagnetic field correlations, provide concise presentations of the fluctuation-dissipation theorem and Rytovian electrodynamics, and detail the structure of this thesis.

In the standard physics curriculum, the relation between thermodynamics and electromagnetism typically begins and ends with Planck's blackbody distribution; a result that beautifully explains both the specific and universal characteristics of the electromagnetic field generated by almost any finite temperature object that can be observed in the far-field¹. The generality and impressiveness of this theory naturally begets a sense that it provides a complete description of thermal electromagnetics, more or less appreciable to any system one may wish to study. However, this sentiment is simply false.

First, there are many important subtleties that limit the domain of applicability of the blackbody spectrum. For instance, it is derived from high level thermodynamic arguments that rely on the object in question being much larger than any of the wavelengths considered, while simultaneously having no fine structural features on the length scale of the electromagnetic radiation that it describes. Second, it is a strictly macroscopic picture that provides no description of how thermal electromagnetic magnetic fields are generated. Therefore, when the validity of the approximations of which the blackbody distribution is based begin to breakdown there is no indication of how the theory should be continued.

¹Field characteristics are actually determined by Kirchhoff law of thermal radiation. This result states that the far-field electromagnetic radiation of any object, under certain approximations that will be discussed later in this thesis, is the product of two factors: the absorptivity of the object, the fraction of light of incident light that is neither transmitted or reflected, and the blackbody distribution.

In order to extend the historically crucial notions of heat energy and thermal electromagnetics to micro and nano length scales it is clear that another concept is needed. It for this reason that we turn to the idea of electromagnetic field correlations.

The notion of a correlation is central to the study of any stochastic system. To quantify dynamic behavior we inherently require a quantity that is meaningful on the time scale of individual events. To extract information from noise we inherently require many measurements. Fundamentally, there is no simpler way to simultaneously satisfy these criteria than by examining the differences and similarities between successive events; and in essence, a correlation is nothing more than a mathematical definition of this concept.

That such a simple idea provides the means to generally bridge hierarchies of macroscopic and microscopic description is perhaps one of the deepest results of 20th century physics. It is naturally intuitive to think that by considering averages we can move to increasingly coarse pictures. However, in taking averages it is not apparent that the microscopic characteristics will persist in any sort of universal way. That such a universal relation does indeed exist in the fluctuation-dissipation theorem is unquestionably startling². That moreover the relation is simple and powerful enough to use as a basis for quantitative calculations is astonishing.

The fluctuation-dissipation theorem holds that the non-equilibrium linear response of an average quantity is determined by the correlation profile of this same quantity in equilibrium. That is, there is a general relation between how average macroscopic quantities will respond to external stimuli, and the finer correlation statistics characterizing their microscopic behavior in equilibrium. Crucially, if one of these two quantities is modified, then so is the other. It is this connection between microscale features and macroscopic behavior that lies at the heart of the contemporary understanding of thermal electromagnetic field correlations.

The current realization of this link, in the field of photonics, began to form in late 1980's with two seminal papers on inhibited spontaneous emission [1], and localization [2] in solid-state systems. Although the idea that physical structures could be used to alter electromagnetic field correlations, and in turn modify spontaneous emission, was already well established³, the effect had been discussed predominately

²We have included a brief history of the fluctuation-dissipation theorem for electromagnetic correlations in the appendix *Historical Perspective*. A derivation of the theorem is given in the next section.

³The first clear result in this direction was given by Purcell in 1946 [3].

for quantum systems^{4,5}. The preceding contributions marked an important shift in perspective. Namely, it was shown not only that correlation characteristics could be controlled in solid state settings, but that structures to achieve this control were within the reach of current fabrication techniques⁶.

Yet, while in retrospect these works contained nearly all the essential kernels, implications for controlling thermal properties of the electromagnetic field were not immediately explored. Perhaps surprisingly, these ramifications waited until turn of the century; beginning in 1999 with Pendry’s discussion of radiative heat exchange between nanostructures [12]^{7,8}, and the works of Le Gall, Olivier, and Greffet [16], and later Carminati, Greffet [17] and Shchegrov [18] on near field thermal coherence⁹. Nevertheless, following these papers it was soon generally realized that:

(1) The effects nanoscale structures were known to induce on the photonic density of states¹⁰ [20–23], extended nearly without modification to the thermal electromagnetic field.

(2) In the presence of nanoscale structures both the magnitude and spectral content of thermal electromagnetic field correlations could be vastly different than expectations based on the blackbody distribution.

From this vista, over the next decade a rich picture of the influence of nanoscale features on thermal electromagnetic correlations emerged. Shortly following the above time-frame, experimental results confirmed the ability of microscale structuring to alter far-field thermal properties. In quick succession, it was shown that the presence of a photonic bandgap produced broadband thermal radiation suppression [24–26]¹¹, and that consequently these media could potentially act as narrow-

⁴In particular see the works of Milonni [4], Bykov [5], Cohen-Tannoudji and Reynaud [6], Kleppner [7, 8], and Goy [9], Gross, and Haroche.

⁵However, this is not to say that macroscopic system had not been discussed. See for instance Agarwal’s 1975 paper [10].

⁶These papers are exemplary illustrations of the spirit of Feynman’s *There’s plenty of room at the bottom* [11].

⁷Again, the fact that radiative heat exchange on the nanoscale is a much stronger phenomena than at larger length scales was already established [13, 14]. For more details see the accompanying appendix: *Historical Perspective*.

⁸Formula for thermal correlations near other simple nanoscale structures were rapidly published by Volokitin and Persson [15].

⁹Note that Greffet had begun pursuing these ideas in the mid nineties [19]

¹⁰The definition of the photonic density of states is nearly identical to the definition of thermal electromagnetic correlations. Distinctions and precise definitions are provided in the appendix *Additional Results for Natural Hyperbolic Media*.

¹¹The first paper cited here generated considerable attention for simultaneously, mistakenly, reporting far-field emissivity greater than the blackbody limit. Within a year, it was determined that the findings were in error [27–29].

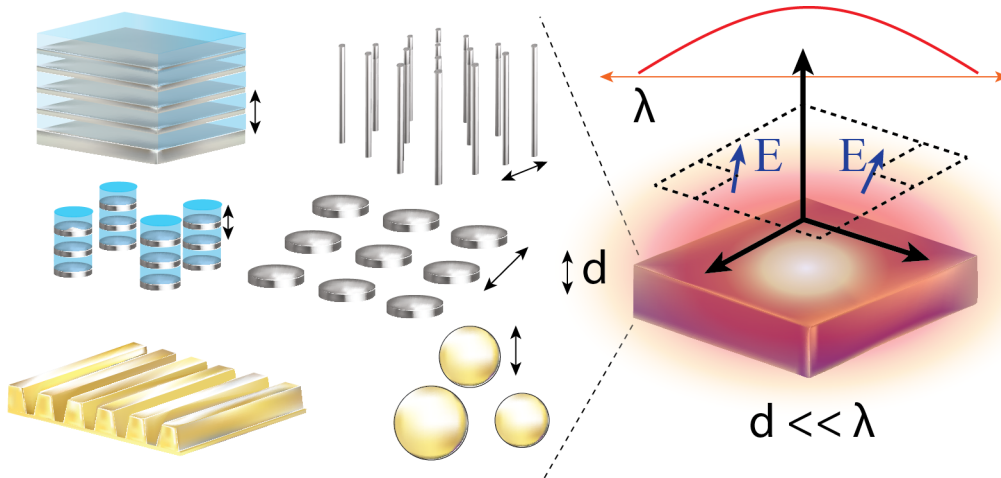


Figure 1.1: **General relations for thermal electromagnetic field correlations of nanophotonic structures.**

The figure shows a schematic illustration of the perspective of thermal electromagnetic field correlations that we will develop in Chapters Two, Three, and Four. Namely, that by investigating the permittivity of a nanostructure, either directly or through effective medium theory, many characteristics of its thermal electromagnetic field correlations can be analytically understood and numerically predicted. Near nanophotonic structures these thermal electromagnetic field correlations may display high degrees of both spectral and spatial coherence, and are commonly orders of magnitude stronger than expectations based on the blackbody distribution.

band thermal emitters [30,31] in the near infrared. (These results were immediately recognized as strong motivation for reevaluating the potential of thermophotovoltaic energy harvesting [32–35].) Over this same period, diffractive grating structures, coupling typically dark plasmon polariton modes¹² to the far-field, were experimentally verified to have resonant, highly angular emission properties, showcasing that both the spectral content and spatial coherence of thermal radiation could be engineered [36,37]. Furthermore, in complement with these far-field results, substantial advancements were also made in confirming the validity of the theory in the near-field. These experiments [38,39], commencing with the thermal scanning tunneling results of Kittel et al. in 2005 [40], cemented that enhanced heat transfer does in fact occur, reestablishing the validity of proximity effects first observed in the late 60’s¹³.

In recognition of this remarkable consistency between theory and experiment, over the past decade interest in applied topics has greatly expanded. Following the

¹²The word polariton describes any optically active material mode. That is, a mode of a material that necessarily generates an average polarization.

¹³These results were seriously doubted following a negative result, contradicting the Rytovian electrodynamics, published by Xu et. al. in 1994 [41].

initial work done on photonic crystals [42, 43], an ever wider variety of potential micro and nanostructures have been considered for controlling far-field thermal radiation, including bullseye’s [44], metasurfaces [45, 46], metamaterials [47–49], inverse opals [50, 51], defect structures [52, 53], wavelength scale resonant structures [54, 55], and self-assembled systems [56]. Experiments measuring the enhancement of near-field energy transfer have pushed to new domains of precision [57–63], and are currently nearing the limits of classical description [64, 65]. Similarly, a broad range of previously unexamined conceptual areas have been pursued; including the extension of electromagnetic correlation theory to novel media [66–68], effects for many bodies [69–71], simplifying theoretical reformulations [72–74], general upper bounds of enhancement [75–77], effects of spatial non-locality [78, 79] and more efficient computational approaches [80–83].

1.1 Thesis structure and motivation

It is in this context of rapidly proliferating systems and approaches to controlling the thermal electromagnetic field that the work undertaken in this thesis has been pursued. Specifically, as highlighted by the recent push for inverse design methods [84–86], although the past decade has seen incredible advancement, reliable design principles for intuitively understanding the general thermal correlation features that will result from a particular structure have yet to emerge. It is clear that light-matter resonances can be used to enhance thermal field correlation; and that contrastingly an absence of photonic modes can be used to induce suppression. However, beyond these characterizations, where significant progress has been made, there is little to clarify what types of structures should be used, and what other general features of a given system impact performance.

Our approach to treating this problem has been to work from the “middle” level of description of captured by relative permittivity, $\epsilon(\omega, T)$ ¹⁴. As this function is itself a catch-all for describing average light-matter interactions [88, 89], its position offers certain natural advantages. Looking up, for a given frequency it directly provides a single number that captures many of the most salient macroscopic characteristics of a medium. Looking down, it provides a relatively straightforward connection to microscopic electronic features, connecting thermal field correlations with electronic band structure and quasi particle material descriptions.

The thesis is structured as follows. To finish our introduction of the topic, the remainder of the introduction is given to a concise presentation of the fluctuation-

¹⁴As opposed to the wavelength scale structuring, or recent atomistic investigations [76, 87].

dissipation theorem and Rytovian electrodynamics. Following these preliminary sections, topics are presented in the order below.

Chapters Two and Three investigate the control and analysis of radiative thermal emission from the perspective of metamaterials. We begin by breaking with previous wavelength scale resonant design approaches; initiating the study of how deeply sub wavelength (nano) structures generally alter a system's far-field radiative properties. From this analysis we introduce two classes of thermal optical response characteristics, epsilon-near-zero (ENZ) and epsilon-near-pole (ENP), that classify all metamaterial (effective medium) selective emitters.

This view is then explored as tool for radiative engineering in the near infrared. Command over thermal radiation between 1 and 3 microns is crucial to thermo photovoltaic energy harvesting technologies, and has far reaching implications for mitigating heat losses in energy production¹⁵. To face this engineering challenge, we conceive both ENP and ENZ metamaterial emitter designs that can be used as part of a thermophotovoltaic device (operating at 1500 K) to surpass the full concentration Shockley-Queisser limit conversion efficiency of 41 %.

To verify these theoretical ideas, we next model and fabricate a refractory metamaterial using simple multilayer nanostructuring to regulate thermal emission in the near infrared (Chapter 2). This structure successfully demonstrate the design principles of Chapter 1, and is shown to be thermally stable up to nearly 1300 K . Notable milestones of this first area of research include:

- Complete classification of the spectrally selective radiative thermal emission properties that can be achieved with metamaterials (any nano structure operating in the effective medium limit) into epsilon-near-zero and epsilon-near-pole archetypes. (Prior to our work, neither type of response had been considered in the context of radiative thermal emission.)
- Introduction of thermally stable (lossy) metals supporting high temperature plasmons as a useful constituent material for metamaterial designs. (Previous work had not considered metamaterial applications above 600 K , and hence was focused entirely on low loss metals, primarily gold and silver.)
- The first experimental demonstration of metamaterial design principles at high temperature (1000 $^{\circ}C$).

In Chapter Four, we reveal the influence of electronic characteristics (band structure) on near-field electromagnetic energy transfer. Approaching the relative permittivity

¹⁵Over 50 % of energy produced globally is lost as waste heat [90].

as a black box response function, subject only to the requirements of causality and bandgap absorption, we derive the ideal characteristics of a near-field photovoltaic cell. This analysis uncovers both that traditional bulk (three dimensional) semiconductors are ill-suited for near-field energy capture, and that media with van Hove singularities, seen in any semiconductor with a quantum confined dimension, allow for vastly improved performance. As an exemplary implementation of these results, we show how a hypothetical carbon nanotube near-field thermophotovoltaic system operating at 1300 K can be designed so that 73 % of the heat energy captured would be converted to electronic modes above the bandgap. These results have advanced this potentially transformative field of study by providing:

- Formulation of extremely near-field photonic heat transfer in terms of the joint density of electronic states, connecting electronic band structure with electromagnetic heat transfer.
- Delineation of a practical method for improving near-field electromagnetic energy harvesting: the switch from bulk to low dimensional semiconductors.

Chapter Five then moves to a reworking of the theory of electromagnetic field fluctuations inside natural hyperbolic media. In this chapter, we construct a method for eliminating the divergences encountered in all previous calculations of these quantities based on the presence of hitherto overlooked charge oscillations. Natural hyperbolic media have long been heralded as a key platform for future nanophotonic devices, but these issues in defining the fundamental electromagnetic correlation characteristics have left many important optical properties undefined. By solving this issue, our theory provides the first precise quantitative estimates for the enhancement features and thermal energy density of these media (a definitive upper bounds). For hexagonal boron nitride and bismuth selenide, two of the most promising naturally occurring candidate materials for future hyperbolic applications, we predict that electromagnetic fluctuations are enhanced over 120 times (and over 800 times larger along specific angular directions). These findings conclusively resolve the following previously open problems:

- Determination of the formal electromagnetic enhancement characteristics of hyperbolic media. (Definitive proof of non-trivial quantum optical sum rules.)
- Revelation of a mathematically rigorous microscopic theory of volume polariton excitations inside hyperbolic media. (These excitations had only been qualitatively described in previous work.)

Finally, in Chapter Six we briefly summarize this thesis and provide an outlook of the field of electromagnetic field correlations going forward.

1.2 Linear response and the fluctuation dissipation theorem

As stated in the initial introduction, Planck's blackbody distribution is not directly applicable to objects on the micro or nanoscale. To proceed, a new theory required. In this section and the next, we present the Rytovian formulation of electrodynamics, thermal electromagnetics based on the fluctuation dissipation theorem. To give a broader view of how general these results are, we first begin by deriving the fluctuation dissipation theorem in the context of arbitrary linear response. In the next section, these findings are applied to electromagnetics. The theoretical results presented in these two sections act as a starting point for all of our original contributions.

Beginning with zero temperature quantum mechanics, to first order the change in the expectation value of a physical observable under the influence of a perturbation is given by the expression [91]

$$\delta \langle \hat{O}(\mathbf{r}, t) \rangle = -\frac{i}{\hbar} \int_{t_o}^t dt' \langle \Psi_o | [\hat{O}_{H_o}(\mathbf{r}, t), \hat{H}_{H_o}(t')] | \Psi_o \rangle \quad (1.1)$$

where H_o is the Hamiltonian of the system in equilibrium, Ψ_o its Heisenberg ground state, $[\cdot, \cdot]$ the commutator, t_o the time that the perturbation is turned on, $\hat{H}_{H_o}(t')$ the Hamiltonian of the perturbation ($\hat{H}_{tot}(t) = \hat{H}_o(t) + \hat{H}(t)$), $\hat{O}(\mathbf{r}, t)$ the operator of interest, and the H_o subscript denotes the Heisenberg picture for an operator in the equilibrium system. If the perturbation is the product of an external, classical, field and an observable of the system $\hat{H}_{H_o}(t') = \int_{V_r} d\mathbf{r} \hat{A}_{H_o}(\mathbf{r}, t') \phi(\mathbf{r}, t')$, where $\phi(\mathbf{r}, t')$ the external field and $\hat{A}_{H_o}(\mathbf{r}, t')$ is the observable then the above becomes

$$\delta \langle \hat{O}(\mathbf{r}, t) \rangle = -\frac{i}{\hbar} \int_{t_o}^t \int_{V_r} dt' d\mathbf{r}' \langle \Psi_o | [\hat{O}_{H_o}(\mathbf{r}, t), \hat{A}_{H_o}(\mathbf{r}', t')] | \Psi_o \rangle \phi(\mathbf{r}', t'). \quad (1.2)$$

Interestingly, this expression is already a type of correlation, with the wavefunction Ψ_o playing the role of the stochastic variable. The analogy is strengthened by the fact that as individual terms either piece of the commutator may be complex. Since $\delta \langle \hat{O}(\mathbf{r}, t) \rangle$ must be real, both pieces are required.

Moreover, by definition, the expression is also a statement about the linear response of the system, defining the *retarded Green function*

$$\mathcal{G}_{oA}(\mathbf{r}, t; \mathbf{r}', t') = -\frac{i\theta(t-t')}{\hbar} \langle \Psi_o | [\hat{O}_{H_o}(\mathbf{r}, t), \hat{A}_{H_o}(\mathbf{r}', t')] | \Psi_o \rangle, \quad (1.3)$$

with $\theta(t - t')$ denoting the Heaviside step function. Using this relation the two quantities are identified by the relation

$$\mathcal{G}_{oA}(\mathbf{r}, t; \mathbf{r}', t') = \frac{2}{\hbar} \text{Im} \left\{ \left\langle \Psi_o | \hat{O}_{H_o}(\mathbf{r}, t), \hat{A}_{H_o}(\mathbf{r}', t') | \Psi_o \right\rangle \right\}, \quad (1.4)$$

showing that even without explicitly introducing temperature the linear response of system is still a sort of statement about its correlations.

Moving to finite temperature this relation becomes exact. Working in the grand canonical ensemble, the change to an observable to first order becomes

$$\delta \langle \hat{O}(\mathbf{r}, t) \rangle = -\frac{i}{\hbar} \int_{t_o}^t dt' \text{Tr} \left\{ \hat{\rho}_G \left[\hat{O}_{H_o}(\mathbf{r}, t), \hat{A}_{H_o}(\mathbf{r}', t') \right] \right\} \phi(\mathbf{r}', t'), \quad (1.5)$$

where $\text{Tr} \{ \dots \}$ denotes the sum over all variable number quantum states, and $\hat{\rho}_G$ is the statistical operator, or density matrix,

$$\hat{\rho}_G = e^{\beta(\Omega - \hat{K})}, \quad (1.6)$$

with $\beta = 1/(k_B T)$, Ω the thermodynamic potential, and $\hat{K} = \hat{H}_o - \mu \hat{N}$ the thermodynamic Hamiltonian, with μ denoting the chemical potential and \hat{N} the number operator. Letting

$$\chi_{oA}(\mathbf{r}, t; \mathbf{r}', t') = \text{Tr} \left\{ \hat{\rho}_G \left[\hat{O}_{H_o}(\mathbf{r}, t), \hat{A}_{H_o}(\mathbf{r}', t') \right] \right\}, \quad (1.7)$$

the second term in the commutator may be expanded as

$$\begin{aligned} \text{Tr} \left\{ \hat{\rho}_G \hat{A}_{H_o}(\mathbf{r}', t') \hat{O}_{H_o}(\mathbf{r}, t) \right\} &= \quad (1.8) \\ e^{\beta\Omega} \text{Tr} \left\{ e^{-\beta\hat{K}} e^{it'/\hbar\hat{H}_o} \hat{A}_S(\mathbf{r}') e^{-i(t'-t)/\hbar\hat{H}_o} \hat{O}_S(\mathbf{r}) e^{-it/\hbar\hat{H}_o} \right\} &= \\ \pm \text{Tr} \left\{ \hat{\rho}_G \hat{O}_{H_o}(\mathbf{r}, t + i\beta/\hbar) \hat{A}_{H_o}(\mathbf{r}', t') \right\}, & \end{aligned}$$

where in the third line the commutativity of the number operator and the cyclic property of the trace have been used. (Here, \pm occurs depending on whether the wave function obeys Fermi or Bose statistics.) Assuming that the original system described by \hat{H}_o is stationary, so that only relative time $t - t'$ differences are meaningful, using (1.8), the Fourier transform of (1.7) shows that

$$\chi_{oA}(\mathbf{r}, \mathbf{r}', \omega) = \left(1 \pm e^{-\beta\omega} \right) S_{oA}(\mathbf{r}, \mathbf{r}', \omega), \quad (1.9)$$

where $S_{OA}(\mathbf{r}, \mathbf{r}', \omega)$, the structure factor, is defined in terms of the correlations of the system as

$$S_{OA}(\mathbf{r}, \mathbf{r}', t) = Tr \left\{ \hat{\rho}_G \delta \hat{O}_{H_o}(\mathbf{r}, t) \delta \hat{A}_{H_o}(\mathbf{r}', 0) \right\}, \quad (1.10)$$

with $\delta \hat{O}_{H_o}(\mathbf{r}, t) = \hat{O}_{H_o}(\mathbf{r}, t) - Tr \left\{ \hat{\rho}_G \hat{O}_{H_o} \right\}$.

In accompaniment, $\chi_{OA}(\mathbf{r}, t; \mathbf{r}', t')$ is also related to the Green function as

$$\mathcal{G}_{OA}(\mathbf{r}, \mathbf{r}', t) = \frac{-i\theta(t)}{\hbar} \chi_{OA}(\mathbf{r}, \mathbf{r}', t), \quad (1.11)$$

so that the Fourier components obey the identity

$$2\hbar Im \left\{ \mathcal{G}_{OA}(\mathbf{r}, \mathbf{r}', \omega) \right\} = \chi_{OA}(\mathbf{r}, \mathbf{r}', \omega). \quad (1.12)$$

Equating these two expressions, the dissipative properties of the system, $Im \left\{ \mathcal{G}_{OA}(\mathbf{r}, \mathbf{r}', \omega) \right\}$, are related to its fluctuation properties as

$$\frac{2\hbar}{1 \pm e^{-\beta\omega}} Im \left\{ \mathcal{G}_{OA}(\mathbf{r}, \mathbf{r}', \omega) \right\} = S_{OA}(\mathbf{r}, \mathbf{r}', \omega). \quad (1.13)$$

The assumptions leading to this result are surprisingly mild. All that is required is that the original system should be stationary, and \hat{O} and \hat{A} be observables. As such, the idea can be used effectively in an amazing variety of physical models and provides a generalized equivalence for both determining and engineering the response of a system in terms of its microscopic properties.

1.3 Electromagnetic field correlations

1.3.1 The classical fluctuation dissipation theorem

In view of the the classical systems that are considered in later chapters, it useful to see how the fluctuation dissipation theorem emerges outside the framework of quantum mechanics. From classical statistical mechanics, the probability of the system being in a certain state at thermal equilibrium is given by the expression

$$p_{eq}(\mathcal{S}) = Z^{-1} e^{-\beta H_o(\mathcal{S})}, \quad (1.14)$$

with Z the canonical partition function, and \mathcal{S} some parameterization of the degree of freedom of the system. From this definition the statistical expectation value of

an observable, taking as a specific example the current density $\mathbf{j}^{avg}(\mathbf{r}, t)$, is

$$\mathbf{j}^{avg}(\mathbf{r}, t) = \int d\mathcal{S} p_{eq}(\mathcal{S}) \mathbf{j}(\mathcal{S}, \mathbf{r}, t), \quad (1.15)$$

where $\mathbf{j}(\mathcal{S}, \mathbf{r}, t)$ is the current density at the position \mathbf{r} under the conditions \mathcal{S} . Letting $H_{tot} = H_o + H$ be the classical Hamiltonian of the system perturbed by an external electromagnetic electric field with

$$H(\mathcal{S}) = \int dV' \mathbf{j}(\mathcal{S}, \mathbf{r}', t) \mathbf{A}(\mathbf{r}', t), \quad (1.16)$$

to first order the change in the statistical average of the current density is

$$\mathbf{j}_{H_{tot}}^{avg}(\mathbf{r}, t) = \frac{\int d\mathcal{S} e^{-\beta(H_o(\mathcal{S})+H(\mathcal{S}))} \mathbf{j}(\mathcal{S}, \mathbf{r}, t)}{\int d\mathcal{S} e^{-\beta(H_o(\mathcal{S})+H(\mathcal{S}))}} \approx \quad (1.17)$$

$$\frac{\int d\mathcal{S} p_{eq}(\mathcal{S}) (1 - \beta H(\mathcal{S})) \mathbf{j}(\mathcal{S}, \mathbf{r}, t)}{\int d\mathcal{S} p_{eq}(\mathcal{S}) (1 - \beta H(\mathcal{S}))} \approx (\mathbf{j}^{avg}(\mathbf{r}, t) - \beta \langle H \mathbf{j}(\mathbf{r}, t) \rangle) (1 + \beta \langle H \rangle).$$

With H as above, and $\delta \mathbf{j}^{avg}(\mathbf{r}, t) = \mathbf{j}_{H_{tot}}^{avg}(\mathbf{r}, t) - \mathbf{j}^{avg}(\mathbf{r}, t)$, this relation then determines the change in the dipole moment to be

$$\delta \mathbf{j}^{avg}(\mathbf{r}, t) = -\beta \int dV' \langle \delta \mathbf{j}(\mathbf{r}, t) \delta \mathbf{j}(\mathbf{r}', t) \rangle \mathbf{A}(\mathbf{r}', t). \quad (1.18)$$

However, just as in the previous section, to first order this same situation must be equally well describe in terms of a linear response function $\tilde{a}_{lm}(\mathbf{r} - \mathbf{r}', t - t')$ which, assuming the system to be stationary and homogeneous, takes the form

$$\delta j_l^{avg}(\mathbf{r}, t) = \int dV' \int_{-\infty}^{\infty} dt' \tilde{a}_{lm}(\mathbf{r} - \mathbf{r}', t - t') E_m(\mathbf{r}', t'), \quad (1.19)$$

where the letter subscripts are used to denote vector components. Now, if the system in the presence of the additional external electric field can be smoothly related to the initial equilibrium system (which is simply a restatement of the validity of a perturbative approach) then it can be freely assumed that $t \rightarrow -\infty \Rightarrow \mathbf{A}(\mathbf{r}', t) \rightarrow 0$. If this is the case, then the perturbation of the Hamiltonian can then be rewritten as

$$H = \int dV' \mathbf{j}(\mathcal{S}, \mathbf{r}', t) \mathbf{A}(\mathbf{r}', t) = \int dV' \int_{-\infty}^{\infty} dt' \Theta(t - t') \frac{d}{dt'} (\mathbf{j}(\mathcal{S}, \mathbf{r}', t') \mathbf{A}(\mathbf{r}', t')). \quad (1.20)$$

Sticking to linear order, Maxwell's equations allows us to identify this expression as

$$H = - \int dV' \int_{-\infty}^{\infty} dt' \Theta(t-t') \mathbf{j}(\mathcal{S}, \mathbf{r}', t') \mathbf{E}(\mathbf{r}', t'). \quad (1.21)$$

so that (1.18) becomes

$$\delta \mathbf{j}^{avg}(\mathbf{r}, t) = \beta \int dV' \int_{-\infty}^{\infty} dt' \Theta(t-t') \langle \delta \mathbf{j}(\mathbf{r}, t) \delta \mathbf{j}(\mathbf{r}', t') \rangle \mathbf{E}(\mathbf{r}', t').$$

Equating (1.19) and (1.18) then shows that

$$\tilde{a}_{lm}(\mathbf{r} - \mathbf{r}', t - t') = \beta \Theta(t - t') \langle \delta j_l(\mathbf{r}, t) \delta j_m(\mathbf{r}', t') \rangle; \quad (1.22)$$

so that again, the first order fluctuations of the system are found to determine its linear response function.

Taking the Fourier transforms of the above, making use of the Wiener-Khintchine theorem, then produces the results

$$\frac{2}{\beta} \langle \delta \hat{j}_l(\mathbf{r}, \omega) \delta \hat{j}_m^*(\mathbf{r}', \omega') \rangle = -\delta(\omega - \omega') (\tilde{a}_{lm}(\mathbf{r} - \mathbf{r}', \omega) + \tilde{a}_{ml}^*(\mathbf{r} - \mathbf{r}', \omega)) \quad (1.23)$$

$$\frac{2}{\beta} \langle \delta \hat{j}_l(\mathbf{k}, \omega) \delta \hat{j}_m^*(\mathbf{k}', \omega') \rangle = -\delta(\mathbf{k} - \mathbf{k}') \delta(\omega - \omega') (\tilde{a}_{lm}(\mathbf{k}, \omega) + \tilde{a}_{ml}^*(\mathbf{k}, \omega)) \quad (1.24)$$

The primary difference between (1.22) and (1.23) and (1.13) lies mainly in difference in the expected average energy per mode. Making the substitution

$$\beta \rightarrow \frac{\hbar\omega}{e^{\beta\hbar\omega} \pm 1} + \hbar\omega \quad (1.25)$$

the two results become identical, up to the way in which the averages are computed, showing again that the formalism of linear response is truly one of the most versatile theoretical pictures. (A derivation of the steps connecting these two energy distribution is included as an appendix¹⁶.)

Inversely, the same steps can be taken assuming that an external current density is introduced to the equilibrium system, rather than an external vector potential. Ex-

¹⁶Note that every result stated in this section can be developed analogously if magnetic, rather than electric, dipoles are considered. However, the magnetic response function of the materials we will consider in later chapters are generally featureless, and so we have not shown these results.

amining the change in the potential field, fixing the scalar potential to be zero,

$$\delta A_l^{avg}(\mathbf{r}, t) = \beta \int dV' \int_{-\infty}^{\infty} dt' \tilde{g}_{lm}(\mathbf{r} - \mathbf{r}', t - t') j_m(\mathbf{r}', t'). \quad (1.26)$$

then yields

$$\frac{2}{\beta} \left\langle \delta \hat{A}_l(\mathbf{r}, \omega) \delta \hat{A}_m^*(\mathbf{r}', \omega') \right\rangle = \frac{\delta(\omega - \omega')}{\omega} (\tilde{g}_{lm}(\mathbf{r} - \mathbf{r}', \omega) - \tilde{g}_{ml}^*(\mathbf{r} - \mathbf{r}', \omega)) \quad (1.27)$$

$$\frac{2}{\beta} \left\langle \delta \hat{A}_l(\mathbf{k}, \omega) \delta \hat{A}_m^*(\mathbf{k}', \omega') \right\rangle = \delta(\mathbf{k} - \mathbf{k}') \frac{\delta(\omega - \omega')}{\omega} (\tilde{g}_{lm}(\mathbf{k}, \omega) - \tilde{g}_{ml}^*(\mathbf{k}, \omega)) \quad (1.28)$$

Consistency demands that (1.22) and (1.27) must agree so long as the assumptions stated above are valid. The two formulations, referred to respectively as the fluctuation theorem of the first and second kind [92], clarify that related linear response parameters are not independent.

1.3.2 Stochastic Maxwell equations

So long as the characteristic length scale of charge fluctuations are much smaller than the particular wavelength of interest, i.e. that dipole approximation is valid, (1.23) and (1.27) can be applied directly to the macroscopic Maxwell equations to determine thermal field characteristics¹⁷. Written in the standard SI convention, these equations are

$$\nabla \times \mathbf{E}(\mathbf{r}, t) = \frac{\partial \mathbf{B}(\mathbf{r}, t)}{\partial t}, \quad (1.29)$$

$$c^2 \nabla \times \mathbf{H}(\mathbf{r}, t) = \frac{\partial \mathbf{D}(\mathbf{r}, t)}{\partial t} + \mathbf{j}_f(\mathbf{r}, t) / \epsilon_o. \quad (1.30)$$

Here, the f subscript denotes that the quantity is free (distinct from the underlying charge and current densities responsible for the magnetic and electric polarizations), and \mathbf{D} and \mathbf{H} are the electric and magnetic displacement fields, related to the electric and magnetic fields \mathbf{E} and \mathbf{B} by the constitutive relations

$$\mathbf{D}(\mathbf{r}, t) = \int dV' \int_{-\infty}^{\infty} dt' \bar{\epsilon}(\mathbf{r} - \mathbf{r}', t - t') \mathbf{E}(\mathbf{r}', t'), \quad (1.31)$$

$$\mathbf{B}(\mathbf{r}, t) = \int dV' \int_{-\infty}^{\infty} dt' \bar{\mu}(\mathbf{r} - \mathbf{r}', t - t') \mathbf{H}(\mathbf{r}', t'), \quad (1.32)$$

where $\bar{\epsilon}(\mathbf{r} - \mathbf{r}', t - t')$ and $\bar{\mu}(\mathbf{r} - \mathbf{r}', t - t')$ are the relative permittivity and permeability tensors of the medium, and $\mathbf{j}(\mathbf{r}, t)$ is the current density. Taking Fourier

¹⁷If the dipole approximation is not valid, then macroscopic charge fluctuations will appear and the form of the perturbation of consider above should properly include the scalar potential.

transforms in space and time, these equations are equivalently written as

$$\mathbf{k} \times \mathbf{E}(\mathbf{k}, \omega) = \omega \mathbf{B}(\mathbf{k}, \omega) \quad (6c)$$

$$ic^2 \mathbf{k} \times \mathbf{B}(\mathbf{k}, \omega) = -i\omega \mathbf{D}(\mathbf{k}, \omega) + \mathbf{j}_f(\mathbf{k}, \omega) / \epsilon_0 \quad (1.33)$$

with

$$\mathbf{D}(\mathbf{k}, \omega) = \bar{\epsilon}(\mathbf{k}, \omega) \mathbf{E}(\mathbf{k}, \omega) \quad (1.34)$$

$$\mathbf{B}(\mathbf{k}, \omega) = \bar{\mu}(\mathbf{k}, \omega) \mathbf{H}(\mathbf{k}, \omega). \quad (1.35)$$

Combining these two relations, the electric field and current are related by the expression

$$\begin{aligned} \mathbf{j}_f(\mathbf{k}, \omega) = \frac{\epsilon_0 c^2}{i\omega} \left(k^2 \left(\bar{I} - \hat{\mathbf{k}} \otimes \hat{\mathbf{k}} \right) - k_0^2 \bar{\epsilon}(\mathbf{k}, \omega) \right) \mathbf{E}(\mathbf{k}, \omega) = \\ (i\omega)^{-1} \bar{\mathcal{G}}^{-1}(\mathbf{k}, \omega) \mathbf{E}(\mathbf{k}, \omega) \end{aligned} \quad (1.36)$$

where $\mathcal{G}(\mathbf{k}, \omega)$ stands for the Green function as it is usually defined in electromagnetics, and the overline superscript is used to denote a matrix. Substituting this result into (1.24) and (1.28) produces tractable expressions for the correlations of both the current and electric field

$$\left\langle \delta \hat{j}_l(\mathbf{k}, \omega) \delta \hat{j}_m^*(\mathbf{k}', \omega') \right\rangle = \beta \epsilon_0 \omega \delta(\mathbf{k} - \mathbf{k}') \delta(\omega - \omega') \text{Im} \{ \epsilon_{lm}(\mathbf{k}, \omega) \} \quad (1.37)$$

$$\left\langle \delta \hat{E}_l(\mathbf{k}, \omega) \delta \hat{E}_m^*(\mathbf{k}', \omega') \right\rangle = \beta \delta(\mathbf{k} - \mathbf{k}') \frac{\delta(\omega - \omega')}{\omega} \text{Im} \{ \mathcal{G}_{lm}(\mathbf{k}, \omega) \}. \quad (1.38)$$

These central results, giving statistical expectation values without the need for statistical computation, form the basis for nearly all of the results presented in later chapters.

1.3.3 Energy and heat transfer from field correlations

The Rytovian formulation of field correlations shown in the previous section reveals surprising physical behavior, particularly in the near-field. The simplest example of this exists in considering the thermal electromagnetic power transfer between two half spaces separated by a thin, lossless, dielectric film. Denoting this quantity as S_z , the component of the Poynting vector just inside the cooler half space is

$$\langle S_z(\omega) \rangle = \text{Re} \left\{ \langle E_x \times H_y^* - E_y \times H_x^* \rangle \right\}, \quad (1.39)$$

where the z subscript denotes the direction perpendicular to the surface of the two plates, and the x and y subscripts the two parallel direction. Using the Green function formalism, (1.39) becomes

$$\begin{aligned} \langle S_z(\omega) \rangle = & \\ & Re \left\{ \left\langle \omega^2 \int dV' \mathcal{G}_{xl}(\mathbf{r}, \mathbf{r}', \omega) j_l(\mathbf{r}', \omega) \int dV'' \nabla \times \mathcal{G}_{ym}^*(\mathbf{r}, \mathbf{r}'', \omega) j_m^*(\mathbf{r}'', \omega) \right\rangle \right\} \\ & - Re \left\{ \left\langle \omega^2 \int dV' \mathcal{G}_{yl}(\mathbf{r}, \mathbf{r}', \omega) j_l(\mathbf{r}', \omega) \int dV'' \nabla \times \mathcal{G}_{xm}^*(\mathbf{r}, \mathbf{r}'', \omega) j_m^*(\mathbf{r}'', \omega) \right\rangle \right\}, \end{aligned} \quad (1.40)$$

where the l and m subscripts stand for free Cartesian components, summed over in the Einstein convention. Freely interchanging averaging and integration, noting that the permittivity tensor is diagonal, (1.37) can be applied directly to give

$$\begin{aligned} \langle S_z(\omega) \rangle = & \epsilon_o \omega^3 H(\omega, T) \\ & Re \left\{ \left\langle \int dV' \mathcal{G}_{xl}(\mathbf{r}, \mathbf{r}', \omega) Im \{ \epsilon_{ll}(\mathbf{r}', \omega) \} (\mathcal{G}_{ly}^*(\mathbf{r}', \mathbf{r}, \omega) \times \nabla) \right\rangle \right\} \\ & - Re \left\{ \left\langle \int dV' \mathcal{G}_{yl}(\mathbf{r}, \mathbf{r}', \omega) Im \{ \epsilon_{ll}(\mathbf{r}', \omega) \} (\mathcal{G}_{lx}^*(\mathbf{r}', \mathbf{r}, \omega) \times \nabla) \right\rangle \right\}, \end{aligned} \quad (1.41)$$

where $\dots \times \nabla$ denotes that the curl is applied to the second (column) index of $\mathcal{G}_{lx}^*(\mathbf{r}', \mathbf{r}, \omega)$. Following the steps outlined in the associated appendix, this thermal power flow is

$$\begin{aligned} \langle S_z(\omega) \rangle = & \sum_n \left(\frac{H(\omega, T_1) - H(\omega, T_3)}{2\pi} \right) \left(\int_0^{k_o \sqrt{\epsilon_2}} dk_\rho \frac{(1 - |r_n^{21}|^2)(1 - |r_n^{23}|^2)}{|1 - r_n^{21} r_n^{23} e^{2ik_{z2}L}|^2} k_\rho \right. \\ & \left. + 4 \int_{k_o \sqrt{\epsilon_2}}^\infty dk_\rho \frac{Im \{ r_n^{21} \} Im \{ r_n^{23} \}}{|1 - r_n^{21} r_n^{23} e^{2ik_{z2}L}|^2} e^{-2Im\{k_{z2}\}L} k_\rho \right), \end{aligned} \quad (1.42)$$

where k_ρ and k_z are the cylindrical coordinates of the reciprocal vector k , $H(\omega, T)$ is energy distribution

$$H(\omega, T) = \frac{\hbar\omega}{1 - e^{-\beta\hbar\omega}}, \quad (1.43)$$

$r_n^{\sigma\phi}$ stands for one of two Fresnel reflection coefficients of the electric field between the media σ , and ϕ , with polarization n , Fig. 1.2,

$$r_p^{\sigma\phi} = \frac{\epsilon_\phi(k, \omega, T) k_{z\sigma} - \epsilon_\sigma(k, \omega, T) k_{z\phi}}{\epsilon_\phi(k, \omega, T) k_{z\sigma} + \epsilon_\sigma(k, \omega, T) k_{z\phi}} \quad r_s^{\sigma\phi} = \frac{k_{z\sigma} - k_{z\phi}}{k_{z\sigma} + k_{z\phi}}, \quad (1.44)$$

with

$$k_{z\sigma} = \sqrt{k_o^2 \epsilon_\sigma(k, \omega, T) - k_\rho^2}, \quad (1.45)$$

L is the thickness of the thin lossless dielectric film, and $k_o = \omega/c$. Note that the dependence of $r_n^{\sigma\phi}$ on k , ω , and T is suppressed in these and all following equations to help increase readability. Similarly, explicit inclusion of the temperature dependencies in the absorptivity and thermal power flow are also suppressed.

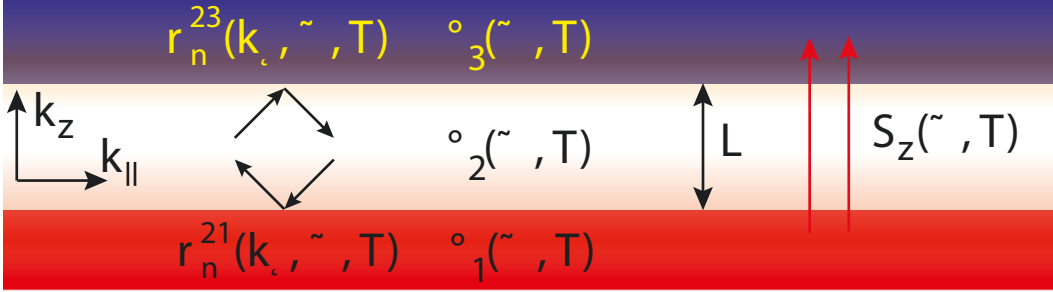


Figure 1.2: **Half space thermal electromagnetic power transfer.**

The figure displays a schematic of the thermal electromagnetic power transfer described by (1.42). When the distance L is smaller than the wavelength, the thermal power transferred per cross sectional area scales as $1/L^2$. As such, on the micro or nanoscale this phenomena may be orders of magnitude larger than expectations based on Kirchhoff's law of thermal radiation. Note that this scaling provides a mechanism by which in the $L \rightarrow 0$ the heat energy transferred between two bodies can approach material thermal conductivity.

The first bracketed term in (1.42) is the wave theory version of Kirchhoff's classical theory of thermal radiation. To recover this results, we begin by setting $\epsilon_3(\omega, T)$ and $\epsilon_2(\omega, T)$ equal to vacuum, $\epsilon(\omega, T) = 1$. For the second integral, $k_o < k_p$, and so $k_{z2} = i\sqrt{k_\rho^2 - k_o^2}$ on the entire domain on integration. As a result, the exponential term in this integral becomes $Exp\left(-2\sqrt{k_\rho^2 - k_o^2} L\right)$. If L is much larger than λ , then the exponent becomes a large negative number and the contribution of this second term in the far-field is vanishingly small.

Returning to the first integral, keeping $\epsilon_3(\omega, T) = \epsilon_2(\omega, T) = 1$ we find

$$\langle S_z(\omega) \rangle = \sum_n \left(\frac{H(\omega, T_1) - H(\omega, T_3)}{4\pi} \right) \int_0^{k_o} dk_\rho \left(\frac{1 - |r_s^{21}|^2}{2} + \frac{1 - |r_p^{21}|^2}{2} \right) k_\rho \quad (1.46)$$

As $k_p < k_o$ this integral can equally be converted to a polar integral,

$$\langle S_z(\omega) \rangle = \frac{\omega^2}{c^2} \left(\frac{H(\omega, T_1) - H(\omega, T_3)}{4\pi} \right) \int_0^\pi d\theta \left(\frac{1 - |r_s^{21}(\theta)|^2}{2} + \frac{1 - |r_p^{21}(\theta)|^2}{2} \right) c(\theta); \quad (1.47)$$

where the factor $c(\theta) = \cos(\theta)$ shows that only the component of the integrand perpendicular to the surface, z direction, is counted. Identifying $(1 - |r_s^{21}|^2)/2 + (1 - |r_p^{21}|^2)/2$ as the absorptivity of an optically thick medium,

$$\alpha(\omega, \theta) = \frac{1 - |r_s^{21}(\theta)|^2}{2} + \frac{1 - |r_p^{21}(\theta)|^2}{2}, \quad (1.48)$$

we then have

$$\langle S_z(\omega) \rangle = \frac{\omega^2}{c^2} \left(\frac{H(\omega, T_1) - H(\omega, T_3)}{4\pi} \right) \int_0^\pi d\theta \alpha(\omega, \theta) c(\theta). \quad (1.49)$$

The integrand of this expression doubles as the definition of emissivity originally given by Kirchhoff. As such, we see that in the limit of geometric optics the amount of thermal radiation emitted by an object as derived by Rytovian electrodynamics agrees exactly with Kirchhoff's law of thermal radiation.

Building from the understanding imparted by this simplification, the meaning of the first integral as originally written can now be interpreted as the product of two phenomena. Kirchhoff law of thermal radiation requires the presence of each factor like $1 - |r_n^{12}|^2$, and these terms dominate in the domain of geometric optics. Likewise, the additional phase information that appears as a denominator for these factors is a consequence of the wave nature of electromagnetics. It must be present to allow for interference.

Compared to this first term, which fits fairly well with the traditional nineteenth century view of far-field thermal radiation, the second term is astonishing. Assuming that for large k_ρ

$$\frac{\text{Im} \{r_n^{21}\} \text{Im} \{r_n^{23}\}}{|1 - r_n^{21} r_n^{23} e^{2ik_z L}|^2} \approx C, \quad (1.50)$$

and that L is small enough so that this approximation can be made for the majority of the domain of integration, the scaling of this additional thermal electromagnetic

power transfer, (1.42), with separation distance L is found to be

$$\int_{k_o}^{\infty} dk_{\parallel} \frac{\text{Im}\{r_n^{21}\} \text{Im}\{r_n^{23}\}}{|1 - r_n^{21} r_n^{23} e^{2ik_z 2L}|^2} e^{-2\text{Im}\{k_z 2\}L} k_{\parallel} \propto \frac{4\pi^2 C}{\lambda^2} \left(\frac{e^{-4\pi L/\lambda}}{(4\pi L/\lambda)^2} + \frac{e^{-4\pi L/\lambda}}{4\pi L/\lambda} \right), \quad (1.51)$$

where $\epsilon_2(k, \omega, T)$ has been set to vacuum $\epsilon_2(k, \omega, T) = 1$. Crucially as the size of the gap is reduced, the amount of thermal energy transferred scales approximately as $1/L^2$. This result directly shows that at nanoscale distances the transport of heat energy by thermal radiation may be orders of magnitude larger than what is observed in the far-field, nearing bulk thermal heat conductivity in the limit $L \rightarrow 0$ [76, 93].

The implication of this model calculation, originally produced by Polder and Van Hove [13, 94], are remarkable. Principally, the energy spectrum of thermal radiation need not resemble a Planckian distribution. It may generally be tailored by controlling the linear response parameter $\epsilon(k, \omega, T)$, and in the near-field can even display resonant characteristics if $|1 - r_n^{21} r_n^{23} e^{2ik_z 2L}|^2 \rightarrow 0$. These coherence properties [12, 95, 96] stand in sharp contrast to the usual picture of thermal radiation as a near perfect example of uncorrelated randomness, and serves as a our primary motivation for reevaluating the application potential of thermal electromagnetic radiation.

Chapter 2

Designing Thermal Emission with Metamaterials

In this chapter, we theoretically propose general methods by which metamaterial concepts can be used to control radiative thermal characteristics.

In the early 2000's Cornelius and Dowling [24], (followed shortly by Hinz et al. [30] and Lin et al. [25]) showed that photonic bandgaps could be used to induced broad-band thermal radiation suppression beneficial for photonic energy harvesting. Since the publication of this result, the use of micro / nanoscale structuring to control far-field radiative emission characteristics has been considered one, if not the, most important practical applications of thermal electromagnetic engineering¹.

Yet, in spite of the multitude of designs that has been considered in the intervening years to provide this control, and the progress that has been made [42, 56], relatively few unifying themes have emerged. Explicitly these themes are:

(1) That interference effects, capable of both enhancing and suppressing thermal emission, will occur if structuring introduces a characteristic size similar to the wavelength [97, 98].

(2) That the creation of a photonic bandgap can be used to effectively suppress thermal emission [99, 100].

(3) That by coupling to polariton modes, the thermal emission of a structure can be

¹In particular photonic crystal structures have received a great deal of attention since this idea was first introduced [26, 31, 33, 35]. However, as listed in the first chapter, almost every popular micro/nanophotonic structure has been considered as a platform for controlling far-field thermal radiation to some extent.

enhanced [101, 102]. Beyond these rules, the specifics of how a given structure will perform, and how it should actually be designed, are commonly not known until it is numerically simulated and recursively optimized.

As a response to this shortcoming, here, we provide a general theory of radiative thermal emission applicable to any deeply sub wavelength (nano) structure: thermal emission from the perspective of metamaterials (effective medium response). Our analysis simultaneously classifies all spectrally selective thermal emission characteristics that can be achieved with metamaterials, and proposes two novel methods for engineering far-field radiative thermal emission by creating epsilon-near-zero, and epsilon-near-pole type responses.

In addition, we also propose the extension of constituent materials for optical metamaterials to include any that support high temperature plasmonics. Although the figure of merit of these metals is typically far below that of conventional metamaterial building blocks, we show that nevertheless strong radiative selectivity can be achieved (without sacrificing thermal stability).

Using our approach, the angular distribution, spectral position, and band width of thermal emission and optical absorption can be both analytically determined and finely tuned in the near infrared. This spectral range is critical to thermophotovoltaic energy harvesting technologies, and we analyze the application of metamaterial emitters for these devices in detail. In particular, we show that metamaterial emitters near 1500 K can be used as part of thermophotovoltaic devices to surpass the full concentration Shockley-Queisser limit of 41 %.

2.1 Introduction

High temperature energy conversion processes, such as combustion, are accompanied by thermal losses which often outstrip usable produced power [90]. As an example, for average oil and coal based energy conversion, thermal losses account for roughly 50 % to 60 % of the total produced power [103, 104]. For small internal combustion engines this number may climb as high as 75 % [105]. These losses can be substantially mitigated by utilizing the waste thermal energy as a heat resource. An ideal set up would convert waste thermal energy directly into usable power.

Thermal losses are also significant for photovoltaic cells. Due to the large spectral range that must be captured, over 60% of incident solar power is lost as thermal energy [106]. Regardless of the material bandgap's spectral position, radiation above

the bandgap loses a portion of its energy to thermalization within the cell. Radiation with energy below the bandgap is essentially unused. These effects are intrinsic and place an upper limit on energy conversion for a single junction semiconductor cell [107]. While proposals of multi-junction cells offer a potential workaround, they also require a shift to expensive materials and structures.

An alternative solution exists in the application of the thermophotovoltaic (TPV) method [108]. In this approach, any combination of conductive, convective or radiated waste energy is concentrated to heat a structure with a spectral emission tailored to match the bandgap of a specific photovoltaic cell. Once the structure is heated, the source energy is converted to electromagnetic radiation which can be transformed into electric power with high efficiency. The method of maintaining the heated source is flexible giving the TPV approach applicability beyond that of large scale solar or solar thermal approaches. For example, TPV methods can be used to create compact devices for cogeneration of heat and electricity.

TPV devices can easily be integrated as efficiency increasing components of larger systems, or function as primary solid state energy converters [109]. Unfortunately, the operational temperatures needed for sufficient power generation and efficient energy conversion [110] as well as our limited ability to tune the thermal radiation spectrum made previous TPV approaches largely impractical. While excellent progress has been made towards designing emitters for far-field TPVs through surface structuring [44, 49, 111, 111–115], planar Fabry-Perot based structures [116–118] and photonic crystals [26, 35, 119], a dominant, broadly applicable set of tools for controlling thermally induced radiation has yet to emerge.

In this chapter, we introduce a class of thermal effects in metamaterials for thermophotovoltaic applications. Our approach rests on engineering the poles and zeros of the dielectric constant which allow for an array of unique optical responses. We show that epsilon-near-zero (ENZ) metamaterials can behave as spectrally tunable, highly selective ultra-thin thermal emitters and introduce a class of artificial media defined by a Lorentzian polarization response, epsilon-near-pole (ENP) metamaterials. This class of ENP media are ideally suited as thermal emitters in a thermophotovoltaic system where the main requirements are:

- omnidirectional thermal emission
- narrow band and high emissivity
- polarization insensitivity

We also address one of the major limitations of conventional metamaterials for ther-

mal applications (high temperature operation) by switching to plasmonic materials with high melting points. Finally, we analyze the performance of these emitters within a practical thermophotovoltaic device and show that the energy conversion efficiency can exceed the Shockley Queisser limit of single junction cells. Note that the ENZ and ENP thermal emitters introduced in this chapter can function as ideal narrow band ultra-thin absorbers as well.

2.2 Epsilon-near-zero (ENZ) and epsilon-near-pole (ENP) narrow band absorbers and emitters

2.2.1 Tailored emission and optical absorption

Making use of Kirchhoff's law of thermal radiation for a body in thermodynamic equilibrium [120], the engineering of thermal emission can be formulated in terms of optical absorptivity

$$\zeta(\lambda, \theta, \phi) = \alpha(\lambda, \theta, \phi), \quad (2.1)$$

with $\alpha(\lambda, \theta, \phi)$ denoting the structure's absorptivity as function of wavelength², azimuthal angle, and polar angle, and ζ the structure's emissivity. It follows directly that spectrally narrow regions of high optical absorption also create spectrally narrow regions of high thermal emission. Consequently, the use of optical resonances provides a natural starting point for designing thin structures to control thermally excited electromagnetic radiation. We introduce the concept of thermal engineering using ENZ and ENP resonances and show how the fundamentally distinct natures of these two bulk material resonances can create a range of thermally induced effects. The proposed approach can be used for a variety of applications and in particular for TPVs, where the main constraints on the emitter are narrow band and omnidirectional emissivity [106].

2.2.2 ENZ and ENP absorption

ENZ

Lossless or near lossless epsilon-near-zero resonances have recently been a topic of broad research interest, and have been shown as a plausible mechanism for creating high performance optical devices ranging from nonlinear optical switches to tailored radiation phase patterns [121, 122]. We show here that ENZ resonances have important applications in general control of thermally induced radiation (explored in Section 2.3). However, the traditional $Re\{\epsilon\} \rightarrow 0$ and $Im\{\epsilon\} \rightarrow 0$ ENZ regime is

²Note that the wavelength used in this and all subsequent definitions is the free space wavelength, and not the wavelength inside emitter. Inside the anisotropic media we will consider, the wavelength is effectively scaled by a factor of $\sqrt{\frac{\cos(\theta)}{\epsilon_{||}} + \frac{\sin(\theta)}{\epsilon_{\perp}}}$, (2.4), where θ is the angle from the \perp axis.

not suited to the requirements of a TPV emitter.

P-polarized radiation incident on an ENZ slab shows increased absorption (non-normal incidence). This resonance arises due to the presence of a field enhancing mechanism that relies on the displacement field boundary condition: $\epsilon_1 E_{1\perp} = \epsilon_2 E_{2\perp}$, where the \perp denotes the direction perpendicular to the slab, and either medium can be assumed to have ENZ behavior (if $\epsilon_2 \rightarrow 0$ then $E_{2\perp} \rightarrow \infty$). Kirchoff's law immediately reveals that such an ENZ slab, given its enhanced absorption characteristics, should possess a high emissivity. However, s-polarized light which does not have a component of the field perpendicular to the slab does not show this field enhancement or the ENZ resonance. By this constraint, no s-polarized light can be thermally excited, and p-polarized radiation cannot be efficiently emitted at low polar angles. Since the emission of an ideal blackbody shows no angular or polarization preference, the maximal averaged emitted spectral power in an ENZ region is less than half of what can be achieved theoretically.

Nevertheless, polarization averaged emissivity near that of a blackbody can still be attained if the $Im\{\epsilon\} \rightarrow 0$ condition is relaxed. In moving away from true ENZ behavior by the addition of extra loss, two separate, but connected, absorption improving effects occur. First, in the $Re\{\epsilon\} \rightarrow 0$ region, the high impedance mismatch between an ENZ material and free space is greatly reduced as the added loss acts to decrease the impedance of the material. Since this also dictates a general relaxation of ENZ resonance characteristics, polarization sensitivity is greatly diminished. Second, at wavelengths shorter than the $Re\{\epsilon\} \rightarrow 0$ crossing where material impedance is similar to that of free space ($Re\{\epsilon\} \approx 1$), the addition of material losses begins to allow for significant absorptivity even if the material film is thin³. Both effects push this pseudo ENZ resonance towards unity near omnidirectional absorptivity of both electromagnetic polarizations, and at higher losses combine to create a single highly absorptive spectral region (Fig. 2.1(A)).

Yet, improving absorptivity in this manner comes at the cost of an increased spectral width. Due to the natural dispersion limitations of a region where $Re\{\epsilon\} \rightarrow 0$, the spectral width over which the additional loss achieves impedance matching is comparatively broad. As a direct result, high emissivity occurs over a much wider range than that ideal for high efficiency TPVs. The onset of this behavior is depicted in Fig. 2.1(A), where the emissivity of a 100 nm thick film moving away from the true ENZ characteristics, following a Drude model, on a perfectly reflecting backing

³Note that if $Im\{\epsilon\}$ is much greater than 1 it not possible to match the impedance of the material with that of free space. In this case, emission from an ENZ medium will be suppressed.

is calculated using (2.1) and the Poynting vector relation $\vec{S} = \frac{1}{2}\vec{E} \times \vec{H}^*$. Again, as will be discussed in Section 2.5, while broader emissivity may be useful for certain TPV applications, it does not match the ideal narrow band criterion. In light of these results, we introduce the concept of ENP resonances for achieving the thermal emission characteristics necessary for high efficiency TPVs. Note that both the ENZ and ENP resonances can be engineered using nanostructured metamaterials.

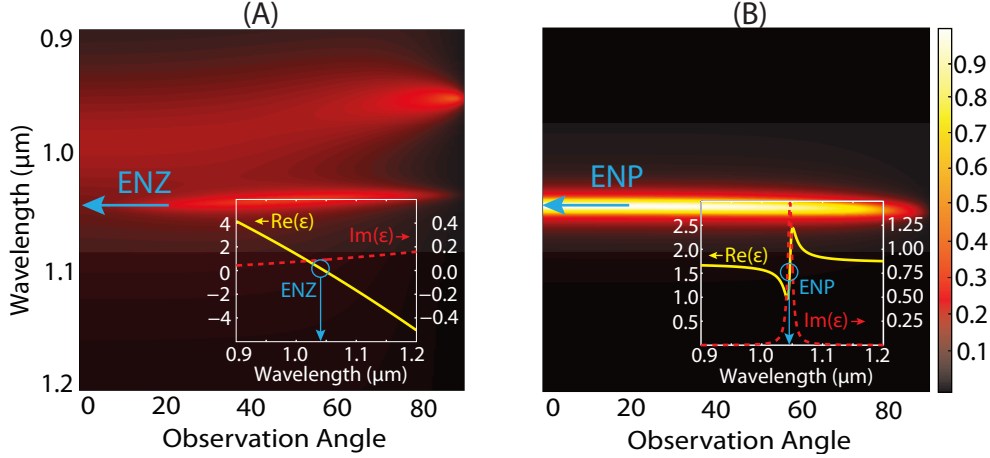


Figure 2.1: **Emission characteristics of ENZ and ENP type resonances.**

(A) Polarization averaged emissivity of a 100 *nm* thick film of ENZ material, following a Drude model, on a perfectly reflecting backing. The spectrally narrow peak is the ENZ resonance. The broad blur at shorter wavelengths is the onset of impedance matching in the $Re\{\epsilon\} \approx 1$ range. As loss is increased, these regions blend together and the magnitude of the emissivity tends towards unity in a broad spectral range. The inset shows the relative dielectric constant used. (B) Polarization averaged emissivity of a 100 *nm* thick material film in the ENP regime, based on a Lorentz model, on a perfectly reflecting backing. The component loss considered is identical to that used in panel (A): $\gamma_A = \gamma_B$. Again, the inset shows the relative dielectric constants used to calculate the polarization averaged emissivity. The spectrally sharp behavior shown here makes ENP type resonances a promising candidate for TPV applications.

ENP

The primary advantage of operating at an ENP resonance is the extremely dispersive nature of these regions. This characteristic allows for tight spectral control even with moderate material losses. Yet, beyond this most important feature, several other benefits for TPV type emitters and absorbers exist. At an ideal pole of the dielectric constant we have, $Re\{\epsilon\} \rightarrow (\pm)\infty$. The addition of losses regularizes the singularity, reduces impedance mismatch and leads to enhanced absorption (high emissivity) in a narrow spectral region (Fig. 2.1 (B)). The ENP resonance associated with such a pole shows no polarization sensitivity and achieves omnidirectional

high emissivity in isotropic media.

We now compare the critical role of losses in the ENZ and ENP resonance. In contrast to the fixed $Re\{\epsilon\} \rightarrow 0$ condition of an ENZ resonance, which forces any impedance matching to be accomplished through the addition of loss or effective permeability μ , the behavior of $Re\{\epsilon\}$ itself in an ENP region is highly loss dependent. When loss is added, the real part of the dielectric function can no longer achieve large absolute values, opening the possibility of impedance matching even with relatively lower losses as compared to the ENZ resonance. This leads to a narrower spectral window of high emission and absorption than the previously mentioned ENZ approach. A comparative visualization of the characteristic spectral emissivity of a 100 nm thick material film in the ENP regime with moderate losses, based on a Lorentz model, on a perfectly reflecting backing is shown in Fig. 2.1(B). Noting that ENP type resonances match all the requirements of a high efficiency TPV emitter, we now focus on practical realizations of ENZ and ENP materials.

2.3 Practical ENZ and ENP with metamaterials

2.3.1 Natural ENZ and ENP resonances

In natural materials, ENZ regions occur at bulk plasmon as well as longitudinal optical phonon resonances, *LO* subscript, while ENP characteristics occur with the excitation transverse optical phonons, *TO* subscript, or strong molecular absorption. Yet, despite the ubiquity of these features in optical responses, few materials exhibit ENZ or ENP characteristics in the 0.5 eV to 1.0 eV range, crucial for TPV devices. The bulk plasmon energy, proportional to $\omega_p \propto (N/m_e)^{1/2}$, is generally pushed to much higher energies due to the small effective electron mass, m_e , and the high electron concentration, $N \approx 10^{22} \text{ cm}^{-3}$, of typical metals [123]. The energy of material phonon resonances, proportional to $\omega_{LO} \propto \omega_{TO} \propto (1/M)^{1/2}$, occurs at significantly lower energies due to the relatively large reduced ionic mass, M [123]. The prospect of natural ENP or ENZ near infrared emitters (in the energy range specified above) is thus limited to a small collection of highly lossy materials such as osmium or molybdenum which are not capable of creating the spectrally narrow emission comparable to wavelength scale structuring approaches.

To engineer ENP and ENZ responses we consider two approaches based on metamaterial crystals. The following subsections show how ENP and ENZ features beyond those found naturally can be created and tuned through the use of either planar material stacks or embedded nanowires. Schematics of the multilayer and nanowire structures are depicted in Fig. 2.2.

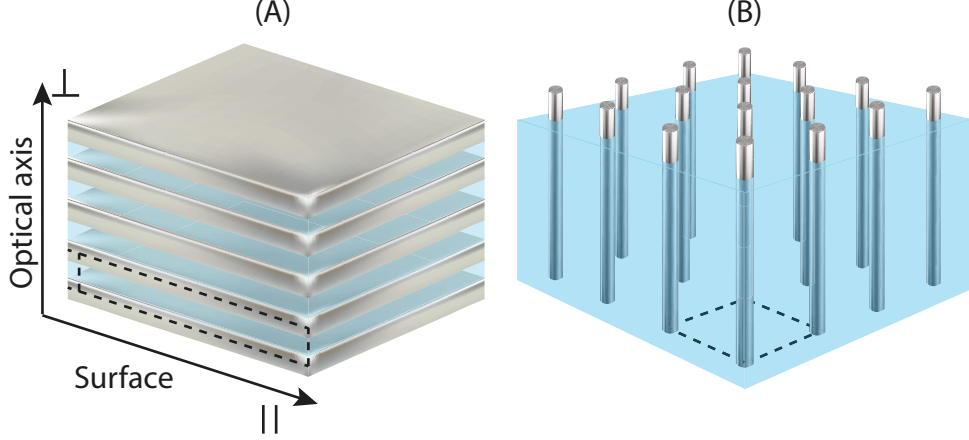


Figure 2.2: **Metamaterial implementations of ENZ and ENP behaviour.** (A) Schematic of a multilayer metamaterial created by interlacing layers of optical metal and dielectric. (B) Schematic of a nanowire metamaterial created by embedding metallic nanowires in a host dielectric matrix. Both structures can be created with current fabrication techniques [121, 124].

2.3.2 One-dimensional multilayer structure

The simplest structure for creating the ENZ/ENP metamaterials consists of alternating layers of metal and dielectric forming a multilayer structure (Fig. 2.2(A)). The effective medium parameters are given by

$$\epsilon_{||} = \epsilon_M \rho + \epsilon_D (1 - \rho) \quad \epsilon_{\perp} = \frac{\epsilon_M \epsilon_D}{\epsilon_M (1 - \rho) + \epsilon_D \rho}, \quad (2.2)$$

where the M subscript is used to denote the metal, the D subscript the dielectric and ρ the relative fill factor of metal in the unit cell. The parallel (||) and perpendicular (\perp) subscripts show the direction convention that will be used in the remainder of the chapter.

The physical characteristics of these effective parameters can be understood in terms of the restrictions placed on the material's electrons. Since the motion of electrons is nearly free within each metal plane (Fig. 2.2(A)) the parallel effective medium parameter follows the frequency dispersion relation of an effective metal. In turn, this creates ENZ behavior at the effective plasmon resonance of the parallel direction. Conversely, in the perpendicular direction nearly free electrons are confined to the thickness of their particular metal plane. On account of this confinement, the frequency dispersion of the perpendicular permittivity mirrors that of an effective Lorentz model dielectric with an accompanying effective ENP resonance. The performance of these effective medium parameters, for calculating emissivity, is compared with the exact theoretical transfer matrix technique for a model tantalum/titanium

dioxide system in Fig. 2.3. Note that throughout the chapter, we verify the predictions of effective medium theory (EMT) using numerical simulations taking into account the finite size of the unit cell, absorption in the constituent materials, dispersion as well as the changes to the electromagnetic field inside the emitter induced by reflections from the substrate.

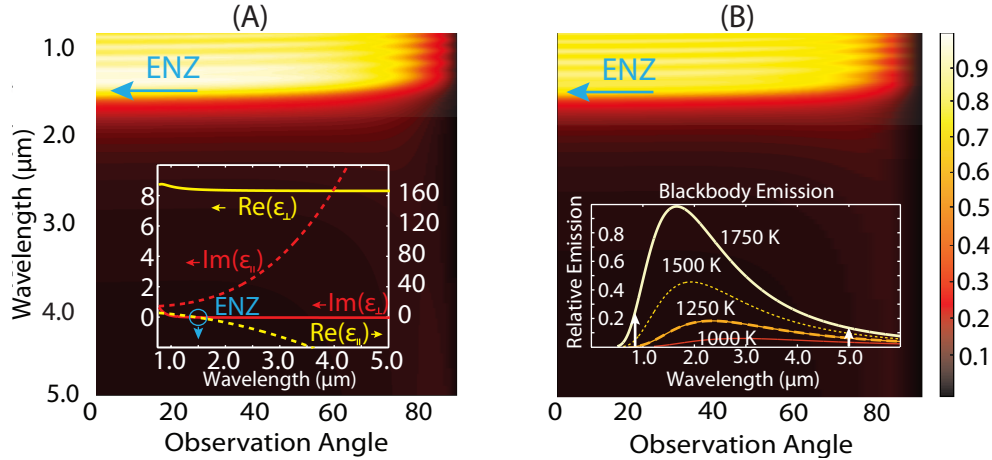


Figure 2.3: **Radiative spectral control of a ENZ metamaterial.**

(A) Effective medium theory calculation of the emissivity of a planar multilayer structure. The metamaterial is composed of twenty unit cells of 5 nm thick tantalum (modeled by a Drude relation) and 45 nm of titanium dioxide ($\epsilon = 7.5$) on optically thick tantalum. Both materials can be deposited by atomic layer deposition [125]. The inset shows the effective medium parameters as functions of wavelength. The ENP resonance is located outside of the plotted area and has little effect due to the spectral power distribution of a blackbody. (B) Transfer matrix calculation of the multilayer structure which shows excellent agreement with EMT. The inset shows the relative emission strength of an ideal blackbody as function of wavelength. The arrows denote the cutoffs of the emissivity plots.

Taking the dispersion characteristics into account, the limitations of the planar structure for thermal applications become apparent. As ENP behavior occurs along the optic axis, its interaction with light is limited to the p-polarization. For realistic materials, this limited domain of interaction leads only to a small lobe of enhanced emissivity at high polar angles. In the parallel direction, the ENZ resonance displays the same characteristics as an isotropic ENZ material. Since the parallel optical response parameter interacts strongly with both polarizations, ENZ behavior dominates the overall emissivity features of the multilayer structure. Correspondingly, the same broad emissivity that earlier caused us to turn toward ENP behavior is also a general feature of the multilayer structure. A visualization of the emissivity of a realizable multilayer system using model tantalum and titanium dioxide is shown in Fig. 2.3. Possible application of this structure as an emitter for

TPVs will be explored in the Section 2.5.

2.3.3 Two-dimensional nanowire structure

Seeking spectral emissivity control beyond what can be accomplished using the multilayer structure, we switch to the nanowire metamaterial system (Fig. 2.2(B)) [124,126]. In contrast to the multilayer structure, embedded nanowires allow nearly free electron propagation along the perpendicular direction (the optic axis), but not in the parallel plane. As the confinement of electrons is flipped from the multilayer structure, so too is the functional frequency dispersion. The perpendicular direction now follows the frequency dispersion characteristics of a metal, while the parallel mimics that of an effective Lorentz model dielectric. Employing the same generalized Maxwell-Garnett approach used for the planar metamaterial, the effective medium parameters for metallic nanowires with a square lattice embedded in a dielectric matrix [127] are defined as

$$\epsilon_{\parallel} = \epsilon_D \left[\frac{\epsilon_M (1 + \rho) + \epsilon_D (1 - \rho)}{\epsilon_M (1 - \rho) + \epsilon_D (1 + \rho)} \right] \quad \epsilon_{\perp} = \rho \epsilon_M + (1 - \rho) \epsilon_D, \quad (2.3)$$

where we have used the same convention earlier introduced for the multilayer structure. Following the general dispersion relations of the effective medium parameters, shown in the inset of Fig. 2.4(B), the ENP and ENZ conditions are now properly aligned for TPV applications. The ENP resonance which results in high narrowband emissivity is located along the parallel direction where it interacts with both s- and p-polarized light. As such, the general emissivity pattern of the nanowire structure is very similar to that of an isotropic ENP material, and nearly ideal for creating a TPV emitter. This is shown in Fig. 2.4, where titanium nitride nanowires embedded in silicon have been used to create a spectrally narrow emissivity spike at a wavelength just below the bandgap of a gallium antimonide (GaSb) photovoltaic cell. The spectral location of GaSb's bandgap, $1.75 \mu m$, makes it well suited for use in a TPV device at realistic operating temperatures (inset Fig. 2.3(B)).

2.3.4 Metamaterial thermal antenna

We now show how the ENZ region of the nanowire array can lead to highly directional thermal emission. Primarily, this occurs as the optical dispersion relation, relating the energy and momentum of an electromagnetic wave in a medium, is altered from the isotropic form of $k_{\perp}^2 + k_{\parallel}^2 = \epsilon \omega^2 / c^2$ (where we have used the previously mentioned direction convention, k denotes the spatial frequency of the wave and ω its frequency) to the anisotropic form of:

$$\frac{k_{\perp}^2}{\epsilon_{\parallel}} + \frac{k_{\parallel}^2}{\epsilon_{\perp}} = \frac{\omega^2}{c^2}. \quad (2.4)$$

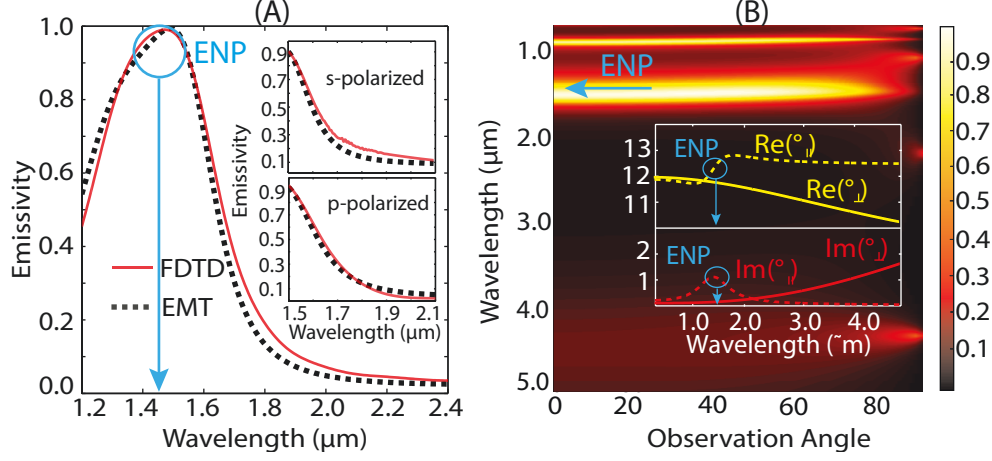


Figure 2.4: **Radiative spectral control of a ENP metamaterial.**

(A) Comparison of the polarization averaged emissivity of a 280 nm thick metamaterial emitter making use of a host matrix of silicon (assumed to be a constant dielectric) and 20 nm diameter titanium nitride nanowires in a 120 nm square unit cell on an optically thick tantalum backing. The two curves compare emissivity as calculated by effective medium theory and finite difference time domain simulation (Lumerical) at normal incidence⁵. The insets show the same comparison for s- and p-polarized emissivity over a compressed wavelength range of 1.5 to 2.1 μm at a polar angle of 50 degrees. Note the excellent agreement between EMT and the full numerical simulation. (B) Polarization averaged emissivity of the nanowire system described in (A) calculated using EMT. Emission peaks occurring below the designed emission are known to be part of the Bragg scattering regime [128]. These peaks have little effect in application due to low emitted power at wavelengths shorter than 800 nm for bodies cooler than 3000 K. The inset shows the effective medium parameters as functions of wavelength. The spectrally narrow, omnidirectional nature of the ENP emissivity peak is nearly ideal for use as an emitter in a TPV device.

If $\epsilon_{\perp} \neq \epsilon_{\parallel}$, $Re\{\epsilon_{\perp}\} > 0$ and $Re\{\epsilon_{\parallel}\} > 0$ the isofrequency surface (generated by fixing ω and allowing k_{\perp} and k_{\parallel} to vary) forms an ellipsoid. If either $Re\{\epsilon_{\perp}\} < 0$ or $Re\{\epsilon_{\parallel}\} < 0$, with the real part of the other dielectric component > 0 , the dispersion relation forms a hyperboloid.

As the perpendicular direction nears low loss ENZ behavior, the isofrequency surface of the anisotropic crystal generated from (2.4), with $Re\{\epsilon_{\parallel}\} > 0$ becomes very narrow, Fig. 2.5. Accordingly, very small changes in incident angle k_{\parallel} result in extreme variation of the material impedance. For instance, an electromagnetic mode at non-normal incidence quickly develops a substantially different relation between its wave vector k and frequency ω leading to high reflections [129]. This effect produces a small angular region (for p-polarized light) over which the free space modes can penetrate the medium and be absorbed, Fig.2.5. Therefore, a metamaterial with these permittivity features will have high emissivity only over this narrow angular region

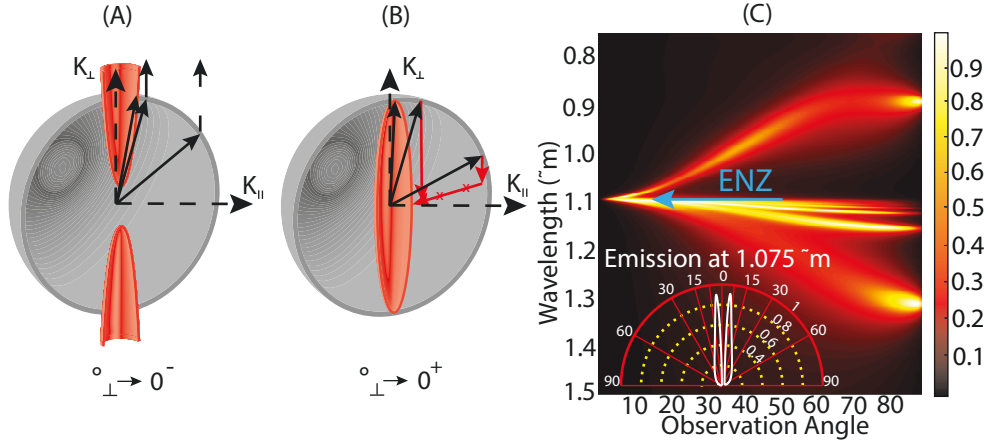


Figure 2.5: **Metamaterial thermal antenna.**

The figure shows a cross-sectional view of the narrow isofrequency surfaces of the metamaterial in the ENZ regime. The spherical isofrequency surface corresponds to vacuum. (A) As the perpendicular permittivity nears zero from the negative side, the dispersion relation inside the metamaterial becomes a narrow hyperboloid. (B) Ellipsoidal isofrequency surface as the perpendicular effective medium constant approaches ENZ from the positive side. Note that only waves at near normal incidence from vacuum penetrate the metamaterial which are immediately absorbed due to the ENZ resonance. Furthermore, the large impedance mismatch at higher angles leads to high reflections. This results in highly directional emissivity patterns. (C) P-polarized emissivity plot for a 450 nm thick metamaterial emitter consisting of a host matrix of aluminum oxide (Al_2O_3) embedded with 15 nm diameter silver nanowires in a 115 nm square unit cell using the effective medium approach. The angularly sharp emission near normal incidence around 1.075 μm is usable for applications requiring coherent thermal radiation. The inset shows a polar plot of the emissivity along the 1.075 μm line. The secondary bands of high emissivity around the ENZ region is due to the impedance matching behavior in the ellipsoidal/hyperboloidal isofrequency regime which moves to higher angles as the $|Re\{\epsilon\} \rightarrow 0|$ condition is relaxed.

at the ENZ wavelength. Concurrently, the closer $Re\{\epsilon_{\perp}\}$ is to 0, the narrower this region becomes, eventually forming a angularly sharp peak. Since spatial coherence is directly connected to the angular spread of an electromagnetic wave, the heating of such an anisotropic crystal near a perpendicular ENZ resonance presents a grating-free method of thermally exciting angularly coherent radiation. The angular and spectral location of this behavior is tunable based on the fraction of metal, ρ , filling the underlying unit cell.

Material	Melting Point (K)	$-\epsilon'/\epsilon''$ ($1 \rightarrow 2\mu m$; $300 K$)
<i>Au</i>	1337	14 \rightarrow 8 [130]
<i>Ag</i>	1235	98 \rightarrow 29 [130]
<i>AZO</i>	≈ 2200 [131]	-15 \rightarrow 4 [132]
<i>TiN</i>	3250 [133]	1 \rightarrow 2 [134]

Table 2.1: **Optical quality and melting point of infrared plasmonic media.** The table displays the range of the optical quality defined as $-\epsilon'(\omega)/\epsilon''(\omega)$ of common low melting point plasmonic metals, *Au* gold, and *Ag* silver and alternative high melting point plasmonic metals, *AZO* aluminum zinc oxide and *TiN* titanium nitride, in the infrared region of $1 \rightarrow 2 \mu m$ crucial for thermophotovoltaics.

2.4 High temperature plasmonic metamaterials

To this present time, optical / near infrared metamaterial applications have been confined to temperatures near or significantly below $300 K$. Yet, many of the most interesting applications of thermal engineering require temperatures in the vicinity of $1500 K$. It follows directly that the scope of traditional optical metamaterials for thermal engineering applications is quite restricted. However, this limitation is strictly material based. In this section, we show that by switching away from the conventional low melting point metals, such as silver and gold, optical metamaterial design principles can be employed for high temperature thermal engineering.

From the results of Tab. 2.1 we observe that several thermally robust materials display weakly metallic optical characteristics and relatively low loss (Fig. 2.6(A)) through the 1 to $2 \mu m$ spectral range. These characteristics prove crucial for thermal engineering. Building on the results of inset Fig. 2.3(B), energy based applications of thermal engineering are most likely in the approximate temperature range of $1500 K$. At significantly cooler temperatures, the spectrally broad and relatively small power density emitted by a blackbody (see Section 2.5) strongly limits the energy conversion performance of any possible far-field TPV device. Returning to the inset of Fig. 2.3(B), since the bulk of the emitted power for a blackbody in this temperature range is positioned at wavelengths slightly longer than $1 \mu m$, this becomes the most important spectral region for emissivity control.

According to the effective medium theory presented in previous sections, both ENP and ENZ resonances require the metallic and dielectric components of the unit cell to have $|Re\{\epsilon\}|$ of the same order. As $Re\{\epsilon\}$ is at most on the order of 10 for a dielectric in the near infrared spectral region, metamaterial based ENP and ENZ behavior in this region of high spectral power density is only possible if the metallic permittivity component satisfies $-10 \leq Re\{\epsilon\} \leq -1$. This condition makes the

replacement of silver or gold with more thermally robust interstitial nitrides such as titanium nitride [134], transition metals such as tantalum, or transparent conductive oxide semiconductors such as aluminum zinc oxide [132], all the more important for metamaterial thermal engineering. Fine-tuning of the ENP resonance using high temperature plasmonic materials is shown in Fig. 2.6(B).

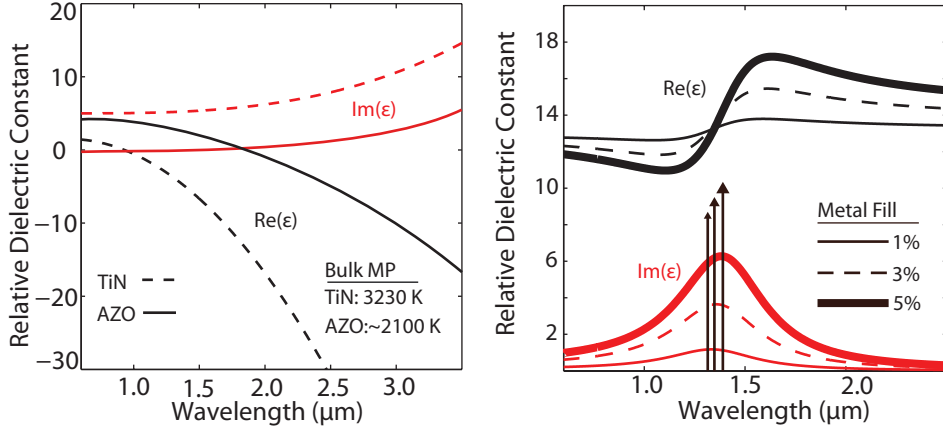


Figure 2.6: **Alternative plasmonic materials and ENP tuning.**

(A) Drude models of the optical properties of TiN and AZO based on the data presented in [132,134]. (B) Fine-tuning of the ENP metamaterial resonance by altering the fill fraction of metal in the unit cell. In this plot the titanium nitride/silicon metamaterial system described in Fig. 2.4 is used. Both AZO and TiN achieve thermally stable plasmonic behavior in the near infrared (Table Section 2.4).

2.5 Energy conversion efficiency of TPV devices

2.5.1 Characteristics of ENZ and ENP emitters for TPVs

We now turn our attention to characterizing the performance of the metamaterial emitters made of high temperature plasmonic materials for TPV systems. We follow the theoretical energy conversion argument developed by Shockley and Queisser [107]. For completeness, we provide a detailed comparison with a blackbody emitter of the various efficiencies that need to be accounted for in a practical device.

The model begins with the primary assumption that the photovoltaic cell, of the larger TPV device, operates with unity quantum efficiency perfectly cutoff at the bandgap energy. Under this assumption, photons with energy greater than the material bandgap create an electron hole carrier pair with energy equal to that of the bandgap, and any additional energy is lost to thermalization within the cell. Photons with energy below the bandgap of the photovoltaic cell are lost to free space. This perfect cutoff model defines an ultimate performance limitation on the TPV

device following the usable power created by the emitter

$$\eta_{ult}(\lambda_{gap}, T) = \frac{\int_0^{\pi/2} d\theta \cos(\theta) \sin(\theta) \int_0^{\lambda_g} d\lambda \frac{\lambda}{\lambda_g} \zeta_E(\lambda, \theta) I_{BB}(\lambda, T)}{\int_0^{\pi/2} d\theta \cos(\theta) \sin(\theta) \int_0^{\infty} d\lambda \zeta_E(\lambda, \theta) I_{BB}(\lambda, T)}, \quad (2.5)$$

$$I_{BB}(\lambda, T) = \frac{8\pi hc}{\lambda^5 \left(e^{\frac{hc}{\lambda k_B T}} - 1 \right)}, \quad (2.6)$$

where $\zeta_E(\lambda, \theta)$ is emissivity of the emitter, λ_g the wavelength of the material bandgap, T the emitter temperature, and $I_{BB}(\lambda, T)$ the spectral radiance of an ideal blackbody. Here, we have assumed the emitter to be planar with no azimuthal angular dependence, and that the emissivity characteristics are temperature invariant following the considerations of [135, 136].

To understand the consequences of this relation, the efficiencies η_{ult} resulting from the angularly averaged emissivity profiles of an ideal blackbody and the titanium nitride/silicon nanowire system, described in Fig. 2.4, are plotted for a gallium antimonide photovoltaic cell with temperatures varying from 500 to 2500 K in Fig. 2.7(A). Gallium antimonide is chosen as the photovoltaic cell as its material bandgap, 0.71 eV , is well matched to the spectral power distribution of the blackbody near 1500 K . At low temperatures, since the blackbody spectral power distribution is broad and flat, the power emitted near the photovoltaic cell bandgap is not an appreciable percentage of the total emitted power. As the temperature increases, the blackbody spectral radiance (2.6) increases and shifts towards shorter wavelengths. This leads to higher percentages of the emitted radiation being usable by the photovoltaic cell and, consequently, increased ultimate efficiency. This effect peaks as the efficiency gained by shifting a larger portion of the spectral power density to lower wavelengths is countered by mounting thermal losses due to the cell only producing electron hole pairs at the bandgap energy. A visualization of the spectral power distributions of an ideal black body, the titanium nitride nanowire design, and the emitter offering peak device efficiency for a gallium antimonide photovoltaic cell are shown in Fig. 2.7(B) at a temperature of 1500 K .

2.5.2 Shockley-Queisser efficiency analysis

To determine the total efficiency of our emitter designs as part of a TPV device, the physical characteristics of the photovoltaic cell must be considered. Assuming standard pn-junction photon conversion, two extra efficiency terms must be introduced. First, we must take into account the additional ways in which charge carriers may be removed from the cell. Second, we must include the specific current voltage

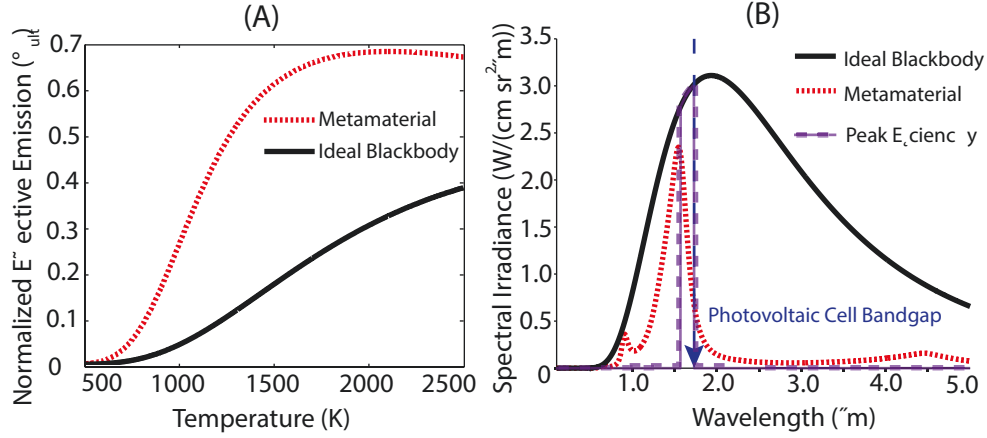


Figure 2.7: **Metamaterial emitter for thermophotovoltaics.**

(A) Comparison of the ultimate efficiency of a titanium nitride metamaterial emitter (Fig. 2.4) to that of a blackbody for a 0.71 eV material bandgap, corresponding to GaSb. Based on bulk material parameters, the metamaterial emitter will be thermally stable up to 1650 K . (B) Comparison of the angularly averaged spectral emission characteristics between the titanium nitride metamaterial design, an ideal blackbody, and an emitter which maximizes the efficiency of energy conversion at 1500 K . The large lobe of the metamaterial ENP resonance closely matches the position and magnitude of the emitter producing the highest TPV device efficiency.

relations of a pn-junction.

In addition to the desired external current, both radiative and nonradiative recombinations reduce the total number of charge carriers within a photovoltaic cell. The characteristics of these recombination mechanisms can be understood through the equilibrium condition of the photovoltaic cell with and without the presence of emitter photons. With no emitter contribution, and the cell in thermodynamic equilibrium, the net number of carriers within the cell is constant, and can be described by

$$Q_{BB}(\lambda_g, T_C) - R_{rad}(T_C) + G_{other}(T_C) - R_{other}(T_C) = 0, \quad (2.7)$$

where $Q_{BB}(\lambda_g, T_C)$ is the number of carriers generated by photons incident on the photocell from its surroundings,

$$Q_{BB}(\lambda_g, T_C) = 2 \int_0^{2\pi} d\phi \int_0^{\pi/2} d\theta \cos(\theta) \sin(\theta) \int_0^{\lambda_g} d\lambda \frac{\lambda}{\lambda_g} I_{BB}(\lambda, T_C), \quad (2.8)$$

$R_{rad}(T_C)$ the number lost by radiative recombination, $G_{other}(T_C)$ any other carrier generation, and $R_{other}(T_C)$ any other carrier recombination. As this equilibrium also requires that energy entering the cell is equal to that exiting, we can immediately

conclude that

$$R_{rad}(T_C) = Q_{BB}(\lambda_g, T_C) \quad R_{other}(T_C) = G_{other}(T_C). \quad (2.9)$$

We now examine the cell with an external incident flux from an emitter source, and an external load through which carriers may exit. Following the standard statistical mechanics model, we assume that the additional carriers perturb the recombination rates within the cell as e^{V/V_C} . Here, V is the difference between the quasi-Fermi levels, and $V_C = k_B T_C / e$. As such,

$$Q_E(\lambda_g, T_E) - Q_{BB}(\lambda_g, T_C) e^{\frac{V}{V_C}} + G_{other}(T_C) - G_{other}(T_C) e^{\frac{V}{V_C}} - \frac{I}{q} = 0, \quad (2.10)$$

$$Q_E(\lambda_g, T_E) = \int_0^{2\pi} d\phi \int_0^{\pi/2} d\theta \cos(\theta) \sin(\theta) \int_0^{\lambda_g} d\lambda \frac{\lambda}{\lambda_g} \zeta_E(\lambda, \theta) I_{BB}(\lambda, T_E), \quad (2.11)$$

as we assume the emitter photons fall on only one side of the photovoltaic cell. Note that we now also assume that the finite volume between the emitter and photovoltaic cell does not contribute to the incident radiation, and that any electromagnetic energy radiated by the solar cell is not reused for energy conversion. Introducing f_{rec} as the percentage of recombinations which are radiative $\left(\frac{Q_{BB}(\lambda_g, T_C)}{Q_{BB}(\lambda_g, T_C) + G_{other}(T_C)} \right)$ and solving for the open circuit voltage we find

$$V_{OC} = V_C \ln \left(\frac{f_{rec}}{2} \frac{Q_E(\lambda_g, T_E)}{Q_{BB}(\lambda_g, T_C)} - f_{rec} + 1 \right), \quad (2.12)$$

which, when functioning within the quasi-static limit of this approximation, is smaller than the initial material bandgap V_g . This consideration leads us to the efficiency factor:

$$\eta_{rec}(\lambda_g, T_E, T_C) = \frac{V_{OC}}{V_g}. \quad (2.13)$$

Returning to (2.10), we can see that a final efficiency reduction arises due to the interrelation of current and voltage in the pn-junction cell. As current is allowed to flow the number of free carriers within the cell drops, reducing the voltage from its open circuit value. As current must be drawn to create usable power, an efficiency factor relating the operational voltage, V_P , to the open circuit voltage, V_{OC} , must be included by finding the maximal power-point ($V_P I(V_P)$) of the photovoltaic cell. Using (2.10) we find

$$\eta_{pow} = \frac{V_P I(V_P)}{V_{OC} I_{SC}} = \frac{v_{pp}^2}{(v_{pp} + \ln(1 + v_{pp}))(1 + v_{pp} - e^{-v_{pp}})}, \quad (2.14)$$

where v_{PP} is defined as the ratio of the operating cell voltage at the maximum power-point to the background cell voltage, $\frac{V_P}{V_C}$, and is determined via the relation

$$V_{OC} = V_P + V_C \ln \left(1 + \frac{V_P}{V_C} \right). \quad (2.15)$$

The product of these two results, $\eta_{rec} \eta_{pow}$, shows the efficiency with which an idealized pn-junction photovoltaic cell converts photons at its material bandgap into usable power. Using the three efficiency parameters computed, we can now determine the overall efficiency of our metamaterial emitter designs functioning as part of a TPV system.

2.5.3 Energy conversion results

From the ultimate efficiency (2.5) and Fig. 2.7 we can begin to see that the principal characteristic of a good emitter for TPVs is the suppression of subbandgap photons. Near unity ultimate efficiency, η_{ult} , requires the spectral emissivity of the emitter, $\zeta_E(\lambda, \theta)$, to become narrow band at a wavelength slightly shorter than that of the material bandgap. Yet, this ultra-sharp spectral behavior is pragmatically undesirable. As the spectral range of emission is narrowed, the power produced at a fixed temperature is decreased. This reduction not only limits the amount of power that can be extracted from the TPV device, but also acts to reduce the total energy conversion efficiency. Reviewing (2.13), if the number of carriers in the pn-junction is near the unilluminated thermal equilibrium amount, a large percentage of the incident emitter energy will be either reradiated or lost within the cell. Consequently, the efficiency of converting the power radiating from the emitter will also be reduced. Since the temperature of the emitter, and thus the amount of usable power it can produce, is intrinsically limited by the materials used, whether a spectrally wider or narrower emission is preferable depends on the particular application. At low temperatures, broader emitters are more efficient and provide greater power densities; however, as temperature is increased their efficiency falls below that of the narrow emitter.

Clearly, this tradeoff has direct consequence for our TPV emitter designs. For applications in which it is not possible to reach emitter temperatures of ≈ 1000 K, broad ENZ type emitters will create better TPV devices. Above this approximate temperature, spectrally thinner ENP type absorption peaks will provide superior net efficiency. Here, even lower emitted power begins to become a benefit of the spectrally thin design. As the emitter is in thermodynamic equilibrium, all emitted energy must be replaced. This becomes increasingly difficult with a spectrally broad emitter at high temperatures. As an alternative view, given a fixed input power,

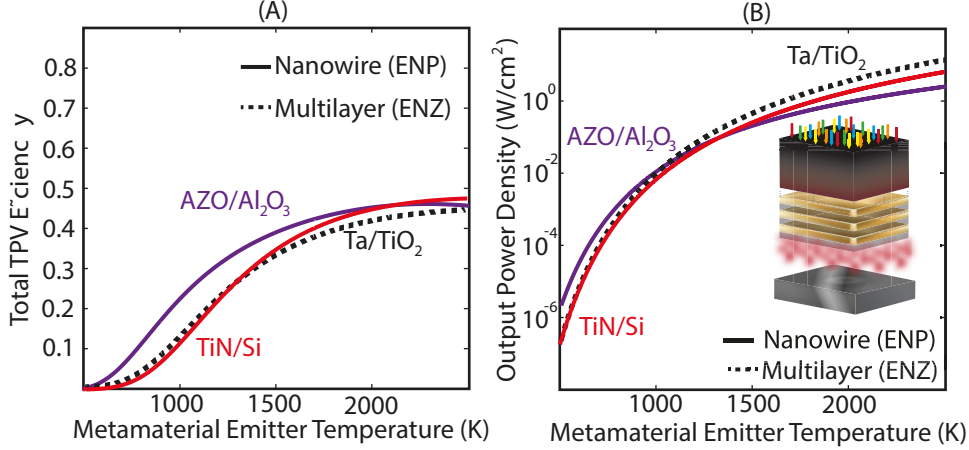


Figure 2.8: **Efficiency of metamaterial thermophotovoltaic systems.**

(A) Theoretical efficiency of three TPV devices taking into account all discussed effects. The cell parameters of the Ta/TiO_2 multilayer and TiN/Si nanowire systems are the same as in Fig. 2.3 and Fig. 2.4. The third system utilizes 250 nm long, 20 nm diameter AZO rods in a 125 nm square Al_2O_3 matrix, set on an optically thick tantalum backing, and an InGaAs photovoltaic cell with bandgap set at 2100 nm. In these plots the efficiency of heating the source is not included. However, due to the tantalum backing included in all designs, the performance of these devices should not be greatly altered by the characteristics of the heat source. (B) Final output power density of the systems described in (A). Due to the lower energy bandgap of the InGaAs photovoltaic cell, the AZO based metamaterial system produces relatively higher power density at lower temperatures. Following the discussion of Section 2.5.1, the opposite is seen at higher temperatures. The high performance metrics of these model systems indicate the potential of TPV systems using metamaterials.

a spectrally thinner emitter will operate at a higher temperature and thus higher efficiency (Fig. 2.8(B)).

Taking all three efficiency considerations into account, the theoretical metrics for TPV devices using metamaterial emitters, neglecting any loss associated with an absorber stage, are shown in Fig. 2.8. The full concentration limit for solar based single junction photovoltaics, following the assumptions of Shockley and Queisser, is surpassed for emitter temperatures near 1500 K in the AZO nanowire system. The overall performance of these designs show either greater high temperature efficiency [35, 112], tighter spectral emissivity, or similar efficiency behavior with a higher emitter power [118] to other contemporary designs.

2.6 Summary

In this chapter we have developed a general means of exerting control over thermally excited far-field electromagnetic radiation through the use of ENP and ENZ resonances. Thermal radiation control through the use of these generalized bulk material resonances shows great potential for creating a new class of realizable thermal devices. In particular, we have shown specific metamaterial implementations for creating emitters for TPVs and coherent thermal sources in the near infrared range crucial for energy applications. We have also introduced the concept of metamaterials based on high temperature plasmonic materials. This switch away from typical plasmonic materials is crucial for many far-field thermal applications and more generally for furthering the scope of optical metamaterial designs. This work paves the way for future use of metamaterials for the control of thermally excited radiation.

Chapter 3

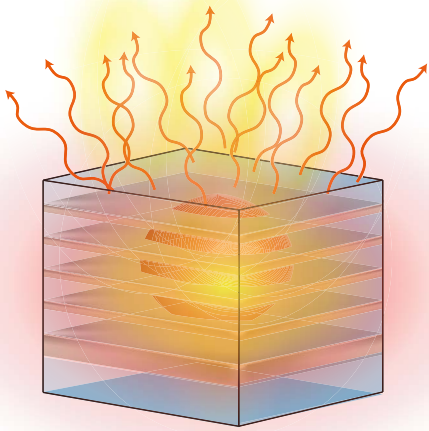
Controlling Thermal Emission with Refractory Epsilon-near-zero Metamaterials via Topological Transitions

In this chapter, we present experimental validation of the thermal design principles developed in Chapter 2.

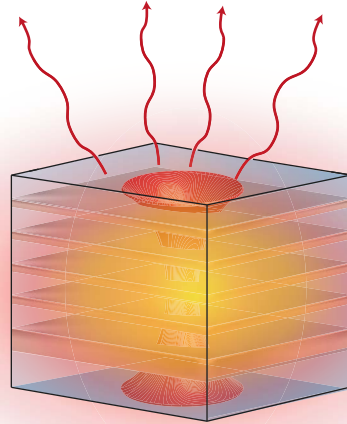
As we have examined in the analysis of the previous chapter, control of thermal radiation at high temperatures in the near infrared is vital for waste heat recovery and for high-efficiency thermophotovoltaic (TPV) conversion. Building on these ideas, in this chapter we demonstrate a refractory $W - HfO_2$ metamaterial, which selectively enhances and suppresses thermal emission through an engineered dielectric response function. This design stands in contrast to previously reported structural resonances techniques such as gratings, thin film resonances, metasurfaces and photonic crystals as it is based on effective material properties and not wavelength scale interference effects or coupling. Importantly, our emitter is fabricated without any surface structuring, and provides near omni-directional spectrally selective radiative emission.

The functionality of our emitter is based on the creation of an epsilon-near-zero frequency and connected optical topological transition (OTT) in the isofrequency surface of a refractory multi-layer metamaterial, Fig. 3.1. We verify that such metamaterial design principles are thermally stable up to the thermal degradation limits of the metamaterial structure, here over 1000 °C.

Spherical isofrequency



Hyperbolic isofrequency



Optical topological transition

Figure 3.1: **Thermal emission across an optical topological transition.**

The figure schematically depicts how an optical topological transition induces selective thermal emission. At energies where the isofrequency relation of the emitter is ellipsoidal, the momenta of its thermally excited electromagnetic modes are similar to those of free space, leading to high emission. However, if the isofrequency is hyperbolic, the momentum of an electromagnetic mode inside the emitter is much greater than a free space mode with same energy. This mismatch leads to a strong suppression of far-field thermal radiation. By engineering a optical topological transition the emitter can transition between these two isofrequency relation over a narrow frequency band, leading to a high degree of control over the spectral content of its thermal radiation.

3.1 Introduction

In natural media, the photonic isofrequency surface is a fixed relation between the momentum and energy of photonic modes which dictates the material’s linear optical response specified by Maxwell’s equations [137]¹. In metamaterials, it is a property that can be engineered in order to produce desired optical characteristics [138]. As opposed to the regular spherical and ellipsoidal shapes seen in natural dielectrics, a wide variety of surfaces and related optical response are possible; including the point-like vanishing surfaces of epsilon-near-zero (ENZ) media [139] and open surfaces of hyperbolic media [140].

In this chapter, our goal is to demonstrate that this control of optical response through the shape of the isofrequency surface works equally well at high temperatures. This is accomplished by fabricating a metamaterial with wavelength selective thermal emission arising from an optical topological transition (OTT) [138] in its photonic isofrequency surface. The design marks an important departure from well established routes of thermal emission control using two dimensional and three dimensional photonic crystals [42, 56, 141–147], thin film resonances [99, 148–150], gratings and metasurfaces [44, 49, 112, 122, 151, 152]. Instead of altering thermal emission through wavelength scale interference effects or coupling, here, we use an intrinsic material property (the ENZ frequency) to manipulate the bulk thermal energy density and consequently selectively excite and suppress the photonic modes that contribute to far-field thermal emission. (This metamaterial design principle is experimentally confirmed by the spectral content of far-field thermal radiation in the vicinity of the topological transition of the isofrequency surface.)

The metamaterial is designed based on a subwavelength super-lattice structure of tungsten and hafnium oxide. This choice of constituent materials stands in stark contrast to previous ENZ and hyperbolic media which have utilized either noble metals with low thermal stability [153], phonon-polaritonic materials [154], graphene [155, 156], or highly doped semiconductors [157]. Specifically, these materials are chosen primarily for their exceptional thermal stability, and secondarily for the relatively low optical absorption and ease of fabrication. Using this design, we conclusively show the high temperature stability of the optical absorption and thermal emission resulting from effective ENZ response at temperatures of up to 1000 °C. The associated OTT is carefully designed to lie in the crucial near infrared window of 1–3 μm , paving the way for metamaterial designs compatible with low bandgap photovoltaic (PV) cells [158–161] (0.3 – 0.6 eV).

¹For additional comments on isofrequency surfaces and optical topological transitions please see the first section of Appendix F *Additional Results for Natural Hyperbolic Media*.

In exchange for improved conversion efficiency and application flexibility the implementation of the TPV concept places stringent requirements on the emissivity characteristics and thermal stability of the selective thermal emitter, Fig. 3.2 (A). Thermodynamic conservation arguments require the radiative thermal emissivity of any object to be less than that of a blackbody at the same temperature. Consequently, to achieve sufficient output radiative power density in the range of contemporary low bandgap photovoltaic receivers [158] with bandgaps of typically 0.55 eV operational temperatures surpassing 1000 °C are required. The emitter should also possess the highly selective emissivity characteristics required to suppress the emission of long-wavelength photons and, at the same time, should provide near unity emissivity at energies above the bandgap of the PV cell, Fig. 3.2 (A). Short wavelength selectivity of the emitter is not required since the blackbody limit at 1000 °C represents a natural boundary due to the BoseEinstein occupation quickly decreasing for shorter wavelengths. Our design has low angular dependence and is tunable within the entire near infrared spectrum. We also reveal the mechanisms leading to thermal degradation of the optical performance through spectral analysis and energy dispersive X-ray spectroscopy (EDS) techniques. Our measurements of the optical absorption and thermal emission at high temperature (1,000 °C) serve as a direct validity of Kirchhoffs laws [120] for bulk effective medium parameters and pave the way for refractory thermal metamaterials. The OTT is obtained in the vicinity of natural material excitations such as plasmons and optical phonons. However, utilizing natural material resonances for thermal emission engineering poses severe challenges as outlined in Fig. 3.2 (B). Conventional plasmonic materials suffer from low melting points and from too high plasma frequencies [162,163], while phonon-polaritonic materials [154] have resonances in the mid infrared range that cannot be moved easily to higher energies in the 2 - 4 μm wavelength region crucial for high temperature nanophotonic applications such as TPV. Thus metamaterials are required to shift OTT to the required spectral range.

3.2 Results

3.2.1 Metamaterial design

Our aim is to engineer an OTT in the near infrared spectral window with refractory building blocks to control thermal emission. The OTT is a change in the isofrequency surface of a metamaterial which changes from a closed ellipsoid to an open hyperboloid and affects fundamental properties such as the photonic density of states and bulk thermal energy density [164,165]. In our case the hyperbolic isofrequency surface does not provide modes that can be coupled out of the metamaterial to the

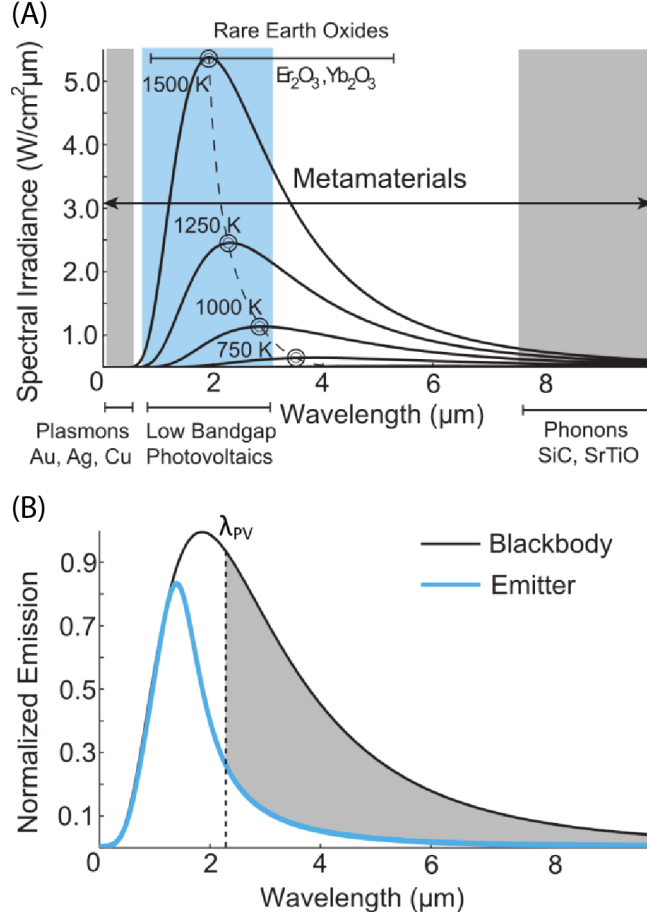


Figure 3.2: **Overlap of the spectral irradiance of a blackbody half-space with natural optical resonances.**

(A) The blackbody emission at 1000 °C (1273 K) normalized to its maximum and the emission of a selective TPV emitter at the same temperature normalized to the maximum of the blackbody emitter are presented. The selective emitter suppresses thermal emission throughout the infrared and simultaneously provides near blackbody emission at energies above the bandgap of the PV cell. The band-edge of a PV cell with 0.55 eV is presented by the dashed line indicating λ_{PV} . (B) Overlap of the spectral irradiance of a blackbody half-space with natural optical resonances. The blackbody spectrum for increasing temperatures between 750 and 1500 K shows the peak lying in the near infrared region for high temperatures (1500 K) which is the spectral range for contemporary low bandgap photovoltaics (blue shaded area). Note, these temperatures are necessary for high-efficiency energy conversion but are beyond the reach of conventional plasmonic building blocks for metamaterials because of their low melting point. On the other hand, thermal engineering approaches based on optical phonons are restricted to the mid infrared spectrum and are difficult to move to the near infrared range. Metamaterial principles extend the spectral range of bulk optical material resonances throughout the infrared.

far-field and thus the emission at longer wavelengths is naturally suppressed. The OTT is a material approach to achieve either enabling or suppression of the thermal

emission since the two isofrequency surfaces lead to very different optical reflectivities. According to Kirchhoffs law the radiative absorptivity and thermal emissivity of a object are identical. Thus, we consider calculated and measured absorptivity and emissivity as equal throughout the chapter. As a consequence the sharp change in reflectivity which affects the optical absorption spectrum also dictates the thermal emission spectrum of the metamaterial.

The simplest realization of a metamaterial with a controllable topological transition consists of alternating subwavelength layers of metal and dielectric, as displayed schematically in Fig. 3.3 (C). Figure 3.3 (D) is the scanning electron microscopic (SEM) image of the fabricated structure. The effective medium response of this basic layered structure is given by the weighted arithmetic average along the material planes, $\epsilon_{\parallel} = (d_M \epsilon_M + d_D \epsilon_D) / (d_M + d_D)$ and the weighted harmonic average along the optical axis, $1/\epsilon_{\perp} = (d_M/\epsilon_M + d_D/\epsilon_D) / (d_M + d_D)$. Note that the effective medium parameters, controlling the topological transition, are determined simply by the permittivities of the individual layers, $\epsilon(\omega)$, and their thicknesses, d_M and d_D , within the unit cell. The D and M subscripts used here denote dielectric and metallic materials. The metamaterial consists of refractory metal tungsten (20 nm layers) and a transparent dielectric hafnium dioxide (100 nm layers) on a 100 nm tungsten substrate as shown in Fig. 3.3 (C), and 3.2 (D). Our refractory material choices with their high temperature stabilities are unique for multilayer metamaterials. Figure 3.3 (B) shows the excellent agreement between dielectric parameters extracted using spectroscopic ellipsometry and an effective medium anisotropic model. It should be noted that the OTT occurs at the ENZ wavelength ($Re\{\epsilon_{\parallel}(\lambda_{OTT})\} \rightarrow 0$) when the real part of the perpendicular dielectric constant changes sign from positive (dielectric) to negative (metal). Furthermore, we emphasize the striking feature that the OTT survives even in the presence of high losses present in tungsten.

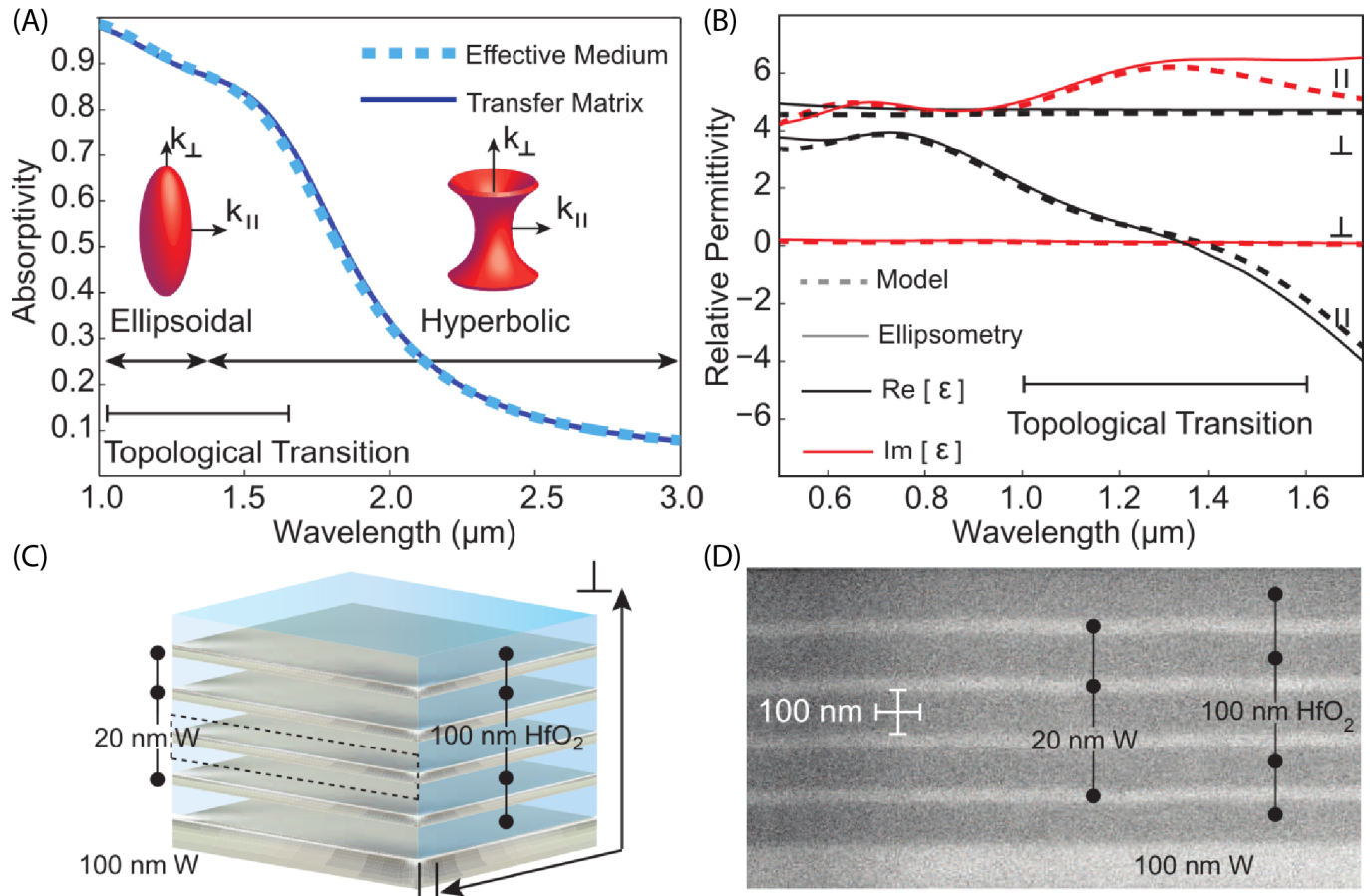


Figure 3.3: Concept and implementation of the tungsten/hafnium dioxide refractory metamaterial.

(A) Calculated absorptivity characteristic of the metamaterial at normal incidence. At vacuum wavelengths below the topological transition the medium supports radiative modes resulting in high absorptivity. Beyond the transition the metamaterial allows only modes with large tangential components of the wavevector which cannot couple to optical modes propagating in vacuum. This leads to a strong suppression of the structures absorptivity and thus of its emissivity. Because of the small unit cell size excellent agreement is seen between the effective medium and rigorous transfer matrix theory. (B) Comparison of the theoretically designed, based on permittivity data provided by Roberts [166], and ellipsometrically extracted relative permittivity parameters for the metamaterial structure (see methods). In all simulations the hafnium dioxide layers are assumed to be lossless and dispersionless with a relative permittivity of $\epsilon = 3.88$. (C) Schematic image of the refractory metamaterial design. The dashed box shows the metamaterial unit cell. (D) SEM image of the fabricated refractory metamaterial. By choosing the thicknesses of the nano-structured refractory metal and oxidic dielectric layers, topological transitions can be tuned throughout the infrared.

Figure 3.3 (A) shows the predicted emissivity of the tungsten/hafnium dioxide multilayer calculated using transfer matrix theory. We emphasize that the topological transition is captured completely by an effective medium theory (EMT). EMT simulations take into consideration the presence of the substrate and the topmost capping layer to account for the finite number of layers forming the metamaterial. The calculated absorptivity of the presented metamaterial with four periods shows $< 1\%$ difference compared with the absorptivity of the same metamaterial with 20 periods. Thus, the transmissivity T is negligible and the designed and fabricated number of layers represents a satisfactory approach to determine the absorptivity and emissivity of an infinite metamaterial.

Figure 3.4 analyzes the angular dependence of the absorptivity of the metamaterial. The angular-dependent emissivity of the structure is the power per area, thermally radiated at a specific angle and wavelength interval divided by the same quantity of an ideal blackbody. As seen in Fig. 3.4, the calculated large absorptivity thus emissivity at a given wavelength between 1.0 and 1.5 μm is largely independent of the angle of incidence or angle of observation up to angles of $\approx 70^\circ$. For larger angles Fresnel reflectivity is increasing and the absorptivity and emissivity drop down to zero. As photons at such large angles will not be emitted no effective heat loss of the source takes place and thus the efficiency of an envisaged TPV-system will not be altered by this fact. Along with spectral selectivity, this is an important characteristic desired for practical TPV applications. In a TPV-system, an omnidirectional emitter is clearly advantageous as it allows extracting and transmitting a much larger radiative power. The dark regions correspond to low thermal emissivity in a broad angular range beyond the OTT as predicted by our effective medium approach whereas the white regions depict high thermal emissivity.

We now discuss the coupling of the thermally excited metamaterial modes with vacuum, which determines the thermal radiation spectrum. The OTT between the closed ellipsoidal and open hyperboloidal isofrequency surface occurs at the ENZ frequency. At wavelengths below the topological transition, the wavevectors of thermally excited modes lie on the surface of the ellipsoid and have tangential components matched to that of vacuum modes. Thus the thermally excited modes can efficiently couple to vacuum modes maximizing the power density of thermal emission (Fig. 3.3 (A)). Above the topological transition wavelength, the isofrequency surface of the refractory metamaterial forms a type II hyperboloid, supporting only extraordinary modes with very large wavevectors which cannot be matched to vacuum modes. Thus there is no coupling between the hyperbolic modes and the vacuum modes leading to a strong suppression of radiative infrared thermal emission.

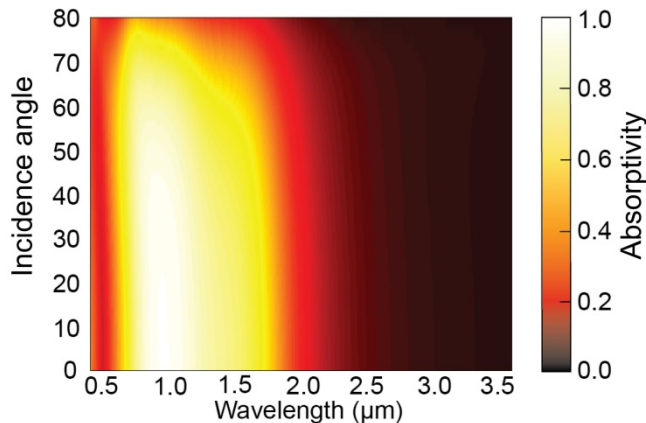


Figure 3.4: **Absorptivity of the metamaterial versus incidence angle.**

Simulated absorptivity of the tungsten/hafnium dioxide metamaterial described in Fig. 3.3 as a function of wavelength of incident light and as a function of the angle of incidence, taking into account both s- and p- polarizations. The simulation is performed using the transfer matrix formalism assuming optical properties of tungsten from Roberts [166], and that hafnium dioxide can be treated as a dispersionless dielectric with a relative dielectric constant of 3.88. The figure shows that the designed topological transition produces largely angularly independent thermal absorptivity up to the blackbody limit (white region in the colour plot) over a narrow spectral bandwidth suited to use with low bandgap photovoltaic cells [159–161,167]. According to Kirchhoffs law and since the transmission through the metamaterial stack is negligible, the expected emissivity is considered identical to the calculated absorptivity. Because of the low coupling of modes between vacuum and hyperbolic regime of the metamaterial thermal radiation in the mid infrared is strongly suppressed. Note that our approach is fundamentally different from structural resonances in metasurfaces and bandgap effects in photonic crystals.

This suppression of thermal emission at low energies beyond the ENZ frequency is critical to TPV-efficiency enhancement since these are sub bandgap photons not absorbed by the cell. We emphasize that the tungsten/hafnium oxide layers are deeply subwavelength and the super-lattice functions in the effective medium limit for temperatures of 1000 °C since the relevant blackbody spectrum is in the near infrared range.

3.2.2 Experimental verification

We first experimentally characterize the absorption spectrum of the ENZ metamaterial at room temperature for unpolarized light with incident angles between 0 and 45 (Fig. 3.5). The figure shows that the structure possesses both near unity angularly independent absorptivity at wavelengths around 800 nm up to the limit of the blackbody emission (Fig. 3.2) along with a strong suppression of absorptivity

throughout the mid infrared. Comparing with Figs. 3.2 (A), (B) and 3.3, these observed characteristics are in complete agreement with the topological transition of the metamaterial design and the effective medium interpretation of the emitter structure. It should be noted that these characteristics are obtained by a route fundamentally different from tungsten photonic crystals [143] which employ resonances to provide selective thermal emission. An important question is whether

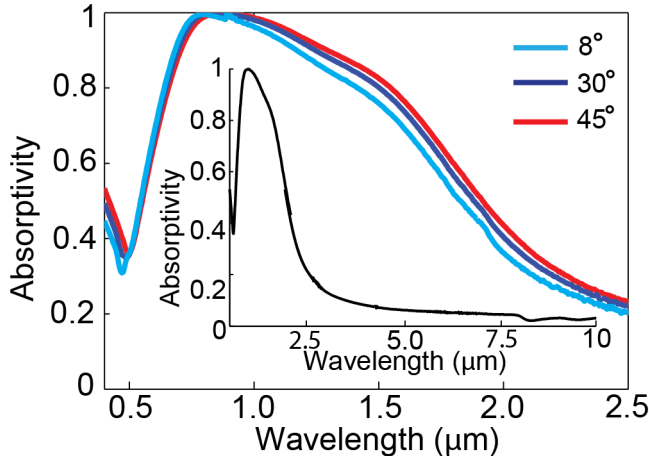


Figure 3.5: **Measured absorptivity versus incidence angle.**

The absorptivity spectrum is obtained as $A(\lambda) = 1 - R(\lambda) - T(\lambda)$, where $A(\lambda)$ is the spectral absorptivity, $R(\lambda)$ the reflectivity of the metamaterial, and $T(\lambda)$ is the transmissivity, which is negligible for the metamaterial with four periods. The measured absorptivity is in complete agreement with the theoretically predicted absorptivity presented in Fig. 3.4. Only reflectivity measurements are needed as we use a 100 nm thick tungsten substrate underneath the metamaterial which is intransparent over the measured wavelength range. The inset shows measured absorptivity of the tungsten/hafnium dioxide metamaterial at a 13° angle of incidence from 0.5 to 10 μm . The observed long-wavelength absorptivity characteristics are in complete agreement with the effective medium calculation.

the topological transition in the refractory metamaterial is thermally stable after being subject to high temperatures. For this, we performed a series of increasingly harsh high temperature annealing steps, each lasting multiple hours. Figure 3.6 (A) compares the absorptivity spectra of the refractory metamaterial at room temperature before and after heat cycling to temperatures between 800 and 1100 °C in vacuum. As shown, the optical characteristics of the metamaterial were practically unaffected by the high temperature treatments, up to 3 h at 1000 °C, demonstrating the heat cycle stability of the designed topological transition. We pushed the annealing temperatures beyond 1000 °C to explore the fundamental causes of degradation of optical properties at high temperatures. Significant deviations in the absorption spectrum were observed after annealing the emitter at 1100 °C for a period of 3 h. To understand the irreversible degradation mechanism of the multilayer

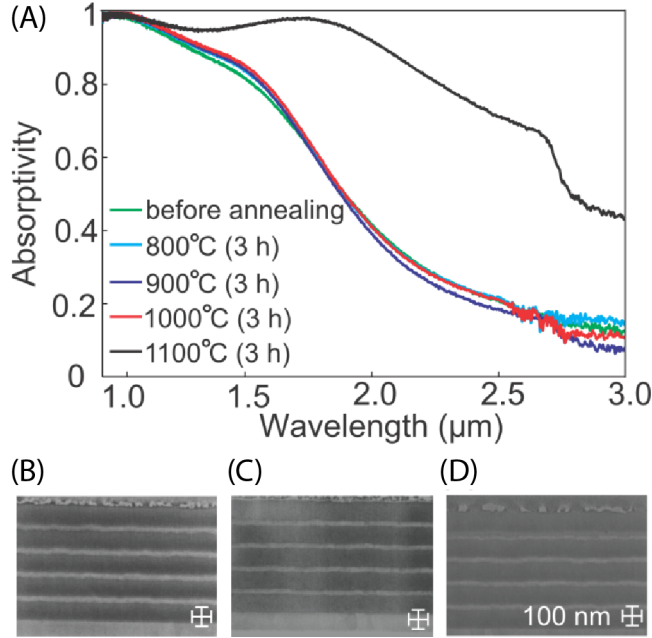


Figure 3.6: **Thermal stability of refractory metamaterial.**

(A) Measured absorptivity of the tungsten/hafnium dioxide metamaterial after annealing for periods of three hours each. Temperatures are displayed in the legend. (B –D) Cross-sectional SEM images of the metamaterial before annealing, after annealing at 1000 °C for 3 h, and after annealing at 1100 °C for 3 h respectively. Although the infrared absorptivity of the metamaterial is greatly altered after the 1100 °C annealing step, no structural degradation is observed.

structure, SEM images of the sample were recorded before annealing (Fig. 3.6 (B)), after annealing at 1000 °C (Fig. 3.6 (C)) and after annealing at 1100 °C (Fig. 3.6 (D)). These images show no structural degradation; however, chemical alterations, as shown below, indicating that higher temperature stability can be achieved with other material choices.

As no structural alterations were observed, we conclude that the primary mechanism of degradation in the multilayer structure at 1100 °C and under vacuum conditions was the diffusion of oxygen from the hafnium dioxide nanolayers and following oxidation of the tungsten nanolayers. This claim is firmly supported by EDS measurements. Figure 3.7 (B) demonstrates a clear increase in the oxygen concentration in the tungsten nanolayers after heat cycling, while Fig. 3.7 (A) shows that the tungsten layers are indeed stable. Interestingly, in addition to the noted interlayer diffusion, an overall gradient of oxygen from the vacuum side of the emitter to the tungsten backing is also visible. The presence of this gradient, despite the protective hafnium dioxide capping layer and the use of rough vacuum pressures ($2 \cdot 10^{-2}$ mbar) during the annealing suggests that higher control of vacuum pressures

(10^{-4} mbar) or an inert atmosphere are required for long-term thermal stability at temperatures above ≈ 1000 °C. Finally, we directly observed the absorption and

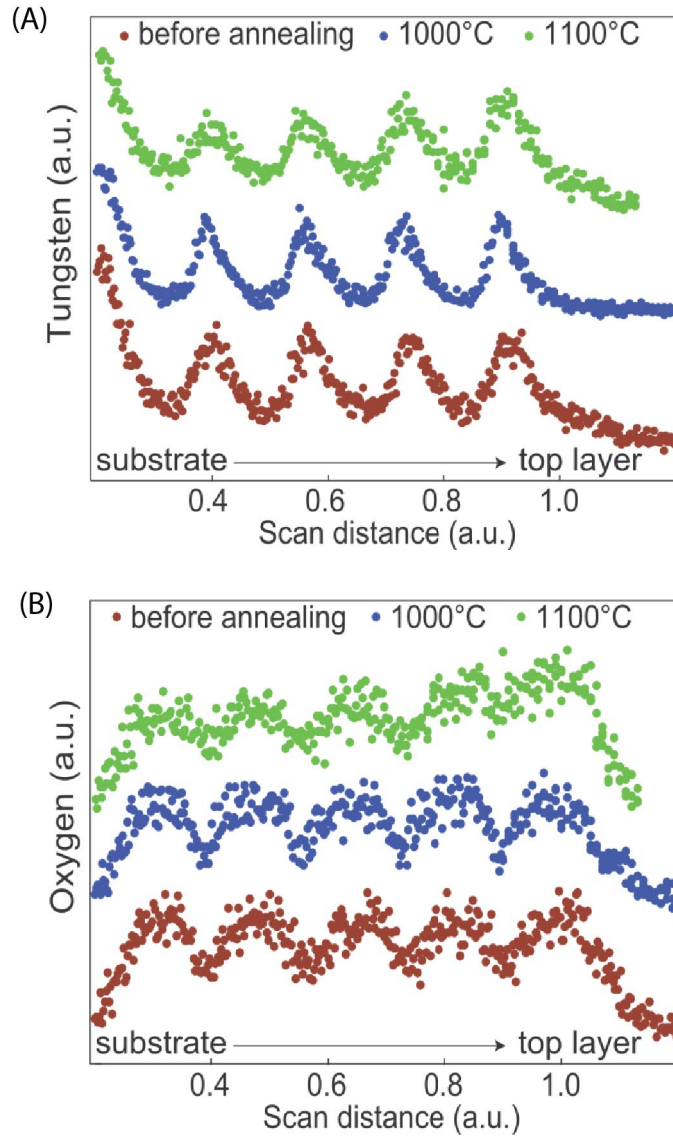


Figure 3.7: **Elemental analysis of thermal stability.**

EDS linescans of (A) tungsten ($W-L$ lines) and (B) oxygen ($O-K$ lines) along cross-sections, running from substrate to top layer, of the refractory tungsten–hafnium dioxide metamaterial before annealing (brown), after heat cycling to 1000 °C (blue), and after heat cycling to 1100 °C (green). The curves are artificially offset along the y axis for clarity. The oxygen figure shows a clear interlayer diffusion as the dips corresponding to tungsten layers are much weaker for the green data set. In contrast, the tungsten figure shows no significant alterations, signaling that the overall multilayer structure is stable beyond 1100 °C.

thermal emission spectrum at high temperatures to verify the spectrally selective excitation of metamaterial modes and presence of the OTT. Kirchhoffs laws dic-

tate that the two spectra have a direct correspondence under critical assumptions of equilibrium. However, temperature dependence of metamaterial parameters is an important issue beyond room temperature. Figure 3.8 shows the absorptivity spectrum for the tungsten/hafnium dioxide metamaterial at temperatures of 23, 300, 500 and 600 °C as well as a direct measurement of the structures emissivity at 1000 °C, see section 3.4 *Experimental Methods*. The observed spectra confirm the existence of the high-temperature topological transition and show the spectral location of the transition to be thermally robust. The only clear variation in the absorptivity/emissivity measurements as the temperature is increased is a reduction of infrared radiation suppression. This slight increase in measured infrared emission is consistent with the increase of electron collision frequency leading to higher optical losses observed in metals and semiconductors at high temperatures [168–171]. It is important to note that despite this increase in infrared emissivity the overall roll-off remains evident, indicating that the engineered topological transition of the refractory metamaterial persists until oxidation.

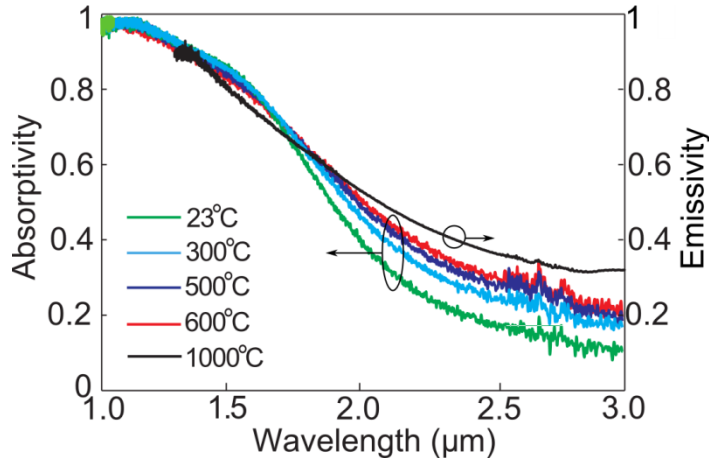


Figure 3.8: **Absorptivity and emissivity at high temperature.**

Experimental observation of the OTT at high temperatures through normal incidence absorptivity measurements for the tungsten/hafnium dioxide metamaterial emitter at temperatures of 23, 300, 500 and 600 °C. The black line represents the experimental emissivity spectrum at normal incidence of the metamaterial emitter at a temperature of 1000 °C. The expected slight increase of the electron collision frequency at high temperatures leads to slightly increasing absorptivities and emissivities in metals. The emission peak and the long-wavelength suppression show only a small variation from room temperature up to 1000 °C, confirming that the topological transition of the metamaterial emitter is thermally robust, and highlighting the potential of the emitter for TPV applications.

3.3 Discussion

Single pn-junction photovoltaic conversion possesses two primary limitations which restrict the efficiency of solar radiation conversion to the Shockley-Queisser limit [107]. First, free carriers excited by radiation with energy greater than the bandgap thermalize before they can be extracted, creating waste heat. Second, radiation with energy lower than the bandgap is either absorbed as waste heat, or unused, and lost to the casing of the photovoltaic cell, thus deteriorating the overall TPV-efficiency. The motivation of high-efficiency TPV extends from the observation that both of these dominant loss mechanisms are consequences of the spectral width of solar radiation. Specifically, neither restriction occurs at energies slightly greater than the bandgap. To take advantage of high conversion efficiencies in TPV one needs to control the radiative characteristics of the source. The usual solar spectrum is replaced by thermal emission from an engineered selective emitter, suppressing the emission of long-wavelength photons, Fig. 3.2 (A). The emission of photons with energies much larger than the bandgap can be avoided by a proper choice of bandgap energy and emitter temperature as the Bose-Einstein occupational factor quickly decays for increasing photon energies.

This concept of TPV employing selective emitters also allows for an expanded range of applications. As the way in which the emitter is heated plays no role in its operation, electrical power can be extracted from any heat source of sufficient temperature. We have calculated the efficiency of a potential TPV system with the presented metamaterial emitter vs. a blackbody emitter. It is assumed that all emitted photons with energies above the bandgap of the PV cell are absorbed and provide electric energy equal to the bandgap energy. The ratio of the generated electric power to the emitted power is the efficiency (called ultimate efficiency [107]). For an InGaAsSb cell [158] with a bandgap of 0.55 eV the efficiency at $1000\text{ }^\circ\text{C}$ increases from 19 % for a blackbody emitter to 34 % for our band-edge metamaterial emitter. Calculations also indicate that the efficiency will further increase above 34 % if the emitter temperature can be increased, making clear the need for refractory metamaterials.

3.4 Experimental Methods

Metamaterial fabrication

All refractory metamaterial samples were fabricated by magnetron sputtering of the constituent materials onto planar polished silicon substrates under ultrahigh-vacuum conditions. Tungsten layers (20 nm thickness) were deposited by direct current at rate of 0.08 nm s^{-1} , while hafnium dioxide layers (100 nm thickness) were deposited

by radio frequency sputtering at a rate of 0.21 nm s^{-1} .

Effective medium parameters and ellipsometry measurements

The extracted effective media permittivities values shown were then determined by fitting polarized multi-angle reflection data from a VASE (J.A. Woollam) ellipsometer system. Using WVASE (J.A. Woollam) analysis software, permittivity values for individual layers of tungsten and hafnium dioxide, separate samples, were determined. Using the three layer model (tungsten layer, metamaterial layer and hafnium dioxide capping layer), this data was then assumed for the tungsten substrate and hafnium dioxide capping layer, and the effective medium parameters of metamaterial were obtained from multi-angle reflection data of the complete structure. The extraction technique used for determining optical parameters from the reflection data of the complete emitter is described by Liberman et al. [172].

Reflection measurements

The specular reflection of the metamaterial between 0.3 and $2.5 \mu\text{m}$ was measured using a UV/VIS spectrometer (Lambda 1050, Perkin Elmer). For wavelength between 2 and $10 \mu\text{m}$ a Fourier transform infrared (FTIR) spectrometer (Vertex 70, Bruker) was used to compare the reflection of the sample against a gold mirror reference.

Annealing of metamaterial samples

In all annealing steps the metamaterial samples were kept under rough vacuum ($\approx 2 \times 10^{-2} \text{ mbar}$) in a high temperature heating stage (TS1500, Linkam) and heated at a rate of $10 \text{ }^\circ\text{C min}^{-1}$. Samples were maintained at the peak annealing temperature for 3 h before cooling back to room temperature.

Characterization of absorption from 300 to 600 $^\circ\text{C}$

The absorptivity spectra of the tungsten/hafnium dioxide metamaterial for temperatures from 300 to $600 \text{ }^\circ\text{C}$ were obtained by collecting reflection measurements using a FTIR microscope (Bruker Hyperion 2000) with 15 times Schwarzschild objective coupled to an FTIR spectrometer (Bruker Vertex 70). The objective operates $\approx 16.7^\circ$ off-normal to the surface of the sample and has a collection cone apex angle of $\pm 7^\circ$. A gold mirror at room temperature was used as reference.

Specimen preparation, SEM-imaging and EDS-measurements

The imaging and EDS measurements of the metamaterials were performed on cross-sections prepared by focused ion beam. To enhance the spatial resolution of the EDS-measurements, the accelerating voltage of the SEM was lowered to 5 kV . This

energy is sufficient to excite the low energy lines of the present elements ($O - K$ 0.523 keV, $Hf - M$ 1.644 keV, $W - M$ 1.774 keV).

Characterization of thermal emission at 1000 °C

Thermal emissivity of the metamaterial at 1000 °C was obtained using a high temperature heating stage (TS1500, Linkam) installed at the focus of the FTIR microscope (Bruker, Hyperion 1000) described previously, Fig. 3.9. To calculate the emissivity, it was necessary to divide the thermal emission spectrum by the black-body spectrum at the same temperature. This step also simultaneously eliminated any artifacts introduced by the setup from the emissivity measurement. As a reference, we replaced the sample with a glassy carbon SIGRADUR G substrate. At elevated temperatures, the glassy carbon is expected to have a wavelength independent emissivity varying between 0.87 and 0.9 in the infrared range.

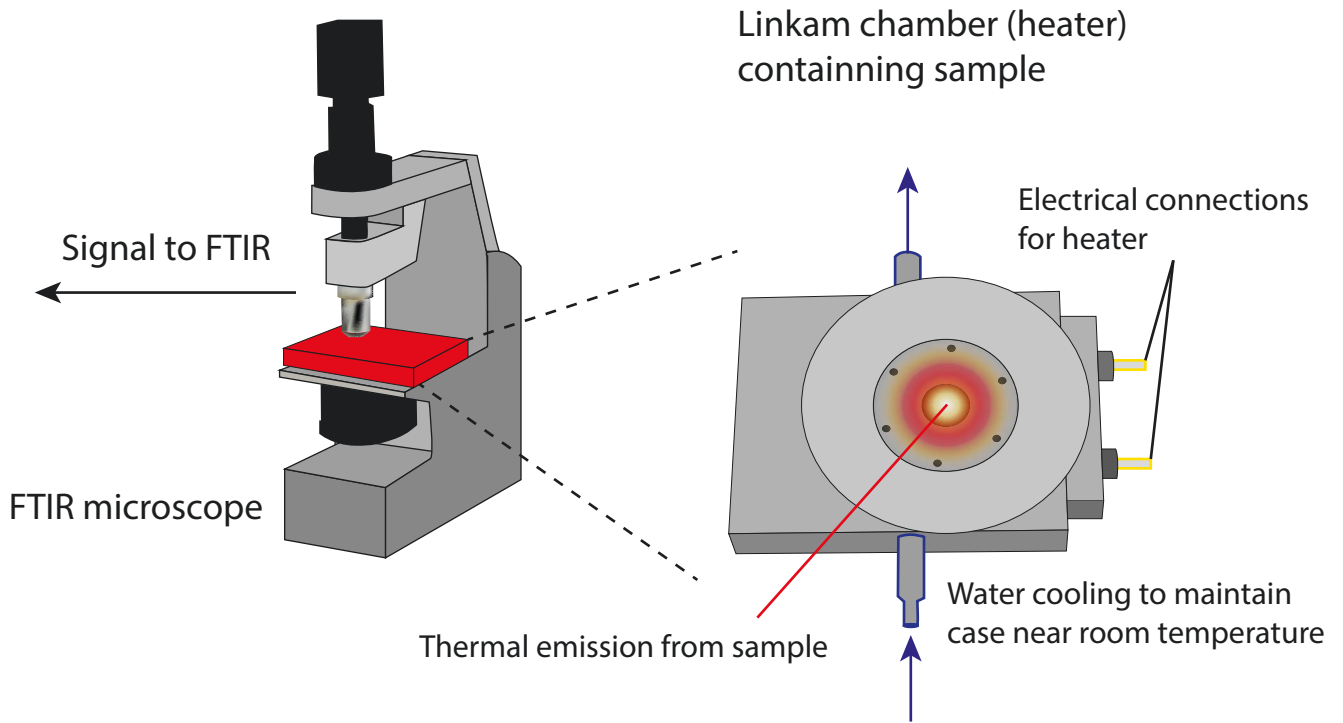


Figure 3.9: **Schematic of experimental setup for measuring metamaterial thermal emission.**

The figure depicts the experimental setup used to measure the thermal emissivity of the metamaterial emitter. First, the emitter is mounted into a Linkam TS1500 vacuum heater stage. The stage acts both to control the temperature of the emitter, and limits interaction with atmospheric gases and particles. The stage is then installed at the focus of a Bruker Hyperion 1000 FTIR microscope, as described in the main text, which passes the thermal emission of the metamaterial emitter into an FTIR for analysis.

3.5 Summary

In summary, we have provided the experimental evidence of OTTs in the thermal radiation spectrum of an ENZ metamaterial. The wavelength dispersion of material parameters changes the intrinsic thermal energy density and thermal radiation spectrum that we ascertained through high temperature thermal emission and optical absorption measurements. This spectrum can be of critical use in TPV where the thermal suppression of sub bandgap photons and enabling of thermal emission above the bandgap boosts the efficiency of energy conversion. Our demonstration of a refractory metamaterial and OTT is in the critical near infrared range opening the possibility of tuning it to the absorption of a low bandgap TPV cell. We demonstrated high temperature stability in the optical/thermal performance till 1000 °C. Our studies on high temperature annealing followed by EDS and spectral analysis can pave the way for a systematic approach to analyzing high temperature stability of optical metamaterials. These findings establish a clear path for exploring the unique photonic thermal conductivity and thermal energy density resulting from ENZ effects and hyperboloidal isofrequency surfaces at high temperature.

Chapter 4

Ideal Near-field Thermophotovoltaic Cells

In this chapter, we outline how permittivity influences near-field radiative heat transfer, and examine how this idea can be used in near-field thermophotovoltaic systems.

One of the most remarkable aspects of near-field radiative heat transfer is the extent to which coupled light-matter resonances can be used to modify both its magnitude and spectral content. For instance, considering coupled surface plasmon polaritons between silver plates, the resulting heat transfer can easily be hundreds of times greater than the blackbody limit and near monochromatic. These characteristics are exactly what is required to improve energy extraction using photovoltaics; and since the early works of DiMatteo et al. [32] on enhanced photogeneration in the near-field, and Chen and Narayanaswamy [34] on the use of surface modes for thermophotovoltaics, the pursuit of new device designs incorporating these advantages of operating in the near-field with a thermophotovoltaic system has stood as a central motivation for studying electromagnetic field correlations.

Over the past decade, considerations based on the use on novel materials [173–175] and coupled modes [176–178] have substantially advanced our understanding of the capabilities that can be ultimately be expected from such devices, and the factors that influence performance. However despite the variety of work that has been done on this idea, prior to the results reproduced in this chapter, one element has remained constant in every design proposal: the actual photovoltaic cell will be a bulk semiconductor. Further, the role that this assumption plays in determining the behavior of near-field radiative heat transfer for energy harvesting applications has remained unexamined.

Here, we bring these issues to light by asking the question: What are the ideal characteristics of a near-field thermophotovoltaic cell? Our search leads us to a reformulation of near-field photonic heat transfer in terms of permittivity $\epsilon(\omega)$ and its underlying joint density of electronic states. This form reveals that the presence of quantum confined van Hove singularities in the thermophotovoltaic cell boosts both the magnitude and spectral selectivity of photonic heat transfer, dramatically improving energy conversion efficiency. Additionally, we also provide the design of such a model near-field thermophotovoltaic system by employing the one-dimensional van Hove singularity present in carbon nanotubes. Detailed balance analysis shows that the predicted spectrally selective heat transfer characteristics of this model implementation are fundamentally better than existing thermophotovoltaic designs.

4.1 Introduction

The thermophotovoltaic (TPV) method generalizes the concept of conventional photovoltaics by replacing the solar spectrum with the thermal emission of an engineered selective emitter [108]. When heated, the emitter is designed to deliver photonic power in a narrow spectral window which can be efficiently converted into electrical power by a matched photovoltaic cell, assumed to be near room temperature. In this way, electrical power can be extracted from any heat reservoir [179, 180]. In principle, the TPV approach avoids the two primary loss mechanisms of single-junction solar photovoltaics: the generation of sub-bandgap photons, and the thermalization of excitons with energy much greater than that of the bandgap [107]. For this reason, the theoretical power conversion limitations of TPVs are near that of an ideal heat engine [106, 181].

However, in practice, implementation of the TPV idea is difficult. The spectral irradiance of any emitter in the far-field is bounded by that of a blackbody with equal temperature [120], see Fig. 4.1. For an emitter with temperature below approximately 1000 K , the fraction of emitted power in the range of contemporary low bandgap photovoltaics (0.4 – 0.75 eV) is negligible [182], making practical photovoltaic conversion problematic. To overcome this limitation, the emitter of the current TPV systems must operate at a temperature between roughly 1200 and 1500 K , creating severe design requirements. Specifically, the emitter must be thermally robust in this temperature range, suppress emission below the bandgap of the photovoltaic cell, which constitutes the majority of the solar spectrum, and have emissivity near the blackbody limit above the bandgap [100, 118]. Even without considering temperature induced degradation of optical properties and structure, current theoretical proposals still require emitter temperatures surpassing 1500 K

to reach 40% conversion efficiency under the Shockley-Queisser analysis [43,142,163].

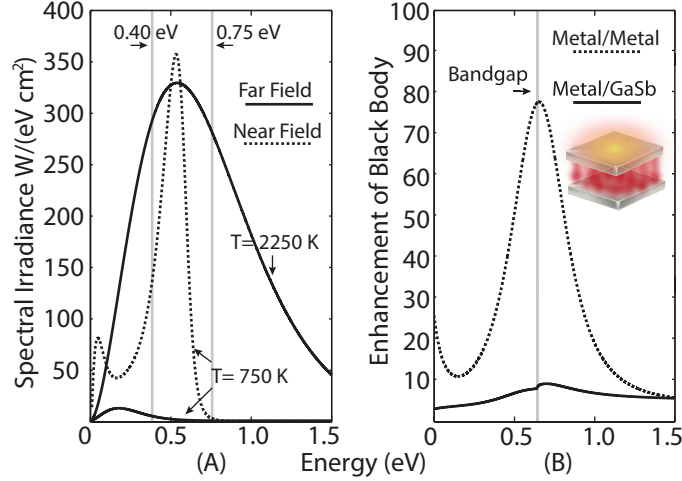


Figure 4.1: **Comparison of photonic heat transfer between the near-field and far-field.**

(A) The small solid far-field blackbody curve and dashed near-field curve are calculated assuming an emitter temperature of 750 K . The larger solid far-field blackbody curve is calculated assuming an emitter temperature of 2250 K . The near-field system consists of two half-spaces of hypothetical Drude metal, one at 750 K , the other at 0 K , with 0.08 eV loss parameter, 0.58 eV plasma frequency, and additional static loss of $1\ i$, separated by a 16 nm gap, shown schematically as an inset in panel (B). The vertical gray lines mark the approximate range of current single-junction low bandgap photovoltaics. The enhancement of photonic heat transfer through evanescent modes relaxes the necessity of maintaining the emitter at extremely high temperature. (B) Comparison of the enhancement of photonic heat transfer beyond the blackbody limit for half-spaces separated by a 16 nm gap, shown schematically as an inset. The enhancement is temperature independent. The dashed curve is found by assuming identical hypothetical Drude metals with 0.21 eV loss parameter, 0.83 eV plasma frequency, a background permittivity of 6 , and an additional static loss of $2.5\ i$. The solid curve results when one of the metal half-spaces is replaced by a gallium antimonide photovoltaic cell. The inclusion of the bulk photovoltaic cell greatly reduces the enhancement effects provided by operating in the near-field

An intriguing prospect to partially alleviate the high emitter temperature requirement is to bring the matched emitter and absorber into the near-field; where the presence of overlapping evanescent fields allows heat transfer to surpass the far-field blackbody limit (near-field thermophotovoltaics, NFTPV [32,34,173]). Making use of matched near-field resonances [69,183], for example surface plasmon polaritons [184] as in Fig. 4.1, photonic heat transfer can be made spectrally sharp and significantly greater than the far-field limit (Super-Planckian emission [66]).

Nevertheless, fundamental design issues persist even in theoretical consideration.

Analysis of near-field photonic heat transfer has conventionally focused on the maximization of total transferred power, leading naturally to designs using coupled modes of symmetric structures. However, to directly extract usable electrical power, one half of the near-field resonant structure must function as a photovoltaic cell. And when realistic bulk semiconductors are included as low temperature absorbers, photonic heat transfer is greatly reduced and spectrally broadened [185,186]. For example, considering a 16 *nm* gap, and hypothetical Drude metals with surface plasmon polariton resonances matched to the bandgap of gallium antimonide photovoltaic cell [187], replacing the symmetric metal absorber with the photovoltaic cell reduces photonic heat transfer by a factor of nearly 10, Fig. 4.1. Furthermore, although the temperature difference between the emitter and the photovoltaic cell can be comparatively reduced, bringing the photovoltaic cell into the near-field increases its operating temperature and thus reduces its conversion efficiency [188]. Resultantly, much of the performance gain offered by moving to the near field is lost.

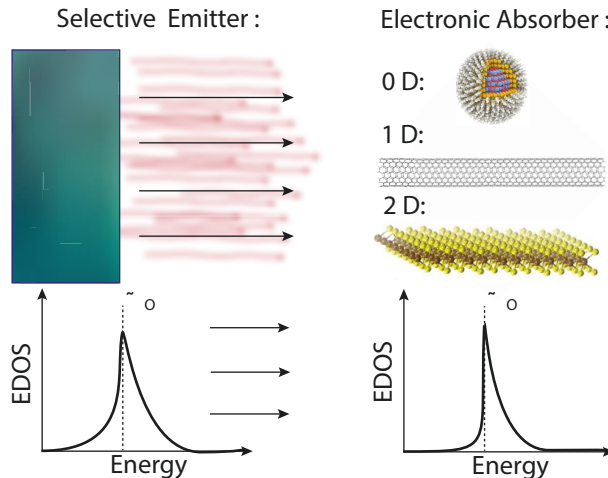


Figure 4.2: **Electronic density and energy harvesting.**

The figure shows a schematic illustration of the central result of this article. Here, EDOS stands for the joint density of electronic states. We will show that by matching peaks in the joint density of electronic states of the emitter to peaks in the joint density of electronic states of the photovoltaic cell the spectral selectivity of near-field radiative heat transfer and efficiency of near-field thermophotovoltaics can be greatly improved.

In this chapter, we take an alternative approach to this problem, focusing on the photovoltaic cell instead of the emitter. Crucially, we show that the narrowband optical absorption spectrum resulting from quantum confinement in low dimensional semiconductors can be used to induce enhanced, spectrally selective near-field heat transfer. We also uncover the fundamental cause of the poor performance of traditional bulk semiconductor photovoltaic cells in the near-field. We begin by recasting

near-field photonic heat transfer in terms of the joint density of electronic states. Combining this result with arguments from Shockley-Queisser analysis and fundamental Kramer-Kronig constraints on optical response, we then show that the photovoltaic impediment to efficient NFTVP devices can be eliminated using electronic van Hove singularities in structures with quantum confined dimensions. Finally, we provide an experimentally realizable near-field thermophotovoltaic system based on carbon nanotubes, and calculate its enhanced performance metrics. The predictions of our analysis can be verified by near-field thermal emission spectroscopy, and pave the way for the use quantum dots, carbon nanotubes, and two dimensional materials as near-field thermophotovoltaic cells.

4.2 Energy considerations for maximal photonic heat transfer

From the pioneering works of Rytov [94], and Polder and van Hove [13], the spectral irradiance between two planar half spaces separated by a vacuum gap is given by

$$\langle Q(T_1, T_2, \omega_o) \rangle = \frac{\omega_o^2 |\Theta(T_1, \omega_o) - \Theta(T_2, \omega_o)|}{4\pi^2 c^2} \sum_{j=s,p} \int_0^1 dk_\rho \frac{(1 - |r_1^j|^2)(1 - |r_2^j|^2)}{|1 - r_1^j r_2^j e^{-2i k_\perp^v d}|^2} k_\rho + 4 \int_1^\infty dk_\rho \frac{Im[r_1^j] Im[r_2^j] e^{-2Im[k_\perp^v d]}}{|1 - r_1^j r_2^j e^{-2i k_\perp^v d}|^2} k_\rho. \quad (4.1)$$

Where c is the speed of light in vacuum, $\Theta(T_i, \omega_o)$ the mean energy expectation value of the canonical harmonic oscillator at temperature T_i and angular frequency ω_o , d the vacuum gap separation normalized by the magnitude of the free space wave vector at ω_o , T_i the temperature of the i th half space, k_ρ the parallel component of the wave vector, again normalized by the magnitude of the free space wave vector at ω_o , r_i^j the j -polarized reflection coefficient of the i th half space, k_\perp^v the normalized perpendicular component of the wave vector in the vacuum gap, and $Im\{\dots\}$ the imaginary part of the enclosed function.

Intuitively, radiative heat transfer between planar half spaces is maximized when the structures are symmetric, and the vacuum gap is made vanishingly small, $d \rightarrow 0$. In this limit the integrand of the spectral irradiance, $H(T_1, T_2, \omega_o, k_\rho)$ from (4.1), is dominated by the high momentum p-polarized evanescent contribution, $k_\rho \gg 1$,

and is well approximated by the bound form

$$H(T_1, T_2, \omega_o, k_\rho) = \frac{\omega_o^2 |\Theta(T_1, \omega_o) - \Theta(T_2, \omega_o)|}{4\pi^2 c^2 \left(1 + (\epsilon'(\omega_o) / \epsilon''(\omega_o))^2\right)} k_\rho; \quad (4.2)$$

with $\epsilon(\omega_o)$ denoting the relative permittivity of both media, and the ' and '' superscripts marking the real and imaginary parts of the function. To achieve the greatest possible radiative heat transfer between identical media at given wave vector and frequency, the so called upper bound of radiative heat transfer per channel [12], the ratio

$$\gamma(\omega_o) = \frac{\epsilon'(\omega_o)}{\epsilon''(\omega_o)}, \quad (4.3)$$

must be made as small as possible. (This condition is antithetical to the plasmonic field enhancement figure of merit where $\gamma(\omega_o)$ is maximized.)

Applying the Kramers-Kronig relation [189] to the real part of the permittivity, the $\gamma(\omega_o)$ factor can be expressed entirely in terms of $\epsilon''(\omega_o)$ as

$$\gamma(\omega_o) = \frac{1}{\epsilon''(\omega_o)} + \frac{2}{\pi \epsilon''(\omega_o)} \mathcal{P} \int_0^\infty d\omega \frac{\omega \epsilon''(\omega)}{\omega^2 - \omega_o^2}. \quad (4.4)$$

For energy harvesting with semiconductor photovoltaic cells, Shockley-Queisser efficiency analysis can be used to provide constraints to the material parameters which minimize $\gamma(\omega_o)$:

(1) No radiative heat transfer should occur below the bandgap frequency ω_g because it cannot be converted into useful electrical power. Mathematically this criterion is stated as $\gamma(\omega_o) \rightarrow \infty$ for all $\omega_o < \omega_g$, equivalent to $\epsilon''(\omega_o) \rightarrow 0$ for all $\omega_o < \omega_g$. The dispersive part of $\gamma(\omega_g)$ then provides an explicitly positive contribution, and its minimization requires $\epsilon''(\omega_o) \rightarrow 0$ for all $\omega_o \neq \omega_g$. This restriction on the global absorption characteristics of the media, $\epsilon''(\omega_o)$, can be immediately translated into two statements concerning its polarization, $\epsilon'(\omega_o)$. First, $\epsilon'(\omega_g) > 0$. Second, the polarization of the media acts as a store for photonic power. From this store the initially transferred power may either be converted into the internal degrees of freedom of the absorber or return to the emitter, limiting the total transferred power. The larger the polarization of the medium is the smaller radiative heat transfer will be.

(2) radiative heat transfer should be made as great as possible at the bandgap frequency, $\epsilon''(\omega_g) \rightarrow \infty$. This second requirement for achieving $\gamma(\omega_g) \rightarrow 0$ is pro-

vided by the fluctuation dissipation theorem. To maximize radiative heat transfer at ω_g , we require $\epsilon''(\omega_g) \rightarrow \infty$ to generate the largest possible thermal currents, the first term of Eq.(4.4). The balance of these two conditions leads unequivocally to the conclusion that to minimize $\gamma(\omega_g)$, under the above Shockley-Queisser constraints, $\epsilon''(\omega_o)$ must be sharply resonant about ω_g . Strictly, simultaneous minimization of $\gamma(\omega_g)$ and complete suppression of heat transfer for all sub-bandgap frequencies is only possible if $\epsilon''(\omega_o)$ is mathematically equivalent to the Dirac delta distribution, $\epsilon''(\omega_o) \rightarrow \delta(\omega_g)$.

The implications of this result to near-field energy harvesting become immediate by recalling the intimate connection between optical dissipation, and the joint density of electronic states, $\rho_\epsilon(\omega)$:

$$\epsilon''(\omega_o) = \frac{e^2}{\pi m_e^2 \omega_o^2} \int dS^d \frac{|\mathbf{a}_o \cdot \mathbf{p}_{ji}|^2}{|\nabla_{\mathbf{k}} \mathcal{E}_{ji}(\mathbf{k})|}, \quad (4.5)$$

$$\rho_\epsilon(\omega) \propto \int \frac{dS^d}{|\nabla_{\mathbf{k}} \mathcal{E}_{ji}(\mathbf{k})|}. \quad (4.6)$$

In these expressions, \mathbf{a}_o denotes the polarization vector of the electromagnetic excitation, \mathbf{p}_{ji} the matrix element of the momentum operator, ω_o the angular frequency, $\mathcal{E}_{ji}(\mathbf{k})$ the constant energy surface between filled and excited states such that $\mathcal{E}_{ji}(\mathbf{k}) = \hbar\omega_o$, dS^d the infinitesimal constant energy surface element in d dimensions, and e and m_e the mass and charge of an electron. It is important to note that suppression/enhancement of electronic states at a given frequency is the key to decreasing/increasing optical absorption. However, the Kramers-Kronig relation introduces dependence on the global frequency characteristics through the polarization of the medium. Both these factors have to be taken into account in order to minimize the factor governing spectrally selective near-field heat transfer, $\gamma(\omega_o)$.

As previously mentioned, the principal method for overcoming the Shockley-Queisser limit in TPV devices is to spectrally tailor the photonic output of the emitter to frequencies just above the bandgap of the photovoltaic cell. But, in the near-field this frequency range also corresponds to the poorest absorption characteristics for a typical bulk semiconductor. Applying (4.5) and (4.6) to model free particle semiconductor we recover the well known energy scaling behavior $\epsilon''(\omega_o) \propto \sqrt{\hbar\omega_o - \mathcal{E}_g}$ ($d=3$) $\rho_\epsilon(\omega_o) \propto \sqrt{\hbar\omega_o - \mathcal{E}_g}$ ($d=3$); so that near the bandgap the semiconductor has both low absorption, $\epsilon''(\omega_g)$, and large polarization. (The fact that the polarization is large can be seen by the positive contribution of principal value part in the Kramers-Kronig relationship, $\epsilon'(\omega_0) = 1 + \frac{2}{\pi} \mathcal{P} \int_0^\infty d\omega \frac{\omega \epsilon''(\omega)}{\omega^2 - \omega_0^2}$.) These two factors lead to a large $\gamma(\omega_o)$ factor (detrimental to spectrally selective heat transfer) when ω_o is near

ω_g , Fig. 4.1. In short, the usual properties of a three dimensional semiconductor are in complete disagreement with those required for maximal radiative heat transfer as given by (4.2).

In stark contrast, significant suppression of the $\gamma(\omega_o)$ factor can be obtained if the absorption, $\epsilon''(\omega_o)$, of the semiconductor cell is strongly peaked at the operating (band gap) frequency. Such optical behavior is achieved when the joint density of electronic states becomes similar to the ideal Dirac distribution at the bandgap. Suppression of the electronic states below the operating frequency is necessary to decrease transfer of inefficient sub-bandgap photons, as dictated by Shockley-Queisser analysis. The suppression of states above the bandgap is necessary to decrease the polarization of the medium at the bandgap, as required by the Kramers-Kronig relations.

A joint density of electronic states approaching this ideal dirac delta like distribution is observed near the van Hove singularities¹ that occur in the free particle model of a semiconductor for low spatial dimensions. Returning to (4.5) and (4.6), as d is reduced to from 3 to 2, and then 2 to 1, the scaling of both the joint density of electronic states and optical dissipation is found to be $\{\epsilon''(\omega_o) \rho_{\mathcal{E}}(\omega_o)\} \propto C$ ($d=2$) and $\{\epsilon''(\omega_o) \rho_{\mathcal{E}}(\omega_o)\} \propto 1/\sqrt{\hbar\omega_o - \mathcal{E}_g}$ ($d=1$). Physically, this relative increase of the joint density of electronic states can be viewed as the result of two effects. First, imagining a cubical volume, if either one or two of the lengths is reduced the energy of the bandgap is increased, causing states with low wave vectors in the large directions effectively pile up. Second, as the reduction of any of the lengths reduces the volume of each mode, inside the volume the probability density is increased².

The corresponding evolution of $\gamma(\omega_o)$ is shown in Fig. 4.3. The increase in near-field photovoltaic performance depicted in this figure is characteristic of any semiconductor with quantum confined spatial dimensions, such as quantum dots, nanotubes, and two dimensional materials. Based on the above analysis, these systems are well suited for achieving spectrally selective radiative heat transfer and can function as superior near-field thermophotovoltaic cells compared to traditional bulk semiconductors.

¹A van Hove singularity refers to any point in the Brillouin zone at which $\nabla_{\mathbf{k}} \mathcal{E}_{j_i}(\mathbf{k}) = 0$.

²Note that these effects also occur with the transition from $d = 1$ to $d = 0$.

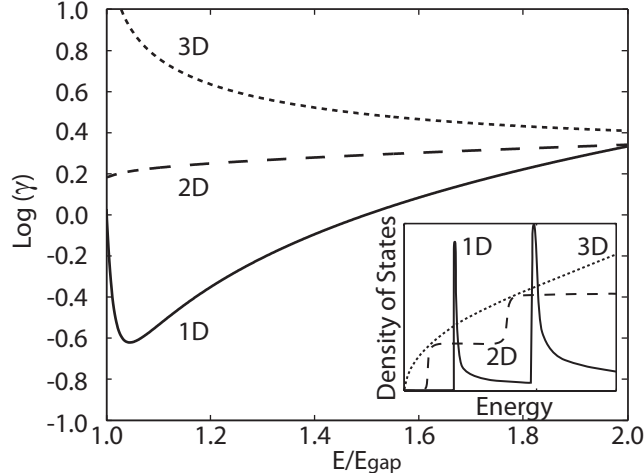


Figure 4.3: **Dimensional scaling of near-field energy transfer.**

Base ten logarithm of the longitudinal $\gamma(\omega_o) := \epsilon''(\omega_o)/\epsilon''(\omega_o)$ factor for one, two, and three dimensional model free particle semiconductors. The inset shows a schematic illustration of the evolution of the joint density of electronic states for zero, one, and two quantum confined spatial dimensions characteristic of a semiconductor based on the work of Kümmel et al [190]. By introducing dimensional constraints the dispersion of the joint density of electronic states can be altered to produce spectrally selective super-Planckian photonic heat transfer near the bandgap of a photovoltaic cell. This result illustrates both the primary drawback of employing traditional bulk semiconductor photovoltaics for near-field photonic energy conversion, and the usefulness of switching to photovoltaics with quantum confined dimensions for this application.

4.3 Model thermophotovoltaic system

In the previous section, it was revealed that the magnitude and selectivity of near-field photonic power transfer for energy conversion applications can be greatly enhanced by employing photovoltaics with spectrally narrow absorption resonances. This type of resonant optical behavior is one of the hallmarks of quantum confinement; making photovoltaic cells utilizing low dimensional materials such as quantum dots, quantum wells, graphene, two dimensional semiconductors, semiconductor nanowires and carbon nanotubes [191–193] excellent candidates for future near-field TPV devices. As a framework of such a device, here we consider an idealized NFTPV system consisting of an emitter absorber pair utilizing carbon nanotubes [194] (CNTs) and calculate the observable radiative heat transfer characteristics of this model.

Our CNT model device is analogous to the one-dimensional free particle semiconductor example shown in Fig. 4.3. The one dimensional confinement of electrons in CNTs leads to strong van Hove singularities [195], spectrally selective absorption, and semiconductor behavior for specific chiral vectors. Nevertheless, nearly

identical performance would occur if the CNTs were exchanged for semiconductor nanowires [196]. We have focused on this CNT design, despite current challenges in fabrication and electron-hole pair collection [197], primarily because the thermal robustness [185,198] and low bandgap features of CNTs seems ideally suited to TPV applications.

Two versions of the CNT system have been created. The first is designed for a 1300 K emitter and 300 K absorber; and the second, for an 800 K emitter and 300 K absorber. In both cases, the absorber is composed of CNTs with chiral vector $(19, 0)$ embedded vertically in a matrix of zirconium dioxide on a tungsten backing. This choice of chiral vector allows the CNTs to operate as semiconductors, with a bandgap of 0.58 eV . This behavior occurs as the Dirac point of the band structure is avoided [199] due to the angular quantization. The exact current voltage characteristics of the CNT photovoltaic cells have not been included, and instead ideal p-n junction behavior has been assumed. This is in accordance with the Shockley-Queisser analysis for ideal performance limitations. (To create fully functioning NFTPV cells the CNT on tungsten absorbers would be attached to external electronics and act as the photovoltaic elements [200–202].)

Both emitters are composed of free standing CNTs with the same chiral vector as the CNTs considered for the absorber, and are set on a zirconium dioxide backing. The absorber and emitter are separated from each other by a 16 nm vacuum gap. In the high temperature case the fill fractions and thickness of the emitter and absorber CNT layers are 65%–8 nm , and 65%–4 nm . For the low temperature case these parameters are altered to 30%–8 nm , and 65%–16 nm in the same order. A schematic of this setup is included as an inset in Fig. 4.5.

The effective perpendicular permittivities of the two considered designs are shown in Fig. 4.4. The absorption spikes, $\epsilon''(\omega_o)$, can be tuned by varying the chiral vector. The first principles calculation of these optical properties is based on the Kubo formalism described by Falkovsky and Varlamov [203], with additional loss included via the relaxation time approximation with an estimate relaxation time of one picosecond [204, 205]. The effective parallel permittivities, which play a secondary role in determining the transferred power, are calculated in identical manner. The main steps of this calculation are outlined in Appendix E. Again, we stress that the above analysis on which these particular designs are based shows that a variety of near-field emitters using other resonances, such as surface plasmon polaritons or phonon polaritons, could be used with any low dimensional semiconductor to obtain very similar results.

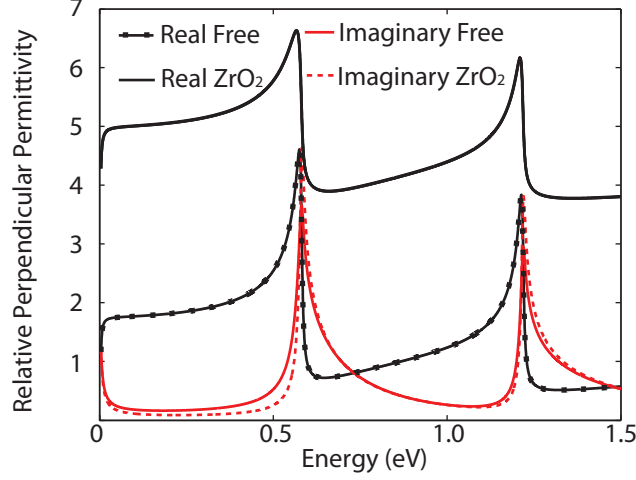


Figure 4.4: **Optical permittivity of a carbon nanotube metamaterial.**

Effective relative permittivity perpendicular to the half spaces for the CNT emitter absorber pair designed to operate at 1300 K, depicted in Fig. 4.3. For vacuum gaps on the order of hundreds of nanometers photonic heat transfer is dominated by evanescent modes with p-polarization. In this case, the overall photonic heat transfer properties are primarily determined by the perpendicular permittivity. As predicted by (4.3), the photonic heat transfer is maximized when the $\gamma(\omega_o)$ factor is minimized for both the emitter and absorber.

In Fig. 4.5, we plot the spectral irradiance for this CNT based emitter-absorber system calculated using Rytov's theory. As can be seen by comparing the perpendicular permittivity, Fig. 4.4, with the spectral irradiance, Fig. 4.5, the spectral position of peak radiative heat transfer corresponds strongly with the van Hove singularities and the minimization of $\gamma(\omega_o)$. In fact, although the analytical theory of (4.3) is valid only in the very near-field, the spectral position of peak photonic transfer varies only 4% as the vacuum gap is increased up to roughly a tenth the wavelength of operation, 200 nm. The spectrally tailored nature of emission and absorption leads to significant enhancement for energy conversion. Using the Shockley-Queisser analysis [107] as an upper-bound performance estimate, the CNT system with the 1300 K emitter (Fig. 4.5) could supply up to 15.00 W/cm² of electrical power with 53.0% power conversion efficiency. Likewise, the 800 K emitter system could supply up to 1.07 W/cm² of electrical power with 15.6% power conversion efficiency. For comparison, an optimized conventional bulk gallium antimonide [187] NFTPV design has also been considered. This system consists of a 18 nm thick Drude metal, with 0.74 eV plasma frequency, 0.21 eV loss parameter, on a tungsten backing with a vacuum gap separation of 16 nm. Under identical Shockley-Queisser analysis at a 1300 K emitter temperature this conventional system could produce 1.62 W/cm² of electrical power with 18.8% power conversion efficiency, whereas

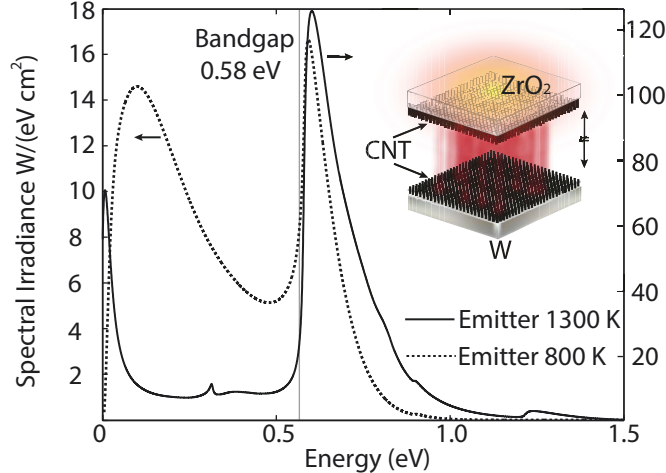


Figure 4.5: **Carbon nanotubes for near-field thermophotovoltaic cells.**

Photonic heat transfer for two metamaterial emitter absorber pairs utilizing semi-conducting CNTs optimized for emitter temperatures of 1300 K and 800 K . In both instances the absorber is assumed to be held at a temperature of 300 K . Parameters for the two systems are given in the main text. A schematic of the system is inset over the plot. The greatly enhanced, spectrally thin, photonic heat transfer peak produced slightly above the energy bandgap of the matched semi-conducting CNT absorber seen here is ideal for near-field photonic energy conversion applications.

with an emitter temperature of 800 K it could create only $0.01 W/cm^2$ of electrical power with 1.6% power conversion efficiency. More concretely, 73.1% of photonic thermal power transferred from the emitter in the CNT NFTPV device lies above the bandgap, $20.7 W/cm^2$, for the 1300 K model system and 25.0%, $1.7 W/cm^2$, in the 800 K model. In comparison, the optimized plasmonic system described above transfers 28.1% of its thermal power above the bandgap of the gallium antimonide photovoltaic cell, $2.4 W/cm^2$, when the emitter is given a temperature of 1300 K and 3.2%, $0.02 W/cm^2$, when the emitter is assumed to have a temperature of 800 K .

Finally, we comment briefly on previous far-field TPV designs which have utilized gallium antimonide [158, 206] as the photovoltaic cell for converting the thermal radiation into electric power [207]. Our analysis shows that the optimum cell design for near-field TPV is fundamentally different and the presence of van Hove Singularities in the material comprising the cell is critical for the spectrally selective nature of the transferred energy. This in turn should lead to fundamental improvements in energy conversion efficiency as shown by the Shockley Queisser analysis. The implementation of near-field TPV designs is more challenging than far-field TPV designs. However, a fundamental promise of near-field TPV, as mentioned before, is enhanced heat transfer for lower operating temperatures. This arises because the black body limit which fundamentally constraints far-field TPV does not apply to

near-field TPV where heat exchange takes place primarily due to evanescent modes.

4.4 Summary

In summary, we have determined that the ideal joint density of electronic states for near-field photonic energy capture (photovoltaic) is mathematically equivalent to the Dirac delta distribution. This result immediately reveals why bulk semiconductors are ill suited to near-field photonic energy capture; and simultaneously shows that switching to photovoltaic cells with van Hove singularities, seen in any semiconductor with a quantum confined dimension, offers a clear path for improving the efficiency of future NFTPV devices. To aid with the design of experimental systems for verifying of these ideas, we have provided model designs utilizing matched metamaterial CNT emitter absorber pairs, and have shown that the Shockley-Queisser limit performance metrics of these designs are well beyond those achievable with current NFTPV device designs based on bulk semiconductor photovoltaics. We emphasize that similar performance improvement is expected for any low dimensional semiconductor functioning in the near-field, and appeal to researchers working in the areas of quantum dot, CNT, nanowire, quantum well, and two dimensional semiconductors to consider the feasibility of adapting their work for thermophotovoltaics.

Chapter 5

Quantum Optical Sum Rules and Field Fluctuations inside Natural Hyperbolic Media

In this chapter, we provide an approach for analytically calculating electromagnetic field fluctuations inside natural hyperbolic media.

In 1987, Yablonovitch and John independently conceived the idea of the photonic crystal as a practical means of rigorously forbidding vacuum fluctuations in a given bandwidth [1,2]; turning one of the most venerated concepts for describing quantum light-matter interactions [3,208] into a core tool for photonic engineering. Connections to this original idea are found in almost every branch of contemporary nanophotonics. By manipulating field fluctuations (the photonic density of states), nearly any aspect of a medium's photonic quantum [209–211], thermal [39,66,96,212–214] and topological properties [138,215,216] can be modified.

Naturally, this has led to considerable interest in various forms of the inverse problem [217–221]: a practical means of indefinitely enhancing field fluctuations inside matter in a defined spectral bandwidth. Remarkably, near ideal complements appear to exist. In particular, hyperbolic (indefinite [222]) media are commonly stated to possess a broadband photonic dispersion singularity, leading to unbounded electromagnetic field fluctuations [223,224].

However, despite the success of this picture for interpreting applications spanning the domains of imaging [225–227], nanophotonics [228–232], quantum [233–237] and thermal interactions [238–242], there is no simple expression defining precisely how large the electromagnetic fluctuations inside a given hyperbolic medium are. And as

such, prior to the results presented in this chapter, it was not possible to rigorously link the experimentally observed features hyperbolic response [243–249] with the wealth of existing theory for macroscopic quantum electrodynamics [250–256].

The prevailing consensus, building off the work of Potemkin et al. [257], is that any quantification of field fluctuations capturing hyperbolic characteristics demands additional quantification of the optical response of the medium beyond what is provided by the permittivity tensor. That is, to produce non divergent results, second order optical effects must be considered. To date, three such approaches have been used: (1) non-local models of the polarization response of the medium [258,259], (2) finite correlation / emitter size approximations [140,257,260,261], and (3) second order fluctuation response [262].

As these normalization techniques do not rely on any specific property of hyperbolic media, a variety of open questions as to the specific nature of the field fluctuation enhancement persist. For instance, in photonic crystals it is well known that the creation of a band gap results from a corresponding enhancement of field fluctuations at the band edge van Hove singularities. The above approaches do not clarify whether a similar mechanism exists inside hyperbolic media, and it is not known if the enhancement in regions of hyperbolic response is accompanied by spectral windows of field fluctuation suppression (i.e. if quantum optical sum rules are valid).

With the discovery of strongly hyperbolic optical response in special van der Waals bonded solids, such as hexagonal boron nitride and bismuth selenide (a topological insulator), the need to understand why this incongruence exists, and if a description of the strength of electromagnetic field fluctuations in terms of secondary effects is truly fundamental, has become increasingly pressing. Here, we address both issues by categorizing the field fluctuations that can exist inside hyperbolic media into three distinct types. Specifically, we show that the central characteristics of hyperbolic response are determined by a coupling of longitudinal and transverse field fluctuations that can not occur in conventional media. This allows for an unambiguous separation of photonic and polaritonic fluctuations and a quantification of the field enhancement set only by material absorption. We apply our results to explore quantum optical sum rules for modified spontaneous emission enhancement, and thermal energy density in hexagonal boron nitride and bismuth selenide. Most notably, we find that while the sum rule is satisfied, it does not constrain the enhancement of quantum and thermal properties inside a hyperbolic medium. We also show that both hexagonal boron nitride and bismuth selenide possess broad spectral regions where polaritonic fluctuations are over 120 times larger (and over 800 times larger

along specific angular directions) than vacuum fluctuations.

5.1 Introduction

For more than a decade, hyperbolic media have been considered to be one of the most intriguing platforms for the future nanophotonic devices [222,263]. The appeal is concisely summarized by the wave condition set by Maxwell's equations in such media. With the inclusion of uniaxial anisotropy, the p-polarized relation between frequency and wave vector for an isotropic medium generalizes to become

$$k = \sqrt{\frac{\epsilon_A(k, \omega) \epsilon_P(k, \omega)}{s(\theta)^2 \epsilon_P(k, \omega) + c(\theta)^2 \epsilon_A(k, \omega)}} \frac{\omega}{c}; \quad (5.1)$$

where the A and P labels denote the optic axis and plane of the uniaxial medium, θ is the polar angle defined from the optic axis, and $s(\dots)$ and $c(\dots)$ are shorthands for the $\sin(\dots)$ and $\cos(\dots)$ functions, Fig. 5.1 For a hyperbolic medium the real parts of the relative permittivity components $\epsilon_A(k, \omega)$ and $\epsilon_P(k, \omega)$ have opposite signs, creating critical angles along which the real part of the dominator vanishes. On the cones in reciprocal space satisfying this requirement, the vector k determined by (5.1) can be both extremely large and nearly real, Fig. 5.1., showing that hyperbolic media support extremely localized excitations. Intuitively, this strong localization allows excitations at a given frequency to effectively interact on much smaller length scale than in any conventional isotropic medium (enhanced light-matter interactions), enabling a host of possible applications [225,228,229,237].

Yet, despite this captivating potential, key properties of these media have remained only superficially understood. Namely, the degree to which light-matter interactions are enhanced by a structure or medium (to linear order) is universally quantified by the strength of its electromagnetic field fluctuations, here referred to as the fluctuation density¹ (5.3). For isotropic media, this measure of interaction strength is known to be simply proportional to the refractive index, $\langle \mathbf{E}(\mathbf{r}, \omega) \otimes \mathbf{E}^*(\mathbf{r}', \omega) \rangle \propto \int d\mathbf{k} \text{Re} \left\{ \sqrt{\epsilon(k, \omega)} \right\}$, relating the wave vector k to the frequency ω in the isotropic wave condition. In contrast, prior to the work presented here, for hyperbolic media the fluctuation density could only be quantified in terms of secondary optical effects, such as the magnitude of spatial non-locality in the permittivity response.

¹If at a given frequency a structure or medium possess large field fluctuations we expect strong light-matter interactions.

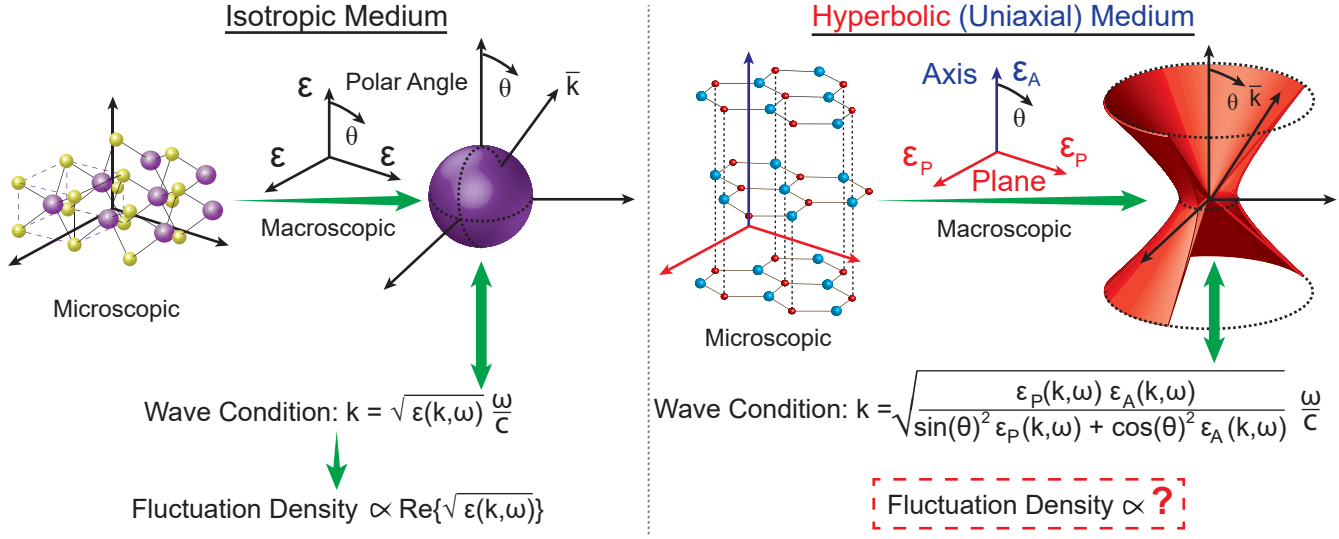


Figure 5.1: Wave conditions and fluctuation density.
 In isotropic media fluctuations in the electromagnetic field are proportionally related to the magnitude of the wave condition $k = \sqrt{\epsilon(k,\omega)} \omega/c$. The p-polarized wave condition for uniaxial media shown above suggests that in the case of hyperbolic (indefinite) polarization response these fluctuations will be strongly enhanced. Presently, all quantifications of this effect are either ill-defined, require the explicit introduction of non-local parameters, or are described by second order corrections. Here, we address this longstanding issue.

In this chapter, we confront these longstanding issues of analytically characterizing field fluctuations inside natural hyperbolic media by revealing the coupling between transverse and longitudinal electromagnetic fields. This previously overlooked connection allows us to provide a concrete description of the link between the polariton excitations that occur in hyperbolic media, and the characteristic near-field optical and thermal properties that they exhibit. It also allows us to produce a regularized characterization of the field fluctuations that occur inside hyperbolic media where material absorption sets the fundamental limit of enhancement. We then apply these results to study the quantum optical sum rule for modified spontaneous emission enhancement in hyperbolic media, and calculate thermal fluctuations in hexagonal boron nitride and bismuth selenide. Most importantly, we conclude that while the quantum optical sum rule is valid, it does not extend to the polariton modes that dominate hyperbolic enhancement. We also show that both hexagonal boron nitride and bismuth selenide have broad spectral regions where fluctuations are over 120 times larger, along specific directions over 800 times larger, than they are in vacuum.

From the fluctuation dissipation theorem [264, 265],

$$\langle \mathbf{E}(\mathbf{r}, \omega) \otimes \mathbf{E}^*(\mathbf{r}', \omega) \rangle = \frac{\omega \Theta(\omega, T)}{\pi} \text{Im} \{ \check{\mathcal{G}}(\mathbf{r} - \mathbf{r}', \omega) \}, \quad (5.2)$$

our objective amounts to regularizing the *fluctuation density* (FD) :

$$\mathcal{F}(\omega) = \lim_{\mathbf{r} \rightarrow \mathbf{r}'} \text{Tr} [\text{Im} \{ \check{\mathcal{G}}(\mathbf{r} - \mathbf{r}', \omega) \}] = \lim_{\mathbf{r} \rightarrow \mathbf{r}'} \int dV_{\mathbf{k}} \text{Tr} \left[\text{Im} \left\{ e^{i\mathbf{k}(\mathbf{r} - \mathbf{r}')} \check{\mathcal{G}}(\mathbf{k}, \omega) \right\} \right], \quad (5.3)$$

for hyperbolic media. Where $\Theta(\omega, T)$ is the energy of a harmonic oscillator at frequency ω and temperature T , $\check{\mathcal{G}}(\mathbf{r}, \mathbf{r}', \omega)$ the dyadic Green function of the medium, $\check{\mathcal{G}}(\mathbf{k}, \omega)$ it's Fourier transform, $\int dV_{\mathbf{k}}$ an integral over reciprocal space and $\text{Im} \{ \dots \}$ the imaginary part. (This quantity is often called the photonic or electromagnetic density of states in nanophotonics (PDoS or DoS). The fluctuation density extends this concept to media supporting polaritonic excitations².)

The chapter is organized into five sections. The first three cover our theoretical work leading to equations (5.28), (5.34), (5.37) and (5.38). The last two sections ex-

²In nanophotonics literature the imaginary part of the Green function(5.3) is usually called the electromagnetic or photonic density of states [266, 267] (DoS/PDoS). However, this definition relies on the fact that emitter is in vacuum. When the emitter is not in vacuum there is an additional factor of the inverse energy density must be considered to achieve the correct scaling, $\propto \sqrt{\epsilon(\mathbf{k}, \omega)}$. (The usual view of the density of states, the differential number of states contained in a shell, yields a proportionality of $\propto \sqrt{\epsilon(\mathbf{k}, \omega)^3}$ [268].) Further, as we will show, the response of the medium contained in the Green function is not strictly electromagnetic.

plore quantum optical sum rules in hyperbolic media and thermal field fluctuations in hexagonal boron nitride and the topological insulator bismuth selenide.

5.2 Polariton excitations in anisotropic media

The defining feature of hyperbolic media is extremely anisotropic polarization response. In this section, we provide the formal relations connecting anisotropy to polariton excitations that are not possible in isotropic media.

We begin by decomposing Maxwell's equations in terms of the direction of the reciprocal space vector \mathbf{k} . Letting

$$\mathbf{w}_L = \left(\hat{\mathbf{k}} \otimes \hat{\mathbf{k}} \right) \mathbf{w}, \quad (5.3a)$$

$$\mathbf{w}_T = \left(\check{I} - \hat{\mathbf{k}} \otimes \hat{\mathbf{k}} \right) \mathbf{w} \quad (5.3b)$$

be the projection of a vector \mathbf{w} along $\hat{\mathbf{k}}$ and onto the plane perpendicular to $\hat{\mathbf{k}}$ respectively, any vector \mathbf{w} can be represented as

$$\mathbf{w} = \mathbf{w}_L + \mathbf{w}_T, \quad (5.3c)$$

where \mathbf{w}_L and \mathbf{w}_T are referred to as the longitudinal and transverse components. From these definitions

$$\mathbf{k} \times \mathbf{w}_L = 0 \quad (5.4a)$$

$$\mathbf{k} \cdot \mathbf{w}_T = 0, \quad (5.4b)$$

so that Maxwell's equations separate to become:

$$\mathbf{k} \cdot \mathbf{E}_L(\mathbf{k}, \omega) = -i\rho(\mathbf{k}, \omega) / \epsilon_0 \quad (5.5a)$$

$$\mathbf{B}_L(\mathbf{k}, \omega) = 0 \quad (5.5b)$$

$$\mathbf{k} \times \mathbf{E}_T(\mathbf{k}, \omega) = \omega \mathbf{B}_T(\mathbf{k}, \omega) \quad (5.5c)$$

$$ic^2 \mathbf{k} \times \mathbf{B}_T(\mathbf{k}, \omega) = -i\omega \mathbf{E}_T(\mathbf{k}, \omega) + \mathbf{j}_T(\mathbf{k}, \omega) / \epsilon_0 \quad (5.5d)$$

$$i\omega \mathbf{E}_L(\mathbf{k}, \omega) = \mathbf{j}_L(\mathbf{k}, \omega) / \epsilon_0.$$

with ϵ_0 and μ_0 denoting the permittivity and permeability of vacuum, $\rho(\mathbf{k}, \omega)$ the charge density, $\mathbf{j}(\mathbf{k}, \omega)$ the current density, $\mathbf{B}(\mathbf{k}, \omega)$ the magnetic field, and $\mathbf{E}(\mathbf{k}, \omega)$ the electric field. Assuming that the relative permeability is negligibly different than vacuum, $\check{\mu}(\mathbf{k}, \omega) = \check{I}$, as we will throughout, macroscopic averaging of (5.5a)-(5.5d)

produces:

$$\mathbf{k} \cdot \mathbf{D}_L(\mathbf{k}, \omega) = -i\rho_f(\mathbf{k}, \omega) / \epsilon_0 \quad (5.6a)$$

$$\bar{\mathbf{B}}_L(\mathbf{k}, \omega) = 0 \quad (5.6b)$$

$$\mathbf{k} \times \bar{\mathbf{E}}_T(\mathbf{k}, \omega) = \omega \bar{\mathbf{B}}_T(\mathbf{k}, \omega) \quad (5.6c)$$

$$ic^2 \mathbf{k} \times \bar{\mathbf{B}}_T(\mathbf{k}, \omega) = -i\omega \mathbf{D}_T(\mathbf{k}, \omega) + \mathbf{j}_{fT}(\mathbf{k}, \omega) / \epsilon_0 \quad (5.6d)$$

$$i\omega \mathbf{D}_L(\mathbf{k}, \omega) = \mathbf{j}_{fL}(\mathbf{k}, \omega) / \epsilon_0.$$

where $\mathbf{D}(\mathbf{k}, \omega) = \check{\epsilon}(k, \omega) \mathbf{E}(\mathbf{k}, \omega)$ is the electric displacement field, and the f subscript is introduced as a shorthand that the quantity is free. (Any quantity X_f is separate from the microscopic densities that have been averaged over in producing the macroscopic equations (5.6a)-(5.6d) from the microscopic equations (5.5a)-(5.5d).) Similarly, the overline \bar{X} serves as a reminder that the electric and magnetic fields appearing in (5.6a)-(5.6d) are spatially averaged, and not equivalent to the identically named fields in (5.5a)-(5.5d).

5.2.1 Characteristics of the microscopic decomposition

This decomposition of the electromagnetic field exposes physical features crucial for characterizing field fluctuations in a medium. Beginning with the microscopic equations, (5.5a) and (5.5b) show that the longitudinal electric and magnetic fields are entirely determined by their respective charge densities as

$$\mathbf{E}_L(\mathbf{k}, \omega) = -i\rho(\mathbf{k}, \omega) \mathbf{k} / (\epsilon_0 k^2) \quad (5.7a)$$

$$\mathbf{B}_L(\mathbf{k}, \omega) = 0. \quad (5.7b)$$

In the absence of charge the longitudinal fields must therefore be zero. Since the most important properties of this type are the Coulomb self-energy and charge momentum [269], we will interchangeably refer to longitudinal fields as *Coulombic*. A homogeneous solution to (5.6a)-(5.6d) is then purely transverse, and from (5.6c) we see that this amounts to correctly defining $\mathbf{E}_T(\mathbf{k}, \omega)$. In the remainder of the chapter, we will refer to all such quantities that define homogeneous solutions as *normal variables*.

5.2.2 Isotropic media

The generalization to isotropic media follows analogously. By symmetry, the relation between $\mathbf{D}(\mathbf{k}, \omega)$ and $\bar{\mathbf{E}}(\mathbf{k}, \omega)$ is defined by scalar multiplication of the relative permittivity, $\check{\epsilon}(k, \omega) = \epsilon(k, \omega) \check{I}$. Using this relation, the longitudinal electric and

magnetic fields are now determined by the average free charge densities to be

$$\bar{\mathbf{E}}_L(\mathbf{k}, \omega) = -i\rho_f(\mathbf{k}, \omega) \mathbf{k} / (k^2 \epsilon_0 \epsilon(k, \omega)) \quad (5.8a)$$

$$\bar{\mathbf{B}}_L(\mathbf{k}, \omega) = 0. \quad (5.8b)$$

Concurrently, so long as $\epsilon(k, \omega) \neq 0$, the normal variables of an isotropic medium are again transverse and defined by $\bar{\mathbf{E}}_T(\mathbf{k}, \omega)$.

The caveat to this congruence is the appearance of the polarization condition

$$\epsilon(k, \omega) = 0. \quad (5.9)$$

From equation (5.6a) we observe that when this condition is met, the displacement field may be zero even if the longitudinal electric field is not. Since the remaining macroscopic equations do not depend on the longitudinal electric field, these Coulombic solutions evolve independent of the transverse, vacuum-like, electromagnetic solutions [270–272]. Rather, averaging (5.5a) directly,

$$\bar{\rho}(\mathbf{k}, \omega) = i\epsilon_0 k \cdot \bar{\mathbf{E}}_L(\mathbf{k}, \omega), \quad (5.10)$$

shows that each Coulombic solution is a mechanical macroscopic oscillation of the microscopic charge density, mediated by the electric field.

These additional solutions demonstrate that (5.6a)-(5.6d) are fundamentally different than a scaled vacuum. The fact that $\epsilon(\mathbf{k}, \omega)$ exists because of the presence of charges is inescapable, even after macroscopic averaging. However, in isotropic media the resulting effects can be considered independent of the electromagnetic (transverse) properties, as Coulombic modes do not couple to external electromagnetic sources. For this reason Coulombic modes may be neglected in many situations.

5.2.3 Anisotropic media

For anisotropic media the relative permittivity tensor, $\check{\epsilon}(k, \omega)$, can not be expressed as single scalar and a more careful analysis is required. Rewriting (5.6a)-(5.6d) in the Coulomb gauge using

$$\bar{\mathbf{E}}_T(\mathbf{k}, \omega) = i\omega \bar{\mathbf{A}}_T(\mathbf{k}, \omega) \quad (5.11a)$$

$$\bar{\mathbf{E}}_L(\mathbf{k}, \omega) = -i\mathbf{k} \bar{V}(\mathbf{k}, \omega) \quad (5.11b)$$

$$\bar{\mathbf{B}}_T(\mathbf{k}, \omega) = i\mathbf{k} \times \bar{\mathbf{A}}_T(\mathbf{k}, \omega) \quad (5.11c)$$

a homogeneous solution requires both

$$\omega (\bar{I}k^2 - \mathbf{k} \otimes \mathbf{k} - k_0^2 \check{\epsilon}(k, \omega)) \bar{\mathbf{A}}_T(\mathbf{k}, \omega) + k_0^2 \check{\epsilon}(k, \omega) \mathbf{k} \bar{V}(\mathbf{k}, \omega) = 0, \quad (5.12)$$

and

$$\mathbf{k} \check{\epsilon}(k, \omega) (\omega \bar{\mathbf{A}}_T(\mathbf{k}, \omega) - \mathbf{k} \bar{V}(\mathbf{k}, \omega)) = 0, \quad (5.13)$$

with $k_0 = \omega/c$, $\bar{\mathbf{A}}(\mathbf{k}, \omega)$ the electromagnetic vector potential, and $\bar{V}(\mathbf{k}, \omega)$ the scalar potential. In order to satisfy (5.13) there are three distinct solutions.

(S1): If in addition to being perpendicular to \mathbf{k} , $\bar{\mathbf{A}}_T(\mathbf{k}, \omega)$ is constrained to directions perpendicular to $\mathbf{k} \check{\epsilon}(\omega)$ then $\bar{V}(\mathbf{k}, \omega) = 0$. As in vacuum, the normal variables are then determined by the transverse electric field. Evaluating the first condition in this case, simplifying to a uniaxial medium as we will throughout, produces the s-polarized, or *ordinary*, wave condition

$$k = \sqrt{\epsilon_P(k, \omega)} k_0, \quad (5.14)$$

with $\bar{\mathbf{A}}_T(\mathbf{k}, \omega)$ confined to the direction $\hat{\mathbf{s}} = [-s(\phi), c(\phi), 0]$ relative to the unit direction in reciprocal space $\hat{\mathbf{k}} = [s(\theta)c(\phi), s(\theta)c(\phi), c(\theta)]$. (Our labeling convention for uniaxial media is shown in Fig. 5.1.)

(S2): If $\mathbf{k} \check{\epsilon}(k, \omega) \mathbf{k} = 0$ then $\bar{V}(\mathbf{k}, \omega)$ can be non-zero independent of the value of $\bar{\mathbf{A}}_T(\mathbf{k}, \omega)$. These purely longitudinal modes bear a straightforward relation to the Coulombic solutions of an isotropic media occurring with the polarization condition, (5.9). The updated criterion

$$\mathbf{k} \check{\epsilon}(k, \omega) \mathbf{k} = 0, \quad (5.15)$$

simply accounts for the loss of complete $\hat{\mathbf{k}}$ symmetry. For uniaxial anisotropy, (5.15) reduces to

$$\epsilon_U(k, \theta, \omega) = 0, \quad (5.16)$$

with

$$\epsilon_U(k, \theta, \omega) = s(\theta)^2 \epsilon_P(k, \omega) + c(\theta)^2 \epsilon_A(k, \omega). \quad (5.17)$$

We will refer to this directional projection of the uniaxial permittivity tensor as the uniaxial permittivity of the medium (U subscript).

(S3): If $\bar{\mathbf{A}}_T(\mathbf{k}, \omega)$ is not perpendicular to $\mathbf{k} \check{\epsilon}(k, \omega)$, then from (5.13)

$$\bar{V}(\mathbf{k}, \omega) = \omega \mathbf{k} \check{\epsilon}(k, \omega) \bar{\mathbf{A}}_T(\mathbf{k}, \omega) / (\mathbf{k} \check{\epsilon}(k, \omega) \mathbf{k}) \quad (5.18)$$

and (5.12) becomes

$$\left(i \frac{k^2}{k_0^2} - \frac{\mathbf{k} \otimes \mathbf{k}}{k_0^2} - \check{\epsilon}(k, \omega) + \frac{\check{\epsilon}(k, \omega) \mathbf{k} \otimes \check{\epsilon}(k, \omega) \mathbf{k}}{\mathbf{k} \check{\epsilon}(k, \omega) \mathbf{k}} \right) \bar{\mathbf{A}}_T = 0. \quad (5.19)$$

Given the directional constraints on $\bar{\mathbf{A}}_T$, satisfaction of this equation for a uniaxial medium requires k to be a solution of the p-polarized, or *extraordinary*, wave condition

$$k = \sqrt{\epsilon_E(k, \theta, \omega)} k_0, \quad (5.20)$$

with $\bar{\mathbf{A}}_T(\mathbf{k}, \omega)$ confined to the direction $\hat{\mathbf{p}} = [-c(\theta) c(\phi), -c(\theta) s(\phi), s(\theta)]$, with $\epsilon_E(\mathbf{k}, \theta, \omega)$ is defined as the extraordinary relative permittivity

$$\epsilon_E(k, \theta, \omega) = \frac{\epsilon_A(k, \omega) \epsilon_P(k, \omega)}{\epsilon_U(k, \theta, \omega)}. \quad (5.21)$$

(Note that (5.21) is strikingly similar to the excitation condition of a surface plasmon polariton [21].)

Using the above definition of the Coulomb gauge, substitution into $\bar{V}(\mathbf{k}, \omega) = \omega \mathbf{k} \check{\epsilon}(k, \omega) \bar{\mathbf{A}}_T(\mathbf{k}, \omega) / (\mathbf{k} \check{\epsilon}(k, \omega) \mathbf{k})$ shows that for the extraordinary family of solutions

$$\bar{\mathbf{E}}_L(\mathbf{k}, \omega) = \hat{\mathbf{k}} \epsilon_H(k, \theta, \omega) \bar{E}_T(\mathbf{k}, \omega), \quad (5.22)$$

where $\bar{E}_T(\mathbf{k}, \omega)$ is the undetermined scalar magnitude of the transverse component of the electric field,

$$\epsilon_\Delta(k, \theta, \omega) = s(\theta) c(\theta) (\epsilon_P(k, \omega) - \epsilon_A(k, \omega)) \quad (5.23)$$

is the relative degree of polarization anisotropy between the optical axis and plane, and

$$\epsilon_H(k, \theta, \omega) = \frac{\epsilon_\Delta(k, \theta, \omega)}{\epsilon_U(k, \theta, \omega)} \quad (5.24)$$

is defined as the hyperbolic permittivity.

Startlingly, from (5.22) we find that the normal variables of the extraordinary family of solutions now possess a mixture of transverse and longitudinal fields. This fundamentally does not occur for isotropic media and is one of the central results of this chapter. Averaging (5a) as before,

$$\bar{\rho}(\mathbf{k}, \omega) = i \epsilon_0 k \epsilon_H(k, \theta, \omega) \bar{E}_T(\mathbf{k}, \omega), \quad (5.25)$$

it is apparent that the electromagnetic part is accompanied by a Coulombic charge oscillation. To keep this fact in mind, we will call these solutions the *anisotropic polariton* (AP) family.

Again, in isotropic media such an excitation is impossible. The global direction of the electric field for a Coulombic mode is uniquely fixed by the propagation direction of the charge oscillation. These electric fields can not couple to the magnetic field, and hence are not electromagnetic solutions. However, in the presence of anisotropy, the normal variables of a homogeneous solution are not required to be either purely electromagnetic or Coulombic; and are in general mixed, or polaritonic. For these solutions, there is no way of fully describing resulting properties and interactions without both components. (Note that the same reasoning can be applied to the magnetic field and relative permeability tensor $\check{\mu}(k, \omega)$.)

(5.24) and (5.25) show that the Coulombic part of an AP type mode grows proportionally with the degree of anisotropy of the medium, (5.23), and is resonant with zeros of the uniaxial permittivity, (5.17). These properties inherently characterize a hyperbolic medium. As we will demonstrate, when this special polarization response is present AP type modes dominate the ordinary electromagnetic excitations.

5.3 Normal variable decomposition of the anisotropic green function

In this second section, we decompose the anisotropic Green function using the solution families (S1)-(S3). Using this form, we then determine the FD of a hyperbolic medium in reciprocal space.

Substituting (5.6c) into (5.6d), the electric field inside a macroscopic medium obeys the equation

$$-\mathbf{k} \times \mathbf{k} \times \bar{\mathbf{E}}(\mathbf{k}, \omega) - k_0^2 \check{\epsilon}(k, \omega) \bar{\mathbf{E}}(\mathbf{k}, \omega) = i\mathbf{j}_f(\mathbf{k}, \omega) / (\epsilon_0 c^2), \quad (5.26)$$

so that any electric field implies a current density as described by

$$i\mathbf{j}_f(\mathbf{k}, \omega) = \epsilon_0 c^2 \left(k^2 \left(\check{I} - \hat{\mathbf{k}} \otimes \hat{\mathbf{k}} \right) - k_0^2 \check{\epsilon}(k, \omega) \right) \bar{\mathbf{E}}(\mathbf{k}, \omega) = \check{\mathcal{G}}^{-1}(\mathbf{k}, \omega) \bar{\mathbf{E}}(\mathbf{k}, \omega) \quad (5.27)$$

The dyadic Green function of a uniaxial medium is exactly the inverse of this relation,

$$\check{\mathcal{G}}^U(\mathbf{k}, \omega) = \frac{k_0}{\epsilon_0 c^2} \left(\frac{\hat{\mathbf{s}} \otimes \hat{\mathbf{s}}}{k^2 - \epsilon_P(k, \omega)} - \frac{\hat{\mathbf{k}} \otimes \hat{\mathbf{k}}}{\epsilon_U(k, \theta, \omega)} + \frac{\left(\hat{\mathbf{p}} + \epsilon_H(k, \theta, \omega) \hat{\mathbf{k}} \right) \otimes \left(\hat{\mathbf{p}} + \epsilon_H(k, \theta, \omega) \hat{\mathbf{k}} \right)}{k^2 - \epsilon_E(k, \theta, \omega)} \right), \quad (5.28)$$

where all reciprocal vectors have been normalized by k_0 , and, recalling our previous definitions,

$$\hat{\mathbf{s}} = [-s(\phi), c(\phi), 0] \quad (5.29a)$$

$$\hat{\mathbf{p}} = [-c(\theta) c(\phi), -c(\theta) s(\phi), s(\theta)] \quad (5.29b)$$

$$\hat{\mathbf{k}} = [s(\theta) c(\phi), s(\theta) s(\phi), c(\theta)]. \quad (5.29c)$$

For isotropic media, $\epsilon_H(k, \omega)$ reduces to zero while $\epsilon_U(k, \omega)$ and $\epsilon_E(k, \omega)$ become the isotropic permittivity $\epsilon(k, \omega)$ so that (5.28) simplifies to

$$\check{\mathcal{G}}^I(\mathbf{k}, \omega) = \frac{k_0}{\epsilon_0 c^2} \left(\frac{\hat{\mathbf{s}} \otimes \hat{\mathbf{s}}}{k^2 - \epsilon(k, \omega)} - \frac{\hat{\mathbf{k}} \otimes \hat{\mathbf{k}}}{\epsilon(k, \omega)} + \frac{\hat{\mathbf{p}} \otimes \hat{\mathbf{p}}}{k^2 - \epsilon(k, \omega)} \right). \quad (5.30)$$

Here, the $_U$ and $_I$ superscripts mark that the results applies specifically to either uniaxial or isotropic media.

Recalling the normal variable picture of the previous section, the meaning of the Green function as an operator is clear. (5.28) determines the electric field generated by a point current source as a modal expansion in terms of the three homogeneous solution families.

(S1): Ordinary electromagnetic (O) type excitations, represented by the purely transverse term

$$\check{\mathcal{G}}_O^U(\mathbf{k}, \omega) = \frac{k_0}{\epsilon_0 c^2} \frac{\hat{\mathbf{s}} \otimes \hat{\mathbf{s}}}{k^2 - \epsilon_P(k, \omega)}. \quad (5.31)$$

(S2): Coulombic polarization (C) type excitations, represented by the purely longitudinal term

$$\check{\mathcal{G}}_C^U(\mathbf{k}, \omega) = -\frac{k_0}{\epsilon_0 c^2} \frac{\hat{\mathbf{k}} \otimes \hat{\mathbf{k}}}{\epsilon_U(k, \omega)}. \quad (5.32)$$

(S3): Anisotropic polariton (AP) type excitations, represented by the mixed term

$$\check{\mathcal{G}}_{AP}^U(\mathbf{k}, \omega) = \frac{k_0}{\epsilon_0 c^2} \frac{\left(\hat{\mathbf{p}} + \epsilon_H(k, \theta, \omega) \hat{\mathbf{k}} \right) \otimes \left(\hat{\mathbf{p}} + \epsilon_H(k, \theta, \omega) \hat{\mathbf{k}} \right)}{k^2 - \epsilon_E(k, \theta, \omega)}. \quad (5.33)$$

Taking the trace of the imaginary part of the uniaxial Green function, the portion of the fluctuation density that will persist as $\mathbf{r} \rightarrow \mathbf{r}'$ is given by

$$\begin{aligned} \mathcal{F}^U(\mathbf{k}, \omega) = Tr [Im \{ \check{\mathcal{G}}^U(\mathbf{k}, \omega) \}] = \frac{k_0}{\epsilon_0 c^2} Tr \left[\right. \\ \left(\frac{Im \{ \epsilon_P(k, \omega) \}}{|k^2 - \epsilon_P(k, \omega)|^2} \hat{\mathbf{s}} \otimes \hat{\mathbf{s}} + \frac{Im \{ \epsilon_E(k, \theta, \omega) \}}{|k^2 - \epsilon_E(k, \theta, \omega)|^2} \hat{\mathbf{p}} \otimes \hat{\mathbf{p}} + \right. \\ \left. \left(\left(\frac{c(\theta) |k^2 - \epsilon_P(k, \omega)|}{|\epsilon_U(k, \theta, \omega)|} \right)^2 \frac{Im \{ \epsilon_A(k, \omega) \}}{|k^2 - \epsilon_E(k, \theta, \omega)|^2} + \right. \right. \\ \left. \left. \left(\frac{s(\theta) |k^2 - \epsilon_A(k, \omega)|}{|\epsilon_U(k, \theta, \omega)|} \right)^2 \frac{Im \{ \epsilon_P(k, \omega) \}}{|k^2 - \epsilon_E(k, \theta, \omega)|^2} \right) \hat{\mathbf{k}} \otimes \hat{\mathbf{k}} \right]. \quad (5.34) \end{aligned}$$

Where $\mathbf{r} - \mathbf{r}'$ has been replaced by \mathbf{r} . (The trace of the $\hat{\mathbf{p}} \otimes \hat{\mathbf{k}}$ and $\hat{\mathbf{k}} \otimes \hat{\mathbf{p}}$ matrices are zero.) The poles of this function show that the first term again represents ordinary (O type) excitations, while the final two terms form the combined contributions of the mixed anisotropic polariton (AP) and pure longitudinal (C type) modes. These two solution classes couple due the presence of shared longitudinal fields. Regardless, the fact that the second transverse $\hat{\mathbf{p}} \otimes \hat{\mathbf{p}}$ term has $|k^2 - \epsilon_E(k, \omega)|^2$ (S3) poles, but not $|\epsilon_U(k, \omega)|^2$ (S2) poles separates the influence of these two types of excitations.

5.4 Model-independent regularization of the fluctuation density through spatial non-locality

Having determined the FD of a hyperbolic medium in reciprocal space in the previous section, (5.34), we now turn to its real space counterpart. This quantity diverges in the approximation of local polarization response. Here, we reveal how the AP contribution, hitherto undefined, can nevertheless be extracted from the FD in a model-independent way.

In the analysis we have carried out so far, all permittivity factors have been written as functions of the magnitudes k and ω . From the inverse Fourier transformation, these dependencies correspond respectively to spatial and temporal non-locality; qualities fundamentally required of any properly defined response function. Never-

theless, in practice, the approximation of local spatial response

$$\begin{aligned} \mathbf{r}' - \mathbf{r} \neq \mathbf{0} &\Rightarrow \epsilon(\mathbf{r} - \mathbf{r}', t - t') = 0 \\ \epsilon(k, \omega) &\rightarrow \epsilon(\omega), \end{aligned} \quad (5.35)$$

is almost always used. Because the momentum of a photon is typically very small compared to the scale set by the material lattice, the difference between $\epsilon(k, \omega)$ and $\epsilon(\omega)$ for electromagnetics is often insubstantial. (Additionally, it is also presently difficult to accurately probe permittivity response at optical and infrared frequencies above $k/k_0 \approx 5$ [273].)

Notwithstanding, the FD contains both transverse (electromagnetic) and longitudinal (Coulombic) parts. For the Coulombic portion, ignoring non-locality implies C type modes with no k dependence. Directly, this leads to divergence when considering a point charge coupling equally well to all k . Inside isotropic media, the simplest solution is to ignore this longitudinal part, and concentrate on the transverse portion of the FD. This can be done without introducing any issues as the electromagnetic and Coulombic fields correspond to different normal variables [269]. However, the mixed field characteristics of AP type modes clearly make this approach unusable for anisotropic media. Recalling that we are working in spherical coordinates, the asymptotic behavior of (5.34) shows that

$$\mathcal{F}^U(\omega) = \lim_{|\mathbf{r}| \rightarrow 0} \int_0^\pi d\theta \int_0^{2\pi} d\phi \int_0^\infty dk \frac{k^2 s(\theta)}{(2\pi)^3} \mathcal{F}^U(\mathbf{k}, \omega) \frac{e^{i\mathbf{k}\cdot\mathbf{r}} + e^{-i\mathbf{k}\cdot\mathbf{r}}}{2} \quad (5.36)$$

diverges as k^3 under the above local approximation³. This term contains the longitudinal fields of both AP and C type modes. Without it, the polaritonic characteristics of a hyperbolic response can not be captured.

To extract the contribution of AP modes we begin by expanding all absolute values and imaginary parts of (5.34), treating k as a real variable. In this form, the resulting expression in k can be extended as an analytic function over the entire complex plane. Taking an equivalent k integral over the entire real line, Jordan's lemma then implies that if $k^2 \mathcal{F}^U(\mathbf{k}, \omega) \rightarrow 0$ as $|k| \rightarrow \infty$ the Cauchy integral theorem will equate $\mathcal{F}^U(\omega)$ to the residues of $\mathcal{F}^U(\mathbf{k}, \omega)$. (Here, we are using infinite semi-circle contours in the upper and lower half spaces depending on the value of $\mathbf{k}\cdot\mathbf{r}$ ⁴.) There-

³This divergence also occurs in vacuum. Classically, the strength of the electric field generated by a point dipole scales as $\propto 1/r^3$. In an absorbing medium the energy loss per unit volume then also scale as $\propto 1/r^3$ or in Fourier space $\propto k^3$.

⁴In our convention the square function is cut along the positive real axis.

fore, we can conclude that any model of non-locality leading to $Im\{\epsilon_A(k, \omega)\}$ and $Im\{\epsilon_P(k, \omega)\}$ having asymptotic k scaling stronger than $\propto 1/k^2$ will make (5.36) convergent.

Interestingly, as we show in first the appendix, this is a generally valid assumption, and the above result allows us to determine key features of (5.36) without assuming any specific model of spatial non-locality. Precisely, for each wave equation there are poles of the form $k_S = \pm\sqrt{\epsilon_X(k_S, \omega)}$ that do not explicitly depend spatial non-locality, i.e. poles that tend to $k_S = \pm\sqrt{\epsilon_X(\omega)}$ in the limit of local response. Using the Cauchy integral theorem as described above and taking the $|\mathbf{r}| \rightarrow 0$ limit, we find that the residues determined by these poles sum to give

$$\begin{aligned} \mathcal{F}_O^U(\omega) &= \int_0^{2\pi} d\phi \int_0^{\pi/2} d\theta s(\theta) Tr [Im\{\check{\mathcal{G}}_O^U(\theta, \phi, \omega)\}] = \\ &= \frac{k_0\pi}{(2\pi)^3 \epsilon_0 c^2} \int_0^{2\pi} d\phi \int_0^{\pi/2} d\theta s(\theta) Re\left\{\sqrt{\epsilon_P(k_O, \omega)}\right\} \end{aligned} \quad (5.37)$$

for O type modes, and

$$\begin{aligned} \mathcal{F}_{AP}^U(\omega) &= \int_0^{2\pi} d\phi \int_0^{\pi/2} d\theta s(\theta) Im\{\check{\mathcal{G}}_{AP}^U(\theta, \phi, \omega)\} = \\ &= \frac{k_0\pi}{(2\pi)^3 \epsilon_0 c^2} \int_0^{2\pi} d\phi \int_0^{\pi/2} d\theta s(\theta) Re\left\{\sqrt{\epsilon_E(k_E(\theta), \theta, \omega)}\right\} \left(1 + |\epsilon_H(k_E(\theta), \theta, \omega)|^2\right) \end{aligned} \quad (5.38)$$

for AP type modes, with k_O and $k_E(\theta)$ standing for the implicitly modified solutions to (5.14) and (5.20) (most like the poles of the local approximation). For (5.38) the first term results from the transverse field and the second term from the longitudinal field. These two expressions provide an unequivocal characterization of the O and AP type parts of the FD, and are crucial to all following results. (For local isotropic response, the sum of these two terms is the photonic density of states [254].)

Convincingly, (5.38) is also precisely the result obtained by considering the normal variables of the AP solution family. In the second section, we showed that any AP excitation has both longitudinal and transverse components, related by (5.22). (5.28) identifies the transverse part of these excitations with the second term of (5.34). Since there is no question as to the convergence of this term, the existence of (5.38) is in fact a requirement of Maxwell's equations. We emphasize that either

approach to (5.38) is independent of the specific form of non-locality considered, and that by virtue of this fact (5.38) is unambiguously *the AP* part of the FD. It is also worthwhile to note that the permittivity dependence of the Coulombic piece of this term

$$\mathcal{F}_{APL}^U(\omega) = \frac{k_0 \pi}{(2\pi)^3 \epsilon_0 c^2} \int_0^{2\pi} d\phi \int_0^{\pi/2} d\theta s(\theta) \operatorname{Re} \left\{ \sqrt{\epsilon_E(k_E(\theta), \theta, \omega)} \right\} |\epsilon_H(k_E(\theta), \theta, \omega)|^2 \quad (5.39)$$

is the same as that observed in calculating the power radiated by a dipole in a losses hyperbolic medium [274, 275], and is essentially an angular version of the FD associated with a surface plasmon polartion excitation [21]. As discussed in the second appendix, for the materials we will examine later in this chapter it is reasonable to assume that the local approximations of (5.37) and (5.38) contain the only O and AP contributions to the FD that need to be considered.

To determine the FD resulting from the (S2) C type poles, a specific model of non-locality is required [126, 213]. To focus our discussion we will not investigate these terms. Still, there are general characteristics worth noting. Considering the real k integral of this term as written in (5.36), once k^2 surpasses $|\operatorname{Re}\{\epsilon_E(k, \theta, \omega)\}|$ we will quickly approach $(|k^2 - \epsilon_P(k, \omega)|/|k^2 - \epsilon_E(k, \theta, \omega)|)^2 \approx (|k^2 - \epsilon_A(k, \omega)|/|k^2 - \epsilon_E(k, \theta, \omega)|)^2 \approx 1$. (Non-locality will not drastically increase the peak magnitude of the polarization response for real k .) Once this condition is achieved, the final term of (5.34) is accurately approximated as

$$\operatorname{Im}\{\check{\mathcal{G}}_C^U(\mathbf{k}, \omega)\} = \frac{k_0}{\epsilon_0 c^2} \left(\frac{\hat{\mathbf{k}} \otimes \hat{\mathbf{k}}}{|\epsilon_U(k, \theta, \omega)|^2} \operatorname{Im}\{\epsilon_U(k, \theta, \omega)\} \right). \quad (5.40)$$

This expression is again the exact result found by considering the normal variables of the Coulombic solutions independently, and a straightforward extension of the Coulombic FD encountered in isotropic media,

$$\operatorname{Im}\{\check{\mathcal{G}}_C^I(\mathbf{k}, \omega)\} = \frac{k_0}{\epsilon_0 c^2} \left(\frac{\hat{\mathbf{k}} \otimes \hat{\mathbf{k}}}{|\epsilon(k, \omega)|^2} \operatorname{Im}\{\epsilon(k, \omega)\} \right). \quad (5.41)$$

For k where the above approximation is valid, the residues from these (S2) type poles can safely be attributed to pure Coulombic modes, and the resulting divergence in the local approximation attributed to an artifact of treating matter in the continuum limit.

5.5 The sum rule for modified spontaneous emission enhancement in hyperbolic media

Building from expressions (5.37) and (5.38), we now turn to applications. In this fourth section we demonstrate that while the quantum optical sum rule for spontaneous emission enhancement is valid for hyperbolic media, it does not capture the most important features of hyperbolic enhancement.

The sum rule for modified spontaneous emission enhancement, formulated by Barnett and Loudon [254,276], states that it is not possible to alter the total relative rate of spontaneous emission into purely electromagnetic (transverse) excitations. That is, if the properties of a medium enhance the relative rate of spontaneous emission into electromagnetic modes in one spectral range, they must equally suppress this relative rate in another. Mathematically, this is written as

$$\int_0^\infty d\omega \frac{\Gamma_T(\mathbf{r}, \omega) - \Gamma_0(\omega)}{\Gamma_0(\omega)} = 0, \quad (5.42)$$

where

$$\Gamma_T(\mathbf{r}, \omega) = \frac{2\omega^2}{\hbar} \mathbf{d} \text{Im} \{ \check{G}_{TT}(\mathbf{r}, \mathbf{r}, \omega) \} \mathbf{d} \quad (5.43)$$

is the relative rate of spontaneous emission of a single level emitter of frequency ω , with transition dipole moment \mathbf{d} , at position \mathbf{r} in a medium described by $\check{G}(\mathbf{r}, \mathbf{r}', \omega)$, and

$$\Gamma_0(\mathbf{r}, \omega) = \frac{k_0^3}{3\pi\hbar\epsilon_0} \mathbf{d} \check{I} \mathbf{d} \quad (5.44)$$

is the rate of spontaneous emission in vacuum. The $_{TT}$ subscript refers to the fact that the transverse projection is applied to both indices of the Green function.

As the frequency dependencies of the uniaxial (5.28) and isotropic (5.30) Green functions are the same, Scheel's argument for the general validity of the sum rule [277] applies, guaranteeing that the transverse part of the uniaxial Green function

$$\begin{aligned} \text{Im} \{ \check{G}_{TT}^U(\omega) \} &= \frac{k_0\pi}{(2\pi)^3 \epsilon_0 c^2} \int_0^{2\pi} d\phi \int_0^{\pi/2} d\theta s(\theta) \\ &\left(\text{Re} \left\{ \sqrt{\epsilon_P(\omega)} \right\} \hat{\mathbf{s}} \otimes \hat{\mathbf{s}} + \text{Re} \left\{ \sqrt{\epsilon_E(\theta, \omega)} \right\} \hat{\mathbf{p}} \otimes \hat{\mathbf{p}} \right), \end{aligned} \quad (5.45)$$

must satisfy (5.42) so long as the permittivities considered satisfy the Kramers-Kronig relations.

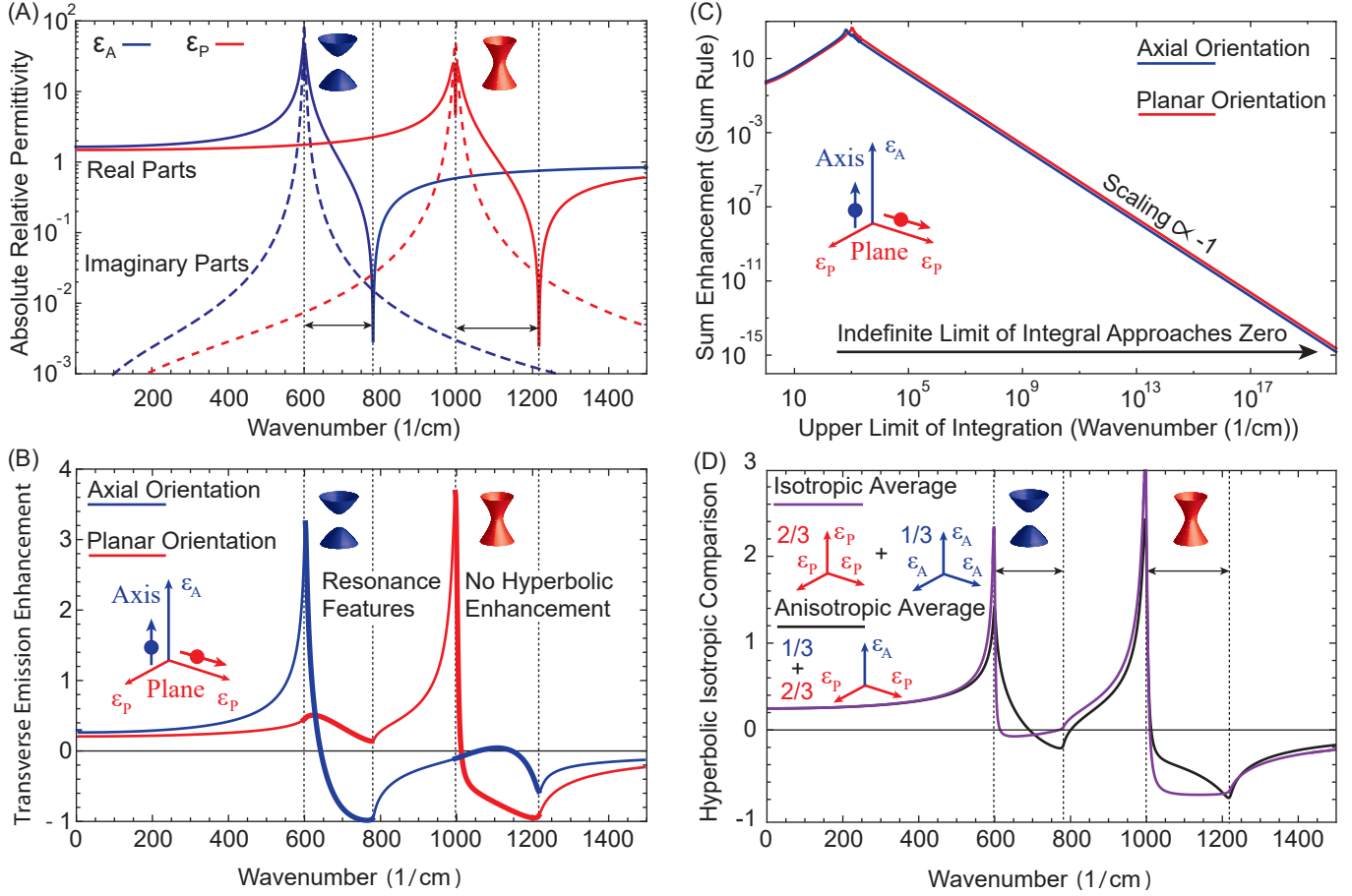


Figure 5.2: **Quantum optical sum rule for transverse spontaneous emission enhancement in hyperbolic media.**

Panel (A) displays the absolute relative permittivity values resulting from (5.46). The thin dashed lines and schematic dispersion surfaces highlight spectral regions of hyperbolic response where one of either $Re\{\epsilon_p(\omega)\}$ or $Re\{\epsilon_A(\omega)\}$ is negative. Panel (B) shows the resulting transverse spontaneous emission enhancement offset by vacuum, the integrand of (5.42). Panel (C) plots the integrated enhancement as function of the upper wavenumber considered. These result confirm that the enhancement sum rule is strictly obeyed inside hyperbolic media [277]. (We have tested a great number of other cases and have always found perfect agreement.) Accounting only for purely electromagnetic (transverse) contributions, emission enhancement in spectral regions of hyperbolic response is unremarkable. Panel (D) further highlights this fact by comparing the orientationally averaged enhancement from (B), black line, with the enhancement found by averaging two isotropic media with $\epsilon(k, \omega) = \epsilon_p(\omega)$ and $\epsilon(k, \omega) = \epsilon_A(\omega)$ weighted by factors of 2/3 and 1/3 respectively. The graphs are found to be nearly identical, even though the two situations correspond to very different electromagnetic environments and have completely different angular behavior.

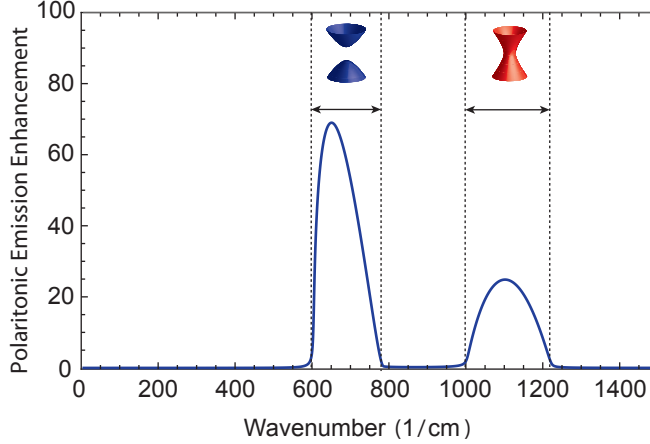


Figure 5.3: **Polaritonic spontaneous emission enhancement surpassing the sum rule in hyperbolic media.**

The figure displays the orientationally averaged spontaneous emission enhancement of the Coulombic (longitudinal) part of the AP contribution, considering a uniaxial media with permittivity model (5.46). Contrasting with Fig. 5.2, this longitudinal enhancement dominates in spectral regions of hyperbolic response. This quantity does not obey a quantum optical sum rule like (5.42).

An illustrative example of this result assuming local Lorentzian polarization responses,

$$\epsilon(\omega) = 1 + \frac{\omega_p^2}{\omega_0^2 - \omega(\omega + i\gamma)}, \quad (5.46)$$

for $\epsilon_A(\omega)$ and $\epsilon_P(\omega)$ with $\omega_p = \{500_A, 700_P\} \text{ cm}^{-1}$, $\omega_0 = \{600_A, 1000_P\} \text{ cm}^{-1}$ and $\gamma = \{5_A, 10_P\} \text{ cm}^{-1}$ is provided in Fig. 5.2.

From the graph, we observe that the regions of hyperbolic response are essentially featureless, and that just as in isotropic media the most important spectral characteristics occur at polarization maximas. Further, Fig. 5.2(D) shows that the orientationally averaged enhancement of this transverse part is nearly equivalent to considering the planar and axial permittivities separately and summing the result. That is, replacing (5.45) with the sum of $(2/3) \mathcal{F}_T^I(\omega)$ with $\epsilon(k, \omega) = \epsilon_P(\omega)$ and $(1/3) \mathcal{F}_T^I(\omega)$ with $\epsilon(k, \omega) = \epsilon_A(\omega)$.

These results for the transverse part of the AP enhancement, which hold to arbitrarily low absorption (γ), follow from the normal variable picture. Any property of a linear macroscopic medium should be consistent with an arrangement of some collection of dipoles in vacuum. Since a dipole does not introduce new electromagnetic modes, the transverse part of the FD must obey the sum rule for modified spontaneous emission enhancement in any such environment. From (5.38) the reso-

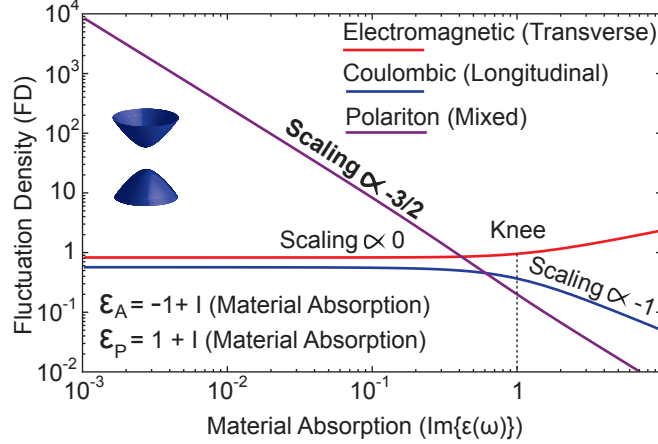


Figure 5.4: **Scaling with material absorption of fluctuation densities in hyperbolic media.**

The figure depicts the power scaling of the transverse O type (5.45), longitudinal C type (5.40), and mixed AP type (longitudinal part only) (5.47) contributions to the FD as a function of material absorption $Im\{\epsilon_{A,P}(\omega)\}$. For the C type contribution, only the angular integrals in (5.36) have been computed as the k integral diverges in the limit of local polarization response. The knee transitioning from a scaling of $\propto -1$ to a scaling of $\propto 0$ is set by the minimum magnitude of the real permittivity components $|Re\{\epsilon_{A,P}(\omega)\}|$, just as in the isotropic case [268]. The AP contribution is found to exhibit a stronger power scaling than either of the two pure solution types. The $x^{-3/2}$ dependence exhibited is identical to the material absorption scaling of a surface plasmon polariton on a flat surface.

nant effects of hyperbolic response for AP type excitations occur in the Coulombic field [237]. In taking the strictly electromagnetic (transverse) part of (5.38) these features are ignored.

The orientationally averaged, equivalent to setting $\mathbf{d} = [1, 1, 1]/\sqrt{3}$, spontaneous emission enhancement resulting from the Coulombic portion of the AP FD

$$\frac{\Gamma_{APL}^U(\omega)}{\Gamma_0(\omega)} = \frac{6\pi\epsilon_0 c^3}{\omega} \mathcal{F}_{APL}^U(\omega) = \frac{3}{2} \int_0^{\pi/2} d\theta s(\theta) Re\left\{\sqrt{\epsilon_E(\theta, \omega)}\right\} |\epsilon_H(\theta, \omega)|^2, \quad (5.47)$$

is plotted in Fig. 5.3. (For numerical convenience in the remainder of this chapter the FD will be taken to be vacuum normalized by the prefactor appearing in (5.47).) Comparing with Fig. 5.2, it is clear that this enhancement does not obey the quantum optical sum rule. To first order, it is an additional positive contribution that grows arbitrarily large as material absorption is decreased. (Since this enhancement stems from charge oscillations, here there is no restriction based on the properties of the vacuum.) By itself, this fact is not particularly unusual. In a general isotropic

medium the absorption of energy into matter is not limited by the number of electromagnetic modes (5.42), and so neither is the enhancement contribution of C type modes. Yet, there are key distinctions that differentiate these two cases:

(1) The AP enhancement of the FD does not diverge in the limit of local permittivity response (non-locality is a second order effect). This is not the case for C type enhancement [213].

(2) The AP enhancement of the FD is not simply related to the magnitude of the polarization, density of charge carriers, as has been shown C type enhancement [277]. Instead, it depends principally on the magnitude of anisotropy and material absorption.

(3) The AP type enhancement of the FD shows a unique scaling with material absorption, which is stronger than the scaling exhibited by either the transverse O type (5.45) or longitudinal C type (5.40) enhancement, Fig. 5.4.

5.6 Thermal fluctuations in hexagonal boron nitride and bismuth selenide

In this fifth section, we examine how AP type excitations alter the thermal energy density in the electric field of natural hyperbolic media. Our discussion focuses on two particular material examples, hexagonal boron nitride and bismuth selenide.

Like the degree of relative spontaneous emission enhancement, the thermal energy density in the electric and magnetic fields is likewise set by the FD through the relation

$$\mathcal{U}(\mathbf{r}, \omega, T) = \frac{\epsilon_0}{2} Tr [\langle \mathbf{E}(\mathbf{r}, \omega) \otimes \mathbf{E}^*(\mathbf{r}, \omega) \rangle] + \frac{1}{2\mu_0} Tr [\langle \mathbf{B}(\mathbf{r}, \omega) \otimes \mathbf{B}^*(\mathbf{r}, \omega) \rangle], \quad (5.48)$$

with

$$Tr [\langle \mathbf{E}(\mathbf{r}, \omega) \otimes \mathbf{E}^*(\mathbf{r}, \omega) \rangle] = \frac{\omega \Theta(\omega, T)}{\pi} \mathcal{F}(\omega) \quad (5.49)$$

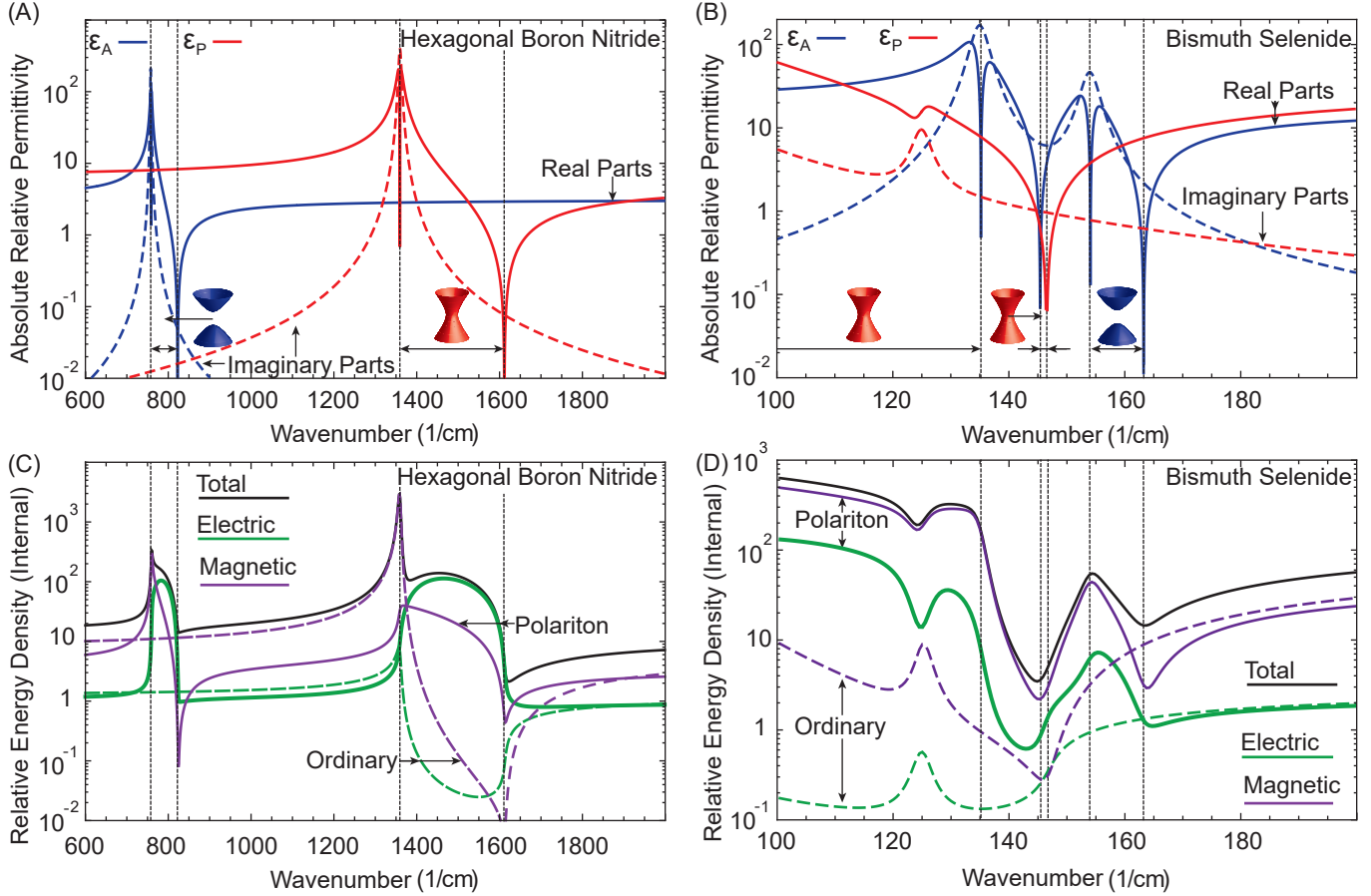


Figure 5.5: **Relative thermal energy and fluctuation densities in natural hyperbolic media.**

The figure shows the contribution that AP type modes, solid lines, and O type modes, dashed lines, make to the electric and magnetic thermal energy densities inside hexagonal boron nitride (C) and bismuth selenide (D). (For comparison the energy densities are normalized by half the thermal energy density of vacuum.) The absolute relative permittivity components of these two materials, based on data from references [245, 247], is plotted in figures (A) and (B). Each sharp peak and dip in these plots signals a sign flip of the corresponding real part (these are all positive at the high end of the given wavenumber ranges). The imaginary part of each component remains positive throughout. The green electric lines (bold polariton, dashed ordinary) double as the respective FDs. Both media show broad spectral regions where this quantity is over 120 times larger than it is in vacuum.

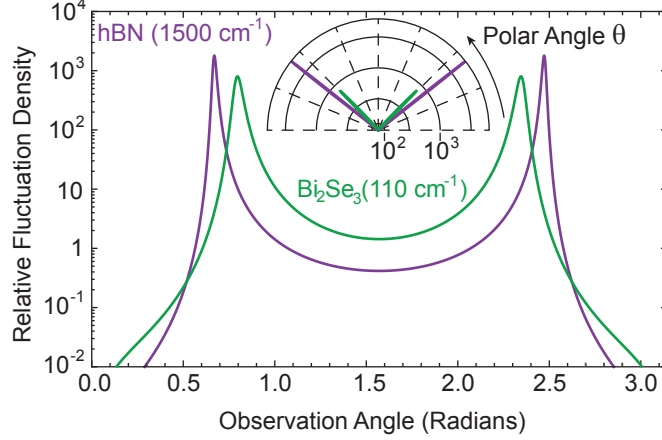


Figure 5.6: **Angular polaritonic fluctuation density in natural hyperbolic media.**

The figure depicts the polaritonic FD inside hexagonal boron nitride at 1500 cm^{-1} , and bismuth selenide at 110 cm^{-1} , as a function of polar angle on a logarithmic scale. The inset shows this same quantity as a polar plot on a linear scale. Although the integrated FDs of these two cases are nearly equal, Fig. 5.6, as hexagonal boron nitride more closely approaches the resonance condition $|\epsilon_U(\theta, \omega)| = 0$, but possess less polarization anisotropy, the angular distribution of its FD is much more radical. Both materials show angular regions where the relative polar FD is over 800 times larger than vacuum.

Using (5.2), (5.37), (5.38), and (5.6c), the energy density in the O and AP type modes of a uniaxial medium is then

$$\mathcal{U}(\mathbf{r}, \omega, T) = \frac{\mathcal{U}_{BB}(\omega, T)}{4} (\mathcal{F}_E(\omega) + \mathcal{F}_M(\omega)), \quad (5.50)$$

with

$$\mathcal{F}_E(\omega) = \text{Re} \left(\sqrt{\epsilon_P(\omega)} \right) + \int_0^{\pi/2} d\theta s(\theta) \text{Re} \left(\sqrt{\epsilon_E(\theta, \omega)} \right) \left(|\epsilon_H(\theta, \omega)|^2 + 1 \right) \quad (5.51)$$

and

$$\mathcal{F}_M(\omega) = |\epsilon_P(\omega)| \text{Re} \left\{ \sqrt{\epsilon_P(\omega)} \right\} + \int_0^{\pi/2} d\theta s(\theta) |\epsilon_E(\theta, \omega)| \text{Re} \left\{ \sqrt{\epsilon_E(\theta, \omega)} \right\} \quad (5.52)$$

denoting the relative electric and magnetic contributions.

The results of this expression for hexagonal boron nitride and bismuth selenide, normalized by $\mathcal{U}_{BB}(\omega, T)/2$ for direct comparison with the FD, are plotted in Fig. 5.5. Following this figure, note that:

(1) The solid green curves, denoting the contribution of AP type modes, confirm that in real media either a high degree of anisotropy $\epsilon_{\Delta}(\theta, \omega)$ or low material absorption $\epsilon_U(\theta, \omega)$ may lead to a large polaritonic FD. Bismuth selenide exhibits substantial material absorption, yet nevertheless a strong enhancement results from the extreme difference between the axial and planar permittivity components. Conversely, hexagonal boron nitride possess much less anisotropy, but lower material absorption leads to a similar FD.

(2) The energy density of the magnetic field is often substantially larger than that of the electric field, particularly near maxima of the polarization response. This observation corresponds to the fact that the magnetic field energy includes the polarization energy of the medium, (5.6d), while the electric field does not.

(3) (5.49) equates the green lines with the FD contributions of AP (bold line) and O (dashed line) type modes. As such, it should be expected that all related quantum phenomena will show this level of enhancement. Importantly, both hexagonal boron nitride and bismuth selenide show broad spectral regions where the FD is over 120 times larger than vacuum. (Contrasting with equations (5.43) and (5.44), this enhancement is equivalent to scaling the frequency ω found in relative rate of spontaneous emission by nearly a factor of 5.)

(4) Moving to Fig. 5.6, the FD is found to have extreme angular dispersion. As the value of $\epsilon_U(\theta, \omega)$ in a hyperbolic medium is highly dependent on the polar angle, θ , the FD from Fig. 5.5 is highly concentrated along the critical angles determined by $Re\{\epsilon_U(\theta, \omega)\} = 0$. Along this cone, the polaritonic FD is observed to be over 800 times larger than vacuum FD in both bismuth selenide and hexagonal boron nitride.

To conclude, it is interesting to compare the results plotted in Fig. 5.5 with the full near-field energy density of a hyperbolic medium [66, 165]. For this purpose, equation (16) of Guo et al. [165] is plotted in Fig. 5.7. Considering that for Fig. 5.5 the contributions of the C type and surface polariton modes are not included, the spectral features of the two figures are in excellent agreement for the smallest observation distances. The additional peaks seen in Fig. 5.7, as compared to Fig. 5.5 (B) and Fig. 5.5 (D), are strongly correlated with the surface polariton condition $Re\{\epsilon(k, \omega)\} = -1$. This observation indicates the consistency of our results with previous theory, and suggests that (5.37) and (5.38), likely play roles similar to the wave conditions inside an isotropic media. (Note that further support of this claim is seen in calculated heat transfer [278] and experimentally reported confinement

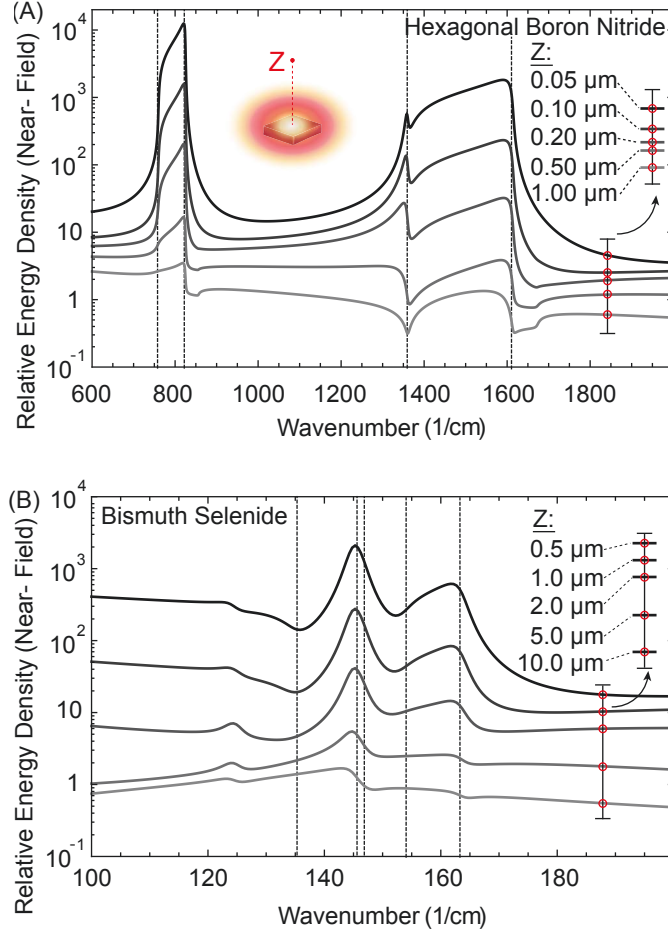


Figure 5.7: **Near-field electromagnetic energy density of natural hyperbolic media.**

The figure plots the sum of the near-field electric and magnetic energy densities above half-spaces of hexagonal boron nitride (A) and bismuth selenide (B) for increasing observation distances using equation (16) of Guo et al. [165]. (Neither hexagonal boron nitride or bismuth selenide is considered in this reference.) For comparison with the FD results this energy is normalized by half the energy density of vacuum. The inset in panel (A) shows a schematic representation. Recalling that surface mode contributions are not included in (5.48), the relative spectral characteristics of the near-field energy density are seen to be in excellent agreement with FDs plotted in Fig. 5.5 for small observation distances.

factors for hexagonal boron nitride resonators [245].)

5.7 Summary

In summary, we have shown that it is possible to analytically quantify the polaritonic FD in a hyperbolic (indefinite) medium using only material absorption. Through

this result, we have studied the quantum optical sum rule for modified spontaneous emission enhancement, and have found that it does not apply to the key polartionic features of a hyperbolic medium. We have also investigated thermal field fluctuations and the FD inside both hexagonal boron nitride and bismuth selenide. We have found that both media have broad spectral regions where these quantities are over 120 times (along specific angular directions 800 times) larger than they are in vacuum.

Chapter 6

Summary

In this final chapter, we summarize the thesis, discuss how our results may motivate future work, and provide a speculative outlook of the field.

In summary, this thesis has provided a collection of results for understanding and manipulating macroscopic thermal electromagnetic field correlations via connections to microscopic electronic and polarization characteristics ($\epsilon(\omega)$).

Our contributions began in Chapters Two and Three with our formulation of far-field thermal emission control from the perspective metamaterial design concepts. In the first of these chapters, we theoretically showed how the features of deeply sub wavelength(nano) structure are manifested in the effective medium parameters of a system, and analyzed how this concept can be used to selectively enhance and suppress thermal radiation in the near infrared to improve the performance of traditional thermophotovoltaic devices. In the second chapter, we experimentally confirmed these ideas by fabricating a refractory metamaterial and measuring its high temperature thermal properties. More specifically this work has provided:

- General design principles for controlling far-field thermal emission that can be applied to any micro or nanophotonic structure in the effective medium limit through the identification of epsilon-near-zero and epsilon-near-pole like response.
- Detailed analysis of the performance of metamaterial emitters for thermophotovoltaics, highlighting the possibility of surpassing the full concentration Shockley-Queossier limit at modest emitter temperatures ($\approx 1500 K$)
- Introduction of thermally stable (lossy, low figure of merit) metals supporting high temperature plasmons for metamaterial device applications. (Previous work had not considered metamaterial applications above $600 K$, and hence

was focused entirely on high figure of merit metals, primarily gold and silver.)

- Experimental confirmation of the thermal stability of effective topological transitions in refractory metamaterials (up to 1000 °C).

Chapter 4 then shifted to the near-field, where we examined the role played by polarization in defining the characteristics of an ideal near-field photovoltaic cells. Here, we depicted how the electronic band structure of a bulk three dimensional semiconductor leads to optical properties that are in direct conflict with those required to maximize the magnitude and efficiency of thermal energy transfer in the very near-field. In contrast, we also unveiled that this issue can be substantially mitigated by the introduction of photovoltaic cells with van Hove singularities (low dimensional semiconductors). The role that the photovoltaic cells could play in improving the performance of near-field thermophotovoltaics had been previously disregarded, and in completing this analysis we have contributed two key results for driving further progress in this area:

- Expression of extremely near-field photonic heat transfer in terms of the joint density of electronic states (a direct connection between thermal electromagnetic correlations and electronic band structure).
- Outline of realistic program for improving near-field thermophotovoltaics; the switch from bulk to low dimensional semiconductors.

Finally, Chapter 5 examined the physical underpinnings of thermal fluctuations in hyperbolic media, and the relation of these fluctuations to the anisotropic permittivity tensor. In this chapter, we revealed that the divergent behavior observed in previous calculations of thermal electromagnetic field correlations in hyperbolic media stems from the excitation of formerly unrecognized charge density resonances. This result allowed us to create a regularized mathematical framework for calculating the electromagnetic enhancement properties of these media without requiring specific knowledge of second order effects, like spatial non-locality in the polarization response of the medium. Importantly, the resulting expressions are the first definitive bounds on electromagnetic enhancement phenomena in hyperbolic media, and have immediately resolved longstanding questions about quantum optical sum rules in these media. The central contributions of these results can be summarized as follows:

- Regularized (non-divergent) characterization of the thermal field fluctuations that occur inside hyperbolic media where material absorption sets the fundamental limit of enhancement.

- Mathematically rigorous physical description of the link between the polariton excitations that occur in hyperbolic media, and the characteristic near-field optical and thermal properties that they exhibit.
- Analysis of quantum optical sum rules showing non-trivial agreement.
- Experimentally verifiable predictions of the electromagnetic fluctuation enhancement in hexagonal boron nitride and bismuth selenide. (Both materials have broad spectral regions where the integrated density of electromagnetic/polaritonic fluctuations is over 120 times larger than vacuum.)

6.1 Outlook

At the outset of this dissertation, we described thermal electromagnetic field correlations as a theoretically mature field. After all, the resolution of current and electric field correlations in terms of linear response functions given by Landau [279], Lifschitz [280], and Rytov [281,282] is now over sixty years old; and while understanding and computational methods have progressed considerably since, nothing about these initial results has ever required a major reformulation. However, on closer inspection this description is not entirely accurate, and there are sound reasons to believe that we may be on the verge of such a first principles reworking.

The foundation of this view rests on the role that statistical spatial independence plays in the current framework. Namely, it is assumed that the random currents at any two distinct points in space are uncorrelated. This assumption is logical when considering macroscopically sized bodies in thermal equilibrium. In this case, the exchange of heat energy between any two points is mediated by an intractably large number of bulk phonon and radiative excitations, with no average flow; and once excited, the heat flux resulting from a given current fluctuation is thought to dephase immediately.

However, in the near-field it is not at all clear how well this idea holds [283]. Crucially, it is well known that radiative heat exchange may be dominated by small collection of excitations [284]. If media at different temperatures exchange heat energy in such a way, then it seems highly likely that fluctuating currents near the two surface will not be independent. Although not explicitly stated, a very similar idea is behind recent proposals for super-radiant thermal emitter assembly [285,286]. In order for super-radiant scaling to occur, current fluctuations in distinct emitters must be correlated.

It is important to note that such possibilities have not been experimentally ruled out. Total heat transfer is known to be in good agreement with the Rytovian theory. However, no experiment has yet to determine if the predicted spectra match equally well. Experimental tests of thermal super-radiance should provide strong evidence either for or against major reformulation. Given that thermal electromagnetic field correlations have been shown to possess nearly all other types of coherence, and were initially thought not to, it would perhaps be more surprising if this idea of correlated current fluctuations turns out to be false.

Bibliography

- [1] E. Yablonovitch, “Inhibited spontaneous emission in solid state physics and electronics,” *Phys. Rev. Lett.*, vol. 58, no. 8, p. 2059, 1987.
- [2] S. John, “Strong localization of photons in certain disordered dielectric superlattices,” *Phys. Rev. Lett.*, vol. 58, no. 23, p. 2486, 1987.
- [3] E. M. Purcell, “modification of spontaneous emission,” vol. 69, p. 681.
- [4] P. W. Milonni and P. Knight, “Spontaneous emission between mirrors,” *Opt. Commun.*, vol. 9, no. 2, pp. 119–122, 1973.
- [5] V. P. Bykov, “Spontaneous emission from a medium with a band spectrum,” *Sov. J. Quan. Electron.*, vol. 4, no. 7, p. 861, 1975.
- [6] C. Cohen-Tannoudji and S. Reynaud, “Modification of resonance raman scattering in very intense laser fields,” *J. Phys. B*, vol. 10, no. 3, p. 365, 1977.
- [7] D. Kleppner, “Inhibited spontaneous emission,” *Phys. Rev. Lett.*, vol. 47, no. 4, p. 233, 1981.
- [8] R. G. Hulet, E. S. Hilfer, and D. Kleppner, “Inhibited spontaneous emission by a rydberg atom,” *Phys. Rev. Lett.*, vol. 55, no. 20, p. 2137, 1985.
- [9] P. Goy, J. Raimond, M. Gross, and S. Haroche, “Observation of cavity-enhanced single-atom spontaneous emission,” *Phys. Rev. Lett.*, vol. 50, no. 24, p. 1903, 1983.
- [10] G. Agarwal, “Quantum electrodynamics in the presence of dielectrics and conductors. i. electromagnetic-field response functions and black-body fluctuations in finite geometries,” *Phys. Rev. A*, vol. 11, no. 1, p. 230, 1975.
- [11] R. P. Feynman, “There’s plenty of room at the bottom,” *Engineering and science*, vol. 23, no. 5, pp. 22–36, 1960.
- [12] J. B. Pendry, “Radiative exchange of heat between nanostructures,” *J. Phys.: Condens. Matter*, vol. 6621, 1999.

- [13] D. Polder and M. Van Hove, “Theory of radiative heat transfer between closely spaced bodies,” *Phys. Rev. B*, vol. 4, no. 10, pp. 3303–3314, 1971.
- [14] J. J. Loomis and H. J. Maris, “Theory of heat transfer by evanescent electromagnetic waves,” *Phys. Rev. B*, vol. 50, no. 24, p. 18517, 1994.
- [15] A. Volokitin and B. Persson, “Radiative heat transfer between nanostructures,” *Phys. Rev. B*, vol. 63, no. 20, p. 205404, 2001.
- [16] J. Le Gall, M. Olivier, and J.-J. Greffet, “Experimental and theoretical study of reflection and coherent thermal emission by a sic grating supporting a surface-phonon polariton,” *Phys. Rev. B*, vol. 55, no. 15, p. 10105, 1997.
- [17] R. Carminati and J. Greffet, “Near-field effects in spatial coherence of thermal sources,” *Phys. Rev. Lett.*, vol. 82, pp. 1660–1663, Feb. 1999.
- [18] A. V. Shchegrov, K. Joulain, R. Carminati, and J.-J. Greffet, “Near-field spectral effects due to electromagnetic surface excitations,” *Phys. Rev. Lett.*, vol. 85, no. 7, p. 1548, 2000.
- [19] A. Sentenac and J.-J. Greffet, “Design of surface microrelief with selective radiative properties,” *Int. J. Heat Mass Trans.*, vol. 37, no. 4, pp. 553–558, 1994.
- [20] V. M. Agranovich and D. L. Mills, *Surface Polaritons*, vol. 1. North-Holland, Amsterdam, 1982.
- [21] G. W. Ford and W. H. Weber, “Electromagnetic interactions of molecules with metal surfaces,” *Phys. Rep.*, vol. 113, no. 4, pp. 195–287, 1984.
- [22] K. Ho, C. T. Chan, and C. M. Soukoulis, “Existence of a photonic gap in periodic dielectric structures,” *Phys. Rev. Lett.*, vol. 65, no. 25, p. 3152, 1990.
- [23] J. D. Joannopoulos, P. R. Villeneuve, and S. Fan, “Photonic crystals: putting a new twist on light,” *Nat.*, vol. 386, no. 6621, p. 143, 1997.
- [24] C. M. Cornelius and J. P. Dowling, “Modification of planck blackbody radiation by photonic band-gap structures,” *Phys. Rev. A*, vol. 59, no. 6, p. 4736, 1999.
- [25] S.-Y. Lin, J. Fleming, E. Chow, J. Bur, K. Choi, and A. Goldberg, “Enhancement and suppression of thermal emission by a three-dimensional photonic crystal,” *Phys. Rev. B*, vol. 62, no. 4, p. R2243, 2000.
- [26] Z. Li, “Modified thermal radiation in three-dimensional photonic crystals,” *Phys. Rev. B*, vol. 66, pp. 1–4, Dec. 2002.

- [27] C. Luo, A. Narayanaswamy, G. Chen, and J. Joannopoulos, “Thermal radiation from photonic crystals: a direct calculation,” *Phys. Rev. Lett.*, vol. 93, no. 21, p. 213905, 2004.
- [28] T. Trupke, P. Würfel, and M. A. Green, “Comment on three-dimensional photonic-crystal emitter for thermal photovoltaic power generation [appl. phys. lett. 83, 380 (2003)],” *Appl. Phys. Lett.*, vol. 84, no. 11, pp. 1997–1998, 2004.
- [29] J. Fleming, “Addendum : Three-dimensional photonic-crystal emitter for thermal photovoltaic power generation [appl. phys. lett. 83, 380 (2003)],” *Appl. Phys. Lett.*, vol. 86, no. 24, p. 249902, 2005.
- [30] A. Heinzl, V. Boerner, A. Gombert, B. Bläsi, V. Wittwer, and J. Luther, “Radiation filters and emitters for the nir based on periodically structured metal surfaces,” *J. Mod. Opt.*, vol. 47, no. 13, pp. 2399–2419, 2000.
- [31] M. Pralle, N. Moelders, M. McNeal, I. Puscasu, A. Greenwald, J. Daly, E. Johnson, T. George, D. Choi, I. El-Kady, and R. Biswas, “Photonic crystal enhanced narrow-band infrared emitters,” *Appl. Phys. Lett.*, vol. 81, no. 25, pp. 4685–4687, 2002.
- [32] R. S. DiMatteo, P. Greiff, S. L. Finberg, K. a. Young-Waithe, H. K. H. Choy, M. M. Masaki, and C. G. Fonstad, “Enhanced photogeneration of carriers in a semiconductor via coupling across a nonisothermal nanoscale vacuum gap,” *Appl. Phys. Lett.*, vol. 79, no. 12, p. 1894, 2001.
- [33] S. Lin, J. Moreno, and J. Fleming, “Three-dimensional photonic-crystal emitter for thermal photovoltaic power generation,” *Appl. Phys. Lett.*, vol. 83, no. 2, pp. 380–384, 2003.
- [34] A. Narayanaswamy and G. Chen, “Surface modes for near field thermophotovoltaics,” *Appl. Phys. Lett.*, vol. 82, no. 20, p. 3544, 2003.
- [35] I. Celanovic, F. O’Sullivan, M. Ilak, J. Kassakian, and D. Perreault, “Design and optimization of one-dimensional photonic crystals for thermophotovoltaic applications,” *Opt. Lett.*, vol. 29, pp. 863–865, Apr. 2004.
- [36] J.-J. Greffet, R. Carminati, K. Joulain, J.-P. Mulet, S. Mainguy, and Y. Chen, “Coherent emission of light by thermal sources,” *Nat.*, vol. 416, pp. 61–64, Mar. 2002.
- [37] B. Lee, C. Fu, and Z. Zhang, “Coherent thermal emission from one-dimensional photonic crystals,” *Appl. Phys. Lett.*, vol. 87, no. 7, p. 071904, 2005.

- [38] Y. De Wilde, F. Formanek, R. Carminati, B. Gralak, P.-A. Lemoine, K. Joulain, J.-P. Mulet, Y. Chen, and J.-J. Greffet, “Thermal radiation scanning tunnelling microscopy,” *Nat.*, vol. 444, no. 7120, pp. 740–743, 2006.
- [39] L. Hu, A. Narayanaswamy, X. Chen, and G. Chen, “Near-field thermal radiation between two closely spaced glass plates exceeding Planck’s blackbody radiation law,” *Appl. Phys. Lett.*, vol. 92, no. 13, pp. 19–22, 2008.
- [40] A. Kittel, W. Müller-Hirsch, J. Parisi, S.-A. Biehs, D. Reddig, and M. Holthaus, “Near-field heat transfer in a scanning thermal microscope,” *Phys. Rev. Lett.*, vol. 95, no. 22, p. 224301, 2005.
- [41] J.-B. Xu, K. Lauger, R. Moller, K. Dransfeld, and I. Wilson, “Heat transfer between two metallic surfaces at small distances,” *J. Appl. Phys.*, vol. 76, no. 11, pp. 7209–7216, 1994.
- [42] V. Rinnerbauer, Y. X. Yeng, W. R. Chan, J. J. Senkevich, J. D. Joannopoulos, M. Soljačić, and I. Celanovic, “High-temperature stability and selective thermal emission of polycrystalline tantalum photonic crystals,” *Opt. Express*, vol. 21, no. 9, pp. 11482–11491, 2013.
- [43] Y. Nam, Y. X. Yeng, A. Lenert, P. Bermel, I. Celanovic, M. Soljačić, and E. N. Wang, “Solar thermophotovoltaic energy conversion systems with two-dimensional tantalum photonic crystal absorbers and emitters,” *Sol. Energy Mater. Sol. Cells*, vol. 122, pp. 287–296, Mar. 2014.
- [44] S. Han and D. Norris, “Beaming thermal emission from hot metallic bulls eyes,” *Opt. Express*, vol. 18, no. 5, pp. 4829–4837, 2010.
- [45] A. V. Kildishev, A. Boltasseva, and V. M. Shalaev, “Planar photonics with metasurfaces,” *Sci.*, vol. 339, no. 6125, p. 1232009, 2013.
- [46] C. Argyropoulos, K. Q. Le, N. Mattiucci, G. D’Aguanno, and A. Alu, “Broadband absorbers and selective emitters based on plasmonic brewster metasurfaces,” *Phys. Rev. B*, vol. 87, no. 20, p. 205112, 2013.
- [47] W. Padilla, “Blackbody Engineering with Metamaterials,” in *Infrared, Millimeter, and Terahertz Waves, 2009. IRMMW-THz 2009. 34th International Conference on*, vol. 78, p. 241103, 2008.
- [48] J. Mason, S. Smith, and D. Wasserman, “Strong absorption and selective thermal emission from a midinfrared metamaterial,” *Appl. Phys. Lett.*, vol. 98, no. 24, p. 241105, 2011.

- [49] X. Liu, T. Tyler, T. Starr, A. Starr, N. Jokerst, and W. Padilla, “Taming the Blackbody with Infrared Metamaterials as Selective Thermal Emitters,” *Phys. Rev. Lett.*, vol. 107, pp. 4–7, July 2011.
- [50] M. Florescu, H. Lee, A. J. Stimpson, and J. Dowling, “Thermal emission and absorption of radiation in finite inverted-opal photonic crystals,” *Phys. Rev. A*, vol. 72, no. 3, p. 033821, 2005.
- [51] S. E. Han, A. Stein, and D. Norris, “Tailoring self-assembled metallic photonic crystals for modified thermal emission,” *Phys. Rev. Lett.*, vol. 99, no. 5, p. 053906, 2007.
- [52] I. Celanovic, D. Perreault, and J. Kassakian, “Resonant-cavity enhanced thermal emission,” *Phys. Rev. B*, vol. 72, no. 7, p. 075127, 2005.
- [53] P. Ben-Abdallah and B. Ni, “Single-defect bragg stacks for high-power narrow-band thermal emission,” *J. Appl. Phys.*, vol. 97, no. 10, p. 104910, 2005.
- [54] M. Diem, T. Koschny, and C. M. Soukoulis, “Wide-angle perfect absorber/thermal emitter in the terahertz regime,” *Phys. Rev. B*, vol. 79, no. 3, p. 033101, 2009.
- [55] J. A. Schuller, T. Taubner, and M. L. Brongersma, “Optical antenna thermal emitters,” *Nat. Photon.*, vol. 3, no. 11, pp. 658–661, 2009.
- [56] K. A. Arpin, M. D. Losego, A. N. Cloud, H. Ning, J. Mallek, N. P. Sergeant, L. Zhu, Z. Yu, B. Kalanyan, G. N. Parsons, G. S. Girolami, J. R. Abelson, S. Fan, and P. V. Braun, “Three-dimensional self-assembled photonic crystals with high temperature stability for thermal emission modification,” *Nat. Commun.*, vol. 4, 2013.
- [57] A. Narayanaswamy, S. Shen, and G. Chen, “Near-field radiative heat transfer between a sphere and a substrate,” *Phys. Rev. B*, vol. 78, no. 11, p. 115303, 2008.
- [58] E. Rousseau, A. Siria, G. Jourdan, S. Volz, F. Comin, J. Chevrier, and J.-J. Greffet, “Radiative heat transfer at the nanoscale,” *Nat. Photon.*, vol. 3, no. 9, pp. 514–517, 2009.
- [59] R. Ottens, V. Quetschke, S. Wise, A. Alemi, R. Lundock, G. Mueller, D. H. Reitze, D. B. Tanner, and B. F. Whiting, “Near-field radiative heat transfer between macroscopic planar surfaces,” *Phys. Rev. Lett.*, vol. 107, no. 1, p. 014301, 2011.

- [60] A. C. Jones and M. B. Raschke, “Thermal infrared near-field spectroscopy,” *Nano Lett.*, vol. 12, no. 3, pp. 1475–1481, 2012.
- [61] T. Kralik, P. Hanzelka, M. Zobac, V. Musilova, T. Fort, and M. Horak, “Strong near-field enhancement of radiative heat transfer between metallic surfaces,” *Phys. Rev. Lett.*, vol. 109, no. 22, p. 224302, 2012.
- [62] K. Kim, B. Song, V. Fernández-Hurtado, W. Lee, W. Jeong, L. Cui, D. Thompson, J. Feist, M. H. Reid, F. J. García-Vidal, *et al.*, “Radiative heat transfer in the extreme near field,” *Nat.*, 2015.
- [63] R. St-Gelais, L. Zhu, S. Fan, and M. Lipson, “Near-field radiative heat transfer between parallel structures in the deep subwavelength regime,” *Nat. Nanotech.*, 2016.
- [64] B. Song, Y. Ganjeh, S. Sadat, D. Thompson, A. Fiorino, V. Fernández-Hurtado, J. Feist, F. J. Garcia-Vidal, J. C. Cuevas, P. Reddy, *et al.*, “Enhancement of near-field radiative heat transfer using polar dielectric thin films,” *Nat. Nanotechnol.*, vol. 10, no. 3, pp. 253–258, 2015.
- [65] K. Kloppstech, N. Können, S.-A. Biehs, A. W. Rodriguez, L. Worbes, D. Hellmann, and A. Kittel, “Giant heat transfer in the crossover regime between conduction and radiation,” *Nat. Commun.*, vol. 8, 2017.
- [66] Y. Guo, C. L. Cortes, S. Molesky, and Z. Jacob, “Broadband super-Planckian thermal emission from hyperbolic metamaterials,” *Appl. Phys. Lett.*, vol. 101, no. 13, p. 131106, 2012.
- [67] A. Volokitin and B. Persson, “Near-field radiative heat transfer between closely spaced graphene and amorphous sio 2,” *Phys. Rev. B*, vol. 83, no. 24, p. 241407, 2011.
- [68] K. Shi, F. Bao, and S. He, “Enhanced near-field thermal radiation based on multilayer graphene-hbn heterostructures,” *ACS Photon.*, 2017.
- [69] P. Ben-Abdallah, K. Joulain, J. Drevillon, and G. Domingues, “Near-field heat transfer mediated by surface wave hybridization between two films,” *J. Appl. Phys.*, vol. 106, no. 4, p. 044306, 2009.
- [70] R. Messina and M. Antezza, “Three-body radiative heat transfer and casimir-lifshitz force out of thermal equilibrium for arbitrary bodies,” *Phys. Rev. A*, vol. 89, no. 5, p. 052104, 2014.
- [71] P. Ben-Abdallah and S.-A. Biehs, “Near-field thermal transistor,” *Phys. Rev. Lett.*, vol. 112, no. 4, p. 044301, 2014.

- [72] M. Krüger, T. Emig, and M. Kardar, “Nonequilibrium electromagnetic fluctuations: Heat transfer and interactions,” *Physical Review Letters*, vol. 106, no. 21, p. 210404, 2011.
- [73] R. Messina and M. Antezza, “Scattering-matrix approach to casimir-lifshitz force and heat transfer out of thermal equilibrium between arbitrary bodies,” *Phys. Rev. A*, vol. 84, no. 4, p. 042102, 2011.
- [74] M. Krüger, G. Bimonte, T. Emig, and M. Kardar, “Trace formulas for nonequilibrium casimir interactions, heat radiation, and heat transfer for arbitrary objects,” *Phys. Rev. B*, vol. 86, no. 11, p. 115423, 2012.
- [75] O. D. Miller, S. G. Johnson, and A. W. Rodriguez, “Shape-independent limits to near-field radiative heat transfer,” *Phys. Rev. Lett.*, vol. 115, no. 20, p. 204302, 2015.
- [76] V. Chiloyan, J. Garg, K. Esfarjani, and G. Chen, “Transition from near-field thermal radiation to phonon heat conduction at sub-nanometre gaps,” *Nat. Commun.*, vol. 6, 2015.
- [77] D. A. Miller, L. Zhu, and S. Fan, “Universal modal radiation laws for all thermal emitters,” *Proc. Nat. Acad. Sci.*, p. 201701606, 2017.
- [78] P.-O. Chapuis, S. Volz, C. Henkel, K. Joulain, and J.-J. Greffet, “Effects of spatial dispersion in near-field radiative heat transfer between two parallel metallic surfaces,” *Physical Review B*, vol. 77, no. 3, p. 035431, 2008.
- [79] F. Singer, Y. Ezzahri, and K. Joulain, “Nonlocal study of the near field radiative heat transfer between two n-doped semiconductors,” *Int. J. Heat Mass Transfer*, vol. 90, pp. 34–39, 2015.
- [80] A. W. Rodriguez, M. H. Reid, and S. G. Johnson, “Fluctuating-surface-current formulation of radiative heat transfer for arbitrary geometries,” *Phys. Rev. B*, vol. 86, no. 22, p. 220302, 2012.
- [81] A. W. Rodriguez, M. H. Reid, and S. G. Johnson, “Fluctuating-surface-current formulation of radiative heat transfer: Theory and applications,” *Phys. Rev. B*, vol. 88, no. 5, p. 054305, 2013.
- [82] B. Liu and S. Shen, “Broadband near-field radiative thermal emitter/absorber based on hyperbolic metamaterials: Direct numerical simulation by the wiener chaos expansion method,” *Physical Review B*, vol. 87, no. 11, p. 115403, 2013.
- [83] C. R. Otey, L. Zhu, S. Sandhu, and S. Fan, “Fluctuational electrodynamics calculations of near-field heat transfer in non-planar geometries: A brief overview,” *J. Quant. Spec. Rad. Trans.*, vol. 132, pp. 3–11, 2014.

- [84] O. D. Miller, “Photonic design: From fundamental solar cell physics to computational inverse design,” *arXiv:1308.0212*, 2013.
- [85] A. Yuksel, A. Heltzel, and J. R. Howell, “Design and optimization of thermal selective emitters for high-efficiency thermophotovoltaic (tpv) power generation,” in *ASME 2015 9th International Conference on Energy Sustainability*, pp. V001T10A003–V001T10A003, American Society of Mechanical Engineers, 2015.
- [86] W. Jin, R. Messina, and A. W. Rodriguez, “Overcoming limits to near-field radiative heat transfer in uniform planar media through multilayer optimization,” *arXiv:1702.02057*, 2017.
- [87] A. Narayanaswamy and Y. Zheng, “Theory of thermal nonequilibrium entropy in near-field thermal radiation,” *Phys. Rev. B*, vol. 88, no. 7, p. 075412, 2013.
- [88] G. Gruner and M. Dressel, *Electrodynamics of Solids: Optical Properties of Electrons in Matter*. Cambridge University Press: Cambridge, UK, 2012.
- [89] F. Wooten, *Optical properties of solids*. Academic press, 2013.
- [90] P. Taylor, O. Lavanagne d’Ortigue, N. Trudeau, and M. Francoeur, “Energy efficiency indicators for public electricity production from fossil fuels,” tech. rep., International Energy Agency, 2008.
- [91] A. L. Fetter and J. D. Walecka, *Quantum theory of many-particle systems*. Courier Corporation, 2012.
- [92] W. Eckhardt, “First and second fluctuation-dissipation-theorem in electromagnetic fluctuation theory,” *Opt. Commun.*, vol. 41, no. 5, pp. 305–309, 1982.
- [93] R. Messina, W. Jin, and A. W. Rodriguez, “Strongly coupled near-field radiative and conductive heat transfer between planar bodies,” *Phys. Rev. B*, vol. 94, no. 12, p. 121410, 2016.
- [94] M. Leontovich and S. Rytov, “On the theory of electric fluctuations,” in *Dokl. Acad. Nauk SSSR*, vol. 87, p. 535, 1952.
- [95] J.-J. Greffet, R. Carminati, K. Joulain, J.-P. Mulet, S. Mainguy, and Y. Chen, “Coherent emission of light by thermal sources,” *Nat.*, vol. 416, no. 6876, pp. 61–64, 2002.
- [96] K. Joulain, J.-P. Mulet, F. Marquier, R. Carminati, and J.-J. Greffet, “Surface electromagnetic waves thermally excited: Radiative heat transfer, coherence

- properties and Casimir forces revisited in the near field,” *Surf. Sci. Rep.*, vol. 57, pp. 59–112, may 2005.
- [97] S. Maruyama, T. Kashiwa, H. Yugami, and M. Esashi, “Thermal radiation from two-dimensionally confined modes in microcavities,” *Appl. Phys. Lett.*, vol. 79, no. 9, pp. 1393–1395, 2001.
- [98] L. Wang, B. Lee, X. Wang, and Z. Zhang, “Spatial and temporal coherence of thermal radiation in asymmetric fabry–perot resonance cavities,” *Int. J. Heat Mass Trans.*, vol. 52, no. 13, pp. 3024–3031, 2009.
- [99] A. Narayanaswamy and G. Chen, “Thermal emission control with one-dimensional metallodielectric photonic crystals,” *Phys. Rev. B*, vol. 70, no. 12, p. 125101, 2004.
- [100] I. Celanovic, N. Jovanovic, and J. Kassakian, “Two-dimensional tungsten photonic crystals as selective thermal emitters,” *Appl. Phys. Lett.*, vol. 92, no. 19, p. 193101, 2008.
- [101] B. Lee, L. Wang, and Z. Zhang, “Coherent thermal emission by excitation of magnetic polaritons between periodic strips and a metallic film,” *Opt. Express*, vol. 16, no. 15, pp. 11328–11336, 2008.
- [102] D. Costantini, A. Lefebvre, A.-L. Coutrot, I. Moldovan-Doyen, J.-P. Hugonin, S. Boutami, F. Marquier, H. Benisty, and J.-J. Greffet, “Plasmonic metasurface for directional and frequency-selective thermal emission,” *Phys. Rev. Appl.*, vol. 4, no. 1, p. 014023, 2015.
- [103] U. Buskies, “The efficiency of coal-fired combined-cycle powerplants,” *Appl. Therm. Eng.*, vol. 16, no. 12, pp. 959–974, 1996.
- [104] M. Rosen and I. Dincer, “Exergoeconomic analysis of power plants operating on various fuels,” *Appl. Therm. Eng.*, vol. 23, pp. 643–658, Apr. 2003.
- [105] E. J. Chaisson, “Long-term global heating from energy usage,” *EOS Trans. Am. Geo. Union*, vol. 89, no. 28, pp. 253–254, 2008.
- [106] A. Datas and C. Algora, “Detailed balance analysis of solar thermophotovoltaic systems made up of single junction photovoltaic cells and broadband thermal emitters,” *Sol. Energy Mater. Sol. Cells*, vol. 94, no. 12, pp. 2137–2147, 2010.
- [107] W. Shockley and H. J. Queisser, “Detailed balance limit of efficiency of p-n junction solar cells,” *J. Appl. Phys.*, vol. 32, no. 3, pp. 510–519, 1961.

- [108] B. D. Wedlockt, “Thermo-Photo-Voltaic Energy Conversion *,” *Proc. IEEE*, vol. 51, no. 5, pp. 694–698, 1963.
- [109] “www.jxcryystals.com, www.mtpv.com,” 2012.
- [110] J. Gee, J. Moreno, S. Lin, and J. Fleming, “Selective emitters using photonic crystals for thermophotovoltaic energy conversion,” in *Photovoltaic specialists, 2002. Conf. Proc. 29th IEEE*, pp. 896–899, 2002.
- [111] J. Mason, S. Smith, and D. Wasserman, “Strong absorption and selective thermal emission from a midinfrared metamaterial,” *Appl. Phys. Lett.*, vol. 98, no. 24, p. 241105, 2011.
- [112] C. Wu, B. Neuner III, J. John, A. Milder, B. Zollars, S. Savoy, and G. Shvets, “Metamaterial-based integrated plasmonic absorber/emitter for solar thermophotovoltaic systems,” *J. Opt.*, vol. 14, p. 024005, Feb. 2012.
- [113] M. Maksimovic, M. Hammer, and Z. Jaksic, “Thermal radiation antennas made of multilayer structures containing negative index metamaterials,” *Proc. of SPIE*, vol. 6896, pp. 689605–689605–11, 2008.
- [114] P. Bermel, M. Ghebrebrihan, M. Harradon, Y. X. Yeng, I. Celanovic, J. D. Joannopoulos, and M. Soljačić, “Tailoring photonic metamaterial resonances for thermal radiation.,” *Nanoscale Res. Lett.*, vol. 6, p. 549, Jan. 2011.
- [115] Y. Chen and Z. Zhang, “Design of tungsten complex gratings for thermophotovoltaic radiators,” *Opt. Commun.*, vol. 269, pp. 411–417, Jan. 2007.
- [116] E. Nefzaoui, J. Drevillon, and K. Joulain, “Selective emitters design and optimization for thermophotovoltaic applications,” *J. Appl. Phys.*, vol. 111, no. 8, p. 084316, 2012.
- [117] P. Chang, Y. Jiang, H. Chen, Y. Chang, Y. Wu, L. Tzuang, Y. Ye, and S. Lee, “Wavelength selective plasmonic thermal emitter by polarization utilizing Fabry Perot type resonances,” *Appl. Phys. Lett.*, vol. 98, no. 7, p. 073111, 2011.
- [118] E. Rephaeli and S. Fan, “Absorber and emitter for solar thermo-photovoltaic systems to achieve efficiency exceeding the shockley-queisser limit,” *Opt. Express*, vol. 17, no. 17, pp. 15145–15159, 2009.
- [119] C. Schuler, C. Wolff, K. Busch, and M. Florescu, “Thermal emission from finite photonic crystals,” *Appl. Phys. Lett.*, vol. 95, no. 24, p. 241103, 2009.

- [120] J. Greffet and M. Nieto-Vesperinas, “Field theory for generalized bidirectional reflectivity: derivation of Helmholtz reciprocity principle and Kirchhoff’s law,” *JOSA A*, vol. 15, no. 10, p. 2735, 1998.
- [121] G. Wurtz, R. Pollard, W. Hendren, G. Wiederrecht, D. Gosztola, V. Podolskiy, and A. Zayats, “Designed ultrafast optical nonlinearity in a plasmonic nanorod metamaterial enhanced by nonlocality,” *Nat. Nanotechnol.*, vol. 6, pp. 107–11, Feb. 2011.
- [122] A. Alù, M. G. Silveirinha, A. Salandrino, and N. Engheta, “Epsilon-near-zero metamaterials and electromagnetic sources: Tailoring the radiation phase pattern,” *Phys. Rev. B*, vol. 75, no. 15, p. 155410, 2007.
- [123] N. Ashcroft and N. Mermin, *Solid state physics*. Brooks Cole, 1968.
- [124] J. Yao, Z. Liu, Y. L., Y. W., C. Sun, G. Bartal, A. Stacy, and X. Zhang, “Optical negative refraction in bulk metamaterials of nanowires,” *Sci.*, vol. 321, p. 930, Aug. 2008.
- [125] B. Lim, A. Rahtu, and R. G. Gordon, “Atomic layer deposition of transition metals,” *Nat. Mater.*, vol. 2, pp. 749–754, Nov. 2003.
- [126] R. J. Pollard, A. Murphy, W. R. Hendren, P. R. Evans, R. Atkinson, G. A. Wurtz, A. V. Zayats, and V. A. Podolskiy, “Optical nonlocalities and additional waves in epsilon-near-zero metamaterials,” *Phys. Rev. Lett.*, vol. 102, no. 12, p. 127405, 2009.
- [127] J. Elser, R. Wangberg, V. Podolskiy, and E. Narimanov, “Nanowire metamaterials with extreme optical anisotropy,” *Appl. Phys. Lett.*, vol. 89, no. 26, p. 261102, 2006.
- [128] G. D’Aguanno, N. Mattiucci, A. Alù, C. Argyropoulos, J. Foreman, and M. Bloemer, “Thermal emission from a metamaterial wire medium slab,” *Opt. Express*, vol. 20, pp. 9784–9789, Apr. 2012.
- [129] L. Alekseyev, E. Narimanov, T. Tumkur, H. Li, Y. Barnakov, and M. Noginov, “Uniaxial epsilon-near-zero metamaterial for angular filtering and polarization control,” *Appl. Phys. Lett.*, vol. 97, no. 13, p. 131107, 2010.
- [130] P. Johnson and R. Christy, “Optical constants of the noble metals,” *Phys. Rev. B*, vol. 1318, no. 1970, pp. 4370–4379, 1972.
- [131] K. Kim, K. Park, and D. Ma, “Structural, electrical and optical properties of aluminum doped zinc oxide films prepared by radio frequency magnetron sputtering,” *J. Appl. Phys.*, vol. 81, no. 12, pp. 7764–7772, 1997.

- [132] G. Naik and A. Boltasseva, “Semiconductors for plasmonics and metamaterials,” *Phys. Status Solidi RRL*, vol. 4, no. 10, pp. 295–297, 2010.
- [133] H. Pierson, *Handbook of refractory carbides and nitrides*. William Andrew, 1996.
- [134] G. Naik, J. Kim, and A. Boltasseva, “Oxides and nitrides as alternative plasmonic materials in the optical range,” *Opt. Mater. Express*, vol. 1, pp. 1090–1099, Mar. 2011.
- [135] Q. Zhang, “Recent progress in high-temperature solar selective coatings,” *Sol. Energy Mater. Sol. Cells*, vol. 62, no. 2000, pp. 63–74, 2000.
- [136] J. Khurgin and A. Boltasseva, “Reflecting upon the losses in plasmonics and metamaterials,” *MRS Bull.*, vol. 37, pp. 768–779, Aug. 2012.
- [137] C. Cortes, W. Newman, S. Molesky, and Z. Jacob, “Quantum nanophotonics using hyperbolic metamaterials,” *J. Opt.*, vol. 14, no. 6, p. 063001, 2012.
- [138] H. N. Krishnamoorthy, Z. Jacob, E. Narimanov, I. Kretzschmar, and V. M. Menon, “Topological transitions in metamaterials,” *Sci.*, vol. 336, no. 6078, pp. 205–209, 2012.
- [139] A. M. Mahmoud and N. Engheta, “Wave–matter interactions in epsilon-and-mu-near-zero structures,” *Nat. Commun.*, vol. 5, 2014.
- [140] A. Poddubny, I. Iorsh, P. Belov, and Y. Kivshar, “Hyperbolic metamaterials,” *Nat. Photonics*, vol. 7, no. 12, pp. 948–957, 2013.
- [141] D. L. Chan, M. Soljačić, and J. Joannopoulos, “Thermal emission and design in 2d-periodic metallic photonic crystal slabs,” *Opt. Express*, vol. 14, no. 19, pp. 8785–8796, 2006.
- [142] P. Nagpal, S. E. Han, A. Stein, and D. J. Norris, “Efficient low-temperature thermophotovoltaic emitters from metallic photonic crystals,” *Nano Lett.*, vol. 8, no. 10, pp. 3238–3243, 2008.
- [143] Y. X. Yeng, M. Ghebregbrhan, P. Bermel, W. R. Chan, J. D. Joannopoulos, M. Soljačić, and I. Celanovic, “Enabling high-temperature nanophotonics for energy applications,” *Proc. Natl. Acad. Sci.*, vol. 109, no. 7, pp. 2280–2285, 2012.
- [144] V. Rinnerbauer, S. Ndao, Y. X. Yeng, W. R. Chan, J. J. Senkevich, J. D. Joannopoulos, M. Soljačić, and I. Celanovic, “Recent developments in high-temperature photonic crystals for energy conversion,” *Energy & Environmental Science*, vol. 5, no. 10, pp. 8815–8823, 2012.

- [145] W. R. Chan, P. Bermel, R. C. Pilawa-Podgurski, C. H. Marton, K. F. Jensen, J. J. Senkevich, J. D. Joannopoulos, M. Soljačić, and I. Celanovic, “Toward high-energy-density, high-efficiency, and moderate-temperature chip-scale thermophotovoltaics,” *Proc. Natl. Acad. Sci.*, vol. 110, no. 14, pp. 5309–5314, 2013.
- [146] T. Inoue, M. De Zoysa, T. Asano, and S. Noda, “Realization of dynamic thermal emission control,” *Nat. Mater.*, vol. 13, no. 10, pp. 928–931, 2014.
- [147] P. Dyachenko, J. do Rosário, E. Leib, A. Y. Petrov, M. Störmer, H. Weller, T. Vossmeier, G. Schneider, and M. Eich, “Tungsten band edge absorber/emitter based on a monolayer of ceramic microspheres,” *Opt. Express*, vol. 23, no. 19, pp. A1236–A1244, 2015.
- [148] N. P. Sergeant, O. Pincon, M. Agrawal, and P. Peumans, “Design of wide-angle solar-selective absorbers using aperiodic metal-dielectric stacks,” *Opt. Express*, vol. 17, no. 25, pp. 22800–22812, 2009.
- [149] M. Shimizu, A. Kohiyama, and H. Yugami, “High-efficiency solar-thermophotovoltaic system equipped with a monolithic planar selective absorber/emitter,” *J. Photonics Energy*, vol. 5, no. 1, pp. 053099–053099, 2015.
- [150] Z. Wang, T. S. Luk, Y. Tan, D. Ji, M. Zhou, Q. Gan, and Z. Yu, “Tunneling-enabled spectrally selective thermal emitter based on flat metallic films,” *Appl. Phys. Lett.*, vol. 106, no. 10, p. 101104, 2015.
- [151] C. Shemelya, D. DeMeo, N. P. Latham, X. Wu, C. Bingham, W. Padilla, and T. E. Vandervelde, “Stable high temperature metamaterial emitters for thermophotovoltaic applications,” *Appl. Phys. Lett.*, vol. 104, no. 20, p. 201113, 2014.
- [152] W. Li, U. Guler, N. Kinsey, G. V. Naik, A. Boltasseva, J. Guan, V. M. Shalaev, and A. V. Kildishev, “Refractory plasmonics with titanium nitride: broadband metamaterial absorber,” *Adv. Mater.*, vol. 26, no. 47, pp. 7959–7965, 2014.
- [153] D. Lu and Z. Liu, “Hyperlenses and metalenses for far-field super-resolution imaging,” *Nat. Commun.*, vol. 3, p. 1205, 2012.
- [154] A. Narayanaswamy, J. Mayo, and C. Canetta, “Infrared selective emitters with thin films of polar materials,” *Appl. Phys. Lett.*, vol. 104, no. 18, p. 183107, 2014.
- [155] I. V. Iorsh, I. S. Mukhin, I. V. Shadrivov, P. A. Belov, and Y. S. Kivshar, “Hyperbolic metamaterials based on multilayer graphene structures,” *Phys. Rev. B*, vol. 87, no. 7, p. 075416, 2013.

- [156] M. A. Othman, C. Guclu, and F. Capolino, “Graphene-based tunable hyperbolic metamaterials and enhanced near-field absorption,” *Opt. Express*, vol. 21, no. 6, pp. 7614–7632, 2013.
- [157] Y. C. Jun, J. Reno, T. Ribaudou, E. Shaner, J.-J. Greffet, S. Vassant, F. Marquier, M. Sinclair, and I. Brener, “Epsilon-near-zero strong coupling in metamaterial-semiconductor hybrid structures,” *Nano Lett.*, vol. 13, no. 11, pp. 5391–5396, 2013.
- [158] M. W. Dashiell, J. F. Beausang, H. Ehsani, G. Nichols, D. M. Depoy, L. R. Danielson, P. Talamo, K. D. Rahner, E. J. Brown, S. R. Burger, *et al.*, “Quaternary ingaassb thermophotovoltaic diodes,” *IEEE Trans. Electron Devices*, vol. 53, no. 12, pp. 2879–2891, 2006.
- [159] M. Bosi and C. Pelosi, “The potential of iii-v semiconductors as terrestrial photovoltaic devices,” *Prog. Photovoltaics Res. Appl.*, vol. 15, no. 1, pp. 51–68, 2007.
- [160] V. Avrutin, N. Izyumskaya, and H. Morkoç, “Semiconductor solar cells: Recent progress in terrestrial applications,” *Superlattices Microstruct.*, vol. 49, no. 4, pp. 337–364, 2011.
- [161] B.-C. Juang, R. B. Laghumavarapu, B. J. Foggo, P. J. Simmonds, A. Lin, B. Liang, and D. L. Huffaker, “Gasb thermophotovoltaic cells grown on gaas by molecular beam epitaxy using interfacial misfit arrays,” *Appl. Phys. Lett.*, vol. 106, no. 11, p. 111101, 2015.
- [162] U. Guler, A. Boltasseva, and V. M. Shalaev, “Refractory plasmonics,” *Sci.*, vol. 344, no. 6181, pp. 263–264, 2014.
- [163] S. Molesky, C. J. Dewalt, and Z. Jacob, “High temperature epsilon-near-zero and epsilon-near-pole metamaterial emitters for thermophotovoltaics,” *Opt. Express*, vol. 21, no. 101, pp. A96–A110, 2013.
- [164] S.-A. Biehs, M. Tschikin, and P. Ben-Abdallah, “Hyperbolic metamaterials as an analog of a blackbody in the near field,” *Phys. Rev. Lett.*, vol. 109, no. 10, p. 104301, 2012.
- [165] Y. Guo and Z. Jacob, “Fluctuational electrodynamics of hyperbolic metamaterials,” *J. Appl. Phys.*, vol. 115, no. 23, p. 234306, 2014.
- [166] S. Roberts, “Optical properties of nickel and tungsten and their interpretation according to drude’s formula,” *Phys. Rev.*, vol. 114, no. 1, p. 104, 1959.

- [167] A. Licciulli, D. Diso, G. Torsello, S. Tundo, A. Maffezzoli, M. Lomascolo, and M. Mazzer, “The challenge of high-performance selective emitters for thermophotovoltaic applications,” *Semicond. Sci. Technol.*, vol. 18, no. 5, p. S174, 2003.
- [168] K. Ujihara, “Reflectivity of metals at high temperatures,” *J. Appl. Phys.*, vol. 43, no. 5, pp. 2376–2383, 1972.
- [169] P. Winsemius, F. Van Kampen, H. Lengkeek, and C. Van Went, “Temperature dependence of the optical properties of au, ag and cu,” *J. Phys. F: Met. Phys.*, vol. 6, no. 8, p. 1583, 1976.
- [170] H. Weakliem and D. Redfield, “Temperature dependence of the optical properties of silicon,” *J. Appl. Phys.*, vol. 50, no. 3, pp. 1491–1493, 1979.
- [171] G. S. Arnold, “Absorptivity of several metals at $10.6 \mu\text{m}$: empirical expressions for the temperature dependence computed from drude theory,” *Appl. Opt.*, vol. 23, no. 9, pp. 1434–1436, 1984.
- [172] T. Tumkur, Y. Barnakov, S. Kee, M. Noginov, and V. Liberman, “Permittivity evaluation of multilayered hyperbolic metamaterials: Ellipsometry vs. reflectometry,” *J. Appl. Phys.*, vol. 117, no. 10, p. 103104, 2015.
- [173] M. Laroche, R. Carminati, and J. Greffet, “Near-field thermophotovoltaic energy conversion,” *J. Appl. Phys.*, vol. 100, no. 6, p. 063704, 2006.
- [174] O. Ilic, M. Jablan, J. Joannopoulos, I. Celanovic, H. Buljan, and M. Soljačić, “Near-field thermal radiation transfer controlled by plasmons in graphene,” *Phys. Rev. B*, vol. 85, pp. 1–4, Apr. 2012.
- [175] J.-Y. Chang, Y. Yang, and L. Wang, “Tungsten nanowire based hyperbolic metamaterial emitters for near-field thermophotovoltaic applications,” *Int. J. Heat Mass Trans.*, vol. 87, pp. 237–247, 2015.
- [176] R. Messina and P. Ben-Abdallah, “Graphene-based photovoltaic cells for near-field thermal energy conversion,” *Sci. Rep.*, vol. 3, p. 1383, 2013.
- [177] T. Bright, L. Wang, and Z. Zhang, “Performance of near-field thermophotovoltaic cells enhanced with a backside reflector,” *J. Heat Trans.*, vol. 136, no. 6, p. 062701, 2014.
- [178] V. Svetovoy and G. Palasantzas, “Graphene-on-silicon near-field thermophotovoltaic cell,” *Phys. Rev. Appl.*, vol. 2, no. 3, p. 034006, 2014.
- [179] R. E. Nelson, “A brief history of thermophotovoltaic,” *Semicond. Sci. Technol.*, vol. 18, p. 141, 2003.

- [180] S. Basu, Y. Chen, and Z. M. Zhang, “Microscale radiation in thermophotovoltaic devices -A review,” *Int. J. Energy Res.*, vol. 31, no. December 2006, pp. 689–716, 2007.
- [181] N. Harder and P. Würfel, “Theoretical limits of thermophotovoltaic solar energy conversion,” *Semicond. Sci. Technol.*, vol. 151, 2003.
- [182] P. Bermel, M. Ghebrebrhan, W. Chan, Y. Yeng, M. Araghchini, R. Hamam, C. Marton, K. Jensen, M. Soljačić, J. Joannopoulos, S. Johnson, and I. Celanovic, “Design and global optimization of high-efficiency thermophotovoltaic systems,” *Opt. Express*, vol. 18 Suppl 3, pp. A314–A334, Sept. 2010.
- [183] S. Biehs, M. Tschikin, R. Messina, and P. Ben-Abdallah, “Super-Planckian near-field thermal emission with phonon-polaritonic hyperbolic metamaterials,” *Appl. Phys. Lett.*, vol. 102, no. 13, p. 131106, 2013.
- [184] O. Ilic, M. Jablan, J. D. Joannopoulos, I. Celanovic, H. Buljan, and M. Soljačić, “Near-field thermal radiation transfer controlled by plasmons in graphene,” *Phys. Rev. B*, vol. 85, p. 155422, Apr. 2012.
- [185] R. Messina and P. Ben-Abdallah, “Graphene-based photovoltaic cells for near-field thermal energy conversion,” *Sci. Rep.*, vol. 3, p. 1383, Jan. 2013.
- [186] T. J. Bright, L. P. Wang, and Z. M. Zhang, “Performance of near-field thermophotovoltaic cells enhanced with a backside reflector,” *J. Heat Transfer*, vol. 136, no. 6, pp. 062701–062701.
- [187] S. Adachi, “Optical dispersion relations for GaP, GaAs, GaSb, InP, InAs, InSb, $\text{Al}_x\text{Ga}_{1-x}\text{As}$, and $\text{In}_{1-x}\text{Ga}_x\text{As}_y\text{P}_{1-y}$,” *J. Appl. Phys.*, vol. 66, no. 12, p. 6030, 1989.
- [188] M. Francoeur, R. Vaillon, and M. P. Menguc, “Thermal impacts on the performance of nanoscale-gap thermophotovoltaic power generators,” *IEEE Energy Conversion*, vol. 26, no. 2, pp. 686–698, 2011.
- [189] L. D. Landau, J. Bell, M. Kearsley, L. Pitaevskii, E. Lifshitz, and J. Sykes, *Electrodynamics of Continuous Media*, vol. 8. Elsevier, 1984.
- [190] S. J. Lee, N. H. Shin, J. J. Ko, M. J. Park, and R. Kümmel, “Density of states of quantum dots and crossover from 3D to Q0D electron gas,” *Semicond. Sci. Technol.*, vol. 1072, 1992.
- [191] A. I. Hochbaum and P. Yang, “Semiconductor nanowires for energy conversion,” *Chem. Rev.*, vol. 110, no. 1, pp. 527–546, 2009.

- [192] H. Fang, H. Bechtel, E. Plis, M. Martin, S. Krishna, E. Yablonovitch, and A. Javey, “Quantum of optical absorption in two-dimensional semiconductors,” *Proc. Natl. Acad. Sci.*, vol. 110, no. 29, pp. 11688–11691, 2013.
- [193] M. J. Shea and M. S. Arnold, “1% Solar Cells Derived From Ultrathin Carbon Nanotube Photoabsorbing Films,” *Appl. Phys. Lett.*, vol. 102, p. 243101, June 2013.
- [194] A. Jorio, G. Dresselhaus, and M. S. Dresselhaus, *Carbon nanotubes: advanced topics in the synthesis, structure, properties and applications*, vol. 111. Springer, 2007.
- [195] C. L. Cortes and Z. Jacob, “Photonic analog of a van Hove singularity in metamaterials,” *Phys. Rev. B*, vol. 88, p. 045407, July 2013.
- [196] K. Arnardottir, O. Kyriienko, M. Portnoi, and I. Shelykh, “One-dimensional Van Hove polaritons,” *Phys. Rev. B*, vol. 87, p. 125408, Mar. 2013.
- [197] L. Wang, H. Liu, R. M. Konik, J. A. Misewich, and S. S. Wong, “Carbon nanotube-based heterostructures for solar energy applications,” *Chem. Soc. Rev.*, vol. 42, no. 20, pp. 8134–8156, 2013.
- [198] O. Ilic, M. Jablan, J. D. Joannopoulos, I. Celanovic, and M. Soljačić, “Overcoming the black body limit in plasmonic and graphene near-field thermophotovoltaic systems,” *Opt. Express*, vol. 20, no. 103, pp. A366–A384, 2012.
- [199] H.-S. P. Wong and D. Akinwande, *Carbon nanotube and graphene device physics*. Cambridge University Press, 2010.
- [200] D. J. Bindl, A. J. Ferguson, M.-Y. Wu, N. Kopidakis, J. L. Blackburn, and M. S. Arnold, “Free carrier generation and recombination in polymer-wrapped semiconducting carbon nanotube films and heterojunctions,” *J. Phys. Chem. Lett.*, vol. 4, no. 21, pp. 3550–3559, 2013.
- [201] E. Kymakis and G. Amaratunga, “Single-wall carbon nanotube/conjugated polymer photovoltaic devices,” *Appl. Phys. Lett.*, vol. 80, no. 1, pp. 112–114, 2002.
- [202] M. Freitag, Y. Martin, J. Misewich, R. Martel, and P. Avouris, “Photoconductivity of single carbon nanotubes,” *Nano Lett.*, vol. 3, no. 8, pp. 1067–1071, 2003.
- [203] L. A. Falkovsky and A. A. Varlamov, “Space-time dispersion of graphene conductivity,” *EPJ B*, vol. 56, pp. 281–284, May 2007.

- [204] C. Köhler, T. Watermann, A. Knorr, and E. Malic, “Microscopic study of temporally resolved carrier relaxation in carbon nanotubes,” *Phys. Rev. B*, vol. 84, p. 153407, Oct. 2011.
- [205] C. Köhler, T. Watermann, and E. Malic, “Time- and momentum-resolved phonon-induced relaxation dynamics in carbon nanotubes,” *J. Phys. Condens. Matter*, vol. 25, p. 105301, Mar. 2013.
- [206] A. Lenert, D. M. Bierman, Y. Nam, W. R. Chan, I. Celanovic, M. Soljacic, and E. N. Wang, “A nanophotonic solar thermophotovoltaic device,” 2014.
- [207] T. Bauer, *Thermophotovoltaics: basic principles and critical aspects of system design*. Springer Science & Business Media, 2011.
- [208] D. Walls and P. Zoller, “Reduced quantum fluctuations in resonance fluorescence,” *Phys. Rev. Lett.*, vol. 47, no. 10, p. 709, 1981.
- [209] K. Nowack, F. Koppens, Y. V. Nazarov, and L. Vandersypen, “Coherent control of a single electron spin with electric fields,” *Sci.*, vol. 318, no. 5855, pp. 1430–1433, 2007.
- [210] P. Schindler, D. Nigg, T. Monz, J. T. Barreiro, E. Martinez, S. X. Wang, S. Quint, M. F. Brandl, V. Nebendahl, C. F. Roos, *et al.*, “A quantum information processor with trapped ions,” *New J. Phys.*, vol. 15, no. 12, p. 123012, 2013.
- [211] G. W. Milton, R. C. McPhedran, and A. Sihvola, “The searchlight effect in hyperbolic materials,” *Opt. Express*, vol. 21, pp. 14926–14942, Jun 2013.
- [212] S. V. Boriskina, H. Ghasemi, and G. Chen, “Plasmonic materials for energy: From physics to applications,” *Mater. Today*, vol. 16, no. 10, pp. 375–386, 2013.
- [213] S. A. R. Horsley and T. G. Philbin, “Canonical quantization of electromagnetism in spatially dispersive media,” *New J. Phys.*, vol. 16, 2014.
- [214] S. A. Biehs, S. Lang, A. Y. Petrov, M. Eich, and P. Ben-Abdallah, “Blackbody Theory for Hyperbolic Materials,” *Phys. Rev. Lett.*, vol. 115, no. 17, pp. 1–5, 2015.
- [215] L. Lu, J. D. Joannopoulos, and M. Soljačić, “Topological photonics,” *Nat. Photonics*, vol. 8, no. 11, pp. 821–829, 2014.
- [216] T. Van Mechelen and Z. Jacob, “Universal spin-momentum locking of evanescent waves,” *Optica*, vol. 3, no. 2, pp. 118–126, 2016.

- [217] J. N. Munday, D. M. Callahan, and H. a. Atwater, “Light trapping beyond the $4n^2$ limit in thin waveguides,” *Appl. Phys. Lett.*, vol. 100, no. 12, p. 121121, 2012.
- [218] C. Belacel, B. Habert, F. Bigourdan, F. Marquier, J. P. Hugonin, S. Michaelis De Vasconcellos, X. Lafosse, L. Coolen, C. Schwob, C. Javaux, B. Dubertret, J. J. Greffet, P. Senellart, and A. Maitre, “Controlling spontaneous emission with plasmonic optical patch antennas,” *Nano Lett.*, vol. 13, no. 4, pp. 1516–1521, 2013.
- [219] A. Raman, W. Shin, and S. Fan, “Upper bound on the modal material loss rate in plasmonic and metamaterial systems,” *Phys. Rev. Lett.*, vol. 110, no. 18, 2013.
- [220] C. Sauvan, J. P. Hugonin, I. S. Maksymov, and P. Lalanne, “Theory of the spontaneous optical emission of nanosize photonic and plasmon resonators,” *Phys. Rev. Lett.*, vol. 110, no. 23, pp. 1–5, 2013.
- [221] Z. Lin, A. Pick, M. Lončar, and A. W. Rodriguez, “Enhanced spontaneous emission at third-order dirac exceptional points in inverse-designed photonic crystals,” *Phys. Rev. Lett.*, vol. 117, no. 10, p. 107402, 2016.
- [222] D. R. Smith and D. Schurig, “Electromagnetic wave propagation in media with indefinite permittivity and permeability tensors,” *Phys. Rev. Lett.*, vol. 90, no. 7, p. 077405, 2003.
- [223] Z. Jacob, J.-Y. Kim, G. V. Naik, A. Boltasseva, E. E. Narimanov, and V. M. Shalaev, “Engineering photonic density of states using metamaterials,” *Appl. Phys. B*, vol. 100, no. 1, pp. 215–218, 2010.
- [224] Z. Jacob, I. I. Smolyaninov, and E. E. Narimanov, “Broadband purcell effect: Radiative decay engineering with metamaterials,” *Appl. Phys. Lett.*, vol. 100, no. 18, p. 181105, 2012.
- [225] Z. Jacob, L. V. Alekseyev, and E. Narimanov, “Optical hyperlens: far-field imaging beyond the diffraction limit,” *Opt. Express*, vol. 14, no. 18, pp. 8247–8256, 2006.
- [226] Z. Liu, H. Lee, Y. Xiong, C. Sun, and X. Zhang, “Far-field optical hyperlens magnifying sub-diffraction-limited objects,” *Sci.*, vol. 315, no. 5819, pp. 1686–1686, 2007.
- [227] Y. Guo, W. Newman, C. L. Cortes, and Z. Jacob, “Applications of hyperbolic metamaterial substrates,” *Adv. OptoElectron.*, vol. 2012, p. 452502, 2012.

- [228] J. Yao, X. Yang, X. Yin, G. Bartal, and X. Zhang, “Three-dimensional nanometer-scale optical cavities of indefinite medium,” *Proc. Natl. Acad. Sci.*, vol. 108, no. 28, pp. 11327–11331, 2011.
- [229] P. Ginzburg, A. V. Krasavin, A. N. Poddubny, P. A. Belov, Y. S. Kivshar, and A. V. Zayats, “Self-induced torque in hyperbolic metamaterials,” *Phys. Rev. Lett.*, vol. 111, no. 3, pp. 1–5, 2013.
- [230] T. Galfsky, H. Krishnamoorthy, W. Newman, E. Narimanov, Z. Jacob, and V. Menon, “Active hyperbolic metamaterials: enhanced spontaneous emission and light extraction,” *Optica*, vol. 2, no. 1, pp. 62–65, 2015.
- [231] K.-H. Kim, Y.-S. No, S. Chang, J.-H. Choi, and H.-G. Park, “Invisible Hyperbolic Metamaterial Nanotube at Visible Frequency,” *Sci. Rep.*, vol. 5, p. 16027, 2015.
- [232] I. V. Iorsh, A. N. Poddubny, P. Ginzburg, P. A. Belov, and Y. S. Kivshar, “Compton-like polariton scattering in hyperbolic metamaterials,” *Phys. Rev. Lett.*, vol. 114, no. 18, p. 185501, 2015.
- [233] Z. Jacob and V. M. Shalaev, “Plasmonics goes quantum,” *Sci.*, vol. 334, no. 6055, pp. 463–464, 2011.
- [234] W. D. Newman, C. L. Cortes, and Z. Jacob, “Enhanced and directional single-photon emission in hyperbolic metamaterials,” *JOSA B*, vol. 30, no. 4, pp. 766–775, 2013.
- [235] P. Shekhar and Z. Jacob, “Strong coupling in hyperbolic metamaterials,” *Phys. Rev. B*, vol. 90, no. 4, p. 045313, 2014.
- [236] A. P. Slobozhanyuk, P. Ginzburg, D. A. Powell, I. Iorsh, A. S. Shalin, P. Segovia, A. V. Krasavin, G. A. Wurtz, V. A. Podolskiy, P. A. Belov, and A. V. Zayats, “Purcell effect in hyperbolic metamaterial resonators,” *Physical Review B - Condensed Matter and Materials Physics*, vol. 92, no. 19, pp. 1–8, 2015.
- [237] C. L. Cortes and Z. Jacob, “Super-coulombic atom-atom interactions in hyperbolic media,” *Nat. Commun.*, vol. 8, p. 14144, 2017.
- [238] S. Molesky, C. J. Dewalt, and Z. Jacob, “High temperature epsilon-near-zero and epsilon-near-pole metamaterial emitters for thermophotovoltaics,” *Opt. Express*, vol. 21, no. 101, pp. A96–A110, 2013.
- [239] Z. Jacob, “Nanophotonics: Hyperbolic phonon-polaritons,” *Nat. Mater.*, vol. 13, no. 12, pp. 1081–1083, 2014.

- [240] L. Gu, T. U. Tumkur, G. Zhu, and M. a. Noginov, “Blue shift of spontaneous emission in hyperbolic metamaterial,” *Sci. Rep.*, vol. 4, p. 4969, 2014.
- [241] P. Li, M. Lewin, A. V. Kretinin, J. D. Caldwell, K. S. Novoselov, T. Taniguchi, K. Watanabe, F. Gaussmann, and T. Taubner, “Hyperbolic phonon-polaritons in boron nitride for near-field optical imaging and focusing,” *Nat. Commun.*, vol. 6, p. 7507, 2015.
- [242] P. Dyachenko, S. Molesky, A. Y. Petrov, M. Störmer, T. Krekeler, S. Lang, M. Ritter, Z. Jacob, and M. Eich, “Controlling thermal emission with refractory epsilon-near-zero metamaterials via topological transitions,” *Nat. Commun.*, vol. 7, 2016.
- [243] M. Esslinger, R. Vogelgesang, N. Talebi, W. Khunsin, P. Gehring, S. De Zuani, B. Gompf, and K. Kern, “Tetradymites as Natural Hyperbolic Materials for the Near-Infrared to Visible,” *ACS Photonics*, vol. 1, no. 12, pp. 1285–1289, 2014.
- [244] S. Dai, Z. Fei, Q. Ma, a. S. Rodin, M. Wagner, A. S. McLeod, M. K. Liu, W. Gannett, W. Regan, K. Watanabe, T. Taniguchi, M. Thiemens, G. Dominguez, a. H. Castro Neto, a. Zettl, F. Keilmann, P. Jarillo-Herrero, M. M. Fogler, D. N. Basov, A. H. C. Neto, a. Zettl, F. Keilmann, P. Jarillo-Herrero, M. M. Fogler, and D. N. Basov, “Tunable phonon polaritons in atomically thin van der Waals crystals of boron nitride,” *Sci.*, vol. 343, pp. 1125–1129, mar 2014.
- [245] J. D. Caldwell, A. Kretinin, Y. Chen, V. Giannini, M. M. Fogler, Y. Francescato, C. T. Ellis, J. G. Tischler, C. R. Woods, A. J. Giles, M. Hong, K. Watanabe, T. Taniguchi, S. a. Maier, and K. S. Novoselov, “Sub-diffraction, volume-confined polaritons in the natural hyperbolic material hexagonal boron nitride,” *Nat. Commun.*, vol. 5, pp. 1–9, 2014.
- [246] E. Yoxall, M. Schnell, A. Y. Nikitin, O. Txoperena, A. Woessner, M. B. Lundberg, F. Casanova, L. E. Hueso, F. H. L. Koppens, and R. Hillenbrand, “Direct observation of ultraslow hyperbolic polariton propagation with negative phase velocity,” *Nat. Photonics*, vol. 9, no. September, pp. 674–679, 2015.
- [247] J. S. Wu, D. N. Basov, and M. M. Fogler, “Topological insulators are tunable waveguides for hyperbolic polaritons,” *Phys. Rev. B*, vol. 92, no. 20, p. 205430, 2015.
- [248] K. Korzeb, M. Gajc, and D. A. Pawlak, “Compendium of natural hyperbolic materials,” *Opt. Express*, vol. 23, no. 20, p. 25406, 2015.

- [249] A. Nemilentsau, T. Low, and G. Hanson, “Anisotropic 2d materials for tunable hyperbolic plasmonics,” *Phys. Rev. Lett.*, vol. 116, no. 6, p. 066804, 2016.
- [250] R. J. Glauber and M. Lewenstein, “Quantum optics of dielectric media,” *Phys. Rev. A*, vol. 43, no. 1, p. 467, 1991.
- [251] J. Knoester, “Optical dynamics in crystal slabs: Crossover from superradiant excitons to bulk polaritons,” *Phys. Rev. Lett.*, vol. 68, no. 5, p. 654, 1992.
- [252] S.-T. Ho and P. Kumar, “Quantum optics in a dielectric: macroscopic electromagnetic-field and medium operators for a linear dispersive lossy medium—a microscopic derivation of the operators and their commutation relations,” *JOSA B*, vol. 10, no. 9, pp. 1620–1636, 1993.
- [253] P. Milonni, “Field quantization and radiative processes in dispersive dielectric media,” *J. Mod. Opt.*, vol. 42, no. 10, p. 1991, 1995.
- [254] S. M. Barnett and R. Loudon, “Sum Rule for Modified Spontaneous Emission Rates,” *Phys. Rev. Lett.*, vol. 77, no. 12, pp. 2444–2446, 1996.
- [255] A. Tip, “Canonical formalism and quantization for a class of classical fields with application to radiative atomic decay in dielectrics,” *Phys. Rev. A*, vol. 56, no. 6, p. 5022, 1997.
- [256] P. de Vries and A. Lagendijk, “Resonant scattering and spontaneous emission in dielectrics: microscopic derivation of local-field effects,” *Phys. Rev. Lett.*, vol. 81, no. 7, pp. 1381–1384, 1998.
- [257] A. S. Potemkin, A. N. Poddubny, P. A. Belov, and Y. S. Kivshar, “Green function for hyperbolic media,” *Physical Review A - Atomic, Molecular, and Optical Physics*, vol. 86, no. 2, pp. 1–9, 2012.
- [258] W. Yan, M. Wubs, and N. A. Mortensen, “Hyperbolic metamaterials: Non-local response regularizes broadband supersingularity,” *Physical Review B - Condensed Matter and Materials Physics*, vol. 86, no. 20, pp. 1–8, 2012.
- [259] O. Kidwai, S. V. Zhukovsky, and J. E. Sipe, “Effective-medium approach to planar multilayer hyperbolic metamaterials: Strengths and limitations,” *Phys. Rev. A*, vol. 85, no. 5, p. 053842, 2012.
- [260] A. N. Poddubny, P. A. Belov, and Y. S. Kivshar, “Spontaneous radiation of a finite-size dipole emitter in hyperbolic media,” *Phys. Rev. A*, vol. 84, no. 2, p. 023807, 2011.

- [261] A. N. Poddubny, P. A. Belov, P. Ginzburg, A. V. Zayats, and Y. S. Kivshar, “Microscopic model of Purcell enhancement in hyperbolic metamaterials,” *Physical Review B - Condensed Matter and Materials Physics*, vol. 86, no. 3, pp. 1–9, 2012.
- [262] S. Krasikov and I. V. Iorsh, “Self-consistent purcell factor and spontaneous topological transition in hyperbolic metamaterials,” *Phys. Status Solidi*, vol. 10, no. 10, pp. 769–773, 2016.
- [263] V. A. Podolskiy and E. E. Narimanov, “Strongly anisotropic waveguide as a nonmagnetic left-handed system,” *Phys. Rev. B*, vol. 71, no. 20, p. 201101, 2005.
- [264] R. Kubo, “The fluctuation-dissipation theorem,” *Rep. Prog. Phys.*, vol. 29, no. 1, p. 255, 1966.
- [265] S. M. Rytov, Y. A. Kravtsov, and V. I. Tatarskii, *Principles of statistical radiophysics 3*. Springer-Verlag New York Inc., New York, NY, 1988.
- [266] A. Narayanaswamy and G. Chen, “Dyadic green’s functions and electromagnetic local density of states,” *J. Quant. Spectrosc. Radiat. Transfer*, vol. 111, no. 12, pp. 1877–1884, 2010.
- [267] R. Carminati, A. Caze, D. Cao, F. Peragut, V. Krachmalnicoff, R. Pierrat, and Y. De Wilde, “Electromagnetic density of states in complex plasmonic systems,” *Surf. Sci. Rep.*, vol. 70, no. 1, pp. 1–41, 2015.
- [268] S. M. Barnett, B. Huttner, R. Loudon, and R. Matloob, “Decay of excited atoms in absorbing dielectrics,” *J. Phys. B: At., Mol. Opt. Phys.*, vol. 29, pp. 3763–3781, 1999.
- [269] C. Cohen-Tannoudji, J. Dupont-Roc, and G. Grynberg, *Photons and Atoms: Introduction to Quantum Electrodynamics (Wiley Professional)*. Wiley-VCH, 1997.
- [270] R. A. Ferrell, “Predicted radiation of plasma oscillations in metal films,” *Phys. Rev.*, vol. 111, no. 5, pp. 1214–1222, 1958.
- [271] D. Berreman, “Infrared absorption at longitudinal optic frequency in cubic crystal films,” *Phys. Rev.*, vol. 130, no. 6, pp. 2193–2199, 1963.
- [272] W. D. Newman, C. L. Cortes, J. Atkinson, S. Pramanik, R. G. Decorby, and Z. Jacob, “Ferrell-berreman modes in plasmonic epsilon-near-zero media,” *ACS Photonics*, vol. 2, no. 1, pp. 2–7, 2015.

- [273] P. Shekhar, M. Malac, V. Gaind, N. Dalili, A. Meldrum, and Z. Jacob, “Momentum-resolved electron energy loss spectroscopy for mapping the photonic density of states,” *ArXiv*, feb 2017.
- [274] L. B. Felsen and N. Marcuvitz, *Radiation and scattering of waves*, vol. 31. Wiley Interscience, 1994.
- [275] S. V. Zhukovsky, O. Kidwai, and J. E. Sipe, “Physical nature of volume plasmon polaritons in hyperbolic metamaterials,” *Opt. Express*, vol. 21, no. 12, pp. 14982–7, 2013.
- [276] S. M. Barnett and R. Loudon, “Sum rule for environmentally modified spontaneous emission rates,” *Quantum Semiclass. Optics*, vol. 10, no. 4, p. 591, 1998.
- [277] S. Scheel, “Sum rule for local densities of states in absorbing dielectrics,” *Phys. Rev. A*, vol. 78, no. 1, p. 013841, 2008.
- [278] X. Liu and Y. Xuan, “Super-planckian thermal radiation enabled by hyperbolic surface phonon polaritons,” *Sci. China Tech. Sci.*, vol. 59, no. 11, p. 1680, 2016.
- [279] L. D. Landau and E. M. Lifshitz, *Electrodynamics of continuous media*. AIP, 1960.
- [280] E. Lifshitz, “Effect of temperature on the molecular attracting forces between condensed bodies,” *Zh. Eksp. Teor. Fiz*, vol. 29, pp. 94–110, 1955.
- [281] S. Rytov, “On thermal fluctuations in distributed systems,” *Dokl. Akad. Nauk SSSR*, vol. 110, p. 371, 1956.
- [282] S. Rytov, “Correlation theory of electric fluctuations and thermal radiation,” *Zh. Eksp. Teor. Fiz.*, vol. 33, no. 166, 1957.
- [283] B. V. Budaev and D. B. Bogy, “On thermal radiation across nanoscale gaps,” *J. Appl. Math. Phys.*, vol. 66, no. 4, pp. 2061–2068, 2015.
- [284] A. Karalis and J. Joannopoulos, “Temporal coupled-mode theory model for resonant near-field thermophotovoltaics,” *Appl. Phys. Lett.*, vol. 107, no. 14, p. 141108, 2015.
- [285] M. Zhou, S. Yi, T. S. Luk, Q. Gan, S. Fan, and Z. Yu, “Analog of superradiant emission in thermal emitters,” *Phy. Review B*, vol. 92, no. 2, p. 024302, 2015.

- [286] S. Mallawaarachchi, M. Premaratne, S. D. Gunapala, and P. K. Maini, “Tunable superradiant thermal emitter assembly,” *Phys. Rev. B*, vol. 95, no. 15, p. 155443, 2017.
- [287] D. Flamm, “History and outlook of statistical physics,” *arXiv Phys. 9803005*, 1998.
- [288] L. Boltzmann, “Weirere studien uber das warmegleich-gewich unter gas-molekulen,” *K. Acad. Wiss.(Wein) Sitzb., II Abt*, vol. 66, 1872.
- [289] J. Loschmidt, “Über den zustand des wärmegleichgewichtes eines systems von körpern mit rücksicht auf die schwerkraft: I [-iv].,” *Kais. Akad. Wiss. Wien, Math. Naturwiss*, vol. 73, pp. 128–142, 1876.
- [290] L. Boltzmann, “On the relation between the second law of the mechanical theory of heat and the probability calculus with respect to the theorems on thermal equilibrium,” *Kais. Akad. Wiss. Wien Math. Natumiss. Classe*, vol. 76, pp. 373–435, 1877.
- [291] G. N. Lewis, “A new principle of equilibrium,” *Proc. Natl. Acad. Sci.*, vol. 11, no. 3, pp. 179–183, 1925.
- [292] R. C. Tolman, “The principle of microscopic reversibility,” *Proc. Natl. Acad. Sci.*, vol. 11, no. 7, pp. 436–439, 1925.
- [293] E. O. Lawrence, “Transition probabilities: Their relation to thermionic emission and the photo-electric effect,” *Phys. Rev.*, vol. 27, no. 5, p. 555, 1926.
- [294] P. Bridgman, “Note on the principle of detailed balancing,” *Phys. Rev.*, vol. 31, no. 1, p. 101, 1928.
- [295] C. Soret, *Sur l'étude expérimentale des coefficients rotationnels de conductibilité thermique*. Bureau des Archives, 1893.
- [296] W. Voigt *Gott. Nachr.*, vol. 87, 1903.
- [297] W. Thomson, “Collected papers i,” *Proc. Roy. Soc. Edinburgh*, pp. 237–241, 1854.
- [298] H. von Helmholtz, *The Correlation and Conservation of Forces*. 1876.
- [299] W. Nernst, “Zur kinetik der in lösung befindlichen körper,” *Z. Phys. Chem*, vol. 2, no. 9, pp. 613–679, 1888.
- [300] E. Eastman, “Thermodynamics of non-isothermal systems,” *J. Am. Chem. Soc.*, vol. 48, no. 6, pp. 1482–1493, 1926.

- [301] J. Peltier, “Nouvelles expériences sur la caloricit  des courants  lectrique,” in *Ann. Chm. Phys.*, vol. 56, pp. 371–386, 1834.
- [302] J. K. Platten, “The soret effect: a review of recent experimental results,” *J. of Appl. Mech.*, vol. 73, no. 1, pp. 5–15, 2006.
- [303] L. Rayleigh, “A stactical theorem,” *The London, Edinburgh, and Dublin Philosophical Magazine and Journal of Science*, vol. 48, no. 320, pp. 452–456, 1874.
- [304] A. Van der Ziel, “History of noise research,” *Adv. Electron. El. Phys.*, vol. 50, pp. 351–409, 1980.
- [305] A. Einstein, *Investigations on the Theory of the Brownian Movement*. Courier Corporation, 1956.
- [306] M. von Smoluchowski, “About brownian motion under the action of external forces and the relationship with the generalized diffusion equation,” *Ann. Phys.*, vol. 353, pp. 1103–1112, 1915.
- [307] A. Einstein and L. Hopf, “Statistische untersuchung der bewegung eines resonators in einem strahlungsfeld,” *Annal. der Physik*, vol. 338, no. 16, pp. 1105–1115, 1910.
- [308] P. Langevin, “Sur la th orie du mouvement brownien,” *CR Acad. Sci. Paris*, vol. 146, no. 530-533, p. 530, 1908.
- [309] N. Campbell, “The study of discontinuous phenomena,” *Proc. Cambridge Philos. Soc.*, vol. 15, pp. 117–136, 1909.
- [310] W. Schottky, “ ber spontane stromschwankungen in verschiedenen elektrizit tsleitern,” *Ann. der Physik*, vol. 362, no. 23, pp. 541–567, 1918.
- [311] J. B. Johnson, “Thermal agitation of electricity in conductors,” *Phys. Rev.*, vol. 32, no. 1, p. 97, 1928.
- [312] H. Nyquist, “Thermal agitation of electric charge in conductors,” *Phys. Rev.*, vol. 32, no. 1, p. 110, 1928.
- [313] L. Onsager, “Reciprocal relations in irreversible processes. i.,” *Phys. Rev.*, vol. 37, no. 4, p. 405, 1931.
- [314] L. Onsager, “Reciprocal relations in irreversible processes. ii.,” *Phys. Rev.*, vol. 38, no. 12, p. 2265, 1931.
- [315] G. E. Uhlenbeck and L. S. Ornstein, “On the theory of the brownian motion,” *Phys. Rev.*, vol. 36, no. 5, p. 823, 1930.

- [316] N. Wiener, “Generalized harmonic analysis,” *Acta Math.*, vol. 55, no. 1, pp. 117–258, 1930.
- [317] J. R. Carson, “The statistical energy-frequency spectrum of random disturbances,” *Bell Labs Techn. J.*, vol. 10, no. 3, pp. 374–381, 1931.
- [318] A. Khintchine, “Korrelationstheorie der stationären stochastischen prozesse,” *Mathe. Annal.*, vol. 109, no. 1, pp. 604–615, 1934.
- [319] H. B. G. Casimir, “On onsager’s principle of microscopic reversibility,” *Rev. Mod. Phys.*, vol. 17, no. 2-3, p. 343, 1945.
- [320] J. G. Kirkwood, “The dielectric polarization of polar liquids,” *J. Chem. Phys.*, vol. 7, no. 10, pp. 911–919, 1939.
- [321] J. Meixner, “Zur thermodynamik der irreversiblen prozesse in gasen mit chemisch reagierenden, dissoziierenden und anregbaren komponenten,” *Annal. der Physik*, vol. 435, no. 4, pp. 244–270, 1943.
- [322] S. Chandrasekhar, “Stochastic problems in physics and astronomy,” *Rev. Mod. Phys.*, vol. 15, no. 1, p. 1, 1943.
- [323] I. Prigogine, “Etude thermodynamique des phénomènes irréversibles,” 1947.
- [324] H. B. Callen, “The application of onsager’s reciprocal relations to thermoelectric, thermomagnetic, and galvanomagnetic effects,” *Phys. Rev.*, vol. 73, no. 11, p. 1349, 1948.
- [325] H. B. Callen and R. F. Greene, “On a theorem of irreversible thermodynamics,” *Physical Review*, vol. 86, no. 5, p. 702, 1952.
- [326] L. Van Hove, “Correlations in space and time and born approximation scattering in systems of interacting particles,” *Phys. Rev.*, vol. 95, no. 1, p. 249, 1954.
- [327] J. G. Kirkwood, “The statistical mechanical theory of transport processes i. general theory,” *J. Chem. Phys.*, vol. 14, no. 3, pp. 180–201, 1946.
- [328] N. Bloembergen, E. M. Purcell, and R. V. Pound, “Relaxation effects in nuclear magnetic resonance absorption,” *Phys. Rev.*, vol. 73, no. 7, p. 679, 1948.
- [329] H. B. Callen and T. A. Welton, “Irreversibility and generalized noise,” *Phys. Rev.*, vol. 83, no. 1, p. 34, 1951.
- [330] H. Takahasi, “Generalized theory of thermal fluctuations,” *J. Phys. Soc. Japan*, vol. 7, no. 5, pp. 439–446, 1952.

- [331] R. Kubo and K. Tomita, “A general theory of magnetic resonance absorption,” *J. Phys. Soc. Japan*, vol. 9, no. 6, pp. 888–919, 1954.
- [332] R. Kubo, “Statistical-mechanical theory of irreversible processes. i. general theory and simple applications to magnetic and conduction problems,” *J. Phys. Soc. Jpn.*, vol. 12, no. 6, pp. 570–586, 1957.
- [333] A. Pais, “Einstein and the quantum theory,” *Rev. Mod. Phys.*, vol. 51, no. 4, p. 863, 1979.
- [334] D. Ter Haar, *The old quantum theory*. Elsevier, 2016.
- [335] A. D. Fokker, “Die mittlere energie rotierender elektrischer dipole im strahlungsfeld,” *Annal. der Physik*, vol. 348, no. 5, pp. 810–820, 1914.
- [336] A. Fokker, “On the contributions to the electric current from the polarization and magnetization electrons,” *Philos. Mag.*, vol. 39, no. 232, pp. 404–415, 1920.
- [337] M. Planck, “An essay on statistical dynamics and its extension in the quantum theory,” *Sitz. Ber. Preuss. Akad. Wiss*, vol. 325, pp. 324–341, 1917.
- [338] A. N. Kolmogorov and S. V. Fomin, “On analytical methods in the theory of probability,” *Math. Ann*, vol. 104, pp. 415–458, 1931.
- [339] W. Bernard and H. B. Callen, “Irreversible thermodynamics of nonlinear processes and noise in driven systems,” *Rev. Mod. Phys.*, vol. 31, no. 4, p. 1017, 1959.
- [340] H. B. Casimir, “On the attraction between two perfectly conducting plates,” in *Proc. KNAW*, vol. 51, pp. 793–795, 1948.
- [341] D. Bijl, “Note on thermal radiation at low temperatures,” *Philos. Mag.*, vol. 43, no. 347, pp. 1342–1344, 1952.
- [342] E. G. Cravalho, C. L. Tien, and R. Caren, “Effect of small spacings on radiative transfer between two dielectrics,” *J. Heat Transfer*, vol. 89, no. 4, pp. 351–358, 1967.
- [343] C. Hargreaves, “Anomalous radiative transfer between closely-spaced bodies,” *Phys. Lett. A*, vol. 30, no. 9, pp. 491–492, 1969.
- [344] G. Domoto, R. Boehm, and C. L. Tien, “Experimental investigation of radiative transfer between metallic surfaces at cryogenic temperatures,” *J. Heat Trans.*, vol. 92, no. 3, pp. 412–416, 1970.

- [345] R. Boehm and C. Tien, “Small spacing analysis of radiative transfer between parallel metallic surfaces,” *J. Heat Transfer*, vol. 92, no. 3, pp. 405–411, 1970.
- [346] R. Caren, “Radiation heat transfer between closely spaced metal surfaces at low temperature: The impact of discrete modes of the radiation field,” *J. Heat Transfer*, vol. 94, no. 3, pp. 295–299, 1972.
- [347] K. Case and S. Chiu, “Electromagnetic fluctuations in a cavity,” *Phys. Rev. A*, vol. 1, no. 4, p. 1170, 1970.
- [348] H. P. Baltes, *Thermal radiation in finite cavities*. PhD thesis, 1972.
- [349] H. Baltes, B. Steinle, and M. Pabst, “Poincaré cycles and coherence of bounded thermal radiation fields,” *Physical Review A*, vol. 13, no. 5, p. 1866, 1976.
- [350] H. Baltes, “I on the validity of kirchhoff’s law of heat radiation for a body in a nonequilibrium environment,” *Progress in Optics*, vol. 13, pp. 1–25, 1976.
- [351] W. Eckhardt, “Corrections to the stefan-boltzmann radiation law in cavities with walls of finite conductivity,” *Opt. Commun.*, vol. 14, no. 1, pp. 95–98, 1975.
- [352] W. Eckhardt, “Correlation tensors of the blackbody radiation in rectangular cavities,” *Zeits. Physik B Cond. Mat.*, vol. 23, no. 2, pp. 213–219, 1976.
- [353] R. J. Glauber, “The quantum theory of optical coherence,” *Phys. Rev.*, vol. 130, no. 6, p. 2529, 1963.
- [354] C. Mehta and E. Wolf, “Coherence properties of blackbody radiation. i. correlation tensors of the classical field,” *Phys. Rev.*, vol. 134, no. 5A, p. A1143, 1964.
- [355] C. Mehta and E. Wolf, “Coherence properties of blackbody radiation. ii. correlation tensors of the quantized field,” *Phys. Rev.*, vol. 134, no. 5A, p. A1149, 1964.
- [356] W. Eckhardt, “Macroscopic theory of electromagnetic fluctuations and stationary radiative heat transfer,” *Phys. Rev. A*, vol. 29, no. 4, p. 1991, 1984.
- [357] J. E. Sipe, “New green-function formalism for surface optics,” *JOSA B*, vol. 4, no. 4, pp. 481–489, 1987.
- [358] D. Van Coevorden, R. Sprik, A. Tip, and A. Lagendijk, “Photonic band structure of atomic lattices,” *Physical review letters*, vol. 77, no. 12, p. 2412, 1996.

- [359] F. Wijnands, J. Pendry, and F. J. García-Vidal, “Green’s functions for Maxwell’s equations: application to spontaneous emission,” *Opt. Quantum Electron*, vol. 29, pp. 199–216, 1997.
- [360] P. J. Hesketh, J. N. Zemel, and B. Gebhart, “Organ pipe radiant modes of periodic micromachined silicon surfaces,” *Nat.*, vol. 324, pp. 549–551, 1986.
- [361] D. Bertilone, “Stokes parameters and partial polarization of far-field radiation emitted by hot bodies,” *JOSA A*, vol. 11, no. 8, pp. 2298–2304, 1994.
- [362] L. Novotny and B. Hecht, *Principles of nano-optics*. Cambridge university press, 2012.
- [363] S. Reich, J. Maultzsch, C. Thomsen, and P. Ordejon, “Tight-binding description of graphene,” *Phys. Rev. B*, vol. 66, no. 3, p. 035412, 2002.
- [364] J. B. Khurgin, “How to deal with the loss in plasmonics and metamaterials,” *Nat. Nanotechnol.*, vol. 10, no. 1, pp. 2–6, 2015.
- [365] V. Drachev, V. Podolskiy, and A. Kildishev, “Hyperbolic metamaterials: new physics behind a classical problem,” *Opt. Express*, vol. 21, no. 12, pp. 1699–1701, 2013.
- [366] A. Abrikosov, L. Gorkov, and I. Dzyaloshinskii, *Methods of Quantum Field Theory in Statistical Physics*. Dover Publications, 1975.
- [367] J. Serrano, A. Bosak, R. Arenal, M. Krisch, K. Watanabe, T. Taniguchi, H. Kanda, A. Rubio, and L. Wirtz, “Vibrational properties of hexagonal boron nitride: Inelastic x-ray scattering and ab initio calculations,” *Phys. Rev. Lett.*, vol. 98, no. 9, p. 095503, 2007.
- [368] W. Zhang, R. Yu, H. J. Zhang, X. Dai, and Z. Fang, “First-principles studies of the three-dimensional strong topological insulators Bi_2Te_3 , Bi_2Se_3 and Sb_2Te_3 ,” *New J. Phys.*, vol. 12, no. 6, p. 065013, 2010.

Appendices

Appendix A

Historical Perspective

In this appendix, we provide a condensed history of the ideas underpinning our current understanding of thermal electromagnetic field correlations.

The lineage of electromagnetic field correlations traces back to the mid nineteenth century. At the time, with the recent rise to prominence of thermodynamics, the development of a microscopic theory of heat (a kinetic theory) was widely considered one of the most pressing questions of scientific thought [287]. As a means to both supplement this problem and gain a better understanding of its implications, a great deal of progress was made in understanding thermal transport processes and fluctuations¹

In particular, two foundational concepts emerged in the collective works of the period². The first crucial supposition, initially put forward by Lord Kelvin [297] in the context of finite temperature circuits, and later echoed by von Helmholtz [298], Nernst [299], and Eastman [300], stated that competing irreversible processes are governed by reciprocal relations. In the language of matrices, for coupled interactions, such as shared thermoelectric transport in a circuit (Peltier effect [301]), or the transfer of electrolytes in liquid heat conduction (Soret effect [302]), the linear “off-diagonal” response terms should be equal (ideally by the principles of thermodynamics³.) Let the linear relation between one type of source, for instance a temperature difference at a metal junction, and the opposite measurable, the current, be denoted as χ_{12} . Then, the converse linear relation between the opposite

¹Much of this development was spurred by Boltzmann’s H-Theorem [288] connecting microscopic states to entropy, the ensuing reversibility paradox [289], and subsequent probabilistic interpretation of the second law of thermodynamics [290–294].

²There were also important attempts to find results contradicting these ideas by Soret and Voigt [295, 296].

³In all these derivations there are additional assumptions or specifications. The most often used simplification was to assume that any one of the mixed processes occurs independently of the others.

source and measurable, source current with measured temperature difference, is also determined by χ_{12} ($\chi_{21} = \chi_{12}$). In this way, the two linear relations are reciprocal, and independent of the “on-diagonal” relations⁴. The second key insight, initiated by Lord Rayleigh, was the principle of least dissipation of energy. In analogy with classical principle of least action, Rayleigh proposed that a given system of linear process can always be recast as an equivalent relation between the measurables and the derivatives of a potential (dissipation [303]) function. By applying variational principles to this function, the behaviour of any system can then be connected with energy, or entropy.

These leaps of advancement in conceptual thermodynamics were further amplified by a collection of powerful results from the nascent field of stochastic process [304]. At the start of the twentieth century, Einstein [305] and von Smoluchowski [306] independently produced two seminal studies of Brownian motion, using statistical arguments to determine the thermodynamic features of liquid suspensions. Importantly, these works showed for the first time that, by fairly simple and regular [307] arguments, the response characteristic of a system could be related to its statistical features of motion (as specific examples Einstein calculated the diffusion constant, 1905, and relation between voltage and capacitance in a noisy circuit, 1907 [305]). These strong initial inroads were quickly followed by improved approaches to the general analysis of stochastic processes by Langevin [308] and Campbell [309]. These works showed that if the response of a system measurable, Y , to a discrete event at time t_i is denoted as $G(t - t_i)$, then the average, \bar{Y} , and variance, $(\Delta Y)^2$, of the measurable for events occurring at a rate λ , on a time frame much longer than the average period between events, are given by

$$\bar{Y} = \lambda \int_0^{\infty} du G(u), \quad (\Delta Y)^2 = \lambda \int_0^{\infty} du G^2(u). \quad (\text{A.1})$$

Following the derivation given in the introduction, it is clear that these equations already possess germs of the fluctuation dissipation theorem.⁵

The most important aspects of these two approaches for connecting linear response and statistical thermodynamics began to coalesce in 1930-1931 with the works of

⁴For the example given here, this means that the temperature current and voltage heat relations are reciprocal, and independent of the usual heat temperature and voltage current relations.

⁵Using this framework further evidence of the existence of a general formula directly relating an arbitrary linear response function to fluctuations was seen in Schottky’s work on shot noise [310] and Johnson’s [311] and Nyquist’s [312] analysis, experimental and theoretical respectively, on the relation between the noise spectra of electrons and fluctuations in the current of resistive circuits.

Onsager [313, 314], and Uhlenbeck and Ornstein [315]⁶. Uhlenbeck and Ornstein showed that Einstein's approach to Brownian motion could both be extended (1) to systems without continuous surroundings and (2) to the calculation of all powers of velocity and position. Together, these results gave a much more general approach to the study of random process. Meanwhile, Onsager showed that the reciprocal nature exhibited by mutually occurring reversible processes could be interpreted as a product of microscopic reversibility; and that in this very general setting the fluctuation characteristics of a system could be connected with entropy production. However, as pointed out by Casimir [319], Onsager's derivation included a number of approximation taken from the theory of Brownian motion that could not be supposed in all cases. Nevertheless, Onsager's conclusion were considered almost undoubtedly valid [320, 321]. Further, as pointedly demonstrated by Chandrasekhar [322], fluctuations were not just useful for examining microscope properties but rather a powerful method for dealing with complex physical problems. The fundamental extension of thermodynamics contained in these ideas only briefly remained an open problem.

In the eight year period between 1946-1954 the landscape of statistical thermodynamics was again radically altered through the works Kirkwood, Prigogine, Takahasi, Van Hove, Bolebergen and Purcell, and Callen (both independently and in collaboration with Welton and Greene). The theory contained in these additions not only placed Onsager's findings on a firm theoretical footing [323, 324], but also established the Green function approach essential for incorporating fluctuations into the theory of quantum mechanics [325, 326], and provided important explicit examples to key physical systems [327, 328]. Complementarily, it was also shown for the first time that fluctuations could be related to linear response characteristics [325, 329, 330]. Quoting Callen and Greene's 1952 paper the first universal fluctuation dissipation theorem was written as⁷

$$\langle \zeta^2 \rangle = \frac{2k_\beta T}{\pi} \int d\omega \frac{\sigma(\omega)}{\omega^2}. \quad (\text{A.2})$$

Where, k_β is the Boltzmann constant, T the absolute temperature, ω the frequency, $\langle \zeta^2 \rangle$ the mean squared of some extensive parameter averaged over the frequency range determined by the integral, and $\sigma(\omega)$ the dissipative part of the corresponding linear system response.

⁶During roughly this same period, 1930-1934, the mathematical theory random processes in the frequency domain was placed on a logically sound footing by the contributions of Weiner [316], Carson [317] and Khintchine [318]. These results, which also highlighted the importance of stationary processes (Khintchine), were immediately understood to be pillars of stochastic analysis, and are still routinely used in modern approaches.

⁷The first true theorem of this kind is attributed to, depending on the author, either Nyquist [312], or Einstein [305]. However, both results depend on the specific models.

Following these results, the initial connections of the fluctuation dissipation theorem with quantum mechanics and perturbative analysis were provided by Kubo in his classic 1954 [331], 1957 [332] and 1966 [264] papers. From the perspective of statistical mechanics, the results contained in this collection of papers form a complete support for the findings we present in this dissertation.

Nevertheless, they represent only one of the two pillars on which the theory of electromagnetic correlations rest. Paralleling the history of advancement of statistical mechanics, the mid nineteenth century also marked two of the most important discoveries of electromagnetics. First, between 1861 and 1862 Maxwell published his treatise on the differential equations governing electrodynamics. Second, in 1860 Kirchhoff [333] proved, based on thermodynamic arguments, that the amount of energy radiated by an object in a given frequency, $\zeta(\omega)$, was related to its absorptivity coefficient, $\alpha(\omega)$, by a yet undetermined function that depended only on frequency, ω , and temperature, T ,

$$\frac{\zeta(\omega)}{\alpha(\omega)} = U_{BB}(\omega, T). \quad (\text{A.3})$$

The challenge posed by Kirchhoff to find the form of this function signified the birth of both the study of electromagnetic field correlations and quantum mechanics.

As the resulting period between 1875 and 1900 is one of the most famous in all of physics, here we will simply note some of the major milestones, and direct the interested reader to the fuller accounts given by Pais [333] and Ter Haar [334]⁸:

- **1879** Based on experimental evidence, Stefan speculated that the total energy radiate by a hot body scales with the fourth power of its temperature.
- **1884** Combining arguments from thermodynamics and electromagnetics Boltzmann showed that the T^4 scaling proposed by Stefan can only hold for black-bodies, i.e. bodies for which $\alpha(\omega) = 1$. The work is credited as the first application of thermodynamics to electrodynamics.
- **1893** Arguing from the perspective of adiabatic expansion Wien proved the displacement law bearing his name; and that $U_{BB}(\omega, T)$ was of the form

$$U_{BB}(\omega, T) = \frac{cf^3}{8\pi} g(f/T), \quad (\text{A.4})$$

where f is the frequency and c the speed of light.

⁸The following information is taken from these references.

- **1896** Wien conjectured the exponential form $g(f/T) = \alpha e^{-\beta f/T}$ with undetermined parameters α and β .
- **1897** Paschen confirmed that Wien's conjecture was accurate in the near-infrared spectral range of 1 to 8 μm .
- **1900** Lummer and Prinsheim, and Rubens and Ferdinand discovered that Wien's exponential law failed in the mid and far infrared (12 to 18 μm and 30 to 60 μm respectively).
- **1900** In a series of three papers Planck derived the correct form of the black-body distribution using an ad hoc statistical quantization.

This connection between thermodynamics and electromagnetics was furthered by Fokker in his 1914 work on a rotating dipole in a radiation field [335], and 1920 description of the relation between polarization and random currents [336]. Combined with Planck's 1917 characterization of the statistical features of quantum radiation [337] these results form the basis of the famous Fokker-Planck equation⁹.

Again mirroring the evolution of the field of stochastic processes, the next major set of developments occurred in the 1950's. Shortly following Kubo's initial publication of the modern form of the fluctuation dissipation theorem, Landau [279], Lifschitz [280], Rytov [281, 282], and subsequently Willam and Callen [339], presented the formalized theory of thermal electromagnetic correlations that serves as the foundation for our original work.

However, while from a theoretical prescriptive complete, the remarkably different characteristics of this new theory compared to Kirchhoff's classical formulation were not realized for some time. In writing on the subject, Hargraves suggests that in the early 1960's it was generally suspected that near-field electromagnetic modes, as discussed by Casimir in 1948 [340], would modified average thermal fields near surfaces [341]. Yet, no major effort to determine the form of these modifications appears until much later in the decade when in 1967 Cravalho, Tien and Caren [342] analyzed radiation between closely spaced dielectrics, and in 1969 and 1970 Hargreaves [343] and Domoto, Boehm and Tien [344] experimentally investigated radiative heat transfer between closely spaced conducting plates. Although later disputed [41], the proximity effects observed in these experiments sparked renewed interest; and the extension of the Rytovian theory to explain the proximity effects observed in these experiments was undertaken by Boehm and Tien in 1970 [345], Polder and van Hove

⁹These dynamics were treated independently from a mathematical perspective by Kolmogorov and Fomin in 1931 [338]

in 1971 [13], and Caren in 1972 [346]. These works, in conjunction with similar analysis for small cavities by Case and Chui [347] and Baltes [348], provided an initial glimpse of many of the most important features of near-field thermal electromagnetic correlations for potential engineering applications; including approximations for distance scaling, and the realization of the possibility of strong spectral features.

This short span of retrospectively major advancement in understanding initiated a new round of theoretical inquiry. Beginning in the mid 1970's major efforts centering around the works of Agarwal [10], Baltes, Steinle and Pabst [349], Baltes [350] and Eckhardt [351, 352] were made to connect the phenomena of coherence and energy transfer observed in Rytovian electrodynamics with previously existing theory, including the validity of Kirchhoff's law¹⁰. Following the positive resolution of these questions, attention turned to developing methods of calculation. While the consistency of the theory was no longer in doubt, it was entirely unclear how calculations could be practically carried out beyond closely separated plates. A first step towards treating this still pressing issue¹¹ was made with the formal proof of the equality of Rytov's original formulation with the so called fluctuation-dissipation of the second kind, positing fluctuating electric fields rather than currents [92, 356]. In this formulation, global field correlations are determined directly from the electromagnetic Green function, which offers a number of computational advantages [357].

The fluctuation-dissipation of the second kind is also much closer to the methods used in quantum optics; and active research interests in the late eighties and early nineties moved almost exclusively to connecting the now relatively mature theory of macroscopic thermal electromagnetic field correlations with the quantization of electromagnetic fields in matter¹². As such, we mention only two other noteworthy contributions predating the time line provided in the introduction: Hesketh et. al's 1986 [360] experimental characterization of the strong spectral features of micromachined silicon surfaces; and Bertilone's 1994 comment on the coherence of thermal correlations, which provided new results for thermal Stokes parameters [361].

¹⁰These works made extensive use of the formulation of coherence developed by Glauber in early sixties [353], and the findings of Mehta and Wolf [354, 355].

¹¹Even with modern computational resources, calculating thermal electromagnetic field fluctuations is a difficult problem in all but the simplest cases. However, substantial progress has been made with the recent formalizations of the scattering approach [72–74] and computationally simpler boundary fluctuation formulations [80, 81].

¹²An importation but by no means complete cross section of this work includes the contributions by Glauber [250], Knoester [251], Ho and Kumar [252], Milonni [253], Barnett and Loudon [254], de Vries and Lagendijk [256], Van Coevorden and Sprik [358], Wijnands, Pendry, and García-Vidal [359], and Tip [255].

Appendix B

The Blackbody Distribution

In this appendix, we review the semiclassical arguments leading to Bose-Einstein, Fermi statistics, and Planck's blackbody distribution.

B.1 Density of free space states

To supplement later argument, we will require an expression for the number of electromagnetic oscillator modes per unit frequency in a cuboid cavity described by the lengths $\{L_x, L_y, L_z\}$ ($V = L_x L_y L_z$). Assuming periodic boundary conditions, along each direction we must have the component of the wave vector, k , obeying the equation

$$e^{\pm ikL} = 1, \quad (\text{B.1})$$

implying that that $kL = 2\pi n$, with $n \in \mathbb{Z}^{\geq 0}$, so that each mode can be thought of as occupying an index volume of $(2\pi)^3/V$. Passing to the continuum limit, $\{L_x, L_y, L_z\} \rightarrow \{\infty, \infty, \infty\}$ the differential number of modes included by increasing k is then

$$dN = \frac{2dV_k}{V_{state}} = \frac{2V}{(2\pi)^3} k^2 \sin(\theta) dk d\theta d\phi. \quad (\text{B.2})$$

Integrating over the angular variables and using the definition of the wave vector $k = \omega/c$ this expression becomes,

$$dN = \frac{V}{\pi^2 c^3} \omega^2 d\omega. \quad (\text{B.3})$$

The density of oscillators per unit frequency, per unit volume, is then

$$\mathcal{D}(\omega) = \frac{1}{V} \frac{dN}{d\omega} = \frac{\omega^2}{\pi^2 c^3}. \quad (\text{B.4})$$

B.2 State expectation in the canonical ensemble

In the micro canonical ensemble, the entropy of a state is given by the relation

$$S = k_B \ln(W(E)), \quad (\text{B.5})$$

where k_B is the Boltzmann constant, and $W(E)$ is the number of states that have same energy, E . From the differential form of the first law of thermodynamics entropy is also connected to energy by the relation

$$dE + PdV = TdS, \quad (\text{B.6})$$

so that at constant volume

$$\frac{1}{T} = \frac{\partial S}{\partial E}. \quad (\text{B.7})$$

Passing to the the contact ensemble, where the original system (now subsystem) is placed in contact with a heat bath¹, the energy of the total system is

$$E_{tot} = E_{sys} + E_{bath}. \quad (\text{B.8})$$

Noting that the total number of states for a particular distribution of energy between the two separated systems is

$$W(E_{sys}) = W_{sys}(E_{sys})W_{bath}(E_{tot} - E_{sys}), \quad (\text{B.9})$$

for any particular energy of the subsystem that occurs only once

$$W(E_{sys}) = W_{bath}(E_{tot} - E_{sys}). \quad (\text{B.10})$$

Returning to (B.7) and (B.5) then shows that the total number of states for one particular state of the subsystem obeys the equation

$$\frac{1}{T} = \frac{\partial S}{\partial E} = \frac{k_B}{W(E)} \frac{\partial W(E)}{\partial E}. \quad (\text{B.11})$$

Correspondingly,

$$W(E_{sys}) = A e^{\beta(E_{tot} - E_{sys})}, \quad (\text{B.12})$$

¹A heat bath is defined to be system so large that its temperature does not change with an infinitesimal addition or subtraction of energy.

with A an undefined constant and $\beta = 1/(k_B T)$. The total number of states for a given energy E of the subsystem is then

$$W(E_{sys}) = A e^{\beta E_{tot}} \sum_{E_{sys}=E} e^{-\beta E_{sys}}, \quad (\text{B.13})$$

and the total number of states

$$Z = \int_{E_{sys}} dE_{sys} W(E_{sys}), \quad (\text{B.14})$$

where Z is referred to as the partition function of the system.

B.3 Planck's quantization

Consider the system to be a single harmonic oscillator of a given frequency ω . From the classical picture of (B.14) the energy of the oscillator can take on any value greater than zero, and so the partition function is

$$Z = \frac{C}{\beta}, \quad (\text{B.15})$$

with C standing for the constant $A e^{\beta E_{tot}}$. The expectation value of the energy of the oscillator is then

$$\langle E \rangle = \beta \int_0^{\infty} dE E e^{-\beta E} = \beta. \quad (\text{B.16})$$

In context of the electromagnetic modes of a cavity, (B.16) produces disastrous results. Recalling (B.4) the number of oscillators between the angular frequency ω and $\omega + d\omega$ scales as ω^2 . The total electromagnetic energy per unit volume in an empty cavity is then

$$\frac{E}{V} = \beta \int_0^{\infty} d\omega \frac{\omega^2}{\pi^2 c^3}, \quad (\text{B.17})$$

which clearly diverges as $\omega \rightarrow \infty$.

The solution to this problem, called the ultra-violet catastrophe, is that energy spectrum of each oscillator is in fact discrete, occurring in steps of $\hbar\omega$, and not continuous. Taking this line, the partition function is instead

$$Z = C \sum_{n=0}^{\infty} e^{-\beta n \hbar \omega} = \frac{C}{1 - e^{-\beta \hbar \omega}}, \quad (\text{B.18})$$

where ω is the angular frequency or strength of the oscillator, $\omega = 2\pi f/\lambda$, \hbar is Planck's energy quantization constant, and C the constant previously introduced for (B.14)². The energy expectation of the oscillator is then

$$\langle E \rangle = \frac{C\hbar\omega}{Z} \sum_{n=0}^{\infty} n e^{-\beta n\hbar\omega} = \frac{C\hbar\omega}{Z(1 - e^{-\beta\hbar\omega})} \sum_{n=1}^{\infty} e^{-\beta n\hbar\omega} = \frac{\hbar\omega}{e^{\beta\hbar\omega} - 1}. \quad (\text{B.19})$$

(If n is limited to be either 0 or 1 then $\langle n \rangle = 1/(e^{\hbar\omega} + 1)$, giving Fermi statistics.) Evaluating the total electromagnetic energy per unit volume in this case we instead have

$$\frac{E}{V} = \frac{\hbar}{\pi^2 c^3} \int_0^{\infty} d\omega \frac{\omega^3}{e^{\beta\hbar\omega} - 1} = \frac{\pi^2}{15(\hbar c)^3} \frac{1}{\beta^4}, \quad (\text{B.20})$$

which is Planck's distribution.

²For Fermi statistic, we find $Z = C(1 + e^{-\beta\hbar\omega})$.

Appendix C

Power Transfer between Half Spaces

In this appendix we outline the steps connecting (1.41) and (1.42).

C.1 S-polarized components

Beginning with the s-polarized component, following the naming conventions of Fig 1.1, the explicit form of the Green function in Cartesian coordinates produces four contributing terms; two of the type

$$\int_{-\infty}^0 \int_0^{\infty} dz' dk_{\rho} \frac{-3ik_{\rho} k_{z3}^* |t_s(k_{\rho})|^2}{2^6 \pi |k_{z1}|^2} e^{-2Im\{k_{z1}\}z'}, \quad (\text{C.1})$$

and two of the type

$$\int_{-\infty}^0 \int_0^{\infty} dz' dk_{\rho} \frac{-ik_{\rho} k_{z3}^* |t_s(k_{\rho})|^2}{2^6 \pi |k_{z1}|^2} e^{-2Im\{k_{z1}\}z'}. \quad (\text{C.2})$$

Bringing these four terms together and carrying out the integral over the z' coordinate, gives

$$\langle S_z(\omega) \rangle_s = -\frac{\omega^2 Im\{\epsilon(\omega, T)\} H(\omega, T)}{c^2} Re \left\{ \int_0^{\infty} dk_{\rho} \frac{k_{\rho} k_{z3}^* |t_s(k_{\rho})|^2}{2^3 \pi Im\{k_{z1}\} |k_{z1}|^2} \right\}. \quad (\text{C.3})$$

Making use of the identity,

$$\frac{\omega^2 Im\{\epsilon(\omega, T)\}}{c^2} = 2Re\{k_{z1}\} Im\{k_{z1}\}, \quad (\text{C.4})$$

and the explicit form of the transmission coefficient for one layer between two semi-infinite media,

$$t_s = \frac{t_s^{12}(k_\rho) t_s^{23}(k_\rho)}{1 + r_s^{12}(k_\rho) r_s^{23}(k_\rho) e^{2ik_{z2}L}} e^{ik_{z2}L}, \quad (\text{C.5})$$

the above becomes

$$\langle S_z(\omega) \rangle_s = -H(\omega, T) \int_0^\infty dk_\rho \frac{k_\rho}{2^2 \pi} \frac{\text{Re}\{k_{z1}\} \text{Re}\{k_{z3}\} |t_s^{12}(k_\rho) t_s^{23}(k_\rho)|^2}{|k_{z1}|^2 |1 + r_s^{12}(k_\rho) r_s^{23}(k_\rho) e^{2ik_{z2}L}|^2} e^{-2\text{Im}\{k_{z2}\}L}. \quad (\text{C.6})$$

Expanding out the transmission coefficients,

$$t_s^{12} = \frac{2k_{z1}}{k_{z1} + k_{z2}}, \quad (\text{C.7})$$

this result becomes

$$\langle S_z(\omega) \rangle_s = -H(\omega, T) \int_0^\infty dk_\rho \frac{k_\rho}{\pi} \frac{\text{Re}\{k_{z1}\} \text{Re}\{k_{z3}\} |k_{z2}|^2 e^{-2\text{Im}\{k_{z2}\}L}}{|(k_{z1} + k_{z2})(k_{z2} + k_{z3})|^2 |1 + r_s^{12} r_s^{23} e^{2ik_{z2}L}|^2}. \quad (\text{C.8})$$

C.2 P-polarized components

Switching to the p-polarized components, again making use of the explicit forms of the Green for Cartesian coordinates contained, results in six contributing terms

$$\int_{z'} \int_{-\infty}^\infty dz' dk_x dk_y \frac{-i}{2^4 \pi^2} \frac{(k_x^2 + k_y^2 + k_{z3}^{*2}) |t_p(k_\rho)|^2}{|k_1|^2 |k_3|^2 (k_x^2 + k_y^2)^2} (k_x^4 k_{z3}) e^{-2\text{Im}\{k_{z1}\}z'}, \quad (\text{C.9})$$

$$\int_{z'} \int_{-\infty}^\infty dz' dk_x dk_y \frac{-i}{2^4 \pi^2} \frac{(k_x^2 + k_y^2 + k_{z3}^{*2}) |t_p(k_\rho)|^2}{|k_1|^2 |k_3|^2 (k_x^2 + k_y^2)^2} (k_x^2 k_y^2 k_{z3}) e^{-2\text{Im}\{k_{z1}\}z'}, \quad (\text{C.10})$$

$$\int_{z'} \int_{-\infty}^\infty dz' dk_x dk_y \frac{-i}{2^4 \pi^2} \frac{(k_x^2 + k_y^2 + k_{z3}^{*2}) |t_p(k_\rho)|^2}{|k_1|^2 |k_3|^2 (k_x^2 + k_y^2)^2} \left(\frac{k_x^2 (k_x^2 + k_y^2)^2 k_{z3}}{|k_{z1}|^2} \right) e^{-2\text{Im}\{k_{z1}\}z'}, \quad (\text{C.11})$$

$$\int_{z'} \int_{-\infty}^{\infty} dz' dk_x dk_y \frac{-i}{2^4 \pi^2} \frac{(k_x^2 + k_y^2 + k_{z3}^{*2}) |t_p(k_\rho)|^2}{|k_1|^2 |k_3|^2 (k_x^2 + k_y^2)^2} (k_x^2 k_y^2 k_{z3}) e^{-2Im\{k_{z1}\}z'}, \quad (C.12)$$

$$\int_{z'} \int_{-\infty}^{\infty} dz' dk_x dk_y \frac{-i}{2^4 \pi^2} \frac{(k_x^2 + k_y^2 + k_{z3}^{*2}) |t_p(k_\rho)|^2}{|k_1|^2 |k_3|^2 (k_x^2 + k_y^2)^2} (k_y^4 k_{z3}) e^{-2Im\{k_{z1}\}z'}, \quad (C.13)$$

$$\int_{z'} \int_{-\infty}^{\infty} dz' dk_x dk_y \frac{-i}{2^4 \pi^2} \frac{(k_x^2 + k_y^2 + k_{z3}^{*2}) |t_p(k_\rho)|^2}{|k_1|^2 |k_3|^2 (k_x^2 + k_y^2)^2} \left(\frac{k_x^2 (k_x^2 + k_y^2)^2 k_{z3}}{|k_{z1}|^2} \right) e^{-2Im\{k_{z1}\}z'} \quad (C.14)$$

Taking the integral over the z' coordinate, summing the six terms, and reincorporating gives

$$\langle S_z(\omega) \rangle_p = \frac{-\omega^2 Im\{\epsilon(\omega, T)\} H(\omega, T)}{c^2} \\ Re \left\{ \iint_{-\infty}^{\infty} \frac{dk_x dk_y}{2^4 \pi^2 Im\{k_{z1}\}} \left(\frac{|t_p(k_\rho)|^2 k_{z3} (k_x^2 + k_y^2 + k_{z3}^{*2})}{|k_{z1}|^2 |k_3|^2} \right) \left(\frac{k_x^2 + k_y^2 + |k_{z1}|^2}{|k_1|^2} \right) \right\}. \quad (C.15)$$

Again making use of identity (C.4), and noting that $Re\{k_{z3}k_{z3}^{*2}\} = Re\{k_{z3}\}|k_{z3}|^2$ the above becomes

$$\langle S_z(\omega) \rangle_p = -H(\omega, T) \\ \iint_{-\infty}^{\infty} \frac{dk_x dk_y}{2^3 \pi^2} \frac{|t_p(k_\rho)|^2}{|k_{z1}|^2} \frac{Re\{k_{z3}\} (k_x^2 + k_y^2 + |k_{z3}|^2)}{|k_3|^2} \frac{Re\{k_{z1}\} (k_x^2 + k_y^2 + |k_{z1}|^2)}{|k_1|^2}. \quad (C.16)$$

Using the identity

$$Re\{k_{zn}\epsilon_n^*\} = \frac{Re\{k_{zn}\}}{|k_o|^2} (k_x^2 + k_y^2 + |k_{zn}^2|). \quad (C.17)$$

we then have

$$\langle S_z(\omega) \rangle_p = -H(\omega, T) \iint_{-\infty}^{\infty} \frac{dk_x dk_y}{2^3 \pi^2} \frac{|t_p(k_\rho)|^2}{|k_{z1}|^2} \frac{Re\{k_{z3}\epsilon_3^*\} Re\{k_{z1}\epsilon_1^*\}}{|\epsilon_3||\epsilon_1|}, \quad (C.18)$$

so that by using the transmission parameter for the layered medium,

$$t_p = \frac{t_p^{12}(k_\rho) t_p^{23}(k_\rho)}{1 + r_p^{12}(k_\rho) r_p^{23}(k_\rho) e^{2ik_{z2}L}}, \quad (C.19)$$

with

$$t_p^{12} = \sqrt{\frac{\epsilon_1(\omega, T)}{\epsilon_2(\omega, T)}} \frac{2\epsilon_2(\omega, T) k_{z1}}{\epsilon_2(\omega, T) k_{z1} + \epsilon_1(\omega, T) k_{z2}} \quad (\text{C.20})$$

and switching to polar coordinates then gives

$$\langle S_z(\omega) \rangle_p = -H(\omega, T) \int_0^\infty \frac{k_\rho}{\pi} \frac{|\epsilon_2|^2 |k_{z2}|^2 \text{Re}\{k_{z3}\epsilon_3^*\} \text{Re}\{k_{z1}\epsilon_1^*\} e^{-2\text{Im}\{k_{z2}\}L}}{|(k_{z1}\epsilon_2 + k_{z2}\epsilon_1)(k_{z3}\epsilon_2 + k_{z2}\epsilon_3)|^2 |1 + r_p^{12} r_p^{23} e^{2ik_{z2}L}|^2}. \quad (\text{C.21})$$

Adding this result to the thermal electromagnetic power transferred by the s-polarized component, we find

$$\begin{aligned} \langle S_z(\omega) \rangle &= (H(\omega, T_3) - H(\omega, T_1)) \\ &\int_0^\infty \frac{dk_\rho}{\pi} \frac{\text{Re}\{k_{z1}\} \text{Re}\{k_{z3}\} |k_{z2}|^2}{|(k_{z1} + k_{z2})(k_{z2} + k_{z3})|^2 |1 + r_s^{12} r_s^{23} e^{2ik_{z2}L}|^2} e^{-2\text{Im}\{k_{z2}\}L} + \\ &\frac{\text{Re}\{k_{z1}^*\epsilon_1\} \text{Re}\{k_{z3}^*\epsilon_3\} |\epsilon_2|^2 |k_{z2}|^2}{|(k_{z1}\epsilon_2 + k_{z2}\epsilon_1)(k_{z2}\epsilon_3 + k_{z3}\epsilon_2)|^2 |1 + r_p^{12} r_p^{23} e^{2ik_{z2}L}|^2} e^{-2\text{Im}\{k_{z2}\}L}. \end{aligned} \quad (\text{C.22})$$

The total power from this expression is given by the over all frequencies, both negative and positive, and switching to strictly positive frequencies introduces a factor of 2.

C.3 Final forms

To bring (C.22) into a form more conducive to evaluation we note that for the s-polarized component

$$|t_s^{12} t_s^{23}|^2 \frac{\text{Re}\{k_{z1}\} \text{Re}\{k_{z3}\}}{|k_{z1}|^2} = \frac{16 |k_{z2}|^2 \text{Re}\{k_{z3}\} \text{Re}\{k_{z1}\}}{(|k_{z2} + k_{z3}| |k_{z1} + k_{z2}|)^2}. \quad (\text{C.23})$$

Comparing this to

$$\begin{aligned} (1 - |r_s^{12}|^2) (1 - |r_s^{23}|^2) &= \left(1 - \frac{|k_{z1} - k_{z2}|^2}{|k_{z1} + k_{z2}|^2}\right) \left(1 - \frac{|k_{z2} - k_{z3}|^2}{|k_{z2} + k_{z3}|^2}\right) = \\ &\frac{4 \left(k_{z3} |k_{z2}|^2 k_{z1}^* + k_{z3}^* k_{z2}^2 k_{z1} + k_{z3} k_{z2}^* k_{z1} + k_{z3}^* |k_{z2}|^2 k_{z1}\right)}{(|k_{z1} + k_{z2}| |k_{z2} + k_{z3}|)^2}, \end{aligned} \quad (\text{C.24})$$

it can be concluded that if k_{z2} is strictly real then the above expressions are equivalent due the complex conjugate relation $xy^* + x^*y = 2\text{Re}[xy^*]$. A similar results

can be shown for the p-polarized light

$$|t_p^{12} t_p^{23}|^2 \frac{Re\{k_{z1}\epsilon_1^*\} Re\{k_{z3}\epsilon_3^*\}}{|\epsilon_1||\epsilon_3||k_{z1}|^2} = \frac{16|\epsilon_2|^2|k_{z2}|^2 Re\{k_{z3}\epsilon_3^*\} Re\{k_{z1}\epsilon_1^*\}}{(|k_{z2}\epsilon_3 + k_{z3}\epsilon_2||k_{z1}\epsilon_2 + k_{z2}\epsilon_1|)^2}, \quad (C.25)$$

$$\begin{aligned} (1 - |r_p^{12}|^2)(1 - |r_p^{23}|^2) &= \left(1 - \frac{|k_{z1}\epsilon_2 - k_{z2}\epsilon_1|^2}{|k_{z1}\epsilon_2 + k_{z2}\epsilon_1|^2}\right) \left(1 - \frac{|k_{z2}\epsilon_3 - k_{z3}\epsilon_2|^2}{|k_{z2}\epsilon_3 + k_{z3}\epsilon_2|^2}\right) = \\ &= \frac{4(k_{z3}\epsilon_3^*|k_{z2}|^2|\epsilon_2|^2 k_{z1}^*\epsilon_1 + k_{z3}^*\epsilon_3 k_{z2}^2 \epsilon_2^2 k_{z1}^*\epsilon_1 + k_{z3}\epsilon_3^* k_{z2}^* \epsilon_2^2 k_{z1}\epsilon_1^* + k_{z3}^*\epsilon_3 |k_{z2}|^2 |\epsilon_2|^2 k_{z1}\epsilon_1^*)}{(|k_{z2}\epsilon_2 + k_{z1}\epsilon_2||k_{z2}\epsilon_3 + k_{z3}\epsilon_2|)^2}. \end{aligned} \quad (C.26)$$

Again, under the assumption that both k_{z2} and ϵ_2 are real quantities these equations are equivalent as $xy^* + x^*y = 2Re\{xy^*\}$. However, for waves decaying in the thin film separating the two half space, with k_{z2} imaginary, these relations for $Im\{r_n^{21}\} Im\{r_n^{23}\}$ do not hold. Instead for p-polarized light

$$\begin{aligned} Im\{r_p^{21}\} Im\{r_p^{23}\} &= \\ Im\left\{\frac{(\epsilon_1 k_{z2} - \epsilon_2 k_{z1})(\epsilon_2^* k_{z1}^* + \epsilon_1^* k_{z2}^*)}{|\epsilon_2 k_{z1} + \epsilon_1 k_{z2}|^2}\right\} Im\left\{\frac{(\epsilon_3 k_{z2} - \epsilon_2 k_{z3})(\epsilon_3^* k_{z2}^* + \epsilon_2^* k_{z3}^*)}{|\epsilon_3 k_{z2} + \epsilon_2 k_{z3}|^2}\right\} &= \\ \left(\frac{2|\epsilon_2||k_{z2}| Re\{k_{z1}\epsilon_1^*\}}{|\epsilon_2 k_{z1} + \epsilon_1 k_{z2}|^2}\right) \left(\frac{2|\epsilon_2||k_{z2}| Re\{k_{z3}\epsilon_3^*\}}{|\epsilon_3 k_{z2} + \epsilon_2 k_{z3}|^2}\right), \end{aligned} \quad (C.27)$$

which is again equivalent to (C.25) when multiplied by a factor of 4. For s-polarized light, the mirror result is

$$\begin{aligned} Im\{r_s^{21}\} Im\{r_s^{23}\} &= Im\left\{\frac{(k_{z2} - k_{z1})(k_{z1}^* + k_{z2}^*)}{|k_{z1} + k_{z2}|^2}\right\} Im\left\{\frac{(k_{z2} - k_{z3})(k_{z2}^* + k_{z3}^*)}{|k_{z2} + k_{z3}|^2}\right\} = \\ \left(\frac{2Re\{k_{z1}\}|k_{z2}|}{|k_{z1} + k_{z2}|^2}\right) \left(\frac{2Re\{k_{z3}\}|k_{z2}|}{|k_{z2} + k_{z3}|^2}\right). \end{aligned} \quad (C.28)$$

Combining these expression the thermal electromagnetic power transfer at a particular frequency is found to be

$$\begin{aligned} \langle S_z(\omega) \rangle &= \sum_n \left(\frac{H(\omega, T_3) - H(\omega, T_1)}{2\pi} \right) \\ &\left(\int_0^{k_o\sqrt{\epsilon_2}} k_\rho \frac{(1 - |r_n^{21}|^2)(1 - |r_n^{23}|^2)}{|1 - r_n^{21} r_n^{23} e^{2ik_{z2}L}|^2} + 4 \int_{k_o\sqrt{\epsilon_2}}^\infty k_\rho \frac{Im\{r_n^{21}\} Im\{r_n^{23}\}}{|1 - r_n^{21} r_n^{23} e^{2ik_{z2}L}|^2} e^{-2Im\{k_{z2}\}L} \right), \end{aligned} \quad (C.29)$$

which is result quoted in the main text.

Appendix D

General Green Function Results

Following *Principles of Nano-Optics* by Novotny and Hecht [362], in this appendix we reproduce a collection of Green function results that are used throughout this thesis.

D.1 Mathematical basis of Green functions

Let $\mathcal{L}(\dots)$ be a differential operator, and $\mathbf{s}(\mathbf{r})$ a source function. The central relation between a Green function $\mathcal{G}(\mathbf{r}, \mathbf{r}')$ and a solution $A(\mathbf{r})$ is then determined by the following set of equations

$$\mathcal{L}(\mathbf{A}(\mathbf{r})) = \mathbf{s}(\mathbf{r}), \quad (\text{D.1})$$

$$\mathcal{L}(\check{\mathcal{G}}(\mathbf{r}, \mathbf{r}')) = \check{I}\delta(\mathbf{r} - \mathbf{r}'), \quad (\text{D.2})$$

$$\mathcal{L}(\mathbf{A}(\mathbf{r})) = \int dV' \mathcal{L}(\check{\mathcal{G}}(\mathbf{r}, \mathbf{r}')) \mathbf{s}(\mathbf{r}'). \quad (\text{D.3})$$

The equality provided by this final result then identifies the solution $A(\mathbf{r})$ as

$$\mathbf{A}(\mathbf{r}) = \int dV' \check{\mathcal{G}}(\mathbf{r}, \mathbf{r}') \mathbf{s}(\mathbf{r}'). \quad (\text{D.4})$$

D.2 Electromagnetic Green function relations

In the Lorentz radiation gauge, the following relations are satisfied by the electromagnetic Green function in a homogeneous local dielectric environment with angular frequency ω , scalar potential $\phi(\mathbf{r}, t)$, magnetic displacement $\mathbf{H}(\mathbf{r}, \omega)$, permittivity $\epsilon(\omega)$, permeability $\mu(\omega)$, vector potential $\mathbf{A}(\mathbf{r}, \omega)$, current density $\mathbf{j}(\mathbf{r}, \omega)$,

and $k = \sqrt{\epsilon(\omega)\mu(\omega)}\omega/c$.

$$\mathcal{G}(\mathbf{r}, \mathbf{r}', \omega) = \frac{e^{ik|\mathbf{r}-\mathbf{r}'|}}{4\pi|\mathbf{r}-\mathbf{r}'|} \quad (\text{D.5})$$

$$\mathbf{A}(\mathbf{r}, \omega) = \mu_o\mu(\omega) \int dV' \mathcal{G}(\mathbf{r}, \mathbf{r}', \omega) \mathbf{j}(\mathbf{r}', \omega) \quad (\text{D.6})$$

$$\phi(\mathbf{r}, \omega) = \frac{1}{\epsilon_o\epsilon(\omega)} \int dV' \rho(\mathbf{r}', \omega) \mathcal{G}(\mathbf{r}, \mathbf{r}', \omega) \quad (\text{D.7})$$

$$\check{\mathcal{G}}(\mathbf{r}, \mathbf{r}', \omega) = \left(\check{I} + \frac{1}{k^2} \nabla \nabla \right) \mathcal{G}(\mathbf{r}, \mathbf{r}', \omega) \quad (\text{D.8})$$

$$\mathbf{E}(\mathbf{r}, \omega) = i\omega \left(\check{I} + \frac{1}{k^2} \nabla \nabla \right) \mathbf{A}(\mathbf{r}, \omega) \quad (\text{D.9})$$

$$\mathbf{E}(\mathbf{r}, \omega) = \mathbf{E}_o(\mathbf{r}, \omega) + i\omega\mu_o\mu(\omega) \int dV' \check{\mathcal{G}}(\mathbf{r}, \mathbf{r}', \omega) \mathbf{j}(\mathbf{r}', \omega) \quad (\text{D.10})$$

$$\mathbf{H}(\mathbf{r}, \omega) = \mathbf{H}_o(\mathbf{r}, \omega) + \int dV' (\nabla \times \check{\mathcal{G}}(\mathbf{r}, \mathbf{r}', \omega)) \mathbf{j}(\mathbf{r}', \omega) \quad (\text{D.11})$$

Here, the o subscript denotes either background fields or constants. Introducing the electric dipole

$$\mathbf{j}(\mathbf{r}, t) = \frac{d}{dt} \mathbf{p}(t) \delta(\mathbf{r} - \mathbf{r}') \quad \mathbf{j}(\mathbf{r}, \omega) = -i\omega \mathbf{p}(\omega) \delta(\mathbf{r} - \mathbf{r}'), \quad (\text{D.12})$$

the electric field and vector potential relations become

$$\mathbf{E}(\mathbf{r}, \omega) = \mathbf{E}_o(\mathbf{r}, \omega) + \omega^2\mu_o\mu(\omega) \check{\mathcal{G}}(\mathbf{r}, \mathbf{r}', \omega) \mathbf{p}(\mathbf{r}', \omega) \quad (\text{D.13})$$

$$\mathbf{A}(\mathbf{r}, \omega) = -i\omega\mu_o\mu(\omega) \mathcal{G}(\mathbf{r}, \mathbf{r}', \omega) \mathbf{p}(\mathbf{r}', \omega). \quad (\text{D.14})$$

D.3 Electromagnetic Green function in Cartesian coordinates

Using the spatial Fourier transform, with $\{k_x, k_y, k_z\}$ denoting the transform indices, the Green function for the vector potential is expanded as

$$\mathcal{G}(\mathbf{r}, \mathbf{r}', \omega) = \frac{e^{ik|\mathbf{r}-\mathbf{r}'|}}{|\mathbf{r}-\mathbf{r}'|} = \frac{i}{2\pi} \iint dk_x dk_y \frac{e^{i(k_x x + k_y y + k_z |z|)}}{k_z}, \quad (\text{D.15})$$

with

$$k_z = \pm \sqrt{\frac{\epsilon(\omega)\mu(\omega)\omega^2}{c^2} - k_x^2 - k_y^2}, \quad (\text{D.16})$$

and the \pm sign used to keep the imaginary part of k_z positive. Using (D.8) the electromagnetic Green function is then

$$\check{\mathcal{G}}(\mathbf{r}, \mathbf{r}', \omega) = \frac{i}{8\pi^2} \iint dk_x dk_y (\check{M}^s + \check{M}^p) e^{i(k_x x + k_y y + k_z z)} \quad (\text{D.17})$$

with

$$\check{M}^s = \frac{1}{k_{z1} (k_x^2 + k_y^2)} \begin{pmatrix} k_y^2 & -k_x k_y & 0 \\ -k_x k_y & k_x^2 & 0 \\ 0 & 0 & 0 \end{pmatrix} \quad (\text{D.18})$$

$$\check{M}^p = \frac{1}{k_1^2 (k_x^2 + k_y^2)} \begin{pmatrix} k_x^2 k_{z1} & k_x k_y k_{z1} & \mp k_x (k_x^2 + k_y^2) \\ k_x k_y k_{z1} & k_y^2 k_{z1} & \mp k_y (k_x^2 + k_y^2) \\ \mp k_x (k_x^2 + k_y^2) & \mp k_y (k_x^2 + k_y^2) & (k_x^2 + k_y^2)^2 \frac{1}{k_{z1}} \end{pmatrix} \quad (\text{D.19})$$

This same representation can also be used to describe the reflected and transmitted Green functions with the corresponding expansion matrices

$$\check{M}_r^s = \frac{r^s(k_x, k_y)}{k_{z1} (k_x^2 + k_y^2)} \begin{pmatrix} k_y^2 & -k_x k_y & 0 \\ -k_x k_y & k_x^2 & 0 \\ 0 & 0 & 0 \end{pmatrix} \quad (\text{D.20})$$

$$\check{M}_r^p = \frac{-r^p(k_x, k_y)}{k_1^2 (k_x^2 + k_y^2)} \begin{pmatrix} k_x^2 k_{z1} & k_x k_y k_{z1} & k_x (k_x^2 + k_y^2) \\ k_x k_y k_{z1} & k_y^2 k_{z1} & k_y (k_x^2 + k_y^2) \\ -k_x (k_x^2 + k_y^2) & -k_y (k_x^2 + k_y^2) & -(k_x^2 + k_y^2)^2 \frac{1}{k_{z1}} \end{pmatrix} \quad (\text{D.21})$$

$$\check{M}_t^s = \frac{t^s(k_x, k_y)}{k_{z1} (k_x^2 + k_y^2)} \begin{pmatrix} k_y^2 & -k_x k_y & 0 \\ -k_x k_y & k_x^2 & 0 \\ 0 & 0 & 0 \end{pmatrix} \quad (\text{D.22})$$

$$\check{M}_t^p = \frac{t^p(k_x, k_y)}{k_1 k_n (k_x^2 + k_y^2)} \begin{pmatrix} k_x^2 k_{zn} & k_x k_y k_{zn} & -k_x (k_x^2 + k_y^2) \frac{k_{zn}}{k_{z1}} \\ k_x k_y k_{zn} & k_y^2 k_{zn} & -k_y (k_x^2 + k_y^2) \frac{k_{zn}}{k_{z1}} \\ -k_x (k_x^2 + k_y^2) & -k_y (k_x^2 + k_y^2) & (k_x^2 + k_y^2)^2 \frac{1}{k_{z1}} \end{pmatrix} \quad (\text{D.23})$$

Here, k_{zn} is used to denote the quantity

$$k_{zn} = \pm \sqrt{\frac{\epsilon_n(\omega) \mu_n(\omega) \omega^2}{c^2} - k_x^2 - k_y^2}, \quad (\text{D.24})$$

where $\epsilon_n(\omega)$ and $\mu_n(\omega)$ are the permittivity and permeability of the n^{th} local homogeneous medium. Similarly, Green functions and expansion matrices can be found for the magnetic displacement field,

$$\check{\mathcal{H}}(\mathbf{r}, \mathbf{r}', \omega) = \nabla \times \check{\mathcal{G}}(\mathbf{r}, \mathbf{r}', \omega) = \frac{i}{8\pi^2} \iint dk_x dk_y (\check{N}^s + \check{N}^p) e^{i(k_x x + k_y y + k_z z)}, \quad (\text{D.25})$$

with

$$\tilde{N}_t^s = \frac{it^s(k_x, k_y)}{k_{z1}(k_x^2 + k_y^2)} \begin{pmatrix} k_{zn}k_xk_y & -k_{zn}k_x^2 & 0 \\ k_{zn}k_y^2 & -k_{zn}k_x^2 & 0 \\ (ky^3 - k_x^2k_y) & (kx^3 - k_xk_y^2) & 0 \end{pmatrix} \quad (\text{D.26})$$

$$\tilde{N}_t^p = \frac{-it^p(k_x, k_y)(k_x^2 + k_y^2 + k_{zn}^2)}{k_1k_n(k_x^2 + k_y^2)} \begin{pmatrix} k_yk_x & k_y^2 & \frac{k_y}{k_{z1}} \\ k_x^2 & k_xk_y & \frac{k_x}{k_{z1}} \\ 0 & 0 & 0 \end{pmatrix} \quad (\text{D.27})$$

Note that the form of these matrices can alternatively be found by taking the external product of the s and p-polarization vectors

$$\hat{\mathbf{s}} = \frac{k_y}{|k_{||}|} \hat{\mathbf{x}} - \frac{k_yk_z}{|k_{||}|} \hat{\mathbf{y}} \quad (\text{D.28})$$

$$\hat{\mathbf{p}} = \frac{1}{|k|} \left(\frac{k_xk_z}{|k_{||}|} \hat{\mathbf{x}} + \frac{k_yk_z}{|k_{||}|} \hat{\mathbf{y}} + |k_{||}| \hat{\mathbf{z}} \right). \quad (\text{D.29})$$

Finally, letting denote $r = |\mathbf{r} - \mathbf{r}'|$, the real space electromagnetic Green function is given by

$$\check{\mathcal{G}}(\mathbf{r}, \mathbf{r}', \omega) = \frac{e^{ikr}}{4\pi r} \left(\left(1 + \frac{ikr - 1}{k^2r^2} \right) \bar{\mathbf{I}} + \left(\frac{3 - 3ikr - k^2r^2}{k^2r^2} \right) \frac{\mathbf{r}\mathbf{r}}{r^2} \right), \quad (\text{D.30})$$

where again $k = \sqrt{\epsilon(\omega)\mu(\omega)}\omega/c$, and no longer denotes a Fourier transform parameter. The small kr behavior of this quantity is of particular importance, and using the Taylor series expansion up to the third power of (ikR) , is found to obey the equality

$$\lim_{\mathbf{r}' \rightarrow \mathbf{r}} \mathbf{n}_p \cdot \text{Im} \{ \check{\mathcal{G}}(\mathbf{r}, \mathbf{r}', \omega) \} \cdot \mathbf{n}_p = \lim_{\mathbf{r}' \rightarrow \mathbf{r}} \frac{1}{3} \text{Im} \{ \text{Tr} [\check{\mathcal{G}}(\mathbf{r}, \mathbf{r}, \omega)] \} = \frac{\omega \text{Re} \{ \epsilon(\omega) \}}{6\pi c}, \quad (\text{D.31})$$

setting $\mu(\omega) = 1$.

D.4 Lehmann representation and the density of states

The Lehmann representation explicitly connects the Green function to the solution basis implied by the delta distribution definition. Although the procedure is completely general, here we present the result specifically for the Helmholtz's equation of a particular system

$$\nabla \times \nabla \times \mathbf{U}_{\mathbf{k}}(\mathbf{r}, \omega_{\mathbf{k}}) - \frac{\omega_{\mathbf{k}}^2}{m^2} \mathbf{U}_{\mathbf{k}}(\mathbf{r}, \omega_{\mathbf{k}}) = 0, \quad (\text{D.32})$$

where m is a medium parameter playing the role of propagation velocity, and $\omega_{\mathbf{k}}$ is the eigenvalue for the mode indexed by \mathbf{k} . Assuming these solutions do indeed form a complete set, they can also be made to fulfill the orthogonality relation

$$\int dV' \mathbf{U}_{\mathbf{k}'}^*(\mathbf{r}', \omega_{\mathbf{k}'}) \mathbf{U}_{\mathbf{k}}(\mathbf{r}', \omega_{\mathbf{k}}) = \delta_{\mathbf{k}\mathbf{k}'}. \quad (\text{D.33})$$

From its defining equations, the Green function is then defined by the expansion

$$\check{\mathcal{G}}(\mathbf{r}, \mathbf{r}, \omega) = \sum_{\mathbf{k}} \mathbf{A}_{\mathbf{k}}(\mathbf{r}', \omega) \mathbf{U}_{\mathbf{k}}(\mathbf{r}, \omega_{\mathbf{k}}) = c^2 \sum_{\mathbf{k}} \frac{\mathbf{U}_{\mathbf{k}}^*(\mathbf{r}', \omega_{\mathbf{k}}) \mathbf{U}_{\mathbf{k}}(\mathbf{r}, \omega_{\mathbf{k}})}{\omega_{\mathbf{k}}^2 - \omega^2}, \quad (\text{D.34})$$

where $\mathbf{A}_{\mathbf{k}}(\mathbf{r}', \omega)$ is the expansion parameter for the mode \mathbf{k} . Using the Cauchy integral theorem, the imaginary part of the Green function is then determined to be

$$\text{Im} \{ \check{\mathcal{G}}(\mathbf{r}, \mathbf{r}', \omega) \} = \frac{\pi c^2}{2\omega} \sum_{\mathbf{k}} \mathbf{U}_{\mathbf{k}}^*(\mathbf{r}', \omega_{\mathbf{k}}) \mathbf{U}_{\mathbf{k}}(\mathbf{r}, \omega_{\mathbf{k}}) \delta(\omega - \omega_{\mathbf{k}}). \quad (\text{D.35})$$

If the strength of the modes are normalized, then in the limit $\mathbf{r}' \rightarrow \mathbf{r}$ this quantity effectively counts the number contributing modes at a specific spatial point, and hence is referred to as the density of states¹. The partial density of states along a direction \mathbf{n}_p is similarly defined as

$$\rho_p(\mathbf{r}, \omega) = \lim_{\mathbf{r}' \rightarrow \mathbf{r}} \frac{6\omega}{\pi c^2} (\mathbf{n}_p \cdot \text{Im} \{ \check{\mathcal{G}}(\mathbf{r}, \mathbf{r}', \omega) \} \cdot \mathbf{n}_p). \quad (\text{D.36})$$

Using the result from the end of the previous section for a local homogeneous medium the partial density of states is then

$$\rho_p(\mathbf{r}, \omega) = \frac{\omega^2 \text{Re} \{ \epsilon(\omega) \}}{\pi^2 c^3}. \quad (\text{D.37})$$

D.5 Connection to energy dissipation

The principle importance of these results is that they connect directly to the rate of energy dissipation, and the first order term in light-matter interactions. Letting W denote work by classical definition

$$P(t) = \frac{dW}{dt} = -\frac{1}{2} \int dV' \text{Re} \{ \mathbf{j}^*(\mathbf{r}, t) \cdot \mathbf{E}(\mathbf{r}, t) \}. \quad (\text{D.38})$$

¹The difference between the photonic density of states found in Appendix A, and this photonic density of states are examined in greater depth in the *Dipoles Inside Hyperbolic Media* Appendix.

The results of this appendix then show

$$P(\omega) = \frac{\omega}{2} (\mathbf{p}(\omega) \cdot \text{Im}\{\mathbf{E}(\mathbf{r}, \omega)\}) \quad (\text{D.39})$$

$$P(\omega) = \lim_{\mathbf{r}' \rightarrow \mathbf{r}} \frac{\omega^3 |p(\omega)|^2 \mu_o}{2} (\mathbf{n}_p \cdot \text{Im}\{\check{\mathcal{G}}(\mathbf{r}, \mathbf{r}', \omega)\} \cdot \mathbf{n}_p), \quad (\text{D.40})$$

giving

$$P(\omega) = \frac{\mu_o \omega^4 |p(\omega)|^2}{12\pi c} \text{Re}\{\sqrt{\epsilon(\omega)}\}. \quad (\text{D.41})$$

Appendix E

Optical Properties of Carbon Nanotubes

As mentioned in Chapter 3, our calculation of the optical properties of carbon nanotubes has followed the Kubo formalism method described by Falkovsky and Varlamov [203]. The central equation for the dielectric permittivity tensor in this approach is

$$\epsilon_{ab}(k, \omega) = \epsilon_{sur} + \frac{e^2}{\hbar c \epsilon_o} \frac{P_{ab}(k, \omega)}{\omega}, \quad (\text{E.1})$$

where

$$P_{ab}(\omega, \mathbf{k}) = \int \frac{dp}{2\pi} \sum_{\omega_n} Tr [V_a(p) \mathcal{G}(\omega_n, p^+) V_b(p) \mathcal{G}(\omega_n, p^-)]. \quad (\text{E.2})$$

Here, P_{ab} denotes the polarization matrix, with the subscripts a and b indicating directions, \mathcal{G} the Matsubara Green function, ω the frequency of the exciting photon, ω_n the discrete frequencies of the Matsubara sum, Tr the trace operation, ϵ_o the permittivity of free space, ϵ_{sur} the relative permittivity of the surrounding medium, V_a the velocity operator matrix defined by the Heisenberg operator evolution equation

$$V_a = \dot{x}_a = \frac{[x_a, H]}{i\hbar} = \frac{\partial H}{\partial p_a}, \quad (\text{E.3})$$

p the momentum integration variable, and the $+$ and $-$ superscripts the values $p + \frac{k}{2}$ and $p - \frac{k}{2}$ with k standing for the momentum of the photon excitation. Moreover, the Green's function is explicitly defined as

$$\mathcal{G} = (i\omega_n - H(p))^{-1}, \quad (\text{E.4})$$

and its the sum over the discrete frequencies of the Matsubara sum, in terms of its matrix elements indexed by the subscripts i and j , by

$$\sum_{\omega_n} \mathcal{G}_i(\omega_n, p^+) \mathcal{G}_j(\omega_n, p^-) = \frac{f_o(\mathcal{E}_j(p^-)) - f_o(\mathcal{E}_i(p^+))}{\omega + i\eta - (\mathcal{E}_j(p^+) - \mathcal{E}_i(p^-))}. \quad (\text{E.5})$$

In these definitions H is the Hamiltonian of the system, η the loss parameter following the relaxation time approximation, and $f_o(\mathcal{E}_j)$ the Fermi distribution at the energy level of the j eigen state.

For the carbon nanotube system treated in the text, only π -orbital interactions have been considered due to the energy range of interest [363]. With these approximations the Hamiltonian is

$$H(p, j) = \gamma \left(e^{i\frac{ipa\sqrt{3}}{2} - \frac{i\pi j}{n}} + e^{i\frac{pa}{2\sqrt{3}} + \frac{i\pi j}{n}} + e^{-i\frac{pa}{\sqrt{3}}} \right), \quad (\text{E.6})$$

where a is the lattice constant for graphene, 2.46 \AA , j the angular number, p the momentum of the electron along the tube, n a constant related to the wrapping of the tube [194], and γ is the orbital overlap energy for graphene, 3.1 eV . The loss parameter $\eta = h/\tau$ is estimated with a relaxation of one picosecond [204, 205] for τ . The energy of the nanotube is similarly defined as

$$\mathcal{E}_j = \pm \gamma \sqrt{1 + 4 \cos\left(\frac{\sqrt{3}pa}{2}\right) \cos\left(\frac{j\pi}{n}\right) + 4 \cos^2\left(\frac{j\pi}{n}\right)}. \quad (\text{E.7})$$

To extend the theory presented by Falkovsky and Varlamov from graphene to the single layer nanotubes, the Hamiltonian associated with graphene is first enlarged to take into account the energy level splitting resulting from the additional confinement in the nanotube. This step is accomplished by the substitution

$$\begin{bmatrix} 0 & H \\ H^* & 0 \end{bmatrix} \rightarrow \begin{bmatrix} 0 & 0 & 0 & H_{\mathcal{E}_1} \\ 0 & 0 & H_{\mathcal{E}_2} & 0 \\ 0 & H_{\mathcal{E}_2}^* & 0 & 0 \\ H_{\mathcal{E}_1}^* & 0 & 0 & 0 \end{bmatrix}, \quad (\text{E.8})$$

with H as above, and the \mathcal{E}_1 and \mathcal{E}_2 subscripts denoting the lowest level energy bands for the particular chiral vector chosen following the discussion provided by Wong and Akinwade [199]. The velocity operators for axial, z , and angular direction, θ ,

are then:

$$V_z = \begin{bmatrix} 0 & 0 & 0 & v_{z\mathcal{E}1} \\ 0 & 0 & v_{z\mathcal{E}2} & 0 \\ 0 & v_{z\mathcal{E}2}^* & 0 & 0 \\ v_{z\mathcal{E}1}^* & 0 & 0 & 0 \end{bmatrix} \quad (\text{E.9})$$

for the axial direction, and

$$V_{\theta+} = \begin{bmatrix} 0 & 0 & v_{\theta\mathcal{E}2} & 0 \\ 0 & 0 & 0 & 0 \\ v_{\theta\mathcal{E}2}^* & 0 & 0 & 0 \\ 0 & 0 & 0 & 0 \end{bmatrix}, \quad V_{\theta-} = \begin{bmatrix} 0 & 0 & 0 & 0 \\ 0 & 0 & 0 & v_{\theta\mathcal{E}1} \\ 0 & 0 & 0 & 0 \\ 0 & v_{\theta\mathcal{E}1}^* & 0 & 0 \end{bmatrix} \quad (\text{E.10})$$

for increasing and decreasing angular momentum along the angular direction respectively, see [194]. Note that for the angular velocity operators the derivative is taken with respect to the natural discrete momenta. These operators are then converted to the eigenbasis of the Hamiltonian by the linear transformation $v \rightarrow U^\dagger v U$, with

$$U = \begin{bmatrix} -\frac{H_{\mathcal{E}1}}{|H_{\mathcal{E}1}|} & 0 & 0 & \frac{H_{\mathcal{E}1}}{|H_{\mathcal{E}1}|} \\ 0 & -\frac{H_{\mathcal{E}2}}{|H_{\mathcal{E}2}|} & \frac{H_{\mathcal{E}2}}{|H_{\mathcal{E}2}|} & 0 \\ 0 & 1 & 1 & 0 \\ 1 & 0 & 0 & 1 \end{bmatrix}. \quad (\text{E.11})$$

An identical procedure is undertaken for the effective mass operators, $M_{ij} = \pm \frac{1}{\hbar^2} \frac{\partial^2 H}{\partial p_i \partial p_j}$, for the calculation of the static conductivities used in the relaxation time approximation. With these substitutions the procedure detailed by Falkovsky and Varlamov [203], equations (E.1) and (E.2), can be followed directly to achieve Fig.4.4.

Appendix F

Additional Results for Natural Hyperbolic Media

As a companion to the results presented in Chapter 5, in this appendix we examine the differences encountered in calculating the Purcell factor, the ratio of the power emitted by an electric dipole compared to vacuum, for isotropic and anisotropic media, and provide additional results for the anisotropic Green function.

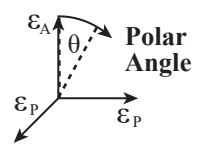
F.1 Issues in the Purcell factor and photonic density of states

In modern convention, the Purcell factor (PF) is defined in terms of quantum fluctuations of the electric field as

$$\mathcal{P}(\omega) = \left(\int_{V_{\mathbf{k}}} dV_{\mathbf{k}} \langle 0 | \hat{E}_{j\ med}^2(\mathbf{k}) | 0 \rangle \delta(\omega_{\mathbf{k}} - \omega) \right)_N, \quad (\text{F.1})$$

(Fermi's Golden Rule) with \mathbf{k} denoting the reciprocal space vector, $V_{\mathbf{k}}$ the volume of reciprocal space, ω the frequency, $\hat{E}_{j\ med}^2(\mathbf{k})$ the component of the effective electric field operator ($\hat{\mathbf{E}}_{med}(\mathbf{k}) = \hat{\mathbf{E}}_{vac}(\mathbf{k}) / \sqrt{\epsilon(\omega)}$ [268]) of the mode \mathbf{k} along the transition dipole moment, $\epsilon(\omega)$ the relative permittivity of the medium, $|0\rangle$ the 'vacuum' state of the medium (equilibrium state), and the N subscript is introduced as a shorthand that the enclosed quantity is normalized by its free space value ($\epsilon(\omega) = 1$). Using the Green function formulation [359], (F.1) is interpreted classically as the relative rate of emission of an electric dipole

$$\mathcal{P}(\omega) = -Re\left\{ \int_V dV \mathbf{j}^*(\mathbf{r}, \omega) \mathbf{E}(\mathbf{r}, \omega) \right\}_N = -Im\left\{ \int_{V_{\mathbf{k}}} dV_{\mathbf{k}} \mathbf{j}^*(\mathbf{k}, \omega) \check{\mathcal{G}}(\mathbf{k}, \omega) \mathbf{j}(\mathbf{k}, \omega) \right\}_N, \quad (\text{F.2})$$

Medium:	Isotropic ($\epsilon_A = \epsilon_P$)			Anisotropic ($\epsilon_A \neq \epsilon_P$)		
	Vacuum	Dielectric	Metal	Uniaxial Crystal	<u>Epsilon-Near-Zero</u>	<u>Hyperbolic</u>
Permittivity:	$\text{Re}(\epsilon) = 1$ $\text{Im}(\epsilon) = 0$	$\text{Re}(\epsilon) > 0$ $\text{Im}(\epsilon) > 0$	$\text{Re}(\epsilon) < 0$ $\text{Im}(\epsilon) > 0$	$\text{Re}(\epsilon_{\{A,P\}}) > 0$ $\text{Im}(\epsilon_{\{A,P\}}) > 0$	$\text{Abs}(\epsilon_{A \text{ or } P}) \approx 0$ $\text{Im}(\epsilon_{\{A,P\}}) > 0$	$\text{Re}(\epsilon_A)\text{Re}(\epsilon_P) < 0$ $\text{Im}(\epsilon_{\{A,P\}}) > 0$
	Si @ 2000 cm^{-1} $\epsilon = 11.7 + i 10^{-9}$	Au @ 5000 cm^{-1} $\epsilon = -158 + i 21$	TiO ₂ @ 850 cm^{-1} $\epsilon_A = 1 + i 0.3$ $\epsilon_P = 0.3 + i 0.4$	Au / Al ₂ O ₃ Nanowire @ 15875 cm^{-1} $\epsilon_A = 0.01 + i 0.05$ $\epsilon_P = 8 + i 0.1$	hBN @ 1500 cm^{-1} $\epsilon_A = 2.6 + i 10^{-4}$ $\epsilon_P = -4 + i 0.2$	

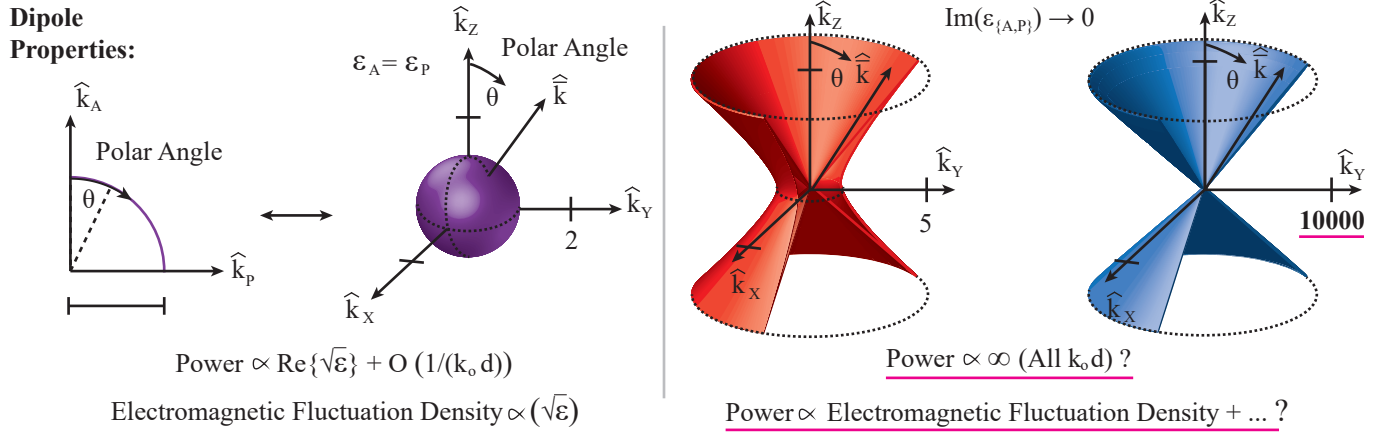


Figure F.1: **Overview of material properties and Purcell factor.**

The top half of the figure displays the material permittivity (ϵ) classifications used throughout this appendix, along with examples for each class. The inset shows the permittivity labeling convention. All factors of ϵ have an unwritten dependence on the frequency ω . The bottom half of the figure shows the permittivity dependence of the Purcell factor and the electromagnetic fluctuation density. In these expressions d is the characteristic size of the emitter, or correlation size of the current density, and $k_0 = \omega/c$. In the anisotropic media column the plotted surfaces correspond to the transverse and longitudinal fluctuation densities, shown with artificial cuts. Building off the results of Chapter 5, we present a more detailed examination of the Purcell factor.

with V standing for the volume of the real space, $\mathbf{j}(\mathbf{r})$ the current density, $\mathbf{E}(\mathbf{r})$ the electric field, and $\check{\mathcal{G}}(\mathbf{k}, \omega)$ the Green function (tensor) for the electric field.

In either view, as describe in the introduction of this thesis, the PF is a first order determination of the interaction between the equilibrium fields of a medium and an external emitter, and thus is of key importance for determining the potential of optical engineering applications. In nanophotonics literature this quantity is also understood in terms of, or directly defined as, the photonic density of states of the medium [267]. As we are considering this quantity inside a medium, for the sake of consistency we will not use this definition (see below). Regardless of the particular definition used, there are major issues in extending the interpretation of the photonic density of states to anisotropic media.

Before facing these concerns, it is worthwhile to recap why the two quantities are typically thought of as interchangeable. By symmetry, in isotropic media the effective electric field operator depends only on the magnitude of \mathbf{k} , and (F.1) is evaluated by the means of the wave equation $k = \omega \sqrt{\epsilon(\omega)}/c$. Using this identity, the PF is broken into the product of two factors: the expectation value of the relative energy density of the electric field, $\langle 0 | \hat{E}_{j m}^2(\omega) | 0 \rangle \propto 1/\epsilon(\omega)$, and the photonic density of states, $\propto \sqrt{\epsilon(\omega)}^3 \omega^2 d\omega/c^2$ as defined by

$$\mathcal{D}(\omega) = \left(\int_{\delta V_{\mathbf{k}}} dV_{\mathbf{k}} \right)_N, \quad (\text{F.3})$$

where $\delta V_{\mathbf{k}}$ stands for the differential volume between the surfaces in reciprocal space found by evaluating the wave equation at ω , and $\omega + \delta\omega$ in the limit $\delta\omega \rightarrow 0$. Multiplying these factors, the PF is found to be $\propto \sqrt{\epsilon(\omega)}$, (first row Tab.1, and purple lines Fig. F.1). Consequently, for a given isotropic media the magnitude of the PF follows the magnitude of the photonic density of states (PDoS); a larger PDoS results in a larger PF, and a smaller PDoS in a smaller PF. Moreover, if the emitter is located in free space, so that $\hat{\mathbf{E}}_{med}(\mathbf{k}) = \hat{\mathbf{E}}_{vac}(\mathbf{k})$, the connections between the PF and PDoS given by (F.1) and (F.2) allow the two quantities to be conflated¹.

This intuitive relation between the magnitude of the PDoS and PF does not hold in anisotropic media. As the value of both the effective electric field operator, $\langle 0 | \hat{E}_{j med}^2(\mathbf{k}) | 0 \rangle$, and differential number of states, $dk^3 \delta(\omega_{\mathbf{k}} - \omega)$, now depend on the direction of \mathbf{k} , the integral expression for the PF (F.1) can not be factorized

¹This is the usual case in nano-photonic problems, and so the usual convention of taking (F.2) as the definition of the photonic density of states $\lim_{\mathbf{r}' \rightarrow \mathbf{r}} \text{Im} \{G(\mathbf{r} - \mathbf{r}', \omega)\}$ [267] is sensible in this context.

Case	Isotropic	Uniaxial axis	Uniaxial plane
$\mathcal{D}(\omega)$	$\epsilon\sqrt{\epsilon}$	$\epsilon_P^{3/2} + \sqrt{\epsilon_P}\epsilon_A$	$\epsilon_P^{3/2} + \sqrt{\epsilon_P}\epsilon_A$
$\mathcal{P}(\omega)$	$\sqrt{\epsilon}$	$\sqrt{\epsilon_P}$	$\frac{\epsilon_A + 3\epsilon_P}{\sqrt{\epsilon_P}}$
$\mathcal{D}(\omega)/\mathcal{P}(\omega)$	ϵ	$\epsilon_P + \epsilon_A$	$\frac{\epsilon_P^2 + \epsilon_A\epsilon_P}{3\epsilon_P + \epsilon_A}$
$\epsilon \rightarrow 0 \mid \epsilon_p \rightarrow 0$	$\rightarrow 0$	$\rightarrow \epsilon_A$	$\boxed{\rightarrow \infty}$

Table F.1: **Permittivity proportionality of the photonic density of states and Purcell factor.**

The table displays the permittivity dependence of the photonic density (PDoS = $\mathcal{D}(\omega)$) and Purcell factor (PF = $\mathcal{P}(\omega)$) for lossless isotropic and uniaxial media. Each permittivity factor has an unwritten dependence on the frequency ω (see Fig. F.2 for labeling conventions). The box highlights the peculiar permittivity dependence of the PF for a dipole in the plane of a uniaxial crystal in the $\epsilon_p \rightarrow 0$ limit.

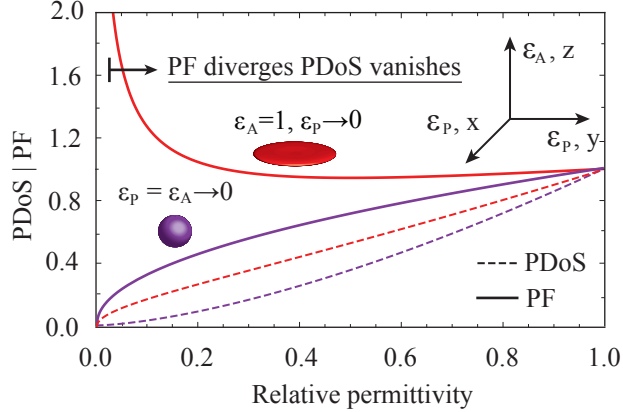


Figure F.2: **Relative scaling of the photonic density of states and Purcell factor.**

The figure shows the photonic density of states (PDoS), dashed lines, and Purcell factor (PF), solid lines, for a dipole in a uniaxial crystal oriented in the optic plane, as either the total ($\epsilon_P(\omega) = \epsilon_A(\omega)$), purple lines, or planar ($\epsilon_p(\omega)$), red lines, permittivity is brought to zero. The inset shows the coordinate system considered throughout (z-axis parallel to the optical axis), and schematic views of the the surfaces produced by solving the respective wave equations in reciprocal space. In isotropic media, the magnitude of the PF follows the magnitude of the PDoS. In anisotropic media this relation does not hold, and anomalous variation is observed in the relative behaviour of the two quantities.

like the isotropic case. As shown in Fig. F.2 and Tab. F.1, this change leads to remarkable variation in the relative values of the PDoS and PF depending on the

orientation of the dipole and specific values of the relative permittivity factors. For example, as displayed in Fig. F.2, as the planar permittivity of a lossless uniaxial crystal approaches zero the PF diverges, despite a vanishing PDoS².

The link between the PDoS and PF is further complicated by the continuation of the PF to absorbing ($Im\{\epsilon(\omega)\} > 0$) and metallic ($Re\{\epsilon(\omega)\} < 0$) media [364]. Using (F.2), the continuation of the PF is found to be

$$\mathcal{P}^I(\omega) = Re\{\sqrt{\epsilon}\} + \frac{2\pi Im\{\epsilon\}}{(k_o^3 d^3) |\epsilon|^2} \quad (\text{F.4})$$

for isotropic media, and

$$\begin{aligned} \mathcal{P}^U(\omega) = \mathbf{n} Re \left\{ \left(\begin{array}{ccc} \frac{\epsilon_A + 3\epsilon_P}{4\sqrt{\epsilon_P}} & 0 & 0 \\ 0 & \frac{\epsilon_A + 3\epsilon_P}{4\sqrt{\epsilon_P}} & 0 \\ 0 & 0 & \sqrt{\epsilon_P} \end{array} \right) + \int_0^\pi d\theta s(\theta) \left(\begin{array}{ccc} c^2(\theta) & 0 & 0 \\ 0 & c^2(\theta) & 0 \\ 0 & 0 & 2s^2(\theta) \end{array} \right) \right. \\ \left. + \frac{3i c^2(\theta) s^2(\theta) (\epsilon_A - \epsilon_P)^2}{4\epsilon_U^2(\theta) (k_o d)} + \left(\begin{array}{ccc} 1 & 0 & 0 \\ 0 & 1 & 0 \\ 0 & 0 & -2 \end{array} \right) \frac{3i c^2(\theta) s^2(\theta) (\epsilon_A^2 - \epsilon_P^2)}{4\epsilon_U^2(\theta) (k_o d)} + \right. \\ \left. \left(\begin{array}{ccc} s^2(\theta) & 0 & 0 \\ 0 & s^2(\theta) & 0 \\ 0 & 0 & 2c^2(\theta) \end{array} \right) \frac{6\pi i \epsilon_U^*(\theta)}{4|\epsilon_U(\theta)|^2 (k_o^3 d^3)} \right\} \mathbf{n} \quad (\text{F.5}) \end{aligned}$$

for uniaxial media in the limit of a vanishingly small Gaussian distributed electric dipole with size parameter d . As in Chapter 5, the I superscript serves to note that the result applies specifically to isotropic media, and the U superscript that the result applies to uniaxial media. Likewise, $s(\theta)$ and $c(\theta)$ again stand as short-hands for the *sin* and *cos* functions, ϵ for $\epsilon(\omega)$, \mathbf{n} for the unit vector direction of the dipole, k_o for the characteristic inverse length ω/c , and $\epsilon_U(\theta)$ for the effective angular permittivity, $\epsilon_U(\theta) = s^2(\theta)\epsilon_P + c^2(\theta)\epsilon_A$, of a uniaxial medium following the coordinate convention shown in Fig. F.1.

²It is primarily for this reason that we introduced the fluctuation density in Chapter 5.

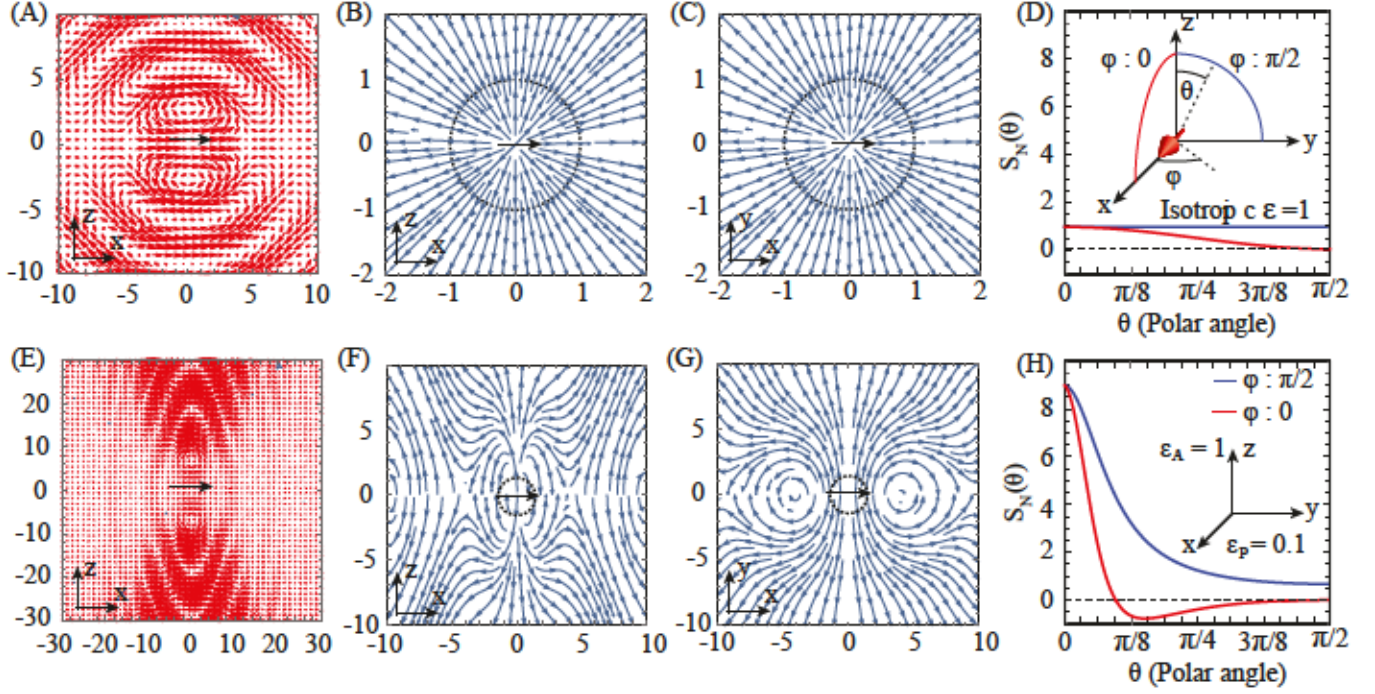


Figure F.3: Dipole emission patterns in a uniaxial media.

The figure shows the real part of the electric field (panels A and E), streamlines (the movement of a point following the vector field) of the Poynting vector (panels B,C,F, and G); and the radial Poynting vector at a distance of one wavelength from the dipole (panels D and H), along the $\phi = 0$ and $\phi = \pi/2$ cut lines shown in the inset panel (D), for a dipole oriented along the x -axis of a uniaxial medium as the planar permittivity ϵ_p is reduced from vacuum ($\epsilon_p = 1$, top row) to 0.1 ($\epsilon_p = 0.1$, bottom row). The axis labels denote distance from the dipole normalized by the wavelength. In panels (D) and (H) the magnitude of the radial Poynting vector is normalized by the peak value of the vacuum case, $S_N \hat{r}$. The inset in (C) shows the coordinate system considered throughout this appendix. As $\epsilon_p \rightarrow 0$ there are two features of importance: (1) the fields and corresponding emission become concentrated along the optical axis (direction of highest permittivity), (2) although $Im\{\epsilon_A, \epsilon_p\} = 0$ and $Re\{\epsilon_A, \epsilon_p\} > 0$ the streamlines near the dipole axis swirl and bend inwards. Since the media considered are not absorbing (F.6) is an equality.

Following the $Re\{\epsilon\} > 0$, $Im\{\epsilon\} = 0$ evaluations of the PF for an isotropic medium given in Tab.1, the suggested pattern would have the PDoS proportional to the PF, (F.4) and (F.5), up to terms depending on the size parameter of the emitter (terms that not depend on d). Yet, for certain values of ϵ_A and ϵ_P the d independent terms of (F.5) (first matrix) may be strangely negative; despite the fact that a negative value would seemingly go against (F.1), and can never occur in the isotropic result (F.4). Furthermore, for hyperbolic media ($Re\{\epsilon_A\}Re\{\epsilon_P\} < 0$) the PDoS is known to diverge in the limit of low loss [137, 365], leading to emission enhancement that has been experimentally observed [138, 257, 261]. These observations suggest that the d independent terms of the uniaxial PF should also diverge. However, (F.5) shows no such characteristic feature.

F.2 Dipole emission in anisotropic media

To help understand the Purcell factor in uniaxial media, and give pictorial view of charge the density resonances discussed in Chapter 5, we now examine the electric field and Poynting vector ($\mathbf{S} = Re\{\mathbf{E} \times \mathbf{H}^*\}$ where \mathbf{H} is the magnetic induction field) of an electric dipole in the optic plane of a uniaxial crystal as anisotropy is introduced (Fig. F.3, Fig. F.4).

As the PF is classically equivalent to the (normalized) power required to maintain the oscillation of an electric dipole, (F.2). By Poynting's theorem, this power is in turn equal to the sum of the power absorbed and the power radiated from the surface of any volume as determined by the expression $R = \int_{\partial V} d\partial V \mathbf{S} \cdot \mathbf{s}$, where \mathbf{s} is the unit vector normal to the surface of the volume, and ∂V the boundary of the volume. If the medium is not absorbing, then R normalized by the emission of an electric dipole in vacuum, R_N , is equal to the PF. More generally, given that energy is used and not produced by a passive medium, the normalized power emitted is a lower bound of the PF,

$$R_N(\omega) = \int_{\partial V} d\partial V \mathbf{S}_N \cdot \mathbf{s} \leq \mathcal{P}(\omega). \quad (\text{F.6})$$

Taking $Im\{\epsilon\} = 0$ so that (F.6) is an equality, Fig. F.3 displays the electric field and Poynting vector as the magnitude of the planar permittivity (ϵ_P) drops below that of the axial permittivity (ϵ_A). Following the figure, the resulting fields are found to be radically different than those of a dipole in an isotropic medium. First, the magnitude electric field is seen to become larger along the optical axis, while the phase accumulation is observed to decrease. This effect is a consequence of the continuity of the electric displacement field, $\nabla \cdot \mathbf{D} = 0$, and the phase propagation of

a plane wave, $Exp(i\sqrt{\epsilon} \mathbf{k} \cdot \mathbf{r})$. Along the axis perpendicular to the dipole, (E), the electric field lies in the $\hat{\mathbf{x}}$ direction so that it interacts exclusively with ϵ_P , and so the accumulation of phase requires large propagation distances. But, as the polar angle increase towards the XY plane the direction of the electric is modified so that it begins to act with both permittivity component, correspondingly modifying the phase accumulation. Similarly, imagining an area with top and bottom edges following the contours traced by the electric field and perpendicular right and left boundaries, satisfying $\nabla \cdot \mathbf{D} = 0$ requires that electric field must be relatively enhanced along the optical axis. Since the magnetic field is determined by $\nabla \times \mathbf{E} = -\partial \mathbf{B} / \partial t$, this enhancement of the electric field is also passed on to the magnetic field, acting to produce an enhancement of the radial Poynting vector along the optical axis that is nearly a factor of ten larger than the total emission enhancement $R_N(\omega) = (\epsilon_A + 3\epsilon_P) / (4\sqrt{\epsilon_P})$, which is in fact equal to the d independent term of the uniaxial PF, (H). Viewing panels (B,C,D) and (F,G,H) the global characteristic of the Poynting vector are equally interesting. Since the only free charge present is the dipole located at the origin, it might be expected that the streamlines, the movement of a point following the vector field, of the Poynting vector field should never turn towards the XY or XZ planes (each coordinate should always increase). Yet, without introducing loss (F,G) clear swirls develop as soon as anisotropy is introduced. (The net power flow into any volume not containing the dipole is still zero. As when the streamlines bend towards the dipole axis in one plane, they bend away from the dipole axis in the other.) Note that logically these swirls must develop if the large emission enhancement observed along the optical axis is to be consistent with the PF as required by the equality of (F.6).

Considering a small amount of loss to avoid divergence, Fig. F.4, the enhanced emission of the electric dipole is observed to increase as the epsilon-near-zero condition is approached, $|\epsilon_P| \approx 0$, following the general trend suggested by the $\mathcal{P}^U(\omega) = R_N(\omega) = (\epsilon_A + 3\epsilon_P) / (4\sqrt{\epsilon_P})$ lossless evaluation of the PF³. Yet contrary to the behaviour predicted by this term, the emission enhancement is seen to continue across the hyperbolic transition, $Re\{\epsilon_P\} < 0$ [257, 261]. By (F.6) this result shows that the uniaxial PF (F.5) remains positive despite the appearance of the d independent terms. Moreover, the influence of the enhanced PDoS occurring from hyperbolic response is clearly visible.

The reconciliation of the observed emission enhancement, acting as a lower bound for the PF, in the hyperbolic regime with the permittivity dependence of the d in-

³Note that as $|\epsilon_P| \rightarrow 0$ even relatively small amounts of loss $Abs[Re\{\epsilon_P\}] \ll Im\{\epsilon_P\}$ drastically alter this behavior

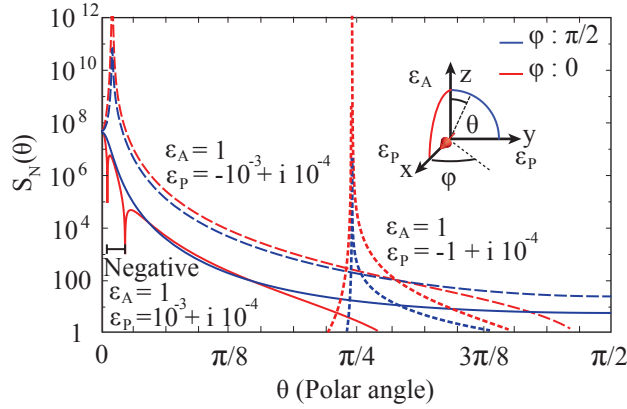


Figure F.4: **Dipole emission across a hyperbolic transition.**

The figure shows the radial component of the Poynting vector, $\mathbf{S}_N \hat{\mathbf{r}}$, normalized to the vacuum maximum ($\epsilon_P = \epsilon_A = 1$) at a distance of one wavelength from the dipole. The permittivity values considered are $\epsilon_A = 1$, $\epsilon_P = 10^{-3} + i10^{-4}$ (solid line), $\epsilon_A = 1$, $\epsilon_P = -10^{-3} + i10^{-4}$ (large dashes), and $\epsilon_A = 1$, $\epsilon_P = -1 + i10^{-4}$ (small dashes), corresponding to the transition from an ellipsoidal to a hyperbolic media. The enhancement of the radial Poynting vector does not decrease or become negative in the hyperbolic regime. By (F.6) this means that the PF must also remain positive. Such behaviour would not be expected from the lossless evaluation of the uniaxial PF (F.5).

dependent terms of (F.5) is achieved through the contribution of the d dependent terms. Rather than tending to zero as optical absorption ($Im\{\epsilon\}$) is decreased, as in isotropic media⁴, the zero approached in the $\epsilon_U(\theta)$ factors causes these terms to become increasingly dominant in low loss hyperbolic and epsilon-near-zero media. In other words, the $Im\{\epsilon_A, \epsilon_P\} = 0$ evaluation of the uniaxial PF is not equivalent to the physically relevant limit of $Im\{\epsilon_A, \epsilon_P\} \rightarrow 0$. Surprisingly, there is no physical situation in which the d dependent terms of (F.5) can be properly ignored [257,261].

F.3 Calculation of the Purcell factor

To calculate the PFs (F.4) and (F.5), we begin with the Green function definition, as given in Chapter 5, and the relative rate of spontaneous emission, (F.2). Switching to spherical coordinates and normalizing the integral by k_o this equation becomes

$$\mathcal{P}^I(\omega) = -Im \left\{ \int_0^\pi \int_0^\infty \int_0^{2\pi} d\theta dk d\phi k^2 s(\theta) \mathbf{j}^*(\mathbf{k}, \omega) \left(\frac{\hat{\mathbf{p}} \otimes \hat{\mathbf{p}}}{k^2 - \epsilon} + \frac{\hat{\mathbf{s}} \otimes \hat{\mathbf{s}}}{k^2 - \epsilon} - \frac{\hat{\mathbf{k}} \otimes \hat{\mathbf{k}}}{\epsilon} \right) \mathbf{j}(\mathbf{k}, \omega) \right\}_N \quad (\text{F.7})$$

⁴A similar pole occurs in isotropic media with $Re\{\epsilon\} = 0$ as $Im\{\epsilon\} \rightarrow 0$. However, this behavior is not dispersive. Integrating over frequency the effect of this pole is removed.

for an isotropic medium, and

$$\mathcal{P}^U(\omega) = -Im \left\{ \int_0^\pi \int_0^\infty \int_0^{2\pi} d\theta dk d\phi k^2 s(\theta) \mathbf{j}^*(\mathbf{k}, \omega) \left(\frac{\hat{\mathbf{p}} \otimes \hat{\mathbf{p}}}{k^2 - \epsilon_E(\theta)} + \frac{\hat{\mathbf{s}} \otimes \hat{\mathbf{s}}}{k^2 - \epsilon_P} - \frac{\hat{\mathbf{k}} \otimes \hat{\mathbf{k}}}{\epsilon_U(\theta)} + \frac{c^2(\theta) s^2(\theta) (\epsilon_P - \epsilon_A)^2}{\epsilon_U^2(\theta)} \frac{\hat{\mathbf{k}} \otimes \hat{\mathbf{k}}}{k^2 - \epsilon_E(\theta)} + \frac{c(\theta) s(\theta) (\epsilon_P - \epsilon_A)}{\epsilon_U(\theta)} \left(\frac{\hat{\mathbf{p}} \otimes \hat{\mathbf{k}} + \hat{\mathbf{k}} \otimes \hat{\mathbf{p}}}{k^2 - \epsilon_E(\theta)} \right) \right) \mathbf{j}(\mathbf{k}, \omega) \right\}_N \quad (\text{F.8})$$

for a uniaxial medium.

Without a model of the current source, there is no systematic way to evaluate (F.7) and (F.8). To proceed to (F.4) and (F.5), a finite Gaussian current source is assumed,

$$\mathbf{j}(\mathbf{r}, \omega) = e^{-i\omega t} \left(\frac{\sqrt{2}}{d} \right)^3 e^{-2\pi r^2/d^2} \hat{\mathbf{n}} \quad (\text{F.9})$$

$$\mathbf{j}(\mathbf{k}, \omega) = e^{-i\omega t} e^{-k^2 d^2/8\pi} \hat{\mathbf{n}},$$

where d acts a size parameter controlling the extent of the distribution. (Due to the k_o normalization of the k integrals in (F.7) and (F.8), when this distribution is substituted into the integral expressions for the PF d is replaced by $k_o d$.) Inserting (F.9) into (F.7) and (F.8), the $d\phi$ integral can be performed using standard trigonometric identities. The dk integrals then fall into two categories, integrals of the form ① $k^2 e^{-k^2 k_o^2 d^2/4\pi}$, and integrals of the form ② $k^2 e^{-k^2 k_o^2 d^2/4\pi} / (k^2 - \sigma)$ where σ is a complex number with a positive imaginary component. Since the bounds of integration do not depend on the size parameter d , the k^2 factor in the numerator of these expressions is removed using the identity $k^2 e^{-k^2 k_o^2 d^2/4\pi} = -2\pi / (k_o^2 d) (\partial/\partial d) e^{-k^2 k_o^2 d^2/4\pi}$ and interchanging the order of operation between the integral and derivative. The resulting integrals are then evaluated as

$$\int_0^\infty dk e^{-k^2 k_o^2 d^2/4\pi} = \frac{\pi}{k_o d}, \quad (\text{F.10})$$

and

$$\int_0^\infty dk \frac{e^{-k^2 k_o^2 d^2/4\pi}}{k^2 - \sigma} = \frac{\pi e^{-\sigma k_o^2 d^2/4\pi} \left(i - \text{Erfi} \left(\sqrt{\frac{\sigma d^2 k_o^2}{4\pi}} \right) \right)}{\sqrt{\sigma}}, \quad (\text{F.11})$$

where $Erfi(\dots)$ is the imaginary error function. Applying the derivative operator $-2\pi/(dk_o^2)(\partial/\partial d)$, these expressions become

$$\textcircled{1} = 2\pi^2/(k_o^3 d^3), \text{ and}$$

$$\textcircled{2} = -\frac{\pi}{k_o d} + e^{-\sigma k_o^2 d^2/4\pi} \frac{\pi\sqrt{\sigma}}{2} \left(-i + Erfi\left(\sqrt{\frac{\sigma d^2 k_o^2}{4\pi}}\right) \right).$$

If $\sigma k_o^2 d^2 \ll 1$, then $\textcircled{2} \approx -\pi/(k_o d) - i\pi\sqrt{\sigma}/2^5$, and substituting into (F.7) and (F.8) yields (F.4) and (F.5)⁶.

F.4 Physical constraints on non-locality in polarization response

Since $\epsilon(k, \omega) - 1 = \chi(k, \omega)$ is a susceptibility, we may assume that it is analytic for all but a finite set of points in the complex k plane for a given ω [366]. Therefore, we can conclude that there is then a convergent Laurent series expansion in complex k such that

$$\chi(k, \omega) = \sum_{n=-\infty}^{\infty} c_n(\omega) k^n \quad (\text{F.12})$$

for $M < |k| < \infty$, where M is magnitude of the largest \mathbf{k} pole of $\chi(k, \omega)$, and $\{c_n(\omega)\}$ is the set of coefficients of the expansion. Accepting that the polarization of any medium must ultimately be limited by some material size parameter, we may also freely assume that $|k| \rightarrow \infty \Rightarrow \chi(k, \omega) \rightarrow 0$ for any ω . And so, $c_n(\omega) = 0$ for all $n \geq 0$.

Now, as we have only considered spaces with inversion symmetry the equality $\epsilon(\mathbf{k}, \omega) = \epsilon(k, \omega)$ has been used throughout. Nevertheless, the true parameter in reciprocal space for the polarization susceptibility is \mathbf{k} , and the above reasoning implies that there must be an equally valid Laurent expansion in k_x, k_y and k_z . To keep inversion symmetry in these expressions only even powers can appear. The equivalence of the two descriptions then implies that $\chi(k, \omega)$ can only contain even values of k^n . Combining this observation with $c_n(\omega) = 0$ for all $n \geq 0$ shows that asymptotically $\chi(k, \omega)$ is at least proportional to $1/k^2$. Therefore, since in the complex plane any polynomial can be decomposed as the product of linear factors, we

⁵In the limit of a lossless hyperbolic or epsilon-near-zero media this limit can not be taken.

⁶To find the uniaxial expression shown in the text expand all terms that do not have a $1/(k_o d)^3$ factor to a common denominator of $\epsilon_V^2(\theta)$, and integrate the d independent term.

must have

$$\chi(k, \omega) = \frac{Z(k + a_1(\omega)) \dots (k + a_n(\omega))}{(k + b_1(\omega)) \dots (k + b_m(\omega))}, \quad (\text{F.13})$$

where $n \geq m + 2$ are the number of factors in the numerator and denominator, and Z is an arbitrary complex number.

Returning to real k , we note that because $\chi(\mathbf{r}, t)$ is a real quantity $\chi(k, \omega)$ must obey the relation $\chi^*(k, -\omega) = \chi(k, \omega)$, where $*$ is the complex conjugate. Since this equality must hold for all values of k and ω , and in the large k limit $\chi(k, \omega) \propto Z/k^2$, we must have $Z = Z^*$. Taking the imaginary part of $\chi(k, \omega)$ we then have

$$\text{Im}\{\epsilon(k, \omega)\} = \text{Im}\{\chi(k, \omega)\} \propto Z/k^l, \quad (\text{F.14})$$

(in the limit of large k) with $l \geq 3$ (since Zk^n is real); confirming that any physically acceptable model of permittivity response will be sufficient to make (5.36) converge.

F.5 Validity of the local response approximation for hexagonal boron nitride and bismuth selenide in the infrared

For hexagonal boron nitride and bismuth selenide, the largest absolute value achieved by the permittivities $\epsilon_A(\omega)$, $\epsilon_P(\omega)$, and $\epsilon_E(\omega)$ in (5.34) is ≈ 400 , and the smallest ≈ 0.1 . Based on the maximum permittivity bound, in the local approximation the poles of the wave equations occur no higher than $k \approx 20 k_0$. Taking the largest lattice spacing present in either material, $\approx 3 \text{ nm}$, this upper limit of k still corresponds to less than 1% of the Brillouin zone for wavelengths longer than $6 \mu\text{m}$. As such a small change will only minimally alter the probed bandstructure around the dominant optical phonon features [247, 367, 368], there is no reason to expect that k dependence will introduce variation in the relative permittivities on the order of the lower magnitude bound. This being the case, it should be expected that including spatial non-locality will not tangibly alter (5.37) or (5.38).

By the same logic, the contribution of additional non-local poles should also be minimal. If a factor of $1/(k^2 - \epsilon_X(k, \theta, \omega))$ at a particular frequency is rewritten in term of linear factors, it will be of the form

$$\frac{1}{k^2 - \epsilon_X(k, \theta, \omega)} = \frac{(k - b_1) \dots (k - b_n)}{(k - a)(k + a)(k - c_1) \dots (k - c_n)}, \quad (\text{F.15})$$

where b_i and c_i are related non-local constants with $\prod_{i=1}^n b_i \approx \prod_{i=1}^n c_i$, and $a \approx \sqrt{\epsilon_x(\theta, \omega)}$. So long as the c_i poles are large compared to the a_i poles, $a_i \ll c_i$, the resulting residues from the c_i poles are likely to be much smaller than the residues resulting from the a_i poles.

F.6 Half-Space transverse thermal electric field fluctuations

Finally, we show that half-space transverse electric field fluctuations follow the same form as the full-space fluctuations, a result assumed in Chapter 5 to show the similarities between the full near-field energy density and the fluctuation density. Requiring that current fluctuations can occur only in the lower half space, the Rytovian expression for current correlations becomes

$$\begin{aligned} \langle j^{B*}(\mathbf{k}, \omega) j^Z(\mathbf{k}', \omega) \rangle_N &= -i (\epsilon^{BZ}(\omega) - \epsilon^{ZB*}(\omega)) \delta((\mathbf{k} - \mathbf{k}') \hat{\rho}) \\ &\quad \left(\frac{i(\mathbf{k}' - \mathbf{k}) \hat{\mathbf{z}}}{((\mathbf{k}' - \mathbf{k}) \hat{\mathbf{z}})^2 + \delta^2} + \frac{\delta}{((\mathbf{k}' - \mathbf{k}) \hat{\mathbf{z}})^2 + \delta^2} \right) \end{aligned} \quad (\text{F.16})$$

$$\begin{aligned} \langle j^B(\mathbf{k}, \omega) j^{Z*}(\mathbf{k}', \omega) \rangle_N &= -i (\epsilon^{BZ}(\omega) - \epsilon^{ZB*}(\omega)) \delta((\mathbf{k} - \mathbf{k}') \hat{\rho}) \\ &\quad \left(\frac{i(\mathbf{k} - \mathbf{k}') \hat{\mathbf{z}}}{((\mathbf{k} - \mathbf{k}') \hat{\mathbf{z}})^2 + \delta^2} + \frac{\delta}{((\mathbf{k} - \mathbf{k}') \hat{\mathbf{z}})^2 + \delta^2} \right). \end{aligned}$$

Here, δ denotes the infinitesimal value used in defining the Fourier transform of the Heaviside function, $\check{\epsilon}(\omega)$ is symmetric, and $\hat{\rho}$ and $\hat{\mathbf{z}}$ are the unit directions of the standard cylindrical coordinates. (In comparing the half-space and full-space there is also an overall factor of $1/2$, but this factor is absorbed in the new normalization.)

Replacing every occurrences of \mathbf{k} in (F.16) with the equivalent cylindrical coordinate expression $\sqrt{k_z^2 + k_\rho^2}$, and analytically continuing into the complex k_z plane, the transverse thermal electric field fluctuation of a half-space is

$$\begin{aligned} \chi_{half}^{XY}(\mathbf{r}, \mathbf{r}', \omega) &= \text{Re} \left\{ \int_{V_k} \int_{-\infty}^{\infty} d\mathbf{k}' dk_z e^{i(k'_x(x'-x) + k'_y(y'-y) + k_z|z| - k'_z|z'|)} \left(\check{I} - \hat{\mathbf{k}} \otimes \hat{\mathbf{k}} \right) \right. \\ &\quad \check{\mathcal{G}}^{U*}(k'_x, k'_y, k_z, \omega) \left(\frac{i(k_z - k'_z)}{(k_z - k'_z)^2 + \delta^2} + \frac{\delta}{(k_z - k'_z)^2 + \delta^2} \right) \\ &\quad \left. \text{Im} \{ \check{\epsilon}(\omega) \} \check{\mathcal{G}}^U(k'_x, k'_y, k'_z, \omega) \left(\check{I} - \hat{\mathbf{k}} \otimes \hat{\mathbf{k}} \right) \right\}_N, \end{aligned} \quad (\text{F.17})$$

with the absolute value signs on $|z|$ and $|z'|$ resulting from explicitly setting the field evaluation points to be in the lower half-space. As the action of $(\check{I} - \hat{\mathbf{k}} \otimes \hat{\mathbf{k}})$ on $\check{G}^U(k'_x, k'_y, k_z, \omega)$ removes all terms in the Green function that have $\hat{\mathbf{k}}$ as the left vector in the exterior product, using the identities $\hat{\mathbf{k}}'_{ord} \otimes \hat{\mathbf{k}}'_{ord} Im\{\check{\epsilon}(\omega)\} \hat{\mathbf{k}}'_{ex} \otimes \hat{\mathbf{k}}'_{ex} = 0$, $\hat{\mathbf{k}}'_{ord} \otimes \hat{\mathbf{k}}'_{ord} Im\{\check{\epsilon}(\omega)\} \hat{\mathbf{k}}' \otimes \hat{\mathbf{k}}'_{ex} = 0$, and $\hat{\mathbf{k}}_{ex} \otimes \hat{\mathbf{k}}' Im\{\check{\epsilon}(\omega)\} \hat{\mathbf{k}}'_{ord} \otimes \hat{\mathbf{k}}'_{ord} = 0$, the remaining integral expression has the form

$$\begin{aligned} \chi_{half}^{XY}(\mathbf{r}, \mathbf{r}', \omega) = Re \left\{ \int_{V'_k} d\mathbf{k}' e^{i(k'_x(x-x') + k'_y(y-y'))} \int_{-\infty}^{\infty} dk_z e^{i(k_z|z| - k'_z|z'|)} \left(\left(\frac{i(k'_z - k_z)}{(k'_z - k_z)^2 + \delta^2} + \frac{\delta}{(k'_z - k_z)^2 + \delta^2} \right) \left(\frac{\hat{\mathbf{p}} \otimes \hat{\mathbf{p}}}{(k_z^2 + k_\rho'^2)(k_z^2 - \gamma_1^{2*})} + \frac{\epsilon_P^* - \epsilon_A^*}{\epsilon_A^*} \frac{\hat{\mathbf{p}} \otimes \hat{\mathbf{k}}'_{z\rho}}{k_z^2 - \gamma_1^{2*}} \right) \right. \\ \left. Im\{\check{\epsilon}(\omega)\} \left(\frac{\hat{\mathbf{p}}' \otimes \hat{\mathbf{p}}'}{(k_z^2 - \gamma_1^2)(k_\rho'^2 + k_\rho'^2)} + \frac{\epsilon_P - \epsilon_A}{\epsilon_A} \frac{\hat{\mathbf{k}}'_{z\rho} \otimes \hat{\mathbf{p}}'}{k_z^2 - \gamma_1^2} \right) \right. \\ \left. + \left(\left(\frac{i(k'_z - k_z)}{(k'_z - k_z)^2 + \delta^2} + \frac{\delta}{(k'_z - k_z)^2 + \delta^2} \right) \left(\frac{\hat{\mathbf{s}}' \otimes \hat{\mathbf{s}}'}{k_z^2 - \gamma_2^{2*}} \right) Im\{\check{\epsilon}(\omega)\} \left(\frac{\hat{\mathbf{s}}' \otimes \hat{\mathbf{k}}'}{k_z^2 - \gamma_2^2} \right) \right) \right\}_N. \end{aligned} \quad (\text{F.18})$$

Here, $\gamma_1 = \sqrt{\epsilon_P - k_\rho'^2 \epsilon_P / \epsilon_A}$, $\gamma_2 = \sqrt{\epsilon_P - k_\rho'^2}$, $\hat{\mathbf{p}}$ and $\hat{\mathbf{k}}$ are written in terms of k'_ρ and k_z , $\hat{\mathbf{k}}'_{ex}$ and $\hat{\mathbf{k}}$ in terms of k'_ρ and k_z , and $\hat{\mathbf{k}}_{z\rho} = \langle 0, 0, k'_\rho \rangle$ with

$$\hat{\mathbf{s}} = [-s(\phi), c(\phi)k_\rho, 0] \quad (\text{F.19})$$

$$\hat{\mathbf{p}} = [-k_z c(\phi), -k_z s(\phi), k_\rho] / k \quad (\text{F.20})$$

$$\hat{\mathbf{k}} = [k_\rho c(\phi), k_\rho s(\phi), k_z] / k. \quad (\text{F.21})$$

Since only the trace is required to find the most pertinent thermodynamic quantities, (F.18) can be simplified as

$$\begin{aligned} \mathcal{F}_{half}(\mathbf{r}, \mathbf{r}', \omega) = Re \left\{ \int_{V'_k} d\mathbf{k}' e^{i(k'_x(x-x') + k'_y(y-y'))} \int_{-\infty}^{\infty} dk_z e^{i(k_z|z| - k'_z|z'|)} \right. \\ \left(\left(\frac{i(k'_z - k_z)}{(k'_z - k_z)^2 + \delta^2} + \frac{\delta}{(k'_z - k_z)^2 + \delta^2} \right) \right. \\ \left. \frac{(k'_z k_z + k_\rho'^2)(k_\rho'^2 Im\{\epsilon_A\} |\epsilon_P|^2 + k'_z k_z Im\{\epsilon_P\} |\epsilon_A|^2)}{|\epsilon_A|^2 (k_z^2 + k_\rho'^2)(k_z^2 + k_\rho'^2)(k_z^2 - \gamma_1^{2*})(k_z^2 - \gamma_1^2)} + \right. \\ \left. \left. \left(\frac{i(k'_z - k_z)}{(k'_z - k_z)^2 + \delta^2} + \frac{\delta}{(k'_z - k_z)^2 + \delta^2} \right) \frac{Im\{\epsilon_P\}}{(k_z^2 - \gamma_2^{2*})(k_z^2 - \gamma_2^2)} \right) \right\}_N. \end{aligned} \quad (\text{F.22})$$

without greatly reducing the utility of the result. By Jordan's lemma, the integral along the real axis of k'_z can again be evaluated by considering an infinite semi-circle

contour in the upper half-plane centered on the real axis. Applying the Cauchy integral theorem to this contour, three distinct pole types contribute:

(A) The pole resulting from the fluctuating current

At this first kind of pole $k_z = k'_z + i\delta$ so that

$$2\pi i \left(\frac{i(k_z - k'_z)}{(k_z - k'_z)^2 + \delta^2} + \frac{\delta}{(k_z - k'_z)^2 + \delta^2} \right) = 2\pi;$$

and resulting expression in \mathbf{k}' is the same as the full-space current fluctuations written in cylindrical coordinates.

(B) The pole resulting from cylindrical coordinates

For the second type and third type of pole, the $\delta \rightarrow 0$ limit of the Heaviside function can be taken immediately since the $k_z = k'_z$ pole has already been evaluated. In this limit, (F.22) reduces to

$$\begin{aligned} \mathcal{F}_{half}(\mathbf{r}, \mathbf{r}', \omega) = \text{Re} \left\{ \int_{V'_k} d\mathbf{k}' e^{i(k'_x(x-x') + k'_y(y-y'))} \right. \\ \left. \int_{-\infty}^{\infty} dk_z e^{i(k_z|z| - k'_z|z'|)} \left(\frac{i}{k'_z - k_z} \frac{(k'_z k_z + k'^2_\rho) (k'^2_\rho \text{Im}\{\epsilon_A\} |\epsilon_P|^2 + k'_z k_z \text{Im}\{\epsilon_P\} |\epsilon_A|^2)}{|\epsilon_A|^2 (k_z^2 + k'^2_\rho) (k'^2_\rho + k'^2_\rho) (k'^2_z - \gamma_1^{2*}) (k'^2_z - \gamma_1^2)} + \right. \right. \\ \left. \left. \frac{i}{k'_z - k_z} \frac{\text{Im}\{\epsilon_P\}}{(k_z^2 - \gamma_2^{2*}) (k'^2_z - \gamma_2^2)} \right) \right\}_N. \end{aligned} \quad (\text{F.23})$$

Focusing on the poles in the γ_1 term at $\pm i k'_\rho$, evaluating the k'_z integral as before, (F.23) becomes

$$\begin{aligned} \mathcal{F}_{half}(\mathbf{r}, \mathbf{r}', \omega) = \text{Re} \left\{ \int_{V'_k} d\mathbf{k}' e^{i(k'_x(x-x') + k'_y(y-y'))} e^{i(k'_\rho|z| - k'_z|z'|)} \right. \\ \left. \frac{k'^2_\rho \text{Im}\{\epsilon_A\} |\epsilon_P|^2 + i k'_z k'_\rho \text{Im}\{\epsilon_P\} |\epsilon_A|^2}{|\epsilon_A|^2 (k_z^2 + k'^2_\rho) (k'^2_\rho + \gamma_1^{2*}) (k'^2_z - \gamma_1^2)} \right\}_N. \end{aligned} \quad (\text{F.24})$$

Extending k'_z to the complex plane, and evaluating the integral along the real k'_z axis using a semi-circle in the lower half space, we find two poles, $-i k'_\rho$ and $-\gamma_1$.

The first of these poles gives

$$\mathcal{F}_{half}(\mathbf{r}, \mathbf{r}', \omega) = Re \left\{ \int_{V'_{\mathbf{k}_\rho}} d\mathbf{k}'_\rho e^{i(k'_x(x-x') + k'_y(y-y'))} \right. \\ \left. - e^{-k'_\rho(|z| + |z'|)} \frac{k'_\rho (Im \{\epsilon_A\} |\epsilon_P|^2 + Im \{\epsilon_P\} |\epsilon_A|^2)}{|\epsilon_A|^2 (k'^2_\rho + \gamma_1^{2*}) (k'^2_\rho + \gamma_1^2)} \right\}_N, \quad (\text{F.25})$$

and the second,

$$\mathcal{F}_{half}(\mathbf{r}, \mathbf{r}', \omega) = Re \left\{ \int_{V'_{\mathbf{k}_\rho}} d\mathbf{k}'_\rho e^{i(k'_x(x-x') + k'_y(y-y'))} \right. \\ \left. e^{-k'_\rho|z| + i\gamma_1|z'|} \frac{i k'^2_\rho Im \{\epsilon_A\} |\epsilon_P|^2 + k'_\rho \gamma_1 Im \{\epsilon_P\} |\epsilon_A|^2}{|\epsilon_A|^2 (k'^2_\rho + \gamma_1^2) (k'^2_\rho + \gamma_1^{2*}) (\gamma_1)} \right\}_N. \quad (\text{F.26})$$

(C) The pole resulting from the wave equations

The last type of pole in (F.23) results from the wave equations (eg. $k_z^2 - \gamma_1^2$). In order to make γ_1 and γ_2 continuous functions of k'_ρ the cut of the $\sqrt{\dots}$ function must be chosen to lie along the positive real axis. ($\gamma_1^2 = (1 - k'^2_\rho Re \{\epsilon_A\} + i k'^2_\rho Im \{\epsilon_A\}) \epsilon_P / |\epsilon_A|$ begins at an arbitrary point above the real axis in the complex plane, $k'^2_\rho = 0$, and proceeds contour clockwise with increasing k'^2_ρ to potentially cross any spoke from the origin other than the real axis.) The k_z integral is now evaluated as before giving

$$\mathcal{F}_{half}(\mathbf{r}, \mathbf{r}', \omega) = Re \left\{ \int_{V'_{\mathbf{k}}} d\mathbf{k}' e^{i(k'_x(x-x') + k'_y(y-y'))} e^{i(-\gamma_1^*|z| - k'_z|z'|)} \right. \\ \left(\frac{1}{k'_z + \gamma_1^*} \frac{(-k'_z \gamma_1^* + k'^2_\rho) (k'^2_\rho Im \{\epsilon_A\} |\epsilon_P|^2 - k'_z \gamma_1^* Im \{\epsilon_P\} |\epsilon_A|^2)}{|\epsilon_A|^2 (\gamma_1^{2*} + k'^2_\rho) (k'^2_z + k'^2_\rho) (\gamma_1^*) (k'^2_z - \gamma_1^2)} \right) \\ \left. + e^{i(-\gamma_2^*|z| - k'_z|z'|)} \left(\frac{1}{k'_z + \gamma_2^*} \frac{Im \{\epsilon_P\}}{(\gamma_2^*) (k'^2_z - \gamma_2^2)} \right) \right\}_N. \quad (\text{F.27})$$

where we have used the fact that the pole in the upper half plane generated by $\sqrt{\gamma^{2*}}$ is $-\gamma^*$. Again, k'_z is also analytically continued into the complex plane and the integral along the real axis evaluated by considering a semicircle in the lower

half-space. The $-ik'_\rho$ pole, which occur only in the extraordinary γ_1 term produces

$$\chi_{T \text{ half}}(\mathbf{r}, \mathbf{r}', \omega) = Re \left\{ \int_{V'_{\mathbf{k}_\rho}} d\mathbf{k}'_\rho e^{i(k'_x(x-x') + k'_y(y-y'))} e^{-k'_\rho|z'| - i\gamma_1^*|z|} \left(\frac{-ik'^2_\rho Im\{\epsilon_A\} |\epsilon_P|^2 + k'_\rho \gamma_1^* Im\{\epsilon_P\} |\epsilon_A|^2}{|\epsilon_A|^2 (k'^2_\rho + \gamma_1^2) (k'^2_\rho + \gamma_1^{2*}) (\gamma_1^*)} \right) \right\}_N, \quad (\text{F.28})$$

while the wave equation pole gives

$$\chi_{T \text{ half}}(\mathbf{r}, \mathbf{r}', \omega) = -Re \left\{ \int_{V'_{\mathbf{k}_\rho}} d\mathbf{k}'_\rho e^{i(k'_x(x-x') + k'_y(y-y'))} e^{i(\gamma_1|z'| - \gamma_1^*|z|)} \left(\frac{(|\gamma_1|^2 + k'^2_\rho) (k'^2_\rho Im\{\epsilon_A\} |\epsilon_P|^2 / |\gamma_1|^2 + Im\{\epsilon_P\} |\epsilon_A|^2)}{2Im\{\gamma_1\} |\epsilon_A|^2 (k'^2_\rho + \gamma_1^{2*}) (k'^2_\rho + \gamma_1^2)} \right) + e^{i(\gamma_1|z'| - \gamma_1^*|z|)} \left(\frac{Im\{\epsilon_P\}}{2Im\{\gamma_2\} |\gamma_2|^2} \right) \right\}_N. \quad (\text{F.29})$$

Summing the results of all (B) and (C) type poles, we find that in the limit $\{z, z'\} \rightarrow 0$ the total is exactly $-1/2$ that of the (A) type pole. Specifically, following the same integral procedure for k'_z the value of the (A) type pole is then

$$\chi_{T \text{ half}}(\mathbf{r}, \mathbf{r}', \omega) = 2Re \left\{ \int_{V'_{\mathbf{k}_\rho}} d\mathbf{k}'_\rho e^{i(k'_x(x-x') + k'_y(y-y'))} e^{-k'_\rho||z| - |z'|} \left(\frac{k'_\rho (Im\{\epsilon_A\} |\epsilon_P|^2 - Im\{\epsilon_P\} |\epsilon_A|^2)}{|\epsilon_A|^2 (k'^2_\rho + \gamma_1^{2*}) (k'^2_\rho + \gamma_1^2)} \right) \right\}_N. \quad (\text{F.30})$$

for the ik'_ρ term and

$$\chi_{T \text{ half}}(\mathbf{r}, \mathbf{r}', \omega) = 2Re \left\{ \int_{V'_{\mathbf{k}_\rho}} d\mathbf{k}'_\rho e^{i(k'_x(x-x') + k'_y(y-y'))} e^{i\gamma_1||z| - |z'|} \left(\frac{k'^2_\rho Im\{\epsilon_A\} |\epsilon_P|^2 / \gamma_1 + \gamma_1 Im\{\epsilon_P\} |\epsilon_A|^2}{|\epsilon_A|^2 Im\{\gamma_1^2\} (k'^2_\rho + \gamma_1^2)} \right) + e^{i\gamma_2||z'| - |z|} \left(\frac{Im\{\epsilon_P\}}{2\gamma_2 Im\{\gamma_2^2\}} \right) \right\}_N \quad (\text{F.31})$$

for the γ_1 , $-\gamma_1^*$, γ_2 , and $-\gamma_2^*$ poles. (The comparative factor of 2 results from the removal of the $\delta / ((k_z - k'_z) + \delta^2)$ piece of the current fluctuation).

The strength of the half-space transverse electric field fluctuation at the boundary is thus exactly half that of the full-space transverse electric field fluctuation. This conclusion is physically intuitive. Considering the full-space case: (1) the ran-

dom electric field is generated symmetrically about the boundary, (2) there is no net effect on the strength of the electric field fluctuation from the interaction of distinct volumes as the generating current is point correlated. Bringing these arguments together we conclude that the electric field fluctuation should be half as large in the half-space case, matching the above mathematical proof.